Stability and performance studies of the PITZ photoelectron gun

Dissertation
zur Erlangung des Doktorgrades
an der Fakultät für Mathematik, Informatik
und Naturwissenschaften
Fachbereich Physik
der Universität Hamburg

vorgelegt von
Igor Isaev

Hamburg
2017

Gutachter der Dissertation:	Prof. Dr. Jörg Roßbach Dr. Mikhail Krasilnikov
Zusammensetzung der Prüfungskomission:	Prof. Dr. Jörg Roßbach Prof. Dr. Jochen Liske Prof. Dr. Robin Santra Dr. Mikhail Krasilnikov Dr. Ye Chen
Vorsitzender der Prüfungskomission:	Prof. Dr. Jochen Liske
Datum der Disputation:	27.09.2017
Vorsitzender Fach-Promotionsausschusses PHYSIK:	Prof. Dr. Wolfgang Hansen
Leiter des Fachbereichs PHYSIK:	Prof. Dr. Michael Potthoff
Dekan der Fakultat für Mathematik, Informatik und Naturwissenschaften:	Prof. Dr. Heinrich Graener

Abstract

The invention of free electron lasers (FELs) opened new opportunities for the investigation of natural phenomena. However, the operation of a FEL requires high energy, high peak current electron beams with very small transverse emittance which causes extreme requirements for the corresponding electron sources. Besides the high beam quality, the electron sources must have very high operational stability and reliability. One of the electron source types which satisfy FEL requirements is a photoelectron gun. Photoelectron guns combine photoemissive electron generation and direct acceleration in a Radio Frequency (RF) cavity. The Photo Injector Test facility at DESY, Zeuthen site (PITZ), was established as a test stand of the electron source for FELs like FLASH and the European XFEL in Hamburg.

The studies of the beam emittance at PITZ showed that the gun is able to produce electron beams with emittance even smaller than it is required by XFEL specifications. But the experiments on the emittance revealed discrepancies between expected gun behavior and observation, such as the difference in optimal parameters for the smallest emittance value, asymmetry of the transverse beam profile and the phase spaces. The work performed at PITZ includes preparation of several RF guns for their subsequent operation at FLASH and the European XFEL. RF conditioning of a gun cavity is one of the major steps of the preparation of a high brightness electron source required for modern FELs. A thorough procedure is applied to increase the peak and average RF power in the gun cavity, including an increase of the repetition rate and RF pulse length combined with a gun solenoid current sweep.

The main goals of this thesis are: (1) an attempt of deep understanding of physical processes taking place during operation of a photoelectron gun (conditioning process, parameters adjustments); (2) definition of operational problems sources and explanation of the experimentally obtained results in the gun behavior; (3) understanding of the differences between models used to describe the gun operation and the real device. Furthermore, this thesis considers a few key problems of the photoelectron gun implementation at European XFEL: the beam quality improvement, understanding of the beam production behavior and beam features that can have an effect on the output radiation and the gun performance stability at the nominal parameters for XFEL.

Zusammenfassung

Die Entwicklung von Freien-Elektronen-Lasern (FELs) eröffnete neue Möglichkeiten für die Untersuchung verschiedenster Naturphänomene. Die Inbetriebnahme eines FELs erfordert jedoch Hochstrom-Elektronenstrahlen mit hoher Energie und sehr geringer transversaler Emittanz, was spezielle Anforderungen an die Elektronenquellen stellt. Neben der hohen Qualität des Teilchenstrahls müssen die Elektronenquellen eine sehr hohe Betriebssicherheit und Zuverlässigkeit aufweisen. Einer der Elektronenquellentypen, die die Anforderungen für den FEL erfüllt, ist die Photoelektronen-Kanone. Photoelektronen-Kanonen erzeugen Elektronen mittels Photoeffekt und beschleunigen diese in einem Hohlraumresonator. Die Photo-Injector Testanlage am DESY, Standort Zeuthen (PITZ), wurde als Teststandort für Elektronenquellen für FELs, wie FLASH und den European XFEL in Hamburg, gegründet.

Die Untersuchungen der Strahl-Emittanz bei PITZ zeigten, dass die Elektronenkanone in der Lage ist, Teilchenstrahlen mit einer Emittanz zu erzeugen, die noch kleiner ist als für den XFEL erforderlich. Aber die Experimente zur Emittanz zeigten auch eine Abweichung zwischen dem erwarteten Kanonenverhalten und den experimentellen Beobachtungen, wie zum Beispiel der Unterschied in den optimalen Parametern für den kleinsten Emittanzwert, die Asymmetrie des transversalen Strahlprofils und der Phasenräume. Zu den Aufgaben von PITZ zählt unter anderem die Vorbereitung mehrerer Hochfrequenz(HF)-Kanonen für den nachfolgenden Betrieb bei FLASH und dem European XFEL. Die HF-Konditionierung des Hohlraumresonators einer Elektronenkanone ist einer der Hauptschritte bei der Vorbereitung einer hochintensiven Elektronenquelle, die für moderne FELs erforderlich ist. Um sowohl die durchschnittliche als auch die Maximalleistung in dem Hohlraumresonator zu erhöhen, wird ein sorgfältiges Verfahren, bestehend aus der Steigerung der Wiederholfrequenz, Verlängerung des HF-Pulses und einem Solenoid-Strom-Sweep, angewendet.

Die Hauptziele dieser wissenschaftlichen Arbeit sind: (1) das tiefere Verständnis der physikalischen Prozesse, die während des Einsatzes einer Photoelektronen-Kanone stattfinden (Konditionierungsprozess, Anpassung der Parameter); (2) Definierung der Fehlerquellen beim Betrieb und Erläuterung der experimentellen Ergebnisse bezüglich des Kanonenverhaltens; (3) Verdeutlichung der Unterschiede zwischen den theoretischen Modellen, die die Elektronenkanone beschreiben, und dem tatsächlichen Aufbau. Darüber hinaus beschäftigt sich diese Dissertation mit einigen wesentlichen Problemen, die die Anwendung der Photoelektronen-Kanone beim European XFEL betreffen: die Verbesserung der Strahlqualität, das Verständnis der Strahl-Erzeugung sowie solcher strahleigenschaften, die sich auf die Ausgangsstrahlung des FEL und die Stabilität der Kanone bei XFEL auswirken können.

Contents

Chapter 1

Introduction

Study of the microscopic structures is of the great importance for the several areas of the modern natural science. It gives us a unique opportunity to observe the highly complex tiny structures of our world. However, to realize those studies and to resolve fine structures the production of the ultra-short coherent electromagnetic waves is requested. Therefore the development of sources of powerful radiation has become an essential task.

The basis of modern light sources of powerful electromagnetic radiation are machines where charged relativistic particles move in electromagnetic fields of various configurations and produce light which is called synchrotron radiation. The radiation name was given regarding the machine type where the radiation was observed at the first time.

The light sources of synchrotron radiation can be characterized by a property which is called brilliance. Brilliance is defined as the number of photons, emitted by the source per time unit in solid angle, per cross-section of the beam within a bandwidth of the central light frequency around the frequency of the emitted light. The units of brilliance are expressed as photons/second/mm^2/mrad^2/(0.1%bandwidth) [1].

In the pursuit of the high output power of radiation, undulators were developed. They became a replacement of bending magnets used at synchrotrons. Undulator is a magnetic system that creates a spatially periodic alternating transverse magnetic field by a combination of multiple dipole magnets. Relativistic electrons moving in the undulator field undergo a sinusoidal or helical path and thus emit photons (Fig. 1.1).

The nature of synchrotron and undulator radiations is the same: charged particles radiate on their way along a curved trajectory. However, the emission spectra are completely different due to the configuration of the trajectory: in a synchrotron a charged particle moves by a circular orbit and in an undulator a particle undergoes small rapid oscillations perpendicular to the direction of its motion due to the action of the periodic magnetic field of the undulator.

The successive step in the development of powerful radiation sources was the invention of Free-Electron Lasers (FELs). The basic principle of FELs is the

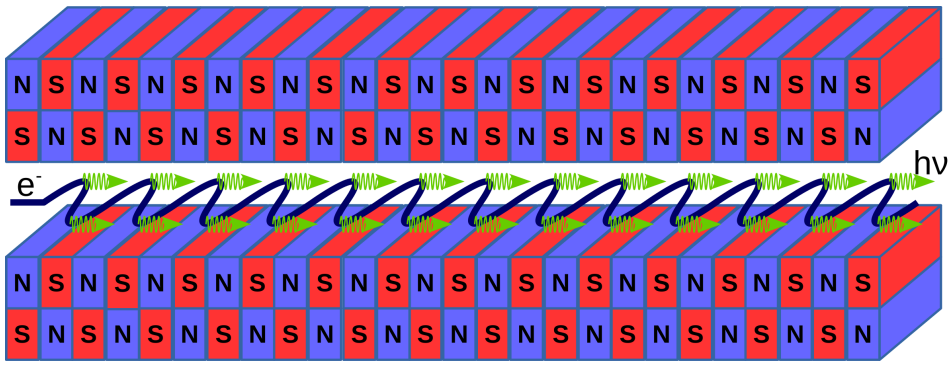

Figure 1.1: Schematic view of an undulator. The electron beam emits photons (green arrows) on its trajectory along a sinusoidal curve (dark blue line) due to interaction with a magnetic field which is created by permanent magnets with alternating polarity.

utilization of high-energy electron beams for coherent radiation production by the use of undulators. The main advantage of FELs is monochromatic radiation at any given wavelength (from 0.1 nm to 1 mm). The average power of FELs may reach an order of 100 kW, while maintaining high diffraction quality of the radiation source. This is possible due to the fact that there is no laser medium that can deteriorate during power increase through heating and appeared density gradients.

Since the construction of optical resonators at wavelengths shorter than 10 nm is complicated (due to the requirement of ultra high mechanical stability and reflectivity of mirrors), FELs should be realized as a single-pass machine. In order to satisfy the radiation parameters required by users a linear accelerator (linac) together with Self-Amplified Spontaneous Emission (SASE) [2] are used for FELs (SASE FELs).

FELs can be based on different types of particle accelerators. From the physical point of view, it is possible to use acceleration mechanisms starting from radio frequency (RF) field acceleration in linacs and up to laser- and plasma-based ([3], [4]) wakefield acceleration. While technologies of wakefield accelerators are still in a development stage, linear normal and superconducting accelerators are already widely used for FEL applications.

The concept of linacs for FELs applications consists of a few common points. First of all, a linac requires many electrons densely packed in short bunches with very small emittance (see more in chapter 2). Due to the high bunch charge, a problem with space charge effects can occur and disturb the emittance during bunch production. Therefore, the electron source must have a high acceleration gradient at the place of the bunch emission. Since it is quite challenging to produce short enough bunches at the electron sources, the bunches must be compressed along the linac. The longitudinal bunch compression must be performed at the ultra-relativistic beam energies, because of the space-charge forces, which are one of the major compression restrictions. The space-charge forces are scaled with the factor of $1/\gamma^2$ [5] and become significantly reduced at

high beam energies.

A usual beam acceleration cycle consists of following stages: electron beam production → pre-acceleration → compression → acceleration → compression → acceleration → radiation production.

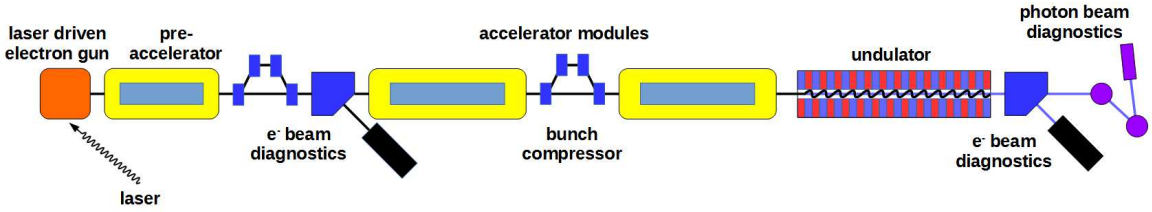

Figure 1.2: Simplified single-pass FEL layout. Major components are the photocathode RF gun, accelerating modules, bunch compressors, undulators, transfer lines guiding the FEL radiation to dedicated experiments and the beam dump.

Usually linac-based FELs consist of the following parts: (a) an electron injector (RF photoelectron or a special thermionic gun in combination with a pre-acceleration stage) where the produced electrons undergo initial acceleration and obtain further kinetic energy in the main accelerator part, (b) bunch compressors which can be installed between the accelerating modules in order to longitudinally compress the bunch and to increase its peak current, (c) undulator magnets and transfer lines, guiding the radiation to photon experiments located at the end of the setup, (d) bending magnet for the separation of electrons and photons, (e) diagnostics components which are typically located in the sections where control of the beam quality parameters is needed. A simplified schematics layout of a single-pass machine is shown in Fig. 1.2.

One of the main advantages of the contemporary SASE FELs compared to the 3rd generation light sources is 8 to 9 orders of magnitude higher peak brilliance. The peak brilliance for the different facilities is presented in Fig. 1.3.

However, at the same time, the fact that FELs are based on the single-pass linacs causes much higher requirements for the electron sources compared to the circular machines (e.g. electron storage rings). The beam quality in a storage ring is mainly defined by characteristics of a circular beamline, such as synchrotron radiation emittance damping, quantum excitation, beam chromaticity, beam current, misalignment of magnets and various beam instabilities. It is also strongly dependent on a design of lattice and bending magnets. An electron source for the FEL applications must provide beams with an ultra-high quality and high intensity. It is of paramount importance to achieve a good emittance of the beam in the injector section because along the rest part of the machine there is no possibility to reduce it[1].

Besides the high beam quality, the electron sources must have very high operational stability and reliability.

[1]The principle possibility for transverse-longitudinal phase space exchange [9] have not come to meaningful practical use at FEL facilities.

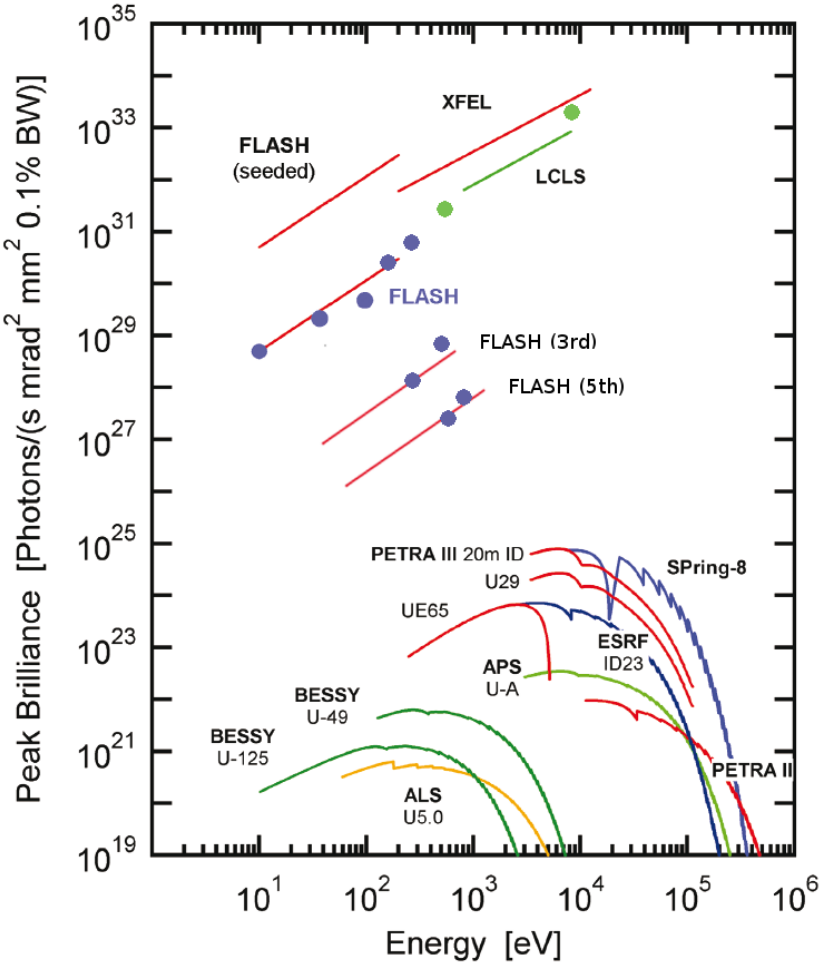

Figure 1.3: Peak brilliance of SASE FELs in comparison to the 3rd generation light sources [1, 6]. The blue and the green dots indicate the operating regime of the FLASH [7] and LCLS [8] facilities respectively.

One of the electron source types which satisfy FEL parameters is a photoelectron gun. Photoelectron guns combine electron generation utilizing photoemission and direct acceleration in the RF cavity. Photoemission not only allows the generation of higher current densities [10] than in the case of thermionic cathodes but also provides better control over the transverse and longitudinal electron pulse distributions. In comparison with a DC (Direct Current) photoelectron gun, an RF cavity [11] provides a higher field amplitude at the cathode and a higher total accelerating voltage. Both of these aspects are important for the mitigation of the space-charge-induced emittance growth.

The Photo-Injector Test Facility at DESY in Zeuthen (PITZ) [12] is built to develop, operate and characterize electron sources meeting the requirements for FELs operated

in the SASE regime as Free-electron LASer in Hamburg (FLASH) [7] and the European X-ray Free Electron Laser (European XFEL or just XFEL) [13]. These requirements include a projected transverse normalized RMS (Root Mean Square) emittance below 1 mm mrad, an RMS bunch length below a few mm and a nominal bunch charge of 1 nC [1].

The main PITZ facility goals are:

- development of an electron source for the European XFEL:
  - very small normalized transverse emittance ($<$ 1 mm mrad at 1 nC bunch charge)
  - stable production of short bunches with a small energy spread
- extensive R&D (Research and Development) on photo-injectors (in parallel to FLASH operation)
- comparison of detailed experimental results with simulations:
  - benchmark theoretical understanding of photo-injectors
- preparation and characterization of the RF guns for subsequent operation at FLASH / XFEL
- testing of new developments (laser, cathodes, beam diagnostics)

A simplified overview of the current PITZ setup is shown in Fig. 1.4. The accelerating sections of PITZ consist of a laser-driven RF gun and a booster cavity.

The beam is accelerated by the gun cavity up to 7 MeV and afterward up to 25 MeV by the normal-conducting Cut-Disc Structure (CDS) type booster cavity [15]. The PITZ beamline consists of two parts: the low-energy one downstream the gun cavity, and the high energy section downstream the booster cavity. Both sections consist of various diagnostics. The similar diagnostics components are named accordingly to their location in the beamline.

The diagnostic[2] includes three Emittance Measurement SYstems (EMSY1, 2 and 3), a Low-Energy and two High-Energy Dispersive Arms (LEDA, HEDA1 and HEDA2), multiple OTR (Optical Transition Radiation) and YAG (Yttrium Aluminium Garnet) observation screens (Low.Scr1..3, High1.Scr1..5, and High2.Scr1,2) for transverse distributions measurements and charge measurement devices (two Faraday Cups (Low.FC1,2) and one Integrating Current Transformer (Low.ICT1) in the low-energy section; two ICTs in the high-energy section (High1.ICT1 and High1.ICT2)).

[2]The list of the diagnostic components includes only the devices which are related to the measurements done for this work. More detailed description can be found under `https://wiki-zeuthen.desy.de/PITZ`.

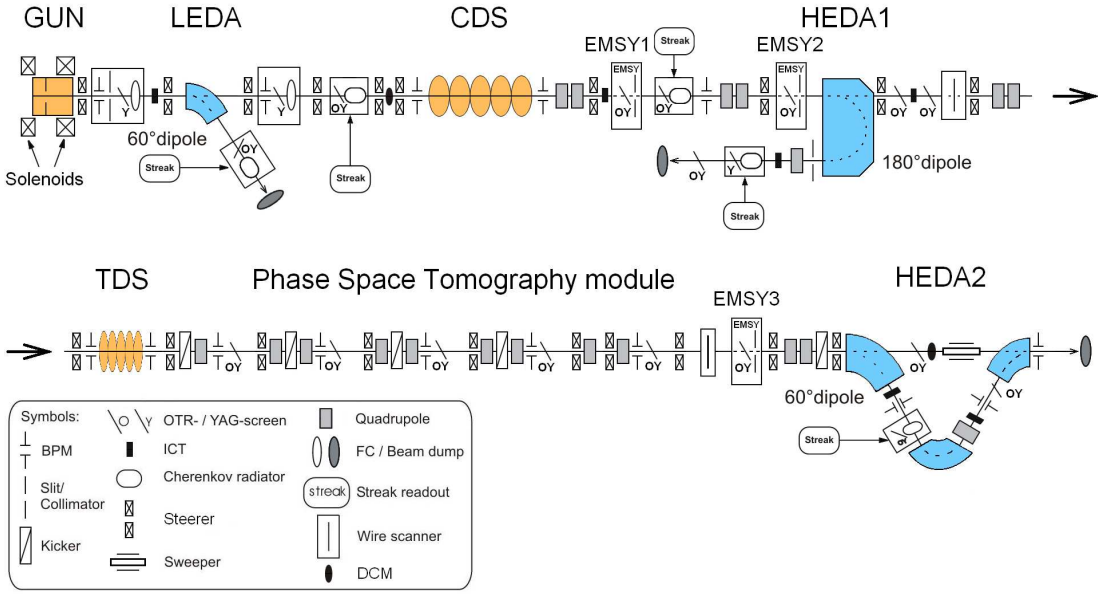

Figure 1.4: Schematic layout of the PITZ facility beamline. The main components of the beamline are described in the body of the text. Blue and orange colors indicate dipole magnets and RF cavities correspondingly. The beam propagates from left to right [14].

The Transverse Deflecting Structure (TDS) [14] and the module for transverse phase-space tomographic diagnostics [16] in the second part of the beamline are placed.

The nominal PITZ parameters that were experimentally demonstrated [17] are summarized in Table 1.1.

Parameter	**Value**
Beam bunch charge [nC]	0.001 - 4
Beam mean momentum after gun / booster [MeV/c]	6.5 / 25
Number of pulses in the train	≤ 800
Repetition rate [Hz]	10
Microbunch spacing in pulse train [μs]	1
Maximum average beam current [μA]	≤ 32
Optimized emittance for 1 nC [mm mrad]	< 0.9

Table 1.1: Main parameters of the PITZ facility.

The PITZ photoelectron gun (Fig. 1.5) consists of a 1.6 cell normal conducting cavity produced from Oxygen-Free high Thermal Conductivity (OFHC) copper. The cavity operates in the standing wave regime in the π-mode with the resonant frequency of

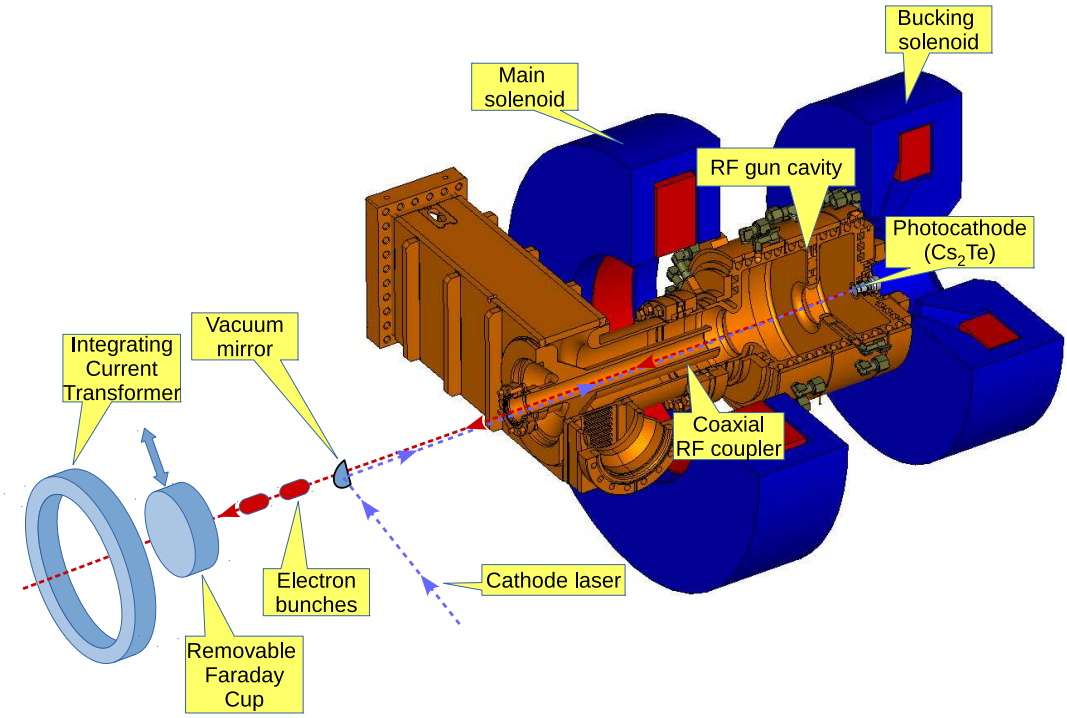

Figure 1.5: The layout of the gun setup at PITZ. The cathode laser beam, transported to the gun vacuum part, reflects from the vacuum mirror and produce photoelectron bunches by hitting the photocathode surface, which is located in the RF cavity. The produced electron bunches are accelerated by the RF fields and focused by the combination of the static magnetic fields from the main and the bucking solenoids. The beam charge measurements are done by the integrating current transformer or the Faraday cup.

1300 MHz. The gun cavity is supplied by RF power via an RF coaxial coupler which has transition to a rectangular WR 650 waveguide. The backplane of the cavity contains a so-called door-knob slot where a molybdenum photocathode plug can be placed by a load-lock system. The photocathode has a Cs_2Te coating on a front surface for photoelectron production. The photocathode vicinity consists of a CuBe spring for better electrical RF contact between the gun cavity and the cathode plug. The RF gun is surrounded by two solenoids. A magnetic field produced by the main solenoid is used to focus the electron beam, and the bucking coil compensates the magnetic field at the cathode. Since the gun cavity operates with RF pulses up to 1 ms, the peak power of 7 megawatts and 10 Hz repetition rate, the cavity body must be heavily cooled. For this purpose water cooling channels in the gun cavity body walls and irises are envisaged by design. The water cooling channels of the gun prototype 4 are presented in Fig. 1.6. The photocathode UV laser beam is delivered to the photocathode surface via a vacuum mirror installed in the PITZ beamline downstream the gun [18].

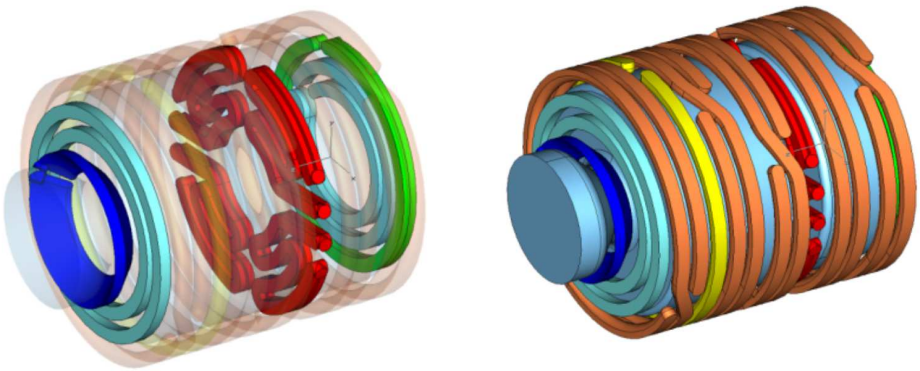

Figure 1.6: The water cooling channels of the gun prototype 4. The channels are located in the gun cavity copper body, around the cavity vacuum volume. Each channel has individual water input and output.

The current PITZ laser, developed by the Max Born Institute, Berlin [19], is designed to fulfill requirements imposed by beam dynamics simulations. The simulations show that minimum transverse emittance can be achieved with a flat-top temporal laser profile having about 20 ps Full Width at Half Maximum (FWHM) pulse duration and 2 ps rise and fall times [17]. The laser is able to generate pulse trains with a repetition rate of 10 Hz with up to 800 micropulses. The spacing within a pulse train is 1 μs. The final laser wavelength is 258 nm. The laser beam parameters can be adjusted by multiple beamline components: (a) a Beam Shaping Aperture (BSA) which is realized as remotely controllable iris diaphragm and used for the transverse beam size adjustments; (b) a temporal pulse shaper which is based on 13 birefringent crystals and dedicated for the temporal beam tuning; (c) a $\lambda/2$ plate attenuator is used for Laser Transmission (LT) intensity adjustment; (d) the laser beam transverse position alignment at the cathode is done by two remotely controllable mirrors (M5 and M6 according to the laser beamline naming). The transverse position and shape of the laser beam is controlled by a CCD (Charge-Coupled Device) camera which is installed in the laser diagnostic section close to the gun and located at the same optical distance as the cathode. This camera is called Virtual Cathode camera 2 (VC2). The combination of the laser beamline components makes the PITZ laser versatile for the adjustments.

The main goals of this thesis are an attempt of deep understanding of physical processes taking place during operation of a photoelectron gun (conditioning process, parameters adjustments), definition of operational problems sources and explanation of the experimentally obtained results in gun behavior, as well as understanding the differences between models used to describe gun operation and the real device. This thesis considers a few key problems of the photoelectron gun implementation at European XFEL: (a) the beam quality improvement, (b) understanding of beam

production behavior and beam features that can have an effect on the output radiation and (c) the gun performance stability at the nominal parameters for XFEL.

The studies of the beam emittance at PITZ [20] showed that the gun is able to produce the electron beams with emittance even smaller than it is required by XFEL specifications. But the experiments on the emittance revealed discrepancies between expected gun behavior and reality, such as difference in optimal main solenoid current and BSA size for the smallest emittance value, difference in charge extraction (especially for the case of the space charge limited regime [21]) and asymmetry of the transverse beam profile and the x and y phase spaces, which contradicts to the axially symmetric design of the gun. These effects may cause problems with adjustments and production of the FEL radiation during the future operation of the XFEL facility. The gun performance and beam dynamics issues in case of non-perfect asymmetric electromagnetic fields as well as possible sources of the asymmetries are presented in chapter 2.

Another gun property which requires detailed consideration is the amplitude and phase stability of the gun RF fields. Since the European XFEL is designed to work with long bunch pulse trains (up to 2700 bunches per train), the gun must be able to provide long and stable RF pulses in order to keep the required bunch parameters within the full pulse train as well as from shot to shot. The issues of the gun stability and RF power jitters are reviewed in the 3rd chapter, where methods and systems applied at PITZ for a jitter decrease are described.

Except of the good output beam parameters the operation of a user facility requires stable operation of the gun on a 24/7 basis. This means that the number of FEL operation interruptions should not be larger than one per week. In combination with the designed gun RF peak power (6.5 MW) and pulse length (650 μs), this requirement leads to the fact that gun preparation (production and conditioning) must be done very carefully in order not to damage the gun parts. The gun reliability and conditioning process issues, as well as PITZ experience with photoelectron guns, are presented in chapter 4.

Chapter 2

Gun performance and beam dynamics

Despite the RF photoelectron gun is designed to be rotational symmetric, the observed electron beam has an asymmetric structure [22]. The gun design for the FLASH and XFEL applications includes the following features: rotational symmetry of the cavity and RF coupler; the water cooling system is made for very high heat exchange and a good temperature stabilization; the Micro Telecommunications Computing Architecture (μTCA) based RF system together with water cooling system provides stable RF field amplitude and phase (requirements: 0.01 ° phase stability and 0.01 % amplitude stability [1]); flexible cathode laser for beam emittance optimization; exchangeable cathode vacuum load-lock system. Nevertheless, during operation of many guns, there were observed irregularities of the transverse beam profile which disturb the beam emittance.

The discussion in this chapter is concentrated on the gun field asymmetry influence on the electron beam dynamics in the photoinjector. The introduction to the photoemission, acceleration, focus and electron beam emittance is presented at the beginning of the chapter followed by discussions about beam shape and phase space irregularities and their possible sources. The information about possible solutions of the problem completes the chapter.

2.1 Beam dynamics in the gun

A charged particle beam dynamics in the PITZ gun is a complex process which combines photoemission, acceleration and focusing effects under space charge forces.

2.1.1 Photoemission process

The formation of an electron beam in the gun starts from the photoelectric effect. In the photoelectric effect, electrons are emitted from a material when a laser pulse

hits its surface. These electrons are called photoelectrons. Photoelectron sources in the accelerator technology typically use metals or semiconductors as materials for photoemission. The PITZ photocathode gun uses semiconductor Cs_2Te photocathodes for photoelectron production. An advantage of the semiconductor cathode compared to metals is a higher quantum efficiency[1] (QE) by several orders of magnitude. The disadvantage is a more difficult production and special requirements for operation with the cathodes (semiconductor cathodes require very high vacuum level).

According to the Spicer model [23], the photoemission consists of three steps: an excitation of the electron by the absorbed photon, migration of the electron towards the surface and electron emission across the surface potential barrier.

The electron excitation means the transition of an electron from the valence band to the conduction band. The PITZ photocathode UV laser has a wavelength of 257.5 nm, which corresponds to a photon energy of $E_{photon} = hc/\lambda \cong 4.82\,eV$. It allows to perform an efficient electron excitation from the upper valence band (the maxima of the state energy density $-0.7\,eV$) to the lower conduction band (the maxima of the state energy density $4.05\,eV$).

After an excitation the electrons travel to the surface where they may escape the photocathode expending a part of their energy for penetrating the band gap ($E_g = 3.3\,eV$), and overcoming the surface potential barrier (also called electron affinity, $E_a = 0.2\,eV$). So, the threshold photon energy for electron emission is $E_{thr} = E_g + E_a = 3.5\,eV$. The final average kinetic energy of the electrons can be calculated by subtracting the band gap and the surface potential barrier values from the maxima of the state energy density of the lower conduction band and, given by: $E_{kin} = (4.05 - E_{thr})\,eV = 0.55\,eV$ [24].

The electron band structure of the Cs_2Te and the excitation process are presented in Fig. 2.1. The structure was measured by Powell et al. [23]. The electrons, emitted from the photocathode surface, have an isotropic angular distribution of the velocities.

For the practical case, the photoemission at high brightness RF guns takes place under the presence of strong space charge forces in the cathode region. This happens due to the fact that often the high charge of the beam is required. The speed of the particles at emission is still close to zero that causes strong space change fields and would let to the beam explode.

2.1.2 Beam acceleration

The emitted electrons gain their energy from the RF electric field of the gun cavity. Particle acceleration in the PITZ gun happens in two connected resonators which are called full and half (or cathode) cells. The full cell has two apertures for beam traveling trough the resonator while the half cell has only one from the side of the full cell and a cathode located at the another side. In a simplified consideration, the cells can be

[1] quantum efficiency is the ratio of gained electrons per incident photon

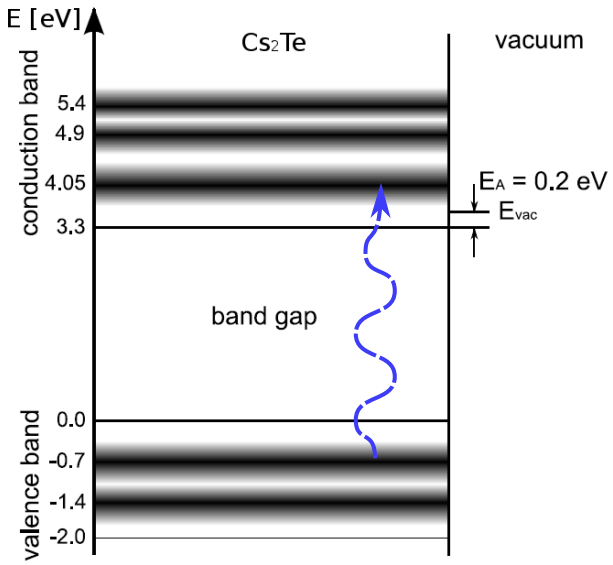

Figure 2.1: Schematic structure of the energy levels of Cs_2Te according to Powell [23]. The maxima of density of states are shown in black.

represented by a pillbox resonator model. Each pillbox resonator operates in a TM_{010}-like standing-wave mode. The E and H field structures in a cell are shown in Fig. 2.2. The electric field along the central axis in a pillbox cavity can be described by [25]:

$$E_z(z,\phi) = \frac{1}{2}E_0[\sin\phi + \sin(\phi + 2kz)]\,, \tag{2.1}$$

and the magnetic field by:

$$B_\theta(z,r,\phi) = \frac{r}{4}\frac{E_0}{c}k[\cos\phi + \cos(\phi + 2kz)]\,, \tag{2.2}$$

where z and r are longitudinal and radial coordinates. The RF phase ϕ is defined as:

$$\phi = \omega t - kz + \phi_0\,. \tag{2.3}$$

Here k is a wave number, c is the speed of light and ϕ_0 is a starting phase. The sum of two sines in Eq. 2.1 and two cosines in Eq. 2.2 illustrates the fact that a standing wave can be described by superposition of a forward and backward traveling wave.

The total electric field activity on a particle in the resonator can be obtained by integration of the field $E_z(z,\phi)$ from Eq. 2.1 over time and longitudinal coordinate of the particle trajectory. The beam energy gain introduced in terms of γ (the ratio of the particle total energy to its rest energy):

$$\frac{d\gamma}{dz} = \frac{eE_0}{2m_ec^2}[\sin(\phi) + \sin(\phi + 2kz)]\,, \tag{2.4}$$

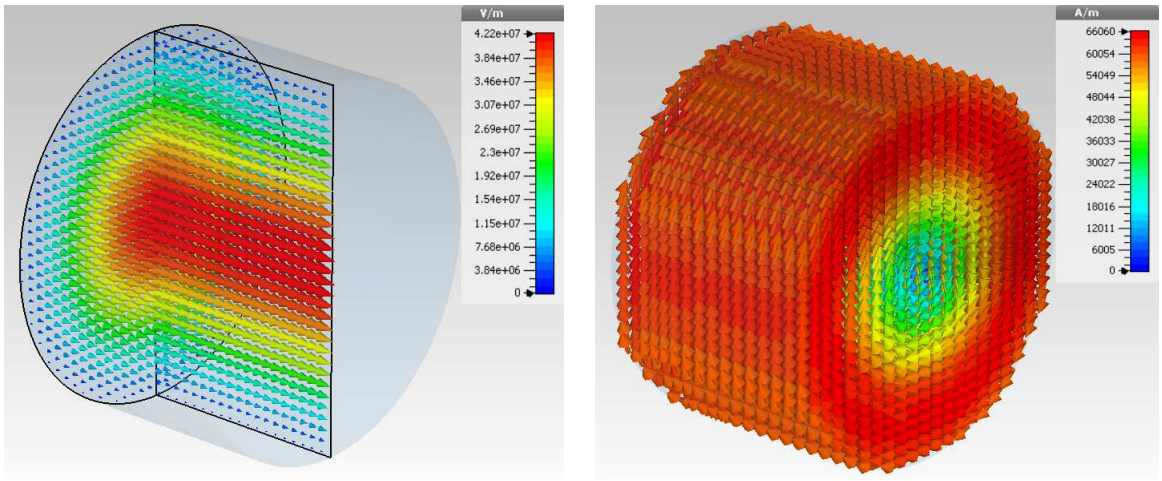

(a) Example of E field in a pillbox resonator

(b) Example of H field in a pillbox resonator

Figure 2.2: An example of RF fields in a pillbox resonator simulated by the CST Microwave studio [26]. The pillbox resonator has a purely axial electric field and a purely azimuthal magnetic field. The magnetic field B has exactly the same structure as the H-field, the only difference is the μ-coefficient in the free-space case. Then $\dot{\mathrm{B}} = \mu_0 \dot{\mathrm{H}}$.

where e is the elementary charge and m_e is the electron rest mass.

In order to efficiently deliver energy to the electrons, so-called the π-mode of the gun RF fields is used. This means that the fields are combined a way so that electric field in one cell is accelerating while in another is decelerating. Alternatively, the RF field phase advance between cells is 180 °. An electron emitted from the cathode accelerates in the first half cell. The length of the first half cell is chosen so that when the electron comes to the entrance of the second full cell the field changes its sign and the electron accelerates further in the full cell. The gun electric field structure for the case of on-crest phase (zero) is presented in Fig. 2.3.

Since the incident laser pulse has a certain transverse and temporal shape, emission of a group of electrons takes place. The response time of the Cs_2Te photocathode is short ($\leq$ ps) compared to the laser pulse duration and therefore the electron bunch is supposed to have similar spatial and temporal shapes as the laser beam pulse. But the emitted electron bunch shape is modified by beam space-charge forces, image charge and field enhanced emission which is taking place during the extraction in RF fields.

When the density of the extracted charge is high, the space charge forces start to play a role in the beam formation. The space-charge forces cause an additional beam defocusing, distort the particle distribution due to their nonlinearity and produce a beam halo surrounding the main core of the beam.

Another aspect of the beam distortion is the image charge effect. Due to this effect between charged particle and conducting wall, electrostatic field lines are perpendicular

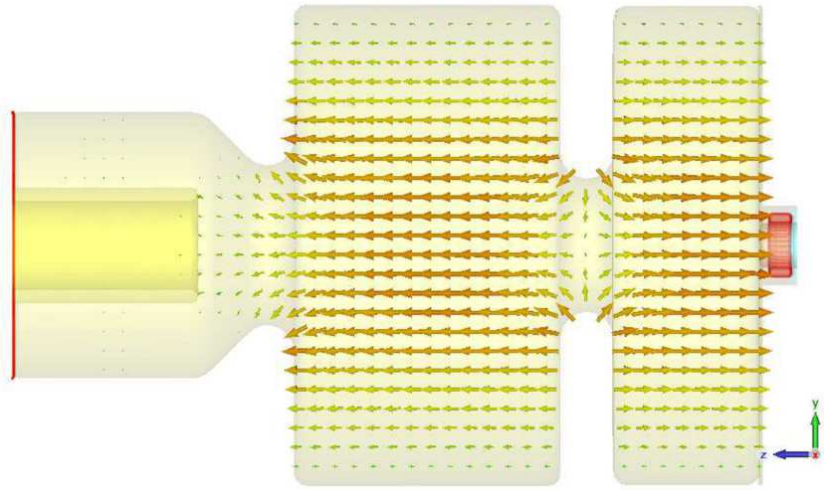

Figure 2.3: Electric RF field structure in the PITZ RF photo gun geometry simulated by the CST Microwave studio [26].

to the wall surface. The field structure can be described by the replacement of the wall by another particle of opposite charge located behind the surface and having the same distance to the surface as the electron itself. In the case of high charge density beams, the electric field produced by the space charge of the bunch reduces the RF accelerating field.

The estimation of the critical charge level, at which a space charge field fully compensates the acceleration field, can be done by the Child-Langmuir law [27] for a constant current streaming from the cathode:

$$J = \frac{4}{9} \cdot \varepsilon_0 \sqrt{\frac{2e}{m_e}} \frac{\phi^{\frac{3}{2}}}{d^2} \,. \tag{2.5}$$

Here m_e is the electron rest mass, e is the elementary charge, ε_0 is the permittivity of free space, ϕ is the potential difference between the cathode surface and a point at the distance d. The maximum current density J causes the field a drop to zero at the cathode surface due to the space charge forces.

The field-enhanced emission gives an additional charge to an emitted beam which depends on the RF field strength. This effect can be named as the Schottky-like effect due to its similarity to the field-enhanced emission from a metal surface (Schottky effect) [28]). The strong electric fields at the surface can assist the electron emission by lowering the surface potential barrier. The energy required to remove an electron from the highest filled level in the Fermi distribution of a solid is called work function ϕ_{work}. The combination of the mirror charge (which acts as deceleration force during emission) and the accelerating electric field decrease the work function by changing the minimum required energy for an electron extraction.

2.1.3 Beam focusing

During the electron beam acceleration in the gun cavity, the beam undergoes strong defocusing due to the space charge effect. In order to compensate this a solenoid pair is applied (Fig. 2.4). The solenoids also help to compensate the emittance during the acceleration in the gun cavity [29].

The focusing in a solenoid is explained by Busch's theorem [30]. The theorem says that a canonical angular momentum of the particle beam is conserved while traveling in the axisymmetric magnetic field of a solenoid. A charged particle traveling in the region of a uniform magnetic field of a solenoid starts rotating with the Larmor frequency that is equal to the half of the cyclotron frequency in the uniform magnetic field. The net force towards the solenoid axis provides a beam focusing in the solenoid field. When the particle exits the solenoid field, the particle azimuthal velocity becomes zero and its radial velocity is proportional to the radial distance of the particle from the solenoid axis.

The PITZ case is more complicated by that fact that the RF field of the gun cavity and the magnetic field of the solenoids are overlapped. This means that focusing by the solenoid field happens while the electron beam is being accelerated. Besides that, transverse components of the RF field (E_r and B_θ) are affecting the transverse dynamics of particles.

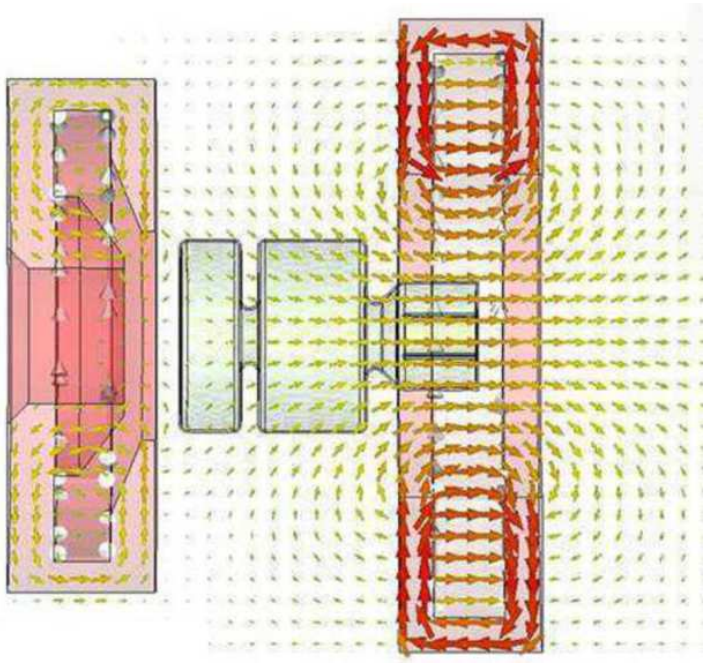

Figure 2.4: Model of the pair of solenoids surrounding the PITZ gun cavity with magnetic field structure. Field structure is simulated in the CST EM studio [26].

2.1.4 Beam characterization

The beam dynamics characterization applies the concept of six-dimensional phase space for description of the particle beam dynamics. The concept evolves out of the Hamilton formalism and based on a set of canonical coordinates: coordinate $\overrightarrow{q} = \{q_1, q_2, q_3\} = \{x, y, z\}$ and momentum $\overrightarrow{p} = \{p_1, p_2, p_3\} = \{p_x, p_y, p_z\}$, where $\overrightarrow{p} = \overrightarrow{\beta}\,\gamma$, $\overrightarrow{\beta} = \overrightarrow{v}/c$, $\gamma = 1/\sqrt{1-\beta^2}$ is the Lorentz factor, and c is the speed of light. The canonical variables provide:

$$\frac{\partial H}{\partial q_i} = \frac{-dp_i}{dt}\,, \tag{2.6}$$

$$\frac{\partial H}{\partial p_i} = \frac{dq_i}{dt}\,, \tag{2.7}$$

where H is the Hamiltonian of the system, t is time and $i = 1, 2, 3$ [31].

Introducing a particle distribution function or density of particles in phase space $\Psi(\overrightarrow{q}, \overrightarrow{p})$, the total number of particles in a six-dimensional volume becomes:

$$N = \int \Psi(\overrightarrow{q}, \overrightarrow{p})\,\mathrm{d}\overrightarrow{q}\,\mathrm{d}\overrightarrow{p}\,, \tag{2.8}$$

where $\mathrm{d}\overrightarrow{q}\,\mathrm{d}\overrightarrow{p} = \mathrm{d}x\,\mathrm{d}y\,\mathrm{d}z\,\mathrm{d}p_x\,\mathrm{d}p_y\,\mathrm{d}p_z$. According to Liouville's theorem of Hamiltonian mechanics, the six-dimensional phase space density along any particle trajectory is a conserved quantity [5].

The phase space of the beam can be characterized using moments of a distribution function.

$$\text{The first oder moment}: \quad \langle\xi\rangle = \int \xi f(\overrightarrow{r}\,\overrightarrow{p})\,\mathrm{d}\overrightarrow{r}\,\mathrm{d}\overrightarrow{p}\,, \tag{2.9}$$
$$\xi = x, ..., p_z\,.$$

$$\text{The second oder moment}: \quad \langle\xi\nu\rangle = \int (\xi - \langle\xi\rangle)(\nu - \langle\nu\rangle) f(\overrightarrow{r}\,\overrightarrow{p})\,\mathrm{d}\overrightarrow{r}\,\mathrm{d}\overrightarrow{p}\,, \tag{2.10}$$
$$\xi, \nu = x, y, ..., p_z\,.$$

All (21) second order moments form 6×6 matrix $\widehat{\mathrm{M}}_{\xi\nu}$:

$$\widehat{M}_{\xi\nu} = \begin{pmatrix} M_{xx} & M_{xp_x} & M_{xy} & M_{xp_y} & M_{xz} & M_{xp_z} \\ M_{p_xx} & M_{p_xp_x} & M_{p_xy} & M_{p_xp_y} & M_{p_xz} & M_{p_xp_z} \\ M_{yx} & M_{yp_x} & M_{yy} & M_{yp_y} & M_{yz} & M_{yp_z} \\ M_{p_yx} & M_{p_yp_x} & M_{p_yy} & M_{p_yp_y} & M_{p_yz} & M_{p_yp_z} \\ M_{zx} & M_{zp_x} & M_{zy} & M_{zp_y} & M_{zz} & M_{zp_z} \\ M_{p_zx} & M_{p_zp_x} & M_{p_zy} & M_{p_zp_y} & M_{p_zz} & M_{p_zp_z} \end{pmatrix}\,. \tag{2.11}$$

The determinant of this matrix corresponds to the 6D beam emittance:

$$\varepsilon_{6D}^{6} = \det||\widehat{M}_{\xi\nu}|| \,. \tag{2.12}$$

And this quantity is an invariant of the Hamiltonian system. In the simplest case of uncoupled x,y, and z phase spaces the matrix becomes:

$$\widehat{M}_{\xi\nu} = \begin{pmatrix} M_{xx} & M_{xp_x} & 0 & 0 & 0 & 0 \\ M_{xp_x} & M_{p_xp_x} & 0 & 0 & 0 & 0 \\ 0 & 0 & M_{yy} & M_{yp_y} & 0 & 0 \\ 0 & 0 & M_{yp_y} & M_{p_yp_y} & 0 & 0 \\ 0 & 0 & 0 & 0 & M_{zz} & M_{zp_z} \\ 0 & 0 & 0 & 0 & M_{zp_z} & M_{p_zp_z} \end{pmatrix}, \tag{2.13}$$

and the corresponding emittance can be expressed as:

$$\varepsilon_{6D}^{6} = \varepsilon_x^2 \cdot \varepsilon_y^2 \cdot \varepsilon_z^2 \,, \tag{2.14}$$

where e.g. $\varepsilon_x^2 = M_{xx}M_{p_xp_x} - M_{xp_x}^2$. Using the projected root mean square (RMS) emittance concept, emittance becomes:

$$\varepsilon_x^2 = \sigma_x^2\sigma_{p_x}^2 - \langle xp_x\rangle^2 \,, \tag{2.15}$$

where $\sigma_x^2 = M_{xx}$, $\sigma_{p_x}^2 = M_{p_xp_x}$ are the RMS values.

In practical case for accelerators it is impossible to perform the direct measurements of p_x and p_y. Therefore the emittance measurements use alternative quantities: $x' = p_x/p_z$ and $y' = p_y/p_z$ ($p_z >> p_x, p_y$). The new coordinates x' and y' represent the angles of particle motion with respect to the longitudinal direction. Using them the beam occupies a volume of the six-dimensional space formed by x, x', y, y', z and p_z which is known as trace space. The trace space emittance:

$$\varepsilon_{tr,x}^2 = \langle x^2\rangle\langle x'^2\rangle - \langle xx'\rangle^2 \,, \tag{2.16}$$

and normalized trace space emittance [32]:

$$\begin{aligned} \varepsilon_{n,tr,x} &= \langle p_z\rangle\varepsilon_{tr,x} \,, \\ \langle p_z\rangle &= \langle\beta_z\rangle\gamma \,. \end{aligned} \tag{2.17}$$

The formula 2.17 is used for emittance measurements.

In case of transverse phase spaces coupling (but no coupling to the longitudinal phase space), the matrix takes the form of 4D trace space matrix:

$$\widehat{M^T} = \begin{pmatrix} \langle x^2 \rangle & \langle xx' \rangle & \langle xy \rangle & \langle xy' \rangle \\ \langle xx' \rangle & \langle x'^2 \rangle & \langle x'y \rangle & \langle x'y' \rangle \\ \langle xy \rangle & \langle x'y \rangle & \langle y^2 \rangle & \langle yy' \rangle \\ \langle xy' \rangle & \langle x'y' \rangle & \langle yy' \rangle & \langle y'^2 \rangle \end{pmatrix} . \tag{2.18}$$

The corresponding 4D trace space emittance:

$$\varepsilon^4_{tr,4D} = \det||\widehat{M^T}|| . \tag{2.19}$$

For example, in case of x transverse kick (x' is impacted) the matrix becomes:

$$\widehat{M^T} = \begin{pmatrix} \langle x^2 \rangle & \langle xx' \rangle & 0 & 0 \\ \langle xx' \rangle & \langle x'^2 \rangle & \langle x'y \rangle & 0 \\ 0 & \langle x'y \rangle & \langle y^2 \rangle & \langle yy' \rangle \\ 0 & 0 & \langle yy' \rangle & \langle y'^2 \rangle \end{pmatrix} . \tag{2.20}$$

The corresponding emittance will be calculated as:

$$\varepsilon^4_{tr,4D} = \varepsilon^2_{tr,x}\varepsilon^2_{tr,y} - \langle x^2 \rangle \langle y'^2 \rangle \langle x'y \rangle^2 , \tag{2.21}$$

where $\langle x^2 \rangle = \sigma_x^2$, $\langle y'^2 \rangle = \sigma_{y'}^2$. Indeed, $\varepsilon_{tr,4D} \leq \sqrt{\varepsilon_{tr,x} \cdot \varepsilon_{tr,y}}$.

If the coupling is linear, it can be compensated by rotated quadrupoles. Definitely, the beam dynamics for coupling effects must be known to perform a proper compensation (for example see Ref. [33]). However, if the coupling is non-linear there is no possibility to compensate it by constant fields.

The possible candidates for the coupling of the x and y moments are: non-zero magnetic field at the cathode surface or RF field asymmetry of the gun. While the magnetic field at the cathode surface can be compensated by the bucking solenoid, the RF field asymmetry can not be canceled by any other external field sources because of its non-linear behavior.

2.2 RF coupler kick

Since the PITZ facility was built, the first and the main task was the experimental verification of the RF photoelectron gun ability to provide a beam with parameters satisfying the XFEL project requirements. The main requirement for the electron beam is a projected emittance value smaller than 1 mm · mrad for 1 nC bunch charge. The emittance measurements technique applied at PITZ is called the single slit scan method [34]. The technique is able to perform accurate measurements of the emittance

of space charge dominated beams. The basic idea of the technique is a measurement of the angular spread of emittance dominated beamlets produced by cutting tiny fractions out of the electron beam by a slit-like shape aperture. The technique allows to measure the emittance in the x and y planes separately.

In addition to the emittance value, the measurements revealed beam shape and phase space asymmetries (Fig. 2.5).

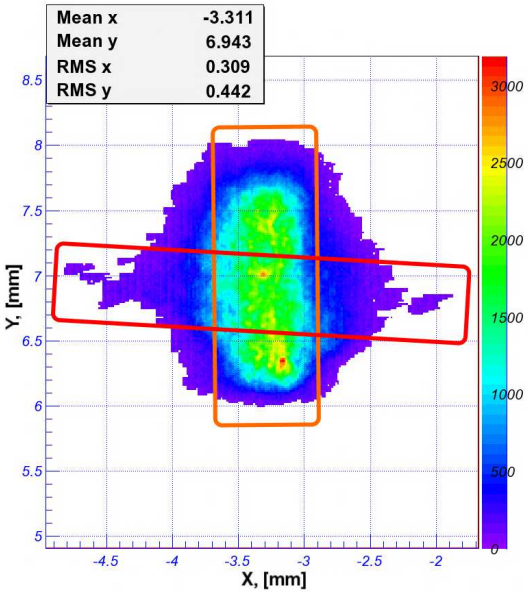

(a) Electron beam at the observation screen

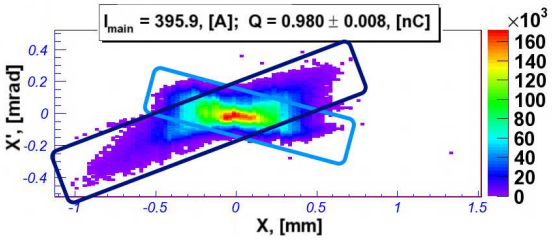

(b) x trace space of the electron beam

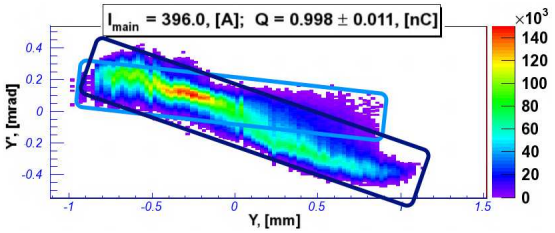

(c) y trace space of the electron beam

Figure 2.5: Measured beam properties. The orange and red rectangles show vertical and horizontal beam tails (an asymmetry of the beam transverse profile). The blue rectangles show the orientation of the main features of the x and y trace spaces.

After a number of experiments, it was found that the source of the beam asymmetries is located in the gun region. Meanwhile, detailed simulations of the RF fields for the full gun geometry revealed the presence of RF field asymmetries in the RF gun power input device called RF coupler. The presence of the field asymmetry in the RF coupler can explain the reason of the electron beam asymmetrical transverse shape and projected trace space. The asymmetric field introduced by the RF couplers is called RF coupler

kick and causes quality reduction of the electron beam.

The effect of the RF coupler kick induced coupling is a distortion of the beam trajectory. The effects are related to the longitudinal and transverse position of individual particles. The longitudinal dependency causes shifts of slice centroids. The transverse dependence causes focusing or defocusing including skew components.

2.2.1 Coupler kick description

The coupler kick influence on a bunch can be described by a complex voltage kick factor [35] and is defined as:

$$\vec{\nu}(x,y) = \frac{\vec{V}(x,y)}{\vec{e_z} \cdot \vec{V}(0,0)} \cong \begin{bmatrix} \nu_{x0} + \nu_{xx}x + \nu_{xy}y \\ \nu_{y0} + \nu_{yx}x + \nu_{yy}y \\ 1 + ... \end{bmatrix} , \tag{2.22}$$

where ν_{x0}, ν_{y0}, ν_{xx}, ν_{xy}, ν_{yx}, ν_{yy} are complex coefficients and $\vec{V}(x,y)$ is the complex voltage kick. The complex voltage kick is given by the integrals of the coupler fields along lines parallel to the z-axis:

$$\vec{V}(x,y) = \int [\vec{E}(x,y) + c\vec{\beta} \times \vec{B}(x,y)] e^{i\omega z/c} dz \, . \tag{2.23}$$

The complex voltage kick factor gives a momentum kick to the electrons [35]:

$$\vec{p} = Re\{\vec{\nu}(x,y) e^{i\omega s/c}\} \frac{eV_{acc}}{c} \, , \tag{2.24}$$

where V_{acc} is the accelerating voltage. The coupler angle kicks can be obtained by dividing the coupler x-y plane momentum kicks by the total momentum:

$$\begin{bmatrix} x' \\ y' \end{bmatrix}_{coupler} = \frac{eV_{acc}}{\beta\gamma mc^2} Re \left(\begin{bmatrix} \nu_{x0} + \nu_{xx}x + \nu_{xy}y \\ \nu_{y0} + \nu_{yx}x + \nu_{yy}y \end{bmatrix} e^{i\omega s/c} \right) . \tag{2.25}$$

2.2.2 Coupler kick in the PITZ gun

The RF cavity is made from copper and consists of two cells where electrons undergo acceleration by interaction with high-frequency electromagnetic fields. At the backplane of the half cell, a re-insertable cathode plug is located. The cathode plug is produced from molybdenum and has a Cs_2Te coating for the production of photoelectrons by interaction with a UV laser beam. In order to provide RF power to the RF cavity, an RF coupler is used. The coupler consists of a WG650 rectangular waveguide, a transformation wave unit formed by a cone and two half torus, and a coaxial waveguide (see Fig. 2.6).

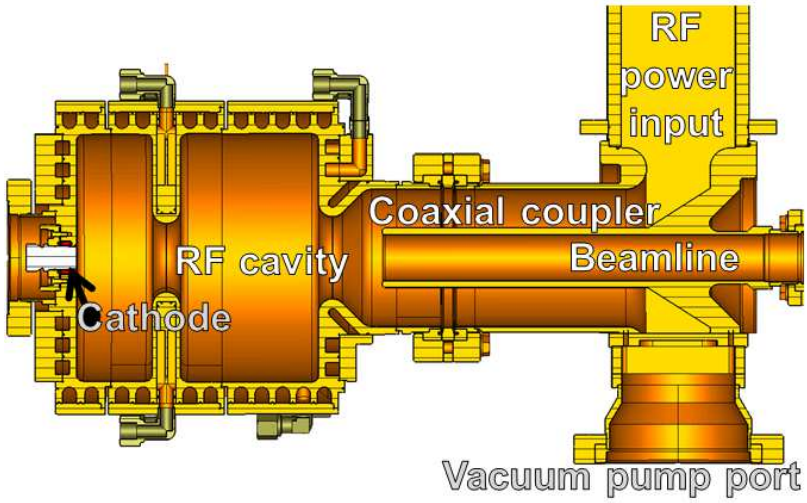

Figure 2.6: Model of the gun cavity and RF coupler.

The traveling wave transformation from the TE_{10} mode of the rectangular waveguide to the $TEM^{\odot}$[2] coaxial waveguide happens at the cone part of the coupler. Part of the traveling wave propagates directly to the coaxial waveguide and another part goes through the cone, reflects from the compensating short waveguide wall and goes back to the coaxial waveguide. In the ideal case, the reflected wave from the short waveguide should compensate the asymmetry of the forward wave in the coaxial part. After the transformation the $TEM^{\odot}$ traveling wave propagates through the coaxial waveguide up to the RF gun cavity, where it fills the cavity. The wave can be reflected backward from the transition to the coaxial waveguide, the enter to the full cell, the diaphragm between the cavity cells, and finally the back wall of the half cell. The combination of the forward and backward waves in the cavity forms a standing TM°_{010} wave [36] in each of the cells, with phase advance 180 ° between them.

RF field simulations in the CST Microwave studio [26] revealed that in the current design of the RF coupler an asymmetrical part of the $TEM^{\odot}$ field is always present.

According to the RF waveguide theory [37] the obtained asymmetric wave can be represented by a combination of two waves: a $TEM^{\odot}$ axisymmetric wave with the frequency of 1300 MHz and a dipole $TE^{\odot}_{11}$ wave. The dipole wave has a wavelength $\lambda \sim 230\,\mathrm{mm}$ which is larger than the cutoff wavelength of the coaxial waveguide $\lambda_{\mathrm{cutoff}}(TE^{\odot}_{11}) \cong 225\,\mathrm{mm}$ [36]. Therefore the dipole wave is an evanescent wave for the coaxial waveguide. The attenuation value is calculated by:

$$\gamma = \frac{2\pi}{\lambda_{cutoff}}\sqrt{1-(\frac{\lambda_{cutoff}}{\lambda})^2} = 0.00579\,\mathrm{mm}^{-1}\,. \tag{2.26}$$

[2]Here and in the following the waves in a circular and a coaxial waveguide or resonator are denoted by $^{\circ}$ and $^{\odot}$, respectively.

The $TE_{11}^{\odot}$ wave decay along the coaxial waveguide of the length $l = 179\,\mathrm{mm}$ can be calculated by:

$$A = 20\log(E_2/E_1) = 20\log(e^{-\gamma l}) = -9.15\,\mathrm{dB}\,. \tag{2.27}$$

Therefore a fraction of the dipole wave can propagate up to the RF cavity and produce transverse electromagnetic fields on the beam trajectory path. These transverse fields interact with the electron beam. The structure of the dipole wave is shown in Fig. 2.7.

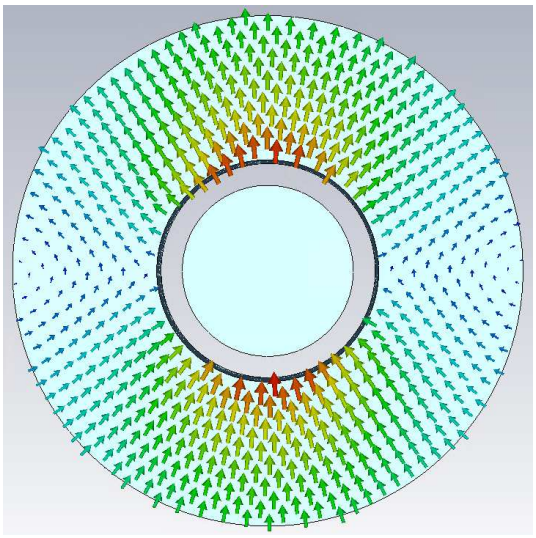

Figure 2.7: The transverse structure of the dipole wave in a coaxial waveguide simulated with the CST Microwave studio. The field intensity is indicated by the size and the color of arrows.

Since the transverse fields on the beam path are not constant in time (changes with forward wave frequency) a passing electron bunch will undergo a transient coupler kick. Therefore, besides a transverse kick of a full bunch, there will be different kicks for each slice of the beam. This introduces an asymmetry to the beam phase space. The beam affected by a kick will have coupled p_x and p_y momenta and increased emittance.

2.3 Modeling of the coupler kick and beam dynamics simulations

The numerical simulations of the three-dimensional gun fields and particle tracking in the gun were performed by using the 3D simulation software the CST Studio [26]. This is a package of tools for designing, simulating and optimizing electromagnetic systems based on finite elements calculations.

In order to make simulations of the field asymmetry and its influence on the beam, the simulation task was divided into four parts: RF fields simulation for the real inner gun and the RF coupler geometry, magnetostatic field simulation of the solenoids, and particle tracking simulations in combined RF and magnetostatic fields without and with space charge forces.

2.3.1 RF field simulations

The RF fields simulations were performed with the CST Microwave studio software [26]. The simulation model is represented by a 3D body with exact inner sizes of the RF coupler and the gun body, the outer sizes are simplified for computer resources economy. The material of the body was set as an annealed copper with conductivity $r_0 = 5.8 \cdot 10^7\,\mathrm{S/m}$. The model consists of an RF coupler with part of a rectangular waveguide (sizes are the same as for the standard WR650 waveguide), simplified vacuum port (just flat wall instead a grid for vacuum pump), connecting ring-like sealing, the gun cavity and a simplified cathode and cathode vicinity geometry. A short wall was made instead of a cathode contact spring, the cathode plug length was reduced to 5 mm. An RF wave port is located at the end of the rectangular waveguide. The port position was adjusted to obtain the minimum power reflection value from the total RF structure. The radii of the gun cavity where pre-adjusted by Eigenmode Solver, the adjustments criteria were the frequency of the second mode (π-mode fields) and the relation of the electric field amplitude at the cathode surface and the center of the full cell (field balance). The radii adjustments were done according to the fact that the sizes of the gun cavity are given for the cold structure (room temperature 22 °C) but the gun operates at temperatures more than 60 °C that makes the sizes change. Particularly the radii increase.

Since the structure combines standing wave in the gun cavity and traveling wave in the waveguides, the Frequency Domain (F-solver) was used. The frequency of the exciting signal is 1299.9996 MHz.

A tetrahedral mesh with second order elements, and the total number of elements $\sim 10^6$ was used for the simulations. The plane $y = 0$ was set as symmetry field plane for the simulations to increase the simulations speed. The results for E and H fields are presented in Fig. 2.8. The clearly visible RF field asymmetry appears already in the coaxial waveguide and propagates up to the transition from the coaxial waveguide to the gun cavity.

2.3.2 Solenoid field simulations

The constant magnetic field simulations were performed in the CST EM studio. The main and the bucking solenoids were modeled by two coils with iron housings. The number of the wire turns and the current strengths were set as changeable parameters and adjusted to obtain a field profile on the axis similar to the real one: 0.16 T, magnetic

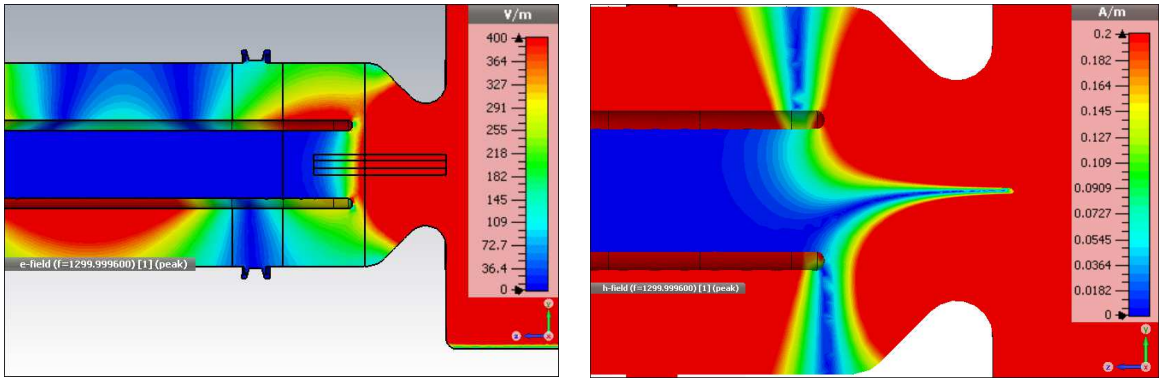

(a) E RF field distribution (b) H RF field distribution

Figure 2.8: The simulated E and H fields for the gun and RF coupler model. The plotted absolute values of the fields show the wave asymmetry which propagates to the beam path region.

field strength at 0.276 m downstream from the cathode and zero field at the cathode. The magnetostatic Ms-solver with hexahedral mesh was used for the simulations. The two symmetry planes $y = 0$ and $x = 0$ were applied. The magnetic field structure is presented in Fig. 2.4.

2.3.3 Particle tracking simulations

As the model for the beam tracking simulations a simplified geometry model consisting of two parts was taken. The first part is the gun region that is represented by a cylinder with a 15 mm diameter consisting of pre-imported E and H RF fields from the CST Microwave studio. The cathode is represented here as a cylinder with variable diameter dedicated for particle source definition (the position, and shape of the emitting part). The length of this first cylinder is 260 mm, it corresponds to the distance from the cathode surface to the end of the coaxial part of the RF coupler. The second part represents the beamline and starts from the end of the RF coupler up to the position of the third observation screen (Low.Scr3). The diameter is selected to be 50 mm and the length is 1340 mm. The solenoid fields are imported for the full volume of the simulation model. The mesh was adopted for the geometry in order to reduce the computational time without an accuracy loss. The density of the mesh is set higher for the central part of the model where the most of the beam movement taking place, and lower for the outer parts.

For the detailed simulations, two particle tracking solvers were used. The first solver is Tracking Solver (Trk solver) which provides an option for the particle tracking without interaction between particles. The particle source was set as a predefined circle surface with a number of emitting points. The particle source model was selected as

Fixed Emission. The second solver is the Particle-In-Cell solver (PIC solver). The solver provides a self-consistent method for the particle dynamics simulations in RF and static fields, and includes the space charge and the self-magnetic effect simulations. This allows to simulate particle dynamics in RF accelerating devices, for example the RF photoelectron gun. The particle source was defined as Gaussian Emission type with the following parameters: initial particle energy 0.55 eV (that corresponds to the initial electron energy emitted from the cathode surface by the photoemission process), beam charge of 1 nC and the flat-top temporal shape. The emitting surface and the source geometry was defined in the similar manner as for the Trk solver by the circle surface.

The simulations were done for the two types of the RF fields: (a) the fields simulated with asymmetry (the full geometry model including RF coupler was used) and (b) fields simulated without asymmetry (the fully symmetrical model was used). The resulting comparison between models with and without asymmetry of the fields give an estimation of the field asymmetry influence on the beam dynamics. The applied solenoid field map was identical for the both cases.

The RF fields amplitudes were scaled to obtain an accelerating gradient of 60 MV/m (nominal operation case) at the cathode what corresponds to about 6.5 MW power in the gun. The RF field phase was adjusted for each case of the simulations (Trk or PIC solvers and fields with of without asymmetry) to obtain the maximum beam energy at the exit of the gun.

2.3.4 Tracking solver results

A phase scan was performed in order to obtain the maximum beam energy at the end of the gun for the field accelerating gradient of 60 MV/m at the cathode surface.

The mean size and position of the particles were calculated by post processing CST internal tools. The results of the simulations by the Trk solver show that particles emitted from the cathode are deflected by the dipole part of the RF field wave. The average beam position (center of mass) and the RMS beam size along the longitudinal coordinate z is shown in Fig. 2.9. The solid lines represent the particle tracking without solenoid field and the dashed lines show the case with solenoid field. The figure shows that the central beam position starts to diverge from the central axes at the longitudinal position of $\sim$ 240 mm that corresponds to the position of the end of the coupler coaxial antenna (transition from the coupler to the full cell of the gun). The calculated x and y kicks are $k_x = 0.01$ mrad, $k_y = 0.66$ mrad for the case without solenoid and $k_x = -0.38$ mrad, $k_y = 0.27$ mrad for the case with solenoid fields.

These simulations show that the kick has an influence on the beam position but it can not provide correct information about the beam transverse and longitudinal shapes, and quantitative estimation of the real beam kick because of the temporal shape of the beam and space charge effects are not considered by this solver.

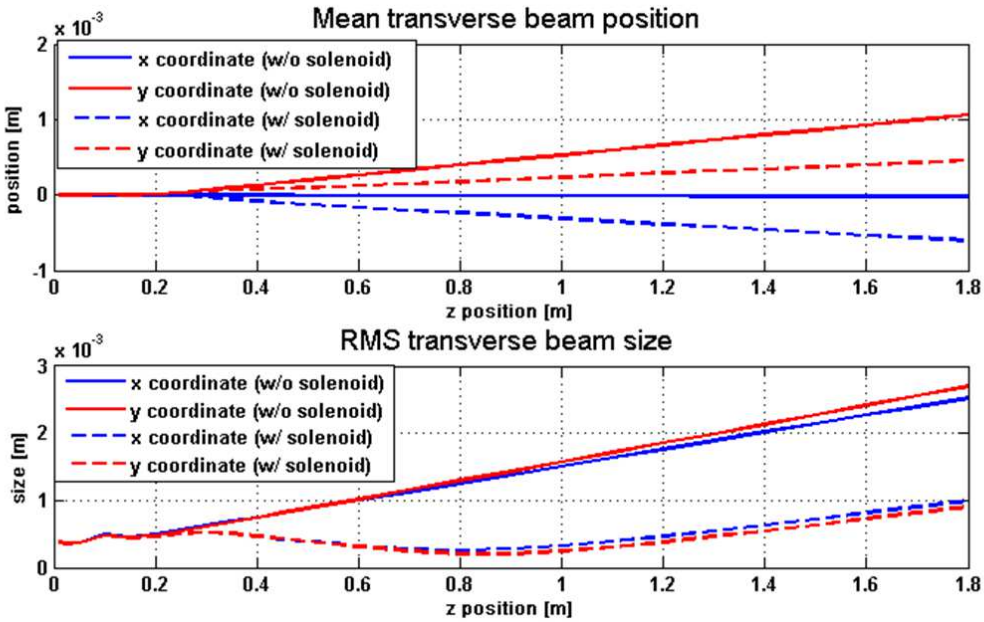

Figure 2.9: Tracking solver simulation results. The solid lines represents the particle tracking without solenoids and the dashed lines with solenoids.

2.3.5 PIC solver results

The simulations by the PIC solver provide the possibility to perform particle tracking for the electron beam with transverse and longitudinal beam parameters close to the real case (1 nC charge, 22 ps flattop longitudinal length and 1.2 mm initial diameter at the cathode).

The RF accelerating gradient was adjusted by the multiplication coefficient to obtain 60 MV/m at the cathode surface and afterward the initial RF phase adjusted to get maximum beam energy at the exit of the gun.

The particle tracking data was taken from the particle monitors at fixed equidistant time intervals were all particle parameters were saved (coordinates and momenta of all the beam particles).

The results of the simulations by the Trk solver proved the influence of the RF field asymmetry on the beam position. Additionally it show that the dipole part of the wave introduces distortions to the beam trace spaces. The x and y beam trace space is shown for the different positions on the beam during the beam movement in the gun in Fig. 2.10. The picture represents a beam at four time frames which correspond to the four positions in the gun: 18 mm (place in the 1st gun cavity cell), 196 mm (location inside the RF coupler region), 803 mm (location of the first observation screen) and 1708 mm (location of the third observation screen). Apparently, the beam has a large transverse size at the position of the coupler where the dipole part of the wave has the maximum influence on the beam. The results show that the beam distortions start

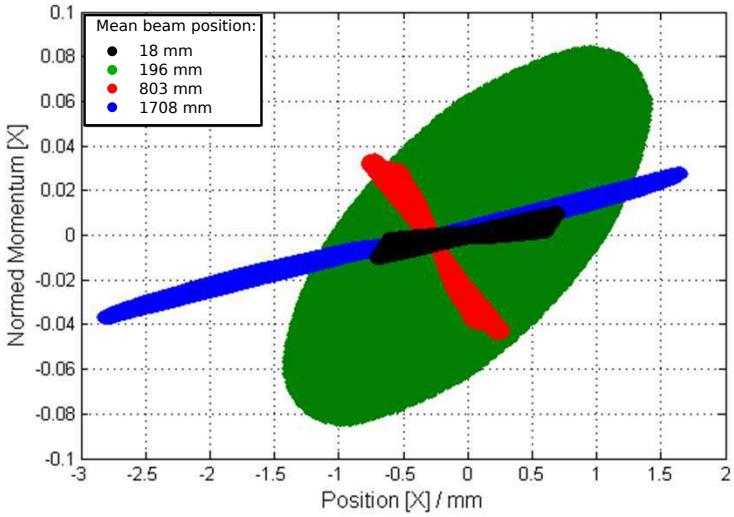

Figure 2.10: PIC solver simulation results. Normed momentum term is defined as $u = \beta\gamma$ (as defined in [26]).

to be visible after the beam movement through the coupler region. The x and y kick calculated by the PIC solver gives us $k_x = 0.31$ mrad, $k_y = 0.37$ mrad values which are compatible with the Trk simulations.

The performed simulations do not show a change in emittance value and beam size between the cases with and without RF field asymmetry. The aim of these simulations was to show the principle possibility of the field asymmetry influence on the beam motion. The full characterization of the coupler kick (it is planned to be performed in the near future) by the investigations on the emittance is outside the scope of this thesis.

2.4 Other possible reasons of the electron beam asymmetry

Additionally to the RF coupler field asymmetry other possible origins of the beam structure asymmetry were considered.

The first is an influence of the vacuum laser mirror installed in the beamline.

Since there is quite a small distance between the vacuum mirror and a passing electron beam several effects can take place:

- the interaction between wake fields produced by an electron beam and the beam itself
- remnant mirror charging (which was a case before, after the effect was noticed, a dielectric mirror was replaced by a metal one)

In order to check the status of the mirror influence on the beam dynamics, there a second identical vacuum mirror was installed and the results of beam asymmetry observations were compared. The schematic representation of the vacuum mirrors installation is presented in Fig. 2.11. The experiments on the cathode surface scan by laser beam (section 2.5.1) and the electron beam Larmor angle (section 2.5.2) were performed for two vacuum mirror setups (one and two mirrors). The results for the two setups were identical which means that the vacuum mirror has no influence on the beam shape.

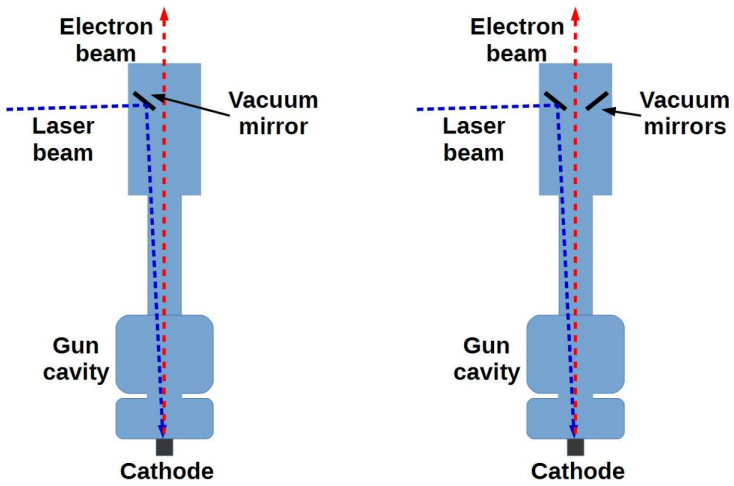

Figure 2.11: Schematic representation of the vacuum mirrors set-up. Usual setup with one mirror (on the left) and setup with two identical mirrors (on the right) for the tests.

Another possible reason for the beam asymmetry is the main solenoid configuration and adjustments inaccuracies.

The main solenoid coil has irregularities of the geometry: connection current cables (Fig. 2.12 left plot) and turn transitions which are located on the inner side of the coil (Fig. 2.12 right plot). Both of these irregularities can introduce asymmetries in the main solenoid magnetic field which can have an influence on the electron beam dynamics. Also, a misalignment of the main solenoid angles can introduce a beam asymmetry additionally to a beam transverse kick.

The studies on the solenoid field asymmetry are very time and power consuming and will be continued in the future.

2.5 Experimental beam asymmetry studies

2.5.1 Experiment on the cathode surface scan by laser beam

In order to check the presence of the field asymmetries or a vacuum mirror influence on the electron beam dynamics an experiment on the beam parameters dependence on

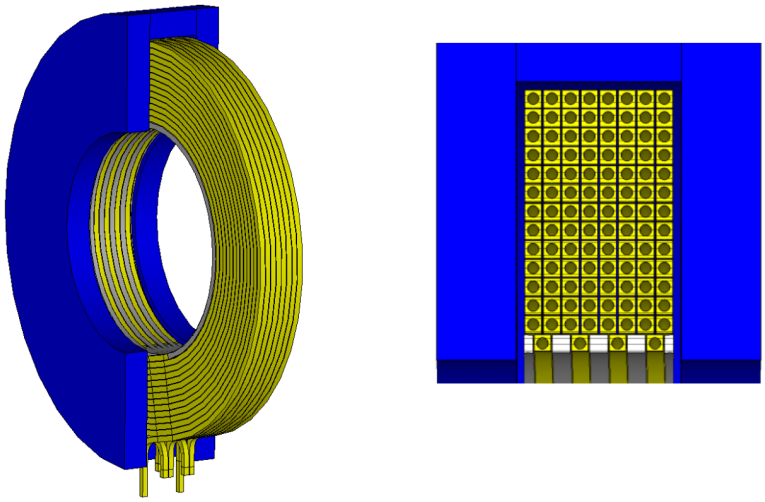

Figure 2.12: 3D model of the main solenoid with an iron jacket (blue part) and coil wires (yellow). Power cables and water cooling tubes are connected to the wires on the bottom at the left picture.

different trajectories in the gun was done. The idea of the experiment is the observation of the beam position and the transverse shape at an observations screen versus different starting beam positions at the cathode. For this purpose the photocathode laser beam was placed at the cathode according to a positions grid with a step width of 1 mm by using mirrors M5 and M6 (for more details see the chapter 1). The picture of the beam positions taken by the VC2 camera is presented in Fig. 2.13. The experiment was done at 5 MW peak RF power in the gun, 1.2 mm of the Beam Shaping Aperture (BSA), 3 MW peak RF power in the booster and 500 pC bunch charge at the Maximum Mean Momentum Gain (MMMG) phase.

The beam position grid measurements at the four observation screens (three screens before the booster cavity and one directly after it) are presented in Fig. 2.14. The beam profiles were scaled down to avoid their overlapping. The scale factors are shown in the titles of the images. The beam profiles presented on the pictures have an asymmetry which is similar for all beam positions at the screens. The observed beam position grids can not provide a clear answer about the coupler kick influence on the beam motion. The observed grid distortions are mainly related to the inaccuracy of the experiment settings and beam shape asymmetry. Summarizing, no correlations in the results at the four screens were found.

Due to the presence of strong magnetic field from the main solenoid the accuracy of this method is not sufficient for quantitative estimation of the RF coupler kick.

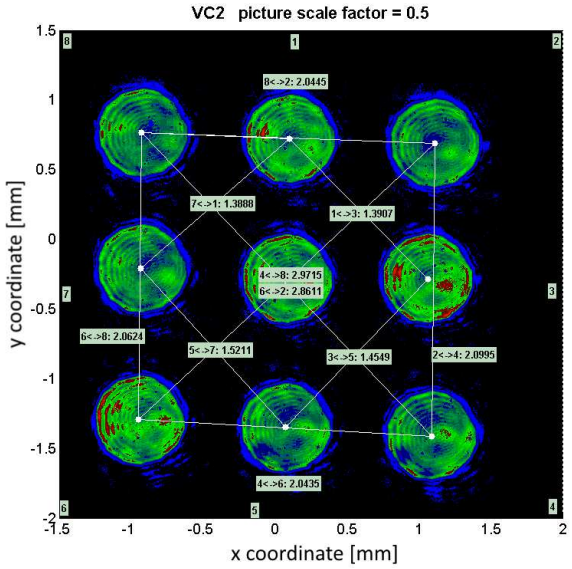

Figure 2.13: Beam positions and transverse shapes at the VC2 camera. The beam picture sizes are scaled by a factor 0.5 to compare the distances between the centers of the pictures. The numbers near to the image edge show a beam profile id while further numbers show distances between the centers of the beam profiles.

2.5.2 Experiment on electron beam Larmor angle

In addition to the fringe field focusing a charged particle beam undergoes a rotation while traveling through a solenoid field. The beam rotation can be also considered as a beam coordinate system rotation. The angle of rotation calls Larmor angle. A schematic representation of this process is shown in Fig. 2.15.

In general case, the Larmor angle of a particle with charge q and longitudinal speed v_z that travels through a magnetic field $B(z)$ can be determined as [38]:

$$\theta = \frac{q}{2mv_z} \int_{z_0}^{z_1} B_z(z) \mathrm{d}z \,, \tag{2.28}$$

where $B_z(z)$ is the longitudinal component of the magnetic field, z_0 is an initial point the particle motion, z_1 is a point where the Larmor angle is calculated, and m is the particle mass.

A description of a beam motion in solenoid fields without acceleration is presented in Ref. [38]. But in case of the PITZ gun, the beam focusing happens during the acceleration. Therefore the accurate beam motion description must be done only numerically, for example using the particle tracking simulation code ASTRA [39].

During operation with a solenoid polarity switcher (the system that changes B_z solenoid field direction) there was noticed that the beam asymmetry features (which look like beam wings) change their orientation with a changing of the main solenoid

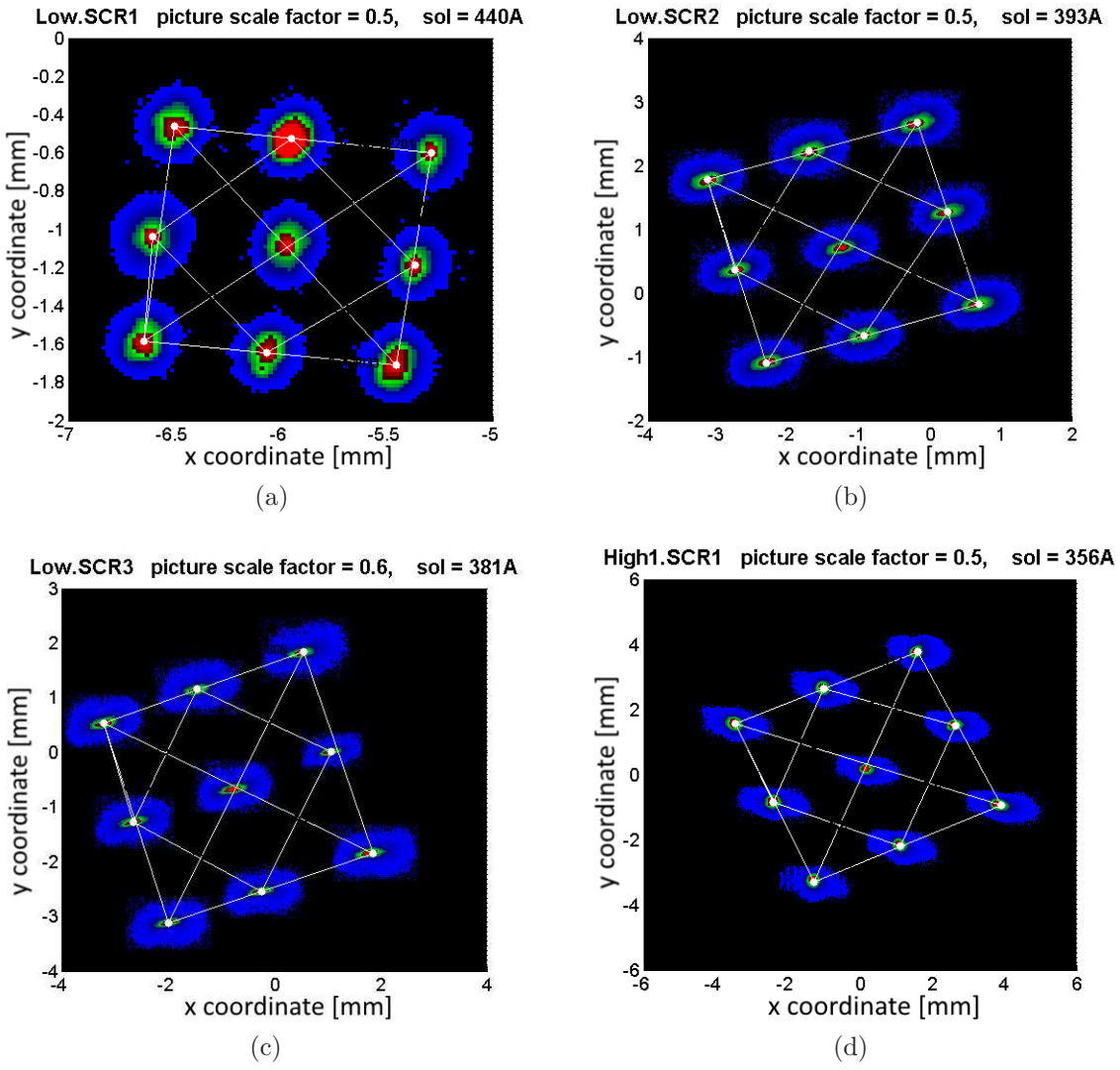

Figure 2.14: The combined beam positions at different screens (a - Low.Scr1, b - Low.Scr2, c - Low.Scr3 and d - High1.Scr1) related to the laser beam positions at the cathode (see Fig. 2.13). The beam pictures scale factors and the applied main solenoid current are given in the corresponding titles.

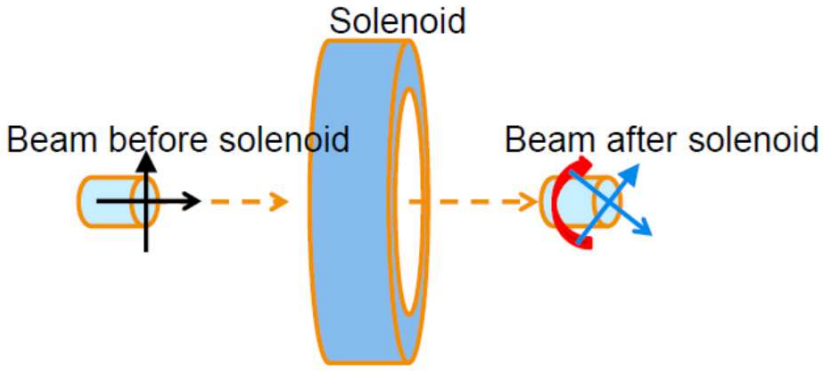

Figure 2.15: A charged particle beam traveling in a solenoid field.

polarity. That fact provides an idea that the origin of the beam asymmetry is located in the region of the main solenoid field.

A charged particle of a beam starting not from the center of the cathode undergo a rotation around the center of the beam while traveling trough a solenoid field. A change of the solenoid current polarity results only in a change of the direction of the rotation while the absolute value of the angle stays the same. The schematic representation of the process is shown in Fig. 2.16.

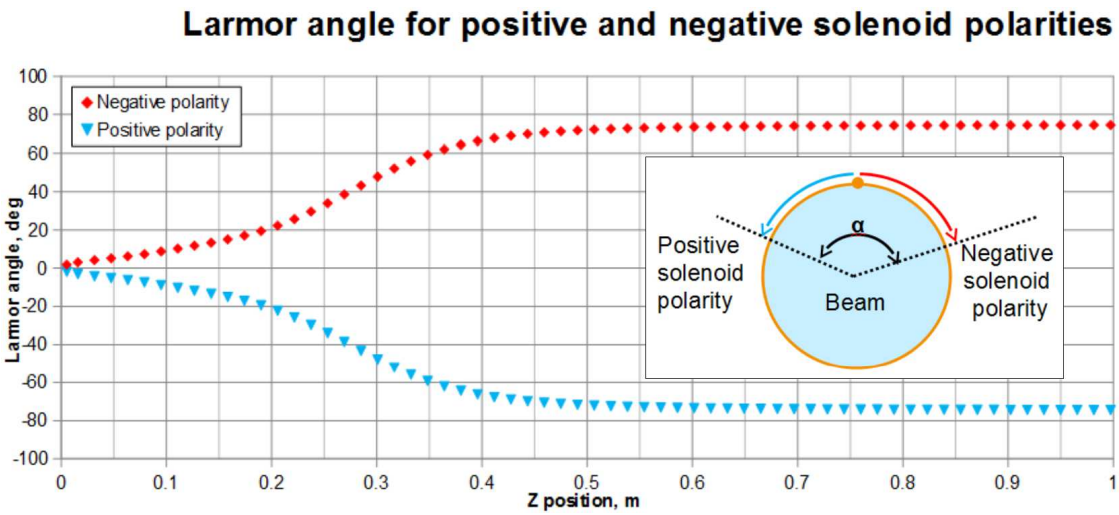

Figure 2.16: Larmor angle dependency on longitudinal beam position for normal and opposite main solenoid polarities simulated by the particle tracking code ASTRA. The beam position z starts from the cathode surface.

The simulation results performed by the particle tracking simulation code ASTRA (see Fig. 2.16) give us direct correlation between total Larmor angle difference for both polarities and the location of the beam asymmetry origin. For example, a particle starting from the cathode surface off-center undergoes a total rotation of an $\alpha/2$ angle

compared to the beam geometry center (see Fig. 2.16). But in case when a particle started off-center at some z position downstream the cathode, the total rotation angle will be smaller ($\beta/2$ in Fig. 2.17) than for a particle starting off-center from the cathode ($\alpha/2$). In order to obtain the z position of the particle source related to the β angle, one should vertically shift the already known curves (obtained for the particle started from the z=0) towards each other so that the angle between them become equal β. The cross of the shifted curves indicates the place of the desired particle source (see Fig. 2.17). The shifted curve parts to the left to the indicated particle source are presented only to show that the Larmor angle dependence on z position is the same for α and β angle cases.

So, knowing the value of the Larmor angle and its dependency on z position, it is possible to determine the position where the particle started to move off-axis. This method was used for the determination of the location of the particle beam asymmetry source.

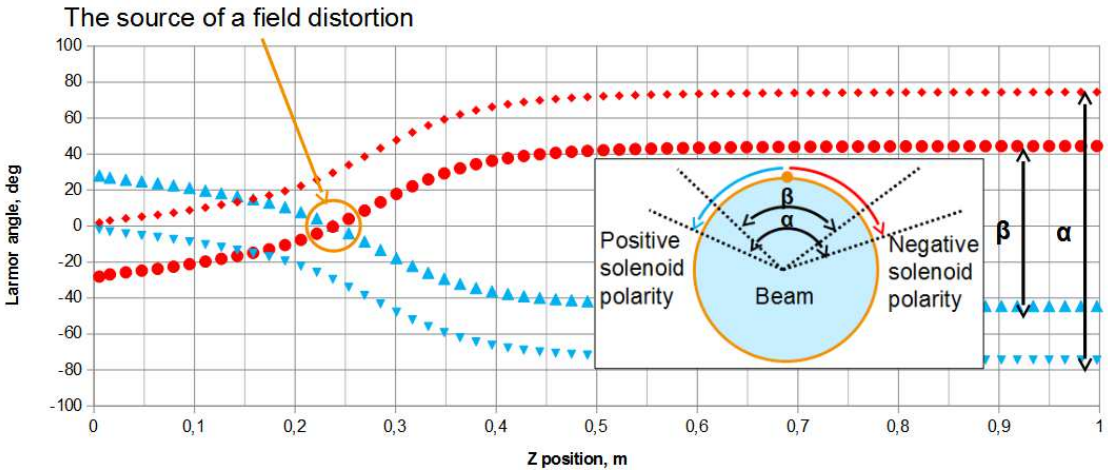

Figure 2.17: Larmor angle for the case of particles starting off-axis from the cathode surface and starting off-axis from some position downstream the cathode. The obtained angle can be recalculated to a specific z position location of the particle or beam distortion source.

The Larmor angle experiment was performed by comparison of two beam pictures from the same screen taken for different solenoid polarities. A rotation was applied to one of the obtained pictures until it was coinciding with the second picture. The obtained angle divided by two is the Larmor angle. Fig. 2.18 shows the experimental observation of an electron beam with asymmetry features for normal and opposite solenoid polarities acceleration in the gun. It also shows the process of the determination of the beam distortion location. The experiment setup parameters were the same as for the experiment with a position grid except the fact that the booster and bucking solenoid were switched off. Since the beam asymmetry has two features located at

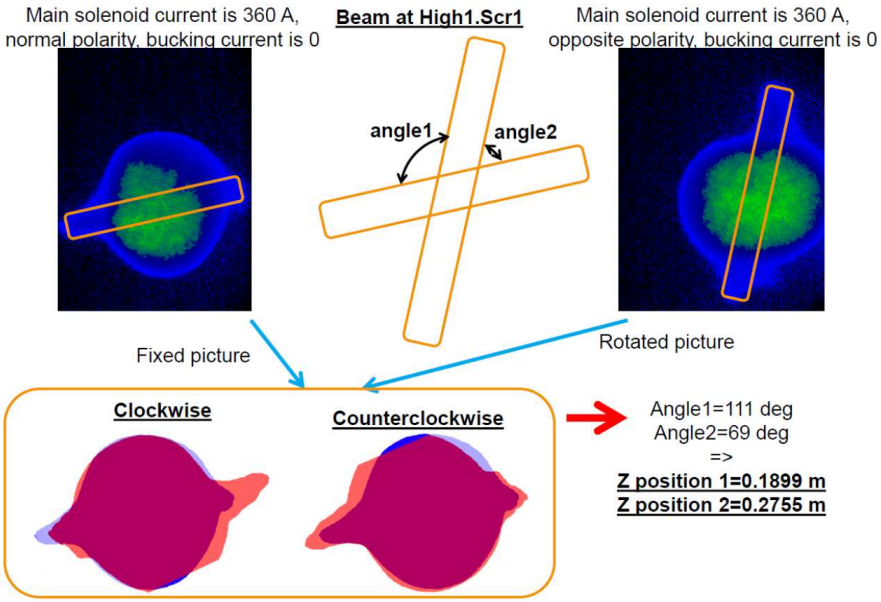

Figure 2.18: A scheme of beam asymmetry determination according to the obtained Larmor angle.

opposite sides of the beam, it gives us two angles on which one of the pictures can be rotated. Consequently we obtain two locations of the supposed asymmetry origin. According to the obtained pictures it is hard to distinguish a preferable rotation angle.

The experiment on the Larmor angle was done in two steps: with one and two vacuum mirrors. During the second part of the experiment the data was taken for 3 levels of RF power in the gun: 5 MW (the same power as for the first part of the experiment), 3 MW and 1.5 MW. The beam size at the first observation screen in the high energy section for 3 and 1.5 MW in the gun is so large that full beam profile pictures were obtained by combination of a few parts. In order to take pictures of the beam parts, steerers were applied. The booster cavity and the bucking solenoid were switched off. The pictures were taken for two solenoid currents: when the beam was focused on the observation screen and when the beam asymmetry wings were most clearly visible.

The results of the experiment are divided into two parts and presented in the tables 2.1, 2.2 and Fig. 2.19, 2.20, for the first and the second parts respectively. The difference between results in part 1 and 2 is the choice of the rotation direction (clockwise or counterclockwise) like it is shown in Fig. 2.18. Positions of the probable asymmetry reason are indicated by black arrows. The green and violet rectangles around an arrow represent an location uncertainty. The width of the rectangles represent a range of possible angle values. The arrows from the top to bottom are drawn for the experiment with a single vacuum mirror and the arrows from the bottom to top for the experiments with two vacuum mirrors.

Num.of vac. mirrors	Gun power, MW	Solenoid current, A	Rotation angle, deg	Position, m
1	5	353	75.1	0.2617
		360	64.8	0.2818
2	1.5	210	55.3	0.2982
		219	59.5	0.2953
2	3	282	69.2	0.2728
		290	67.7	0.2786
2	5	353	74.0	0.2636
		360	68.5	0.2754

Table 2.1: Larmor angle experiment results (part 1).

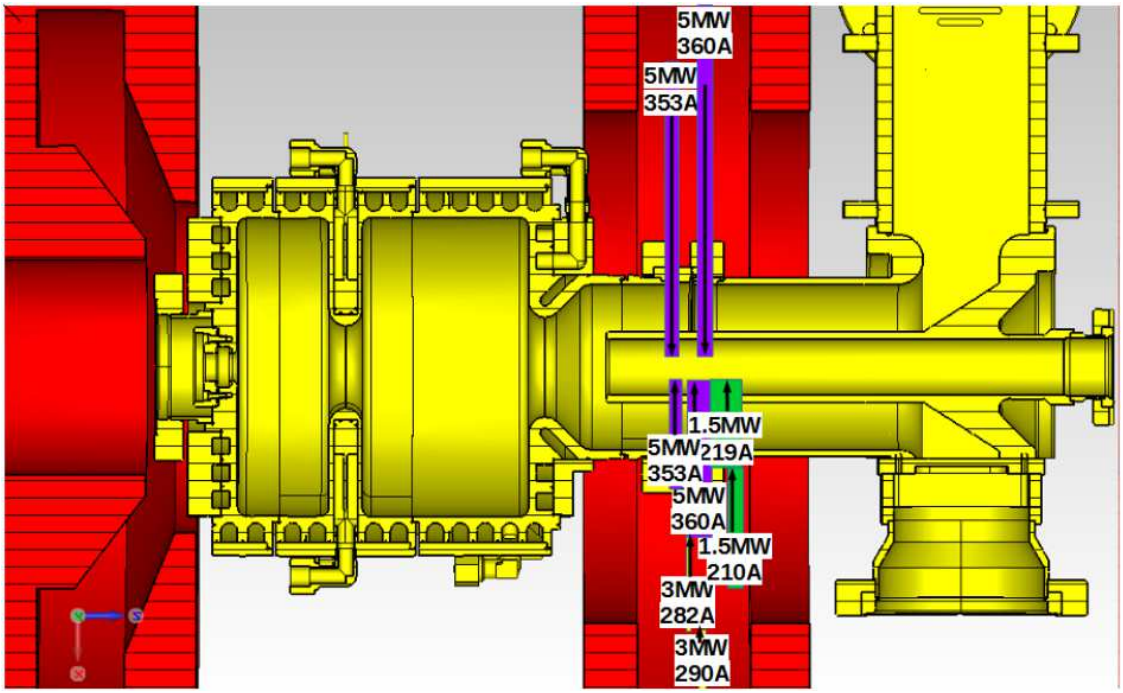

Figure 2.19: A graphical representation of the Larmor angle results given in the table 2.1.

From the shape of the wings, it seems that the counterclockwise rotation (the part 2 of the results) better fits the pictures with each other. The results of the experiment indicate mainly two areas in the gun geometry. The first region is the middle of the main solenoid geometry and the second is the transition from the coaxial coupler to the full cell of the gun. This is a place where an electron beam can see a kick from the RF field asymmetry. Even though the simulations show that the coupler kick has an influence on the beam motion, the fact of the possible main solenoid field asymmetry

Num.of vac. mirrors	Gun power, MW	Solenoid current, A	Rotation angle, deg	Position, m
1	5	353	104.9	0.2000
		360	115.2	0.1750
2	1.5	210	124.7	0.1350
		219	120.5	0.1760
2	3	282	110.8	0.1850
		290	112.3	0.1870
2	5	353	106.0	0.1970
		360	111.5	0.1880

Table 2.2: Larmor angle experiment results (part 2).

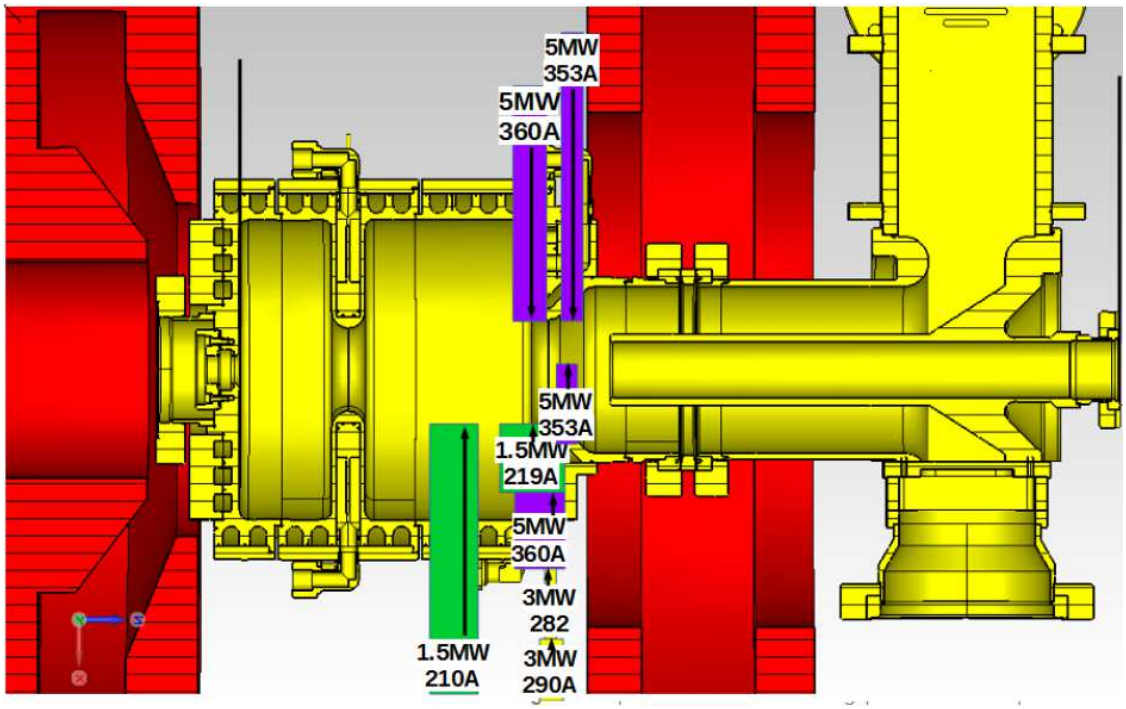

Figure 2.20: A graphical representation of the Larmor angle results given in the table 2.2.

(presented in Ref. [33]) tells us that we should consider the second region as the beam distortion source as well. Therefore it is not possible to distinguish where most probably asymmetry does originate. Both of the regions must be considered as the result of the experiment.

2.5.3 Experiment on electron beam acceleration without forward RF wave

Since it is hard to separate the asymmetry origins from the RF field and the solenoid an additional idea for the verification of the field asymmetry was developed. The idea is based on utilizing only the stored power in the gun cavity without forward RF wave. The original idea was that the electron beam undergoes a kick by the field asymmetry that comes with the forward wave and the stored RF power should not have this asymmetry or at least a much smaller one.

The filling of the gun cavity by RF power takes a few microseconds. An illustration of the filling process can be shown on a cavity model based on a waveguide terminated with an iris followed by a shorting plane. The schematics is presented in Fig. 2.21. The turn-on of an RF drive corresponds to the launching of a forward wave in a waveguide, towards the cavity formed by the iris and the short. For a small iris, one expects that most of the incident wave will be promptly reflected. Some of the waves will scatter through the obstacle. In the cavity the forward wave travels to the short, reflects, returns to the iris, and reflects again. Over the time, the cavity fills, and in steady-state, the prompt reflection of the incident wave at the iris interferes with the radiation from the cavity. The opposite to filling process takes place when an RF driver turns off. The RF power leaving from a cavity also takes some microseconds (for details see Ref. [40]).

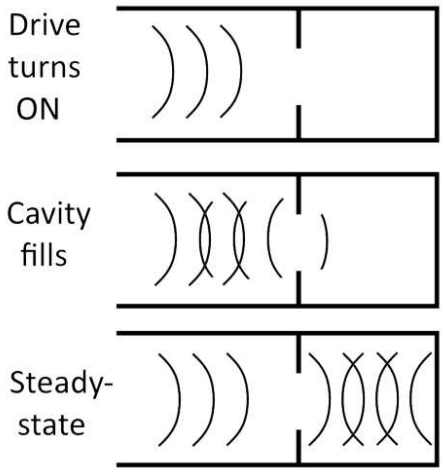

Figure 2.21: Illustration of the transient filling of a cavity.

During the experiment at PITZ, the time needed for the RF power to leave the gun cavity after the RF drive was switched off was used for acceleration of electron bunches. For this purpose the timing of a bunch was changed so that the bunch was placed at the end of an RF pulse, where the power is still stored in the cavity. The comparison of the usual timing of a bunch and the time for this experiment is illustrated in Fig. 2.22.

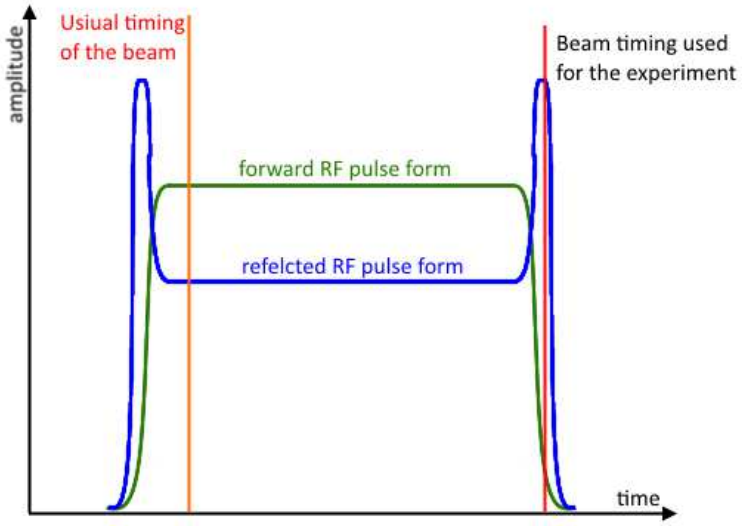

Figure 2.22: Beam bunch timing inside an RF pulse for normal operation and for the described experiment.

The experiment was utilizing following gun parameters:

- peak power in the gun: 6 MW
- peak power in the booster: 2.77 MW
- paser transmission: 90 % (almost full available photocathode laser intensity)
- BSA: 1.2 mm
- bunch charge: 0.5 nC

The beam bunch timing adjustment was done by tuning the number of laser pulses, the RF pulse starting point and its length and the camera timing adjustment because there were difficulties with the laser timing adjustment which would have simplified the experiment. RF pulse length was set to 200 μs, the falling time of the pulse to 0 μs for better determination of the needed time gate while the pulse rising time was kept at around 35 μs (the standard operation value) at that time of the experiment. The forward and reflected RF pulse signals are presented in Fig. 2.23. To be noted from the figure is a much higher reflected power spike at the end of the RF pulse. This happens due to 0 μs falling time compared for the non-zero time of the rising of the RF pulse. The determination of the number of bunches needed for the experiment was done according to the charge measurements with a Low.FC1 (see chapter 1 for more details). The dark current signal and the combination of dark current with electron

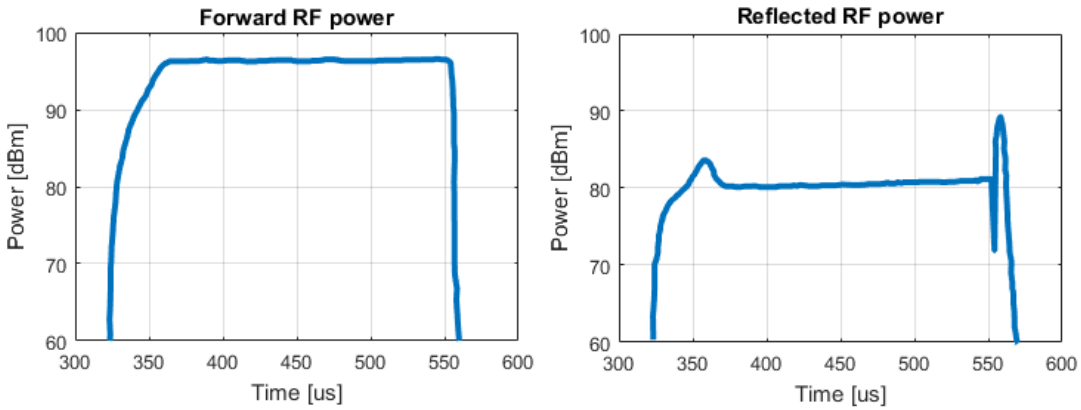

Figure 2.23: The forward (on the left) and reflected (on the right) signals of the used RF pulse settings during the experiment.

bunches on the top of it, are presented in Fig. 2.24. The dark current signal repeats the signal of the RF pulse in the gun cavity, therefore it can be used as a reference signal for determining the bunch timing. The bunches accelerated within an RF pulse have higher charge that bunches outside of the pulse due to a few factors: the Schottky-like effect when additional charge is extracted due to high-intensity electrical field on the cathode surface, desynchronization of the half cell RF field phase and laser pulse timing and mismatching of the RF field in both gun cells as a result of surface current losses. The total number of bunches that fits inside the RF pulse was 15. The pulses starting from 16^{th} were believed to see an acceleration without forward RF wave. The total number

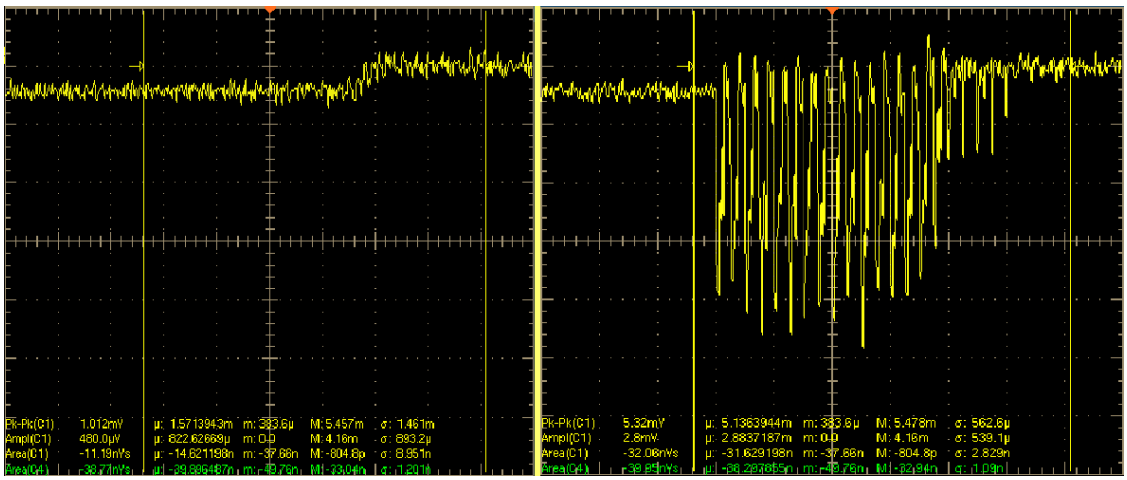

Figure 2.24: The dark current signal (left) and the combination of the dark current signal with electron bunches signal on the top of it (right). The strong variation of bunch charge amplitudes is due to the too small sampling value of the oscilloscope. The numbers on the plot show technical information and are not relevant to this context.

of accelerated pulses is 21. For the experiment, the transverse profiles of pulse were observed at the first observation screen in the high energy section (after the booster cavity). The pictures of the pulses 15 (last inside a normal acceleration regime), 16 (first outside of forward RF wave) and 17 at the High1 Screen 1 are presented in Fig. 2.25. It is visible that beam asymmetry features are observed for all settings. However, there

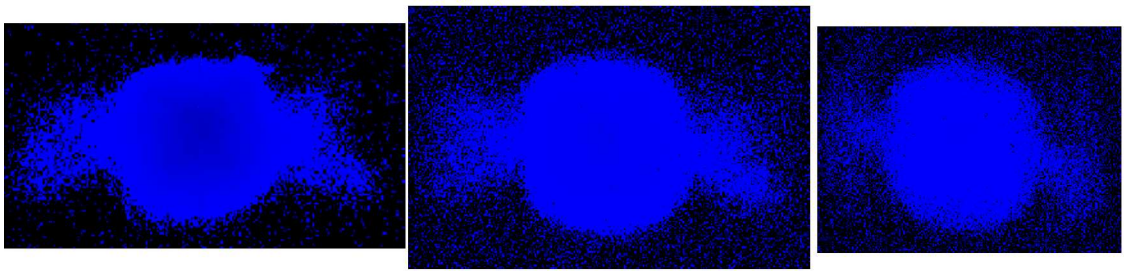

Figure 2.25: The transverse profiles of electron bunches corresponding to the laser pulses 15 (last inside the normal acceleration regime), 16 (first outside of forward RF wave) and 17 at the High1 Screen 1.

is a difference in the orientation of the beam wings. With increase of the number of pulses, it turns slightly clockwise.

The explanation of the observed beam asymmetries for the bunches accelerated outside of the forward RF power can be based on the fact that RF fields inside the cavity filled by a wave with any asymmetry have the same type of asymmetry. Inside the cavity, the wave undergoes a symmetrization due to ohmic losses but it is insufficient to damp the asymmetrical part of the wave. Therefore, the gun cavity radiates an RF wave back and produces the same kind of the beam kick in the coupler region.

2.5.4 Experiment on the main solenoid tilt

During studying the beam asymmetry it was noticed that beam wings observed at screens in the high energy section are not visible at screens in the low energy section for the same main solenoid current. The beam asymmetry in the low section has a four-pointed star like shape when the electron beam is focused on dedicated screens. That shape is a transitional geometry between a vertically oriented ellipse like beam shape at a slightly lower main solenoid current and a horizontally oriented ellipse-like beam shape at slightly higher main solenoid currents. The process of beam shape modifications with the main solenoid current change is presented in Fig. 2.26. A similar beam shape transformation was observed during particle tracking simulations in the PITZ gun with tilted main solenoid fields. Based on this knowledge, an experiment on the beam shape dependence on main solenoid tilts was done. During the experiment, yaw and pitch angles of the main solenoid were varied. The results of the experiment presented in Fig. 2.27 show that the beam shape does not significantly change for the extreme values of the main solenoid angles. The beam shape stays similar and has a

four-pointed star-like shape. The results can be explained by the hypothesis that the beam shape undergoes a transformation due to the main solenoid angles misalignment,

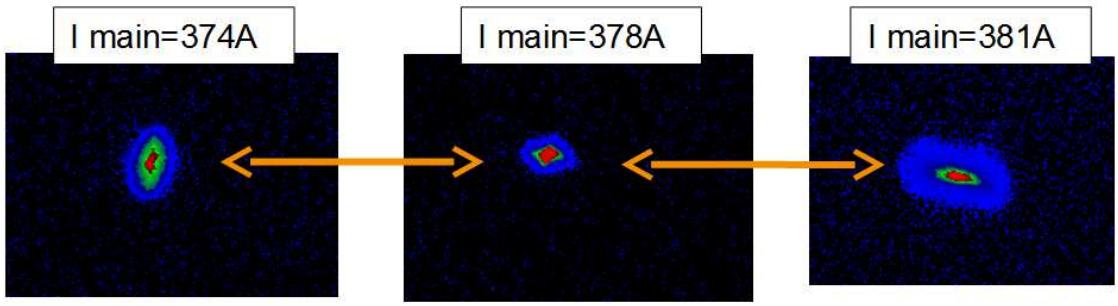

Figure 2.26: A transverse beam shape transformation at Low.Scr3 (see chapter 1for more details).

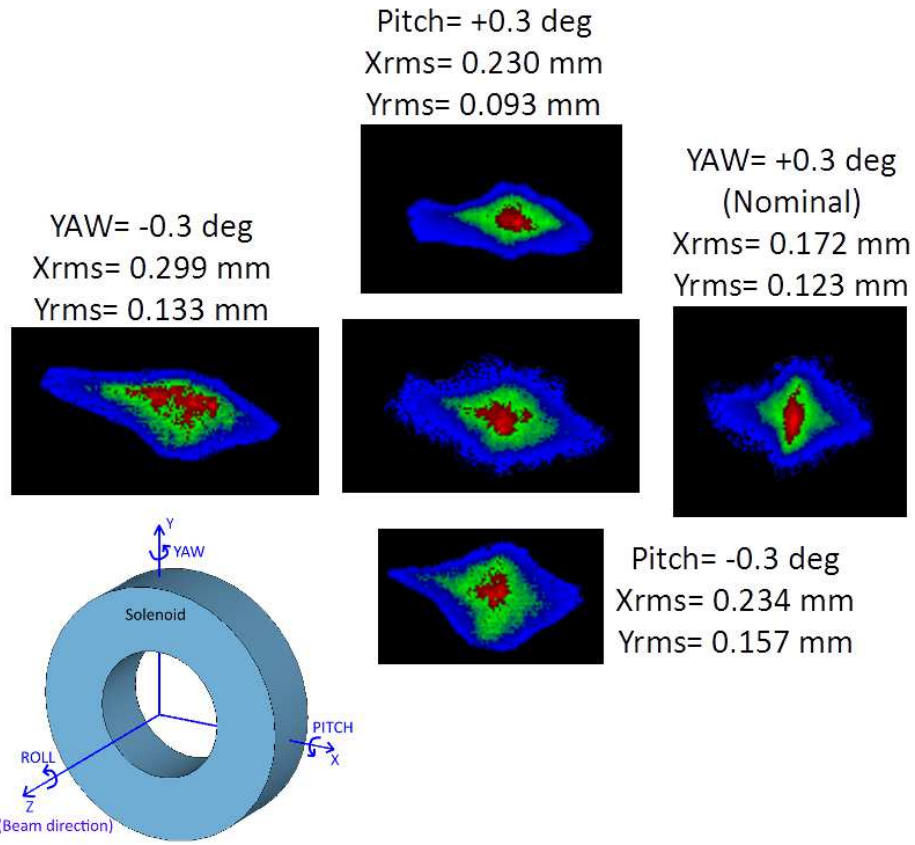

Figure 2.27: A transverse beam shape transformation at the 3rd screen in the low energetic section. The schematic representation of the solenoid rotation is shown in the bottom left picture.

together with the RF field asymmetry. The experiment was not able to distinguish between both effects: it neither proves the idea of a beam shape dependence on the solenoid tilt nor refutes it. For more clearness further experiments are required.

2.6 Proposal of another RF coupler design

Since the usual way of an RF coupler tuning by a compensating waveguide wall (in our case it is the coupler back wall where the vacuum pump grid is located) position adjustments did not show successful results, there appeared an idea of introduction an asymmetry to the internal RF coupler geometry for the field asymmetry compensation.

Based on the geometry and mechanical design of the coupler the internal cone parameters were selected for adjustments of the coaxial wave structure because that changes would be the easiest during the coupler production. For each set of the cone parameters, the position of the coupler back wall was tuned so that the fields in the coaxial waveguide become most symmetrical and the value of the S_{21} parameter get maximal (the parameter characterizes the forward wave gain). The results showed that the asymmetric field is always present in the coaxial waveguide, even in the case when the parameters were set to get the smallest possible field asymmetry and not optimized S_{21} value.

The next step of coupler geometry adjustments was utilizing an idea of the asymmetrical changes of the coupler geometry. The following changes of the coupler geometry were applied for the studies: the cone with the ellipsoidal base, cone tilt, the coaxial waveguide with the transition from ellipsoidal to circular shape, and back wall position adjustment. This changes were used due to the assumption of asymmetric wave compensation by an asymmetric geometry.

Unfortunately, these simulations did not show positive results. The dipole mode of the wave was always present in the coaxial waveguide.

Since attempts at internal geometry change without coaxial waveguide length change did not succeed, the model of the current coupler design with lengthened coaxial part was checked. The result showed that in order to let the dipole wave amplitude decay exponentially, the coaxial waveguide must be elongated by 200 mm in order to obtain -20 dB attenuation. However, the elongated coupler has also disadvantages. The installation of it to PITZ would be difficult due to space limitations, and many devices in the gun region should be reordered or even removed.

A few different coupler designs were proposed due to the fact that it is not possible to obtain a symmetrical wave from the existing design. Some coupler designs used for another kind of accelerating structures were selected as candidates for replacement of the current coupler design. In addition, some new coupler design ideas were checked for the possibility of obtaining a symmetrical wave and an eligible S_{21} parameter. The coupler designs are presented in Fig. 2.28. The design in Fig. 2.28a is the original PITZ RF coupler design with the short coaxial part. The design in Fig. 2.28b is based

on the TESLA coupler design [41] with a narrowed rectangular waveguide around the transition part and a relatively long compensating waveguide. The idea of the design in Fig. 2.28f is taken from Ref. [42]. It uses a rounded compensating waveguide end. The designs in Fig. 2.28c and Fig. 2.28d are modifications of the design in Fig.2.28b, they apply an elongated coaxial waveguide and two additional side rectangular waveguides, correspondingly for compensation of the wave asymmetry by additional reflections. The design in Fig. 2.28e uses a resonator with diaphragms for the transition from the rectangular to the coaxial waveguides. The design in Fig. 2.28g is also based on the TESLA coupler design, but the symmetrical input to the coaxial waveguide is organized by splitting a wave by a T-combiner.

The simulation showed that only designs with the symmetrical location of two rectangular waveguides can satisfy the requirements. Accordingly, the design of the axisymmetric gun must include the symmetrical design of an RF coupler.

One of these designs was applied at Daresbury Laboratory. The H-like shape coupler is applied for the CLARA project (Fig. 2.29) [43]. The design allows the coupler to be tuned to achieve the best possible match. Movable shorts allow fine tuning of each arm separately, allowing the best possible compensation of phase errors in the two arms as well as the overall match of the transition. The shorts also give a good access for pumping if this is required. Currently, the coupler is in the fabrication phase and the first tests are planned in the near future.

Three designs were selected as proper candidates:

- design with the connection of two rectangular waveguides at the coaxial part (as illustrated in Fig. 2.28g but without T-combiners):
  - advantage: the design is relatively simple for production and development
  - disadvantages: expected difficulties of phase shift adjustments between two rectangular waveguides (any phase shifts introduce field asymmetries), there is no possibility of directional coupler installation for combined wave in order to organize feed back loop for the RF control
- design with two T-combiners (Fig. 2.28g):
  - advantages: guaranty of no asymmetric wave and the possibility of directional coupler installation for combined wave
  - disadvantages: difficult and bulky design with possible huge power losses and risk of sparks in a high power common input line
- H-like RF coupler (Fig. 2.29)
  - advantages: the option of the phase adjustments in the waveguides
  - disadvantages: bulky design, no option of directional coupler installation

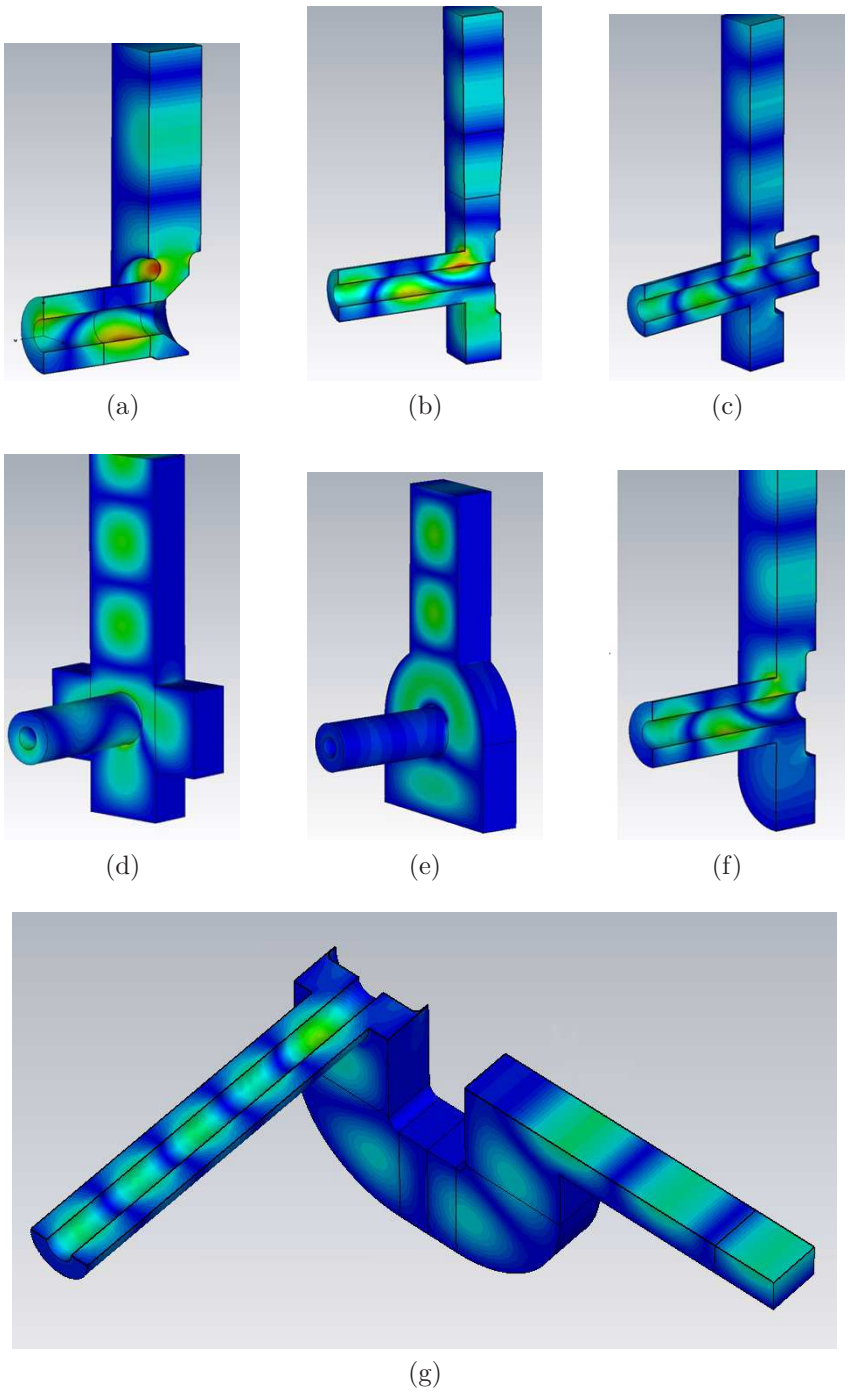

(a) (b) (c)

(d) (e) (f)

(g)

Figure 2.28: Alternative RF coupler designs. Designs at subfigures (a) and (b) show asymmetrical wave in the coaxial waveguide. Subfigure (g) shows the design with symmetrical power input and lengthened coaxial part show a fully symmetrical wave.

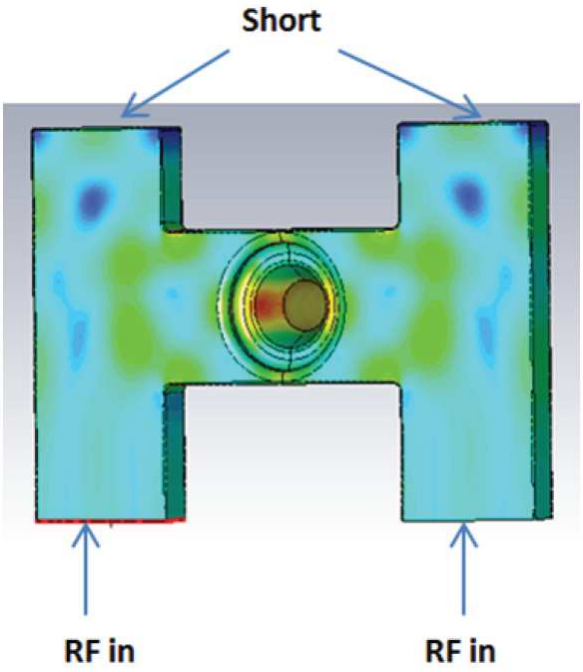

Figure 2.29: Electrical fields in the H-feed coupler applied for the CLARA project [43].

2.6.1 Summary

The results of the electron beam asymmetry studies can be summarized as follows:

- the experiment on the cathode scan by the laser beam does not reveal any distortion of the beam positions grid
- the experiment on Larmor angle showed that the origin of the beam distortion is located at the position of the main solenoid center or the coaxial coupler transition to the full cell
- the experiment on the beam acceleration outside of the forward power pulse showed that the bunch asymmetry does not depend on the bunch timing and is always present in the transverse bunch profile
- the experiment on the main solenoid tilt has not shown any strong dependence of the transverse beam shape on different solenoid tilts
- the most probable reasons of the beam distortion are considered to be the coupler field asymmetry and main solenoid imperfections
- designs for an improved coupler have been presented
- there are also ideas to correct solenoid imperfections by a small normal and skew quadrupoles in the solenoid region

- as well as a detailed design of the magnetic quadrupole correctors, complete coupler kick and main solenoid field simulations, and studies of the field asymmetries influence on the beam emittance still have to be performed, but they are out of the scope of this thesis.

Chapter 3

Stability and jitter studies

The operation of high gain single pass FELs with precision control and stabilization of the longitudinal electron bunch profile and its arrival at the FEL undulator is one of the most challenging tasks. One significant contribution to the arrival time jitter and the longitudinal bunch profile variation is coming from the laser-driven RF gun. That is why the stability the RF photoinjector gun is one of the most important factors for the successful operation of linac-based free-electron lasers. Several types of jitter can impact the stability of a laser-driven RF gun, but the most substantial influence on the performance of a high brightness electron source have fluctuations of the RF launch phase and the cathode laser energy.

The studies on the photoelectron gun stability presented in this chapter include a description of the measurement methods and systems applied at PITZ for the RF phase jitter decrease.

3.1 RF amplitude and phase stability

Single pass FELs apply a large electron bunch compression factor (order of 10 to 100). Therefore any small gun RF amplitude or phase fluctuations can cause significant bunch length variations, unacceptable arrival time jitter due to energy fluctuations and decreases the peak current. The main sources of slow beam parameters drift and fast fluctuations are instabilities of the RF fields a linac.

The control of the gun incoming power is realized via analyzing forward and reflected wave signals from directional couplers near the T-combiner. This control scheme is applied because no direct field pickups are realized inside the current gun cavity prototypes.

The 2009 configuration of the power supply system [44] had just two 5 MW directional couplers on the SF_6 side before the T-combiner (RF waveguides in this part are filled with SF_6 gas [45] to decrease breakdown probability due to the dielectric gas properties) for control and adjustment of the incoming power to the gun. The realization of an efficiently working feedback system, based on the two 5 MW couplers,

did not show successful results due to cross-talk between the two waveguides and power reflections from RF vacuum windows. As a result, a high gun phase jitter has been observed.

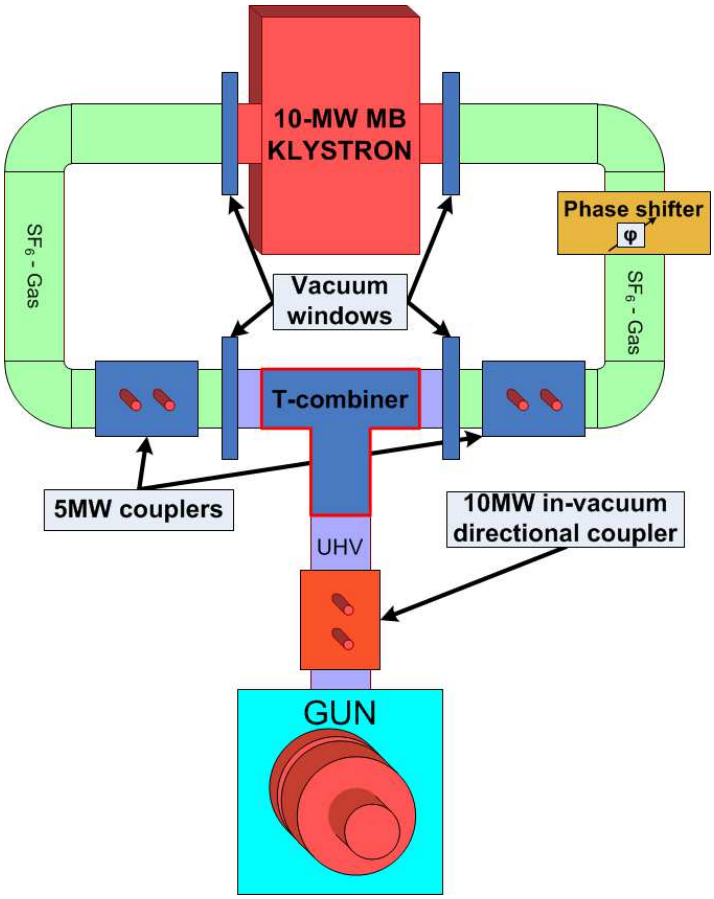

Figure 3.1: General layout of the RF system for the gun.

Measurements of the combined wave and the realization of a feedback system to regulate the incoming power were possible after installation of a new 10 MW directional coupler [46] in the spring of 2010. The 10 MW directional coupler is installed in a vacuum waveguide, downstream the T-combiner. The 10 MW coupler allows control of the combined forward wave and the wave reflected from the gun cavity.

3.2 RF feedback impact on the beam properties

The resonance frequency of the RF gun can be tuned by changing the gun temperature via the cooling water. The temperature in the gun can be stabilized up to 0.01 °C which corresponds to 0.23 kHz detuning and 0.2 ° of RF phase shift [47]. More precise

stabilization of the RF field can be done only by a control system which regulates the input drive of the klystron.

The stabilization of RF amplitude and phase of the gun cavity is organized employing a Low-Level RF (LLRF) system [48]. The stabilization is implemented via measurements of RF field changes in the cavity combined with calculation of its errors and comparing with a set point and application of a closed Feed Back (FB) loop to a forward signal (so-called Feed Forward or FF). That is an active control algorithm which is working in the real-time regime. The main tuning FB parameter is an FB loop gain. This parameter defines how strong the FB will impact on the forward signal and determines the behavior of the FB in general. The LLRF system functionally is based on closely cooperating hardware and software layers like measurement and control, quick calculations, signal processing, data acquisition, synchronization [47].

To regulate the power going to the cavity and to correct the field amplitude and phase, a controller must be provided with information about the current level of the field inside the cavity. The current PITZ RF gun (as the FLASH and XFEL guns) has no field probe inside the cavity which can be used as an indicator. The only information about the field in the cavity is available via a directional coupler placed just in front of the gun (Fig. 3.1). It provides two signals: power going to the gun and power reflected from it. The use of both signals and an appropriate calibration allows to calculate a probe signal of the cavity field.

The calculation of the field is done by a Field Programmable Gate Array (FPGA). An FPGA chip is installed on a μTCA board which is a recent replacement of an old VME board (a board which is based on the Versa Module Europa Bus). A block diagram of the RF control gun system is presented in Fig. 3.2 [47]. The measured forward and reflected power signals are converted into the baseband, and I and Q components are separated in an IQ detector. Decomposed signals are sampled with high-speed ADCs and sent to the main processing unit, the FPGA chip. Digitized signals are calibrated inside the FPGA. A calibration stage of the FPGA controller is used to compensate phase shifts and the amplitude attenuation. Control algorithms based on the feedback signal make the gun field more stable which is directly reflected in the beam parameters stability (see section 3.5).

3.3 Gun water cooling system

RF pulse heating is a well-known problem for the very high-frequency high power devices. This effect restricts peak and average power in resonant cavities like RF guns. During the RF pulse, heat propagates from the surface into the cavity body with a quite sharp temperature front. Cooling of the PITZ gun is realized by 14 water cooling channels located in the gun walls. According to the photoinjector specifications for the European XFEL, the RF gun has to provide an electric RF field of 60 MV/m at the cathode, which implies peak power of ~ 6.5 MW. RF pulses of 700 μs length at 10 Hz

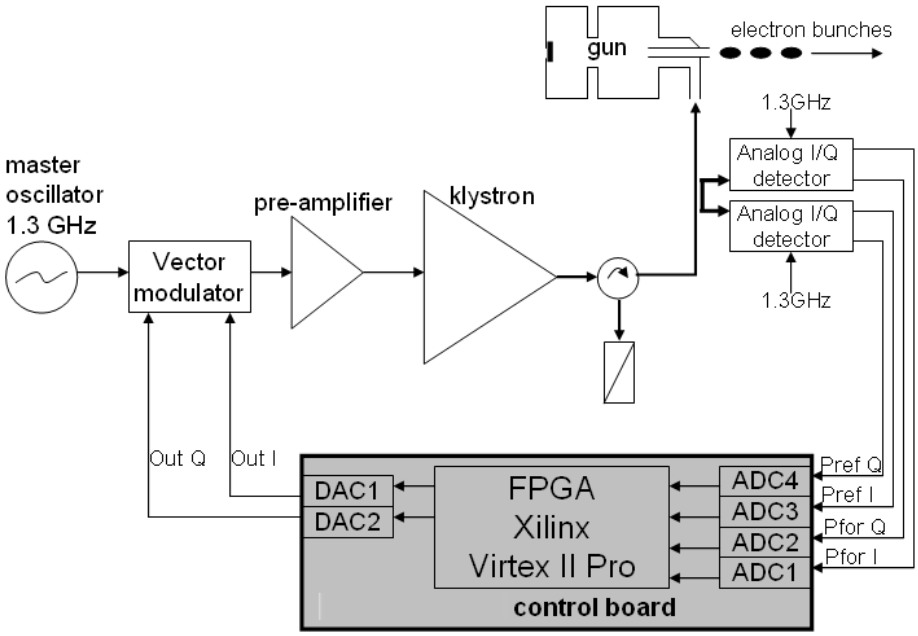

Figure 3.2: Block diagram of the gun RF control system.

repetition rate correspond to an average RF power of $\sim 46\,\mathrm{kW}$. Besides heat transfer, the water cooling system (WCS) of PITZ has the goal to keep the gun cavity at sharp resonance. Rather challenging specifications on amplitude and phase stability (0.01 % and 0.01 °, respectively) require high precision and stability of the WCS.

The WCS of the PITZ gun is realized by control of the heat exchange between cooling water and copper body of the cavity. The WCS can work in 3 modes: conditioning, operation, and stabilization. The conditioning and operation modes include direct cold water from the cooling tower whereas the stabilization mode excludes cold water flow from the cooling tower and activates a heat exchanger system. Fig. 3.3 shows the control panel of the PITZ gun WCS, where the schematic cooling water circle for stabilization mode is presented.

The difference between conditioning and operation modes is in the response velocity of the controller only. The controller reacts faster in the conditioning than in the operation mode, but the settings of this mode introduce additional fluctuations. Therefore the gun works more stable in the operation regime. Normal operation requires only one heater, but four additional heaters can be activated by request of the control system in case of a strong temperature deviation. This helps to heat up the water temperature more quickly. The schematics of the WCS is shown in Fig. 3.4.

The water cooling system in the stabilization mode consists of two water circulations systems (shown in Fig. 3.5). One system contains a constant water temperature of 40 °C, which is cooled by the main cooling system, and the other runs with an adjustable water temperature that can be preselected by the control system.

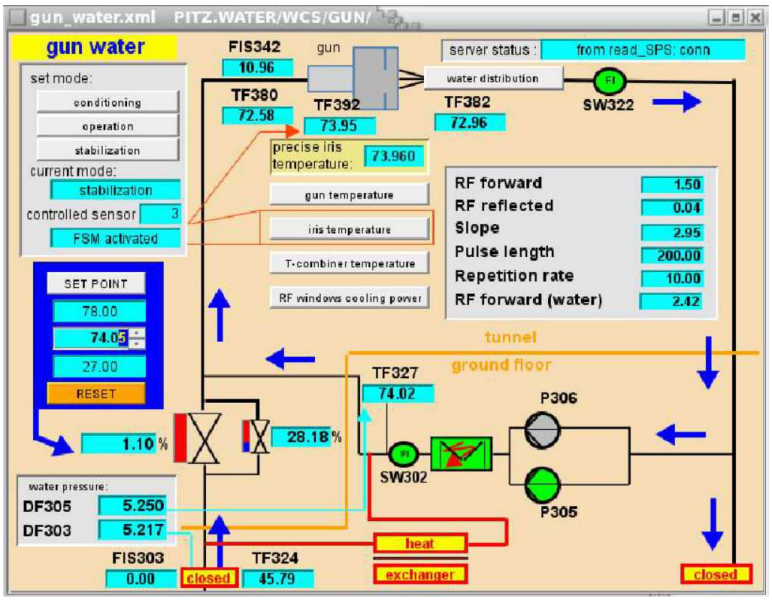

Figure 3.3: The control panel of the Water Cooling System (WCS) used in the PITZ control system. The black line and the blue arrows show the direction of the water flow. The presented WCS is in the stabilization mode: the incoming and outcoming water flows are closed, the WCS uses only inner water circle with the heat exchanger shown in Fig.3.5. The numbers in this figure figure present specific technical data and can be ignored.

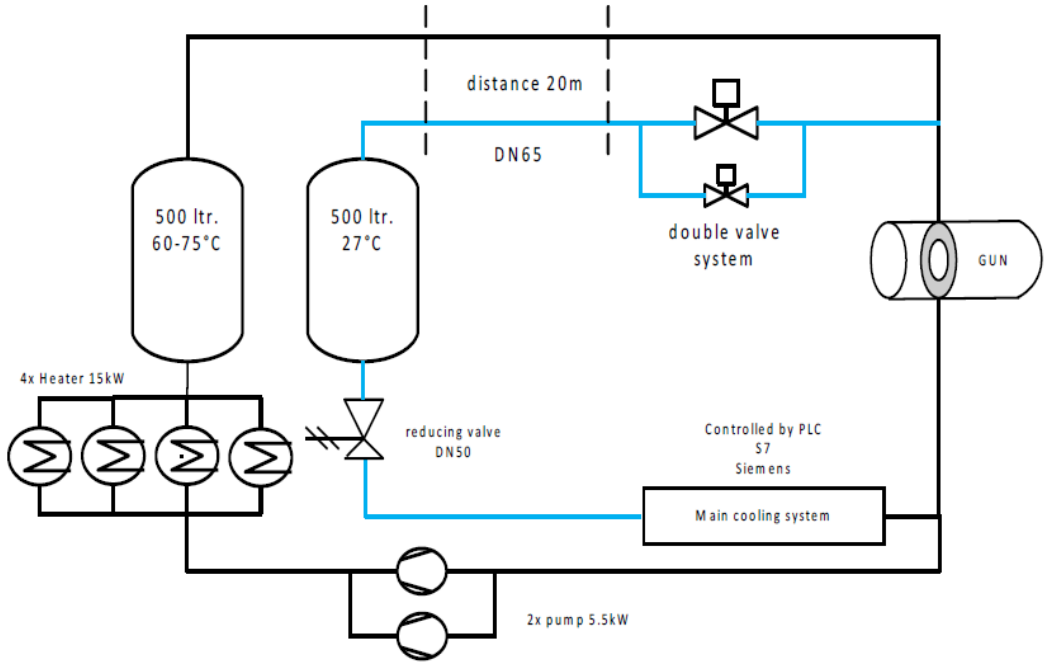

Figure 3.4: Water cooling system layout operation or conditioning mode of run.

For the stabilization mode, both water circulation systems are hydraulically separated from the main cooling system and therefore are independent of pressure fluctuations in the main cooling system. Automatic valves realize the switch-over from the operation mode to the stabilization mode. The mixing of the water of both circulation systems is performed by a double valve solution where the total control signal is divided in a base and variable load for more precise control.

Each water circulations system includes a tank with a capacity of 500 liters. The task of these two tanks is to damp additional oscillations in the temperature of both circulations systems. The implemented control unit is Simatic S7-300 from Siemens [49]. This PLC realizes a digital PID controller to generate the control signal for the double valve solution, switches all pumps, and monitors the safety system.

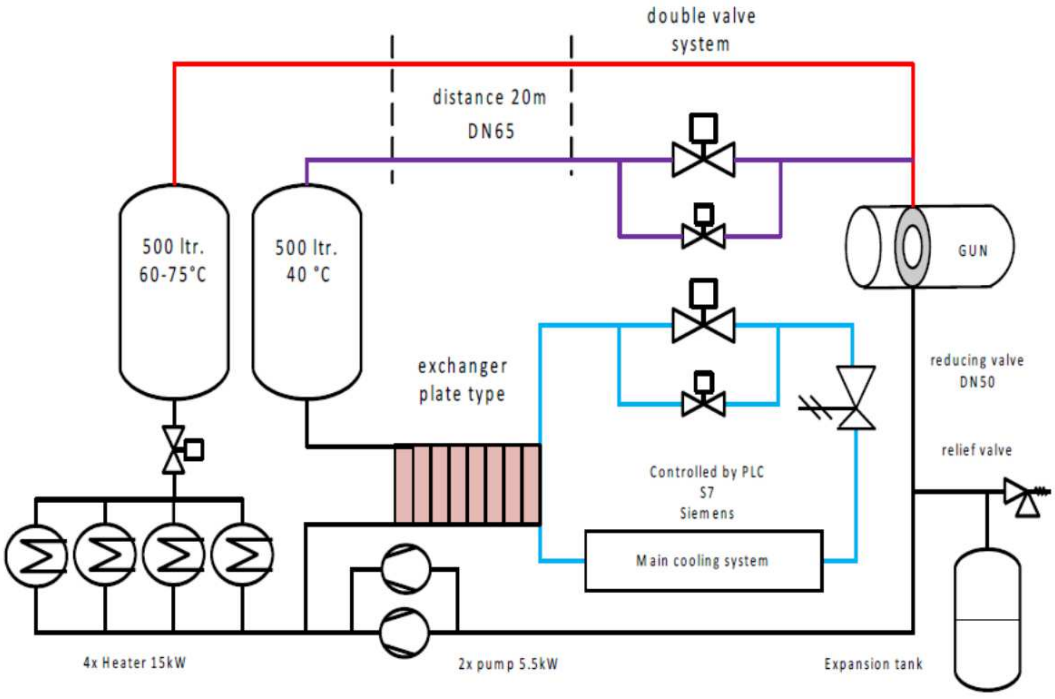

Figure 3.5: Water cooling system layout for stabilization mode of run.

In order to provide a high thermal stability of the gun cavity, the temperature measurement should have sufficient resolution. In the case of PITZ gun, it has to be better than 0.01 °C. The required resolution was achieved by installation of a new readout temperature sensor from National Instruments [50]. The resolution of the new sensor is 0.001 °C, while an old sensor from Siemens has a resolution of 0.025 °C. Additionally, the corresponding controller has been upgraded. The results of the system upgrade are presented in Fig. 3.6. The histogram clearly shows the improvement in the water temperature readout: better resolution for the same RMS temperature value.

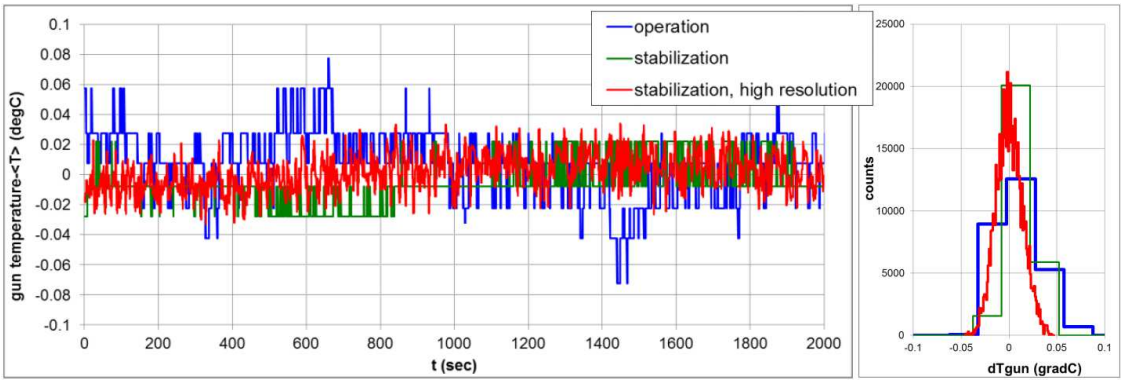

Figure 3.6: Left: the history of the gun temperature for various WCS modes; right: corresponding histograms. The temperature reading is done with the new temperature sensor (red) from National Instruments while the other reading was done with the old Siemens sensor.

3.4 RF phase jitter measurement techniques

Methods applied at PITZ for the gun RF phase stability measurements can be divided into two types: direct measurement by the LLRF system and electron beam based phase stability measurements. There were applied three beam based measurement techniques: single point on-line measurement, 2D scan and Gaussian beam charge Phase Scan and multidimensional Fit (GaussPSF).

All of the beam based measurement techniques use charge-phase scan measurements.

3.4.1 Charge-phase scan

A charge-phase scan measurement is the measurement of the beam charge dependence on the gun RF phase. The beam charge measurements are done by Low.ICT1 and Low.FC1 (see chapter 1), which are located 0.9 m and 0.803 m downstream the cathode, respectively.

The beam charge-on-phase-dependence is impacted by many factors like the space charge density at the cathode, the Schottky-like effect, synchronization of RF fields and beam particles.

A typical bunch charge dependence on gun phase is shown in Fig. 3.7. The following aspects can describe the charge dependence: no electron bunch charge will be extracted when the decelerating field gradient is at the photocathode when the laser pulse hits the photocathode (phase $> 30\,^{\circ}$); the phase when the RF field becomes accelerating and electrons can already be extracted is called zero-crossing phase, starting from this phase more and more electrons can be emitted, accelerated, and transported to the exit of the cavity where they can be detected by the ICT or FC. The right slope (phases from -20 $^{\circ}$ to 30 $^{\circ}$) of the charge-phase dependence can be described by the combination of the laser

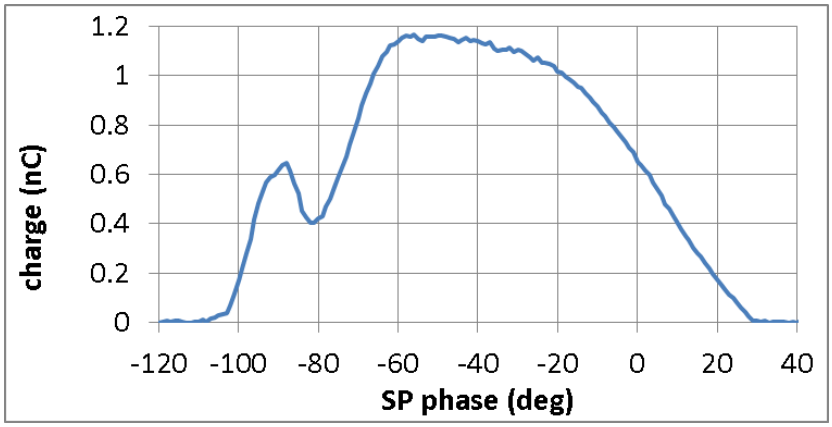

Figure 3.7: Charge phase scan for laser transmission 24 %, 7.8 MW power in the gun and 0.3 mm laser transverse RMS size.

pulse shape, the space charge density of the beam and the accelerating gradient. The contour of this slope mainly depends on the laser pulse temporal profile. The slope of the top part (phases -60 ° – -20 °) represents the Schottky-like effect, when additionally to the photoemission the field emission due to high RF field strength on the cathode can take place (the Schottky-like effect starts to act even shortly after zero-crossing phase, but its effect is negligible). The left slope of the charge-phase dependence can be described by desynchronization of RF fields and beam motion. At this moment the beam undergoes deceleration in the full cell in the gun and particles from the beam tail are transported back to the cathode. The bump on the left part of the plot represents complicated multistage acceleration process which is described in Ref. [51].

3.4.2 Single point on-line phase measurement

This technique was suggested in Ref. [52] and is based on the dependence of bunch charge fluctuations on RF phase jitter, photocathode laser pulse energy fluctuations, and electronics noise (Fig. 3.8).

The jitter of the measured charge can be recalculated to the jitter of the RF phase, using their linear correlation when a working point is chosen on the right-hand side of the phase scan plot (Fig. 3.8, phase range around 20 ° phase). If the laser pulse energy is stable enough, the charge fluctuation becomes a direct measure of the phase stability.

Typical phase stability measurements are shown in Fig. 3.9. Here the measured charge fluctuations are converted to the phase jitter via multiplication by the charge-phase slope coefficient. From the obtained phase jitter data, the RMS value was directly calculated (it is shown as RMS value in the legend), additionally the phase fluctuation due to the water temperature instability is estimated by temperature measurements and presented by the red line. The RMS phase jitter without drift is a quadratic subtraction of the measured phase jitter and the phase fluctuations due to water fluctuations.

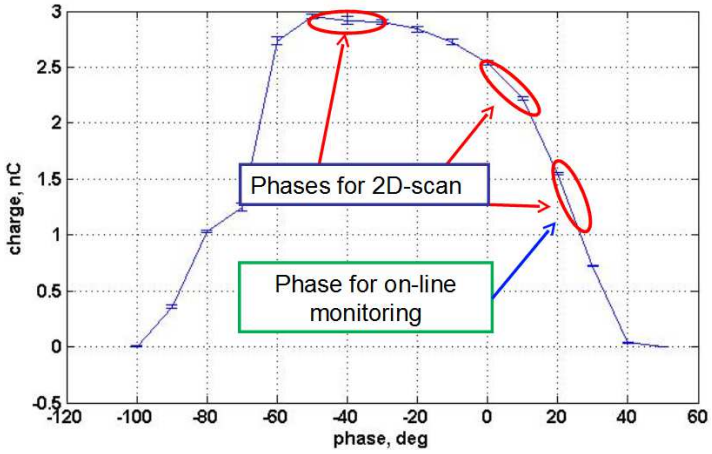

Figure 3.8: Charge phase scan for the beam based phase jitter measurements. The phase range around 20° is used for the single point on-line phase measurement due to the most linear charge vs phase dependence. The phase ranges around -40°, 0° and 20° is used for 2D phase scan measurement.

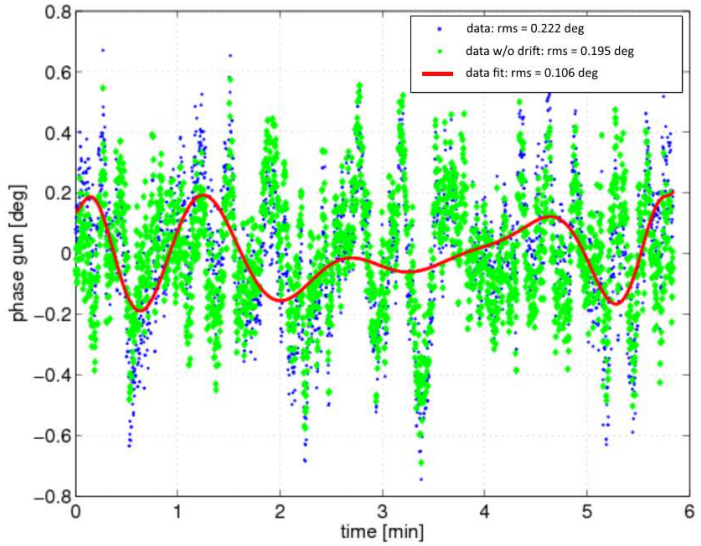

Figure 3.9: Phase stability measurement by the on-line monitoring tool. The RMS phase jitter is 0.222°, while the RMS jitter with respect to the drift is 0.195°.

3.4.3 2D phase scan measurement

The technique was proposed in Ref. [53]. The technique uses a 2D phase scan taking the laser pulse energy jitter into account. The idea of the technique is to decouple the laser and phase jitters by measuring charge jitter for different gun RF phases and laser energies. The jitter of the charge has a different contribution from the laser energy and RF phase jitters. For example, on the plateau of the charge-phase scan (Fig. 3.8 phase = -40 °), the main contribution to the charge jitter is caused by the laser energy jitter while at the slope the phase jitter makes a minor contribution. However, at the steepest and linear slope (Fig. 3.8 phase = 20 °), the input of the phase jitter to the charge jitter is much larger while the contribution from the laser energy jitter stays the same.

The charge histograms, measured for different gun phases (see Fig. 3.8, the phases around -40 °, 0 ° and 20 °) and cathode laser intensities, improve the accuracy of the measurements during the analysis of the gun phase and laser energy jitters.

The main assumption of this method is an independence of the normally distributed jitters of the RF launch phase and the cathode laser pulse energy, so the distribution function of the RF launch phase σ_ϕ and the laser energy σ_E do not depend on the gun phase set point and laser pulse energy. In other words, both error sources do not have any correlations and can be presented by a 2D Gaussian distribution:

$$P(\phi, E) = \frac{1}{2\pi\sigma_\phi\sigma_E} \exp\left(-\frac{\Delta\phi^2}{2\sigma_\phi^2} - \frac{\Delta E^2}{2\sigma_E^2}\right), \tag{3.1}$$

where $\Delta\phi = \phi - \phi_0$ and $\Delta\mathrm{E} = \mathrm{E} - \mathrm{E}_0$ are RF phase and laser energy centered around the point of interest, and σ_ϕ and σ_E are the RMS jitters of the phase and laser energy, respectively.

In order to find the RMS charge jitter, one should determine the charge probability distribution function $W(Q)$. This function can be derived from the integration of Eq. 3.1 along the curve of equal charge:

$$G(\phi, E) = Q\,. \tag{3.2}$$

This equation can be roughly estimated by the Taylor expansion up to linear terms:

$$Q = \left.\frac{\partial Q(\phi, E)}{\partial\phi}\right|_{(\phi=0)} \Delta\phi + \left.\frac{\partial Q(\phi, E)}{\partial E}\right|_{(E=0)} \Delta E\,, \tag{3.3}$$

where the partial derivatives are taken at the point of interest. By introduction of a parameterization (with scalar parameters Q and ξ) for the curve of Eq. 3.2 we get:

$$\begin{aligned} \phi &= F_\phi(Q, \xi)\,, \\ E &= F_E(Q, \xi)\,. \end{aligned} \tag{3.4}$$

The charge probability distribution can be found from:

$$W(Q) = \int P(F_\phi(Q,\xi), F_E(Q,\xi)) \cdot \sqrt{\left(\frac{\partial F_\phi}{\partial \xi}\right)^2 + \left(\frac{\partial F_E}{\partial \xi}\right)^2}\, d\xi \,. \tag{3.5}$$

The integration yields the charge fluctuations function which is represented via a Gaussian distribution function with RMS width:

$$\sigma_Q = \sqrt{\left(\left.\frac{\partial Q(\phi,E)}{\partial \phi}\right|_{(\phi=0)}\right)^2 \sigma_\phi^2 + \left(\left.\frac{\partial Q(\phi,E)}{\partial E}\right|_{(E=0)}\right)^2 \sigma_E^2} \,. \tag{3.6}$$

The estimation of the RF phase σ_ϕ and the laser energy σ_E jitter can be obtained from Eq. 3.6 by solving a linear system for at least two equations of the charge jitter σ_Q at different combinations of RF phases and cathode laser pulse energies:

$$\begin{pmatrix} \left(\left.\frac{\partial Q}{\partial \phi}\right|_{\phi=\phi_1}\right)^2 & \left(\left.\frac{\partial Q}{\partial E}\right|_{E=E_1}\right)^2 \\ \left(\left.\frac{\partial Q}{\partial \phi}\right|_{\phi=\phi_2}\right)^2 & \left(\left.\frac{\partial Q}{\partial E}\right|_{E=E_2}\right)^2 \end{pmatrix} \times \begin{pmatrix} \sigma_\phi^2 \\ \sigma_E^2 \end{pmatrix} = \begin{pmatrix} \sigma_{Q1}^2 \\ \sigma_{Q2}^2 \end{pmatrix} \,. \tag{3.7}$$

3.4.4 Phase jitter measurement technique utilizing Gaussian beam charge Phase Scan and multidimensional Fit

Implementation of the new water temperature control system including the water temperature stabilization mode and upgrade of the LLRF system based on μTCA in November 2014 [54] improved the gun RF phase stability so that on-line and 2D scan phase jitter techniques were not able to distinguish between phase jitter, laser energy jitter, and electronic noise. The beam based phase stability measurement became a more sophisticated task which was solved by the refinement of the phase scan technique [55].

This technique uses the information about the photocathode laser temporal profile. A simple implementation can be done for a Gaussian profile and for this particular case the phase scan can be analytically approximated (Fig. 3.10). Based on the approximation it is possible to evaluate the RMS phase jitter σ_ϕ from the bunch charge fluctuations.

Additionally, the technique yields the laser pulse energy jitter σ_{laser} and RMS electronic noise $\sigma_{\text{el.noise}}$. The technique requires space charge relaxed conditions for the measurements. This means that the charge density at the cathode must be as low as possible, but sufficient to provide a clear signal (above the electronic noise). The Schottky effect should be taken into account due to significant influence on the charge at high gun gradients (>60 MV/m).

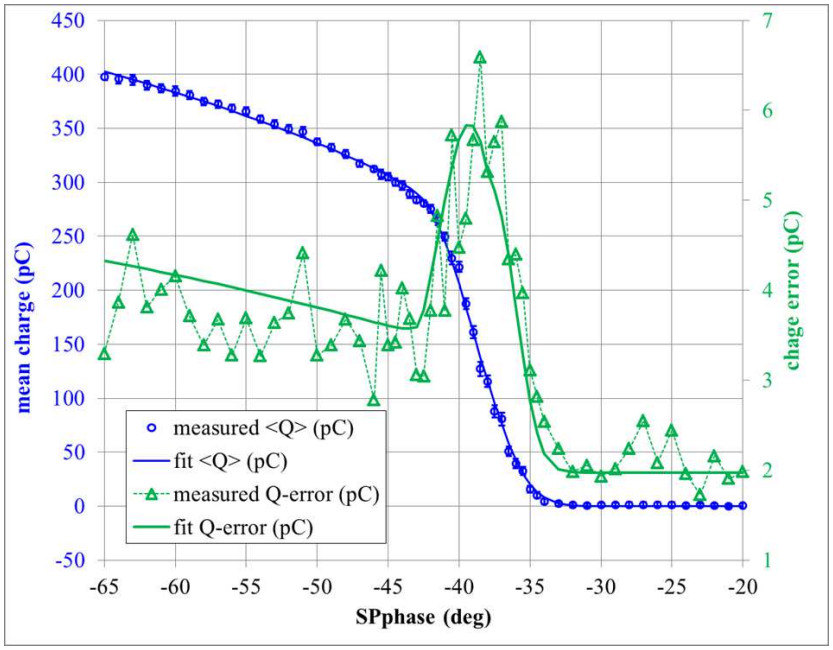

Figure 3.10: Measured charge dependence on the RF launching phase (left blue axis) with the fit and its error function (right green axis). The set point RF phase (SPphase) has an arbitrary (but fixed) offset to the mathematical phase of the gun cavity resonator.

The bunch charge phase scan can be fitted assuming a Gaussian temporal profile using the formula:

$$Q_{fit}(SPphase) = Q_{bkg} + A \cdot F_{schottky}(\phi) \cdot (1 - Erf\,[C \cdot \phi])\ ,$$
$$F_{schottky}(\phi) = \begin{cases} \sqrt{1 - S \cdot \sin\frac{\pi\phi}{180}} & \text{if } \phi \leqslant 0\,, \\ 1 & \text{if } \phi > 0\,, \end{cases} \tag{3.8}$$

where the error function Erf represents the Gaussian temporal shape of the laser pulse, $\phi = \phi_{\mathrm{q0}} - \mathrm{SPphase}$, with ϕ_{q0} is the zero-crossing phase. C, A and S are fitting parameters, $\mathrm{Q_{bkg}}$ is the background charge (dark current) and $F_{schottky}$ is the Schottky factor.

A reliability improvement of this technique can be made by measuring different combinations of the WCS mode and RF FB settings. While changing these settings a few common factors (laser pulse length and energy jitter) stay the same but the phase jitter is changed. An example of the approach is presented in Fig. 3.11. The measurements were performed for two WCS modes and two states of the RF FB. The difference between the phase jitter values for different combinations of the gun operation is shown by the white arrows: WCS stabilization mode together with FB gives 82% phase jitter reduction.

An example of the technique is shown in Fig. 3.10, which yields the following RMS jitter list:

- phase jitter $\sigma_\phi = (0.114 \pm 0.036)^\circ$
- cathode laser pulse energy RMS jitter $\sigma_{\text{laser}} = (0.951 \pm 0.127)\,\%$
- electronic noise RMS fluctuations $\sigma_{\text{el.noise}} = (1.976 \pm 0.205)\,\text{pC}$

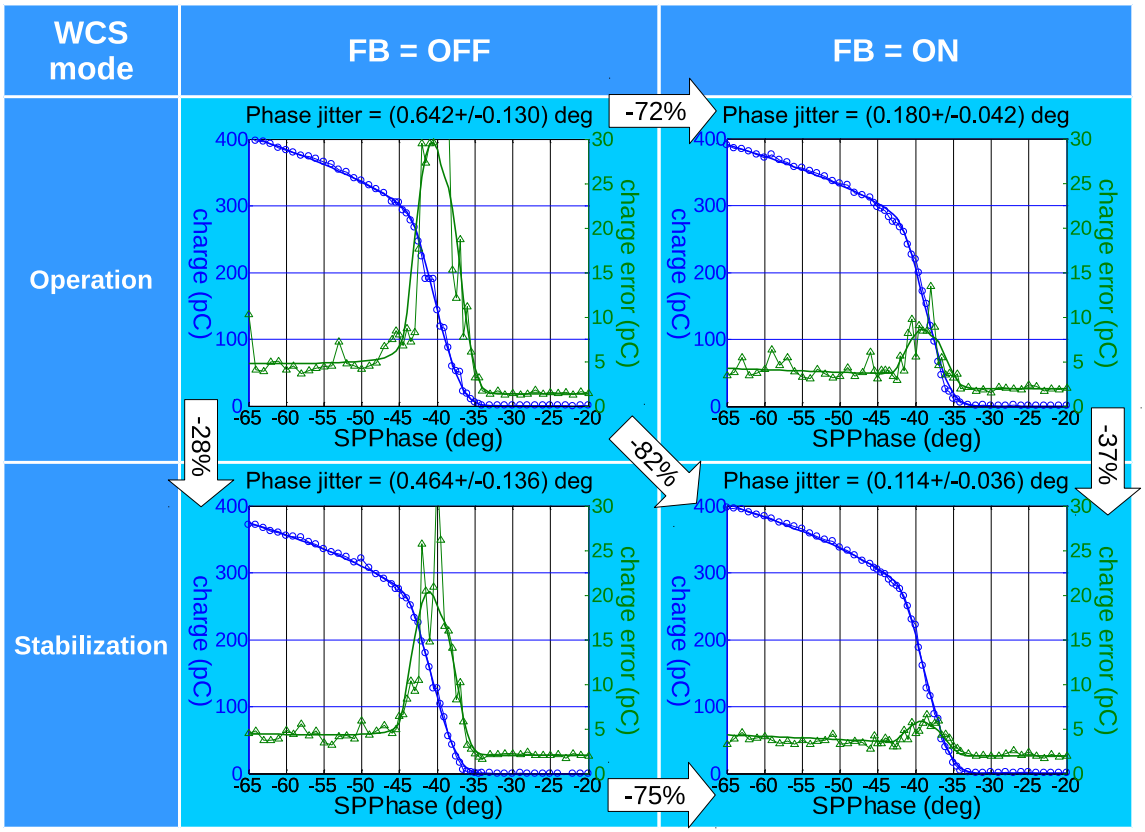

Figure 3.11: RF gun stability measurements by GaussPSF technique. The measurements are performed for several RF gun operation combinations: with and without RF feedback (FB, the table columns), operation and stabilization WCS modes (the table lines). The white arrows emphases the role of different factors in the RF gun stability improvement.

3.4.5 μTCA LLRF tools for phase measurements

The newly implemented (November 2014) μTCA based LLRF gun system allowed [56] to perform phase and amplitude stability measurements using the LLRF readout. An

example of the stability monitoring using the μTCA readout is shown in Fig. 3.12, where the RMS jitters of the phase (left plot) and the amplitude (right plot) are presented.

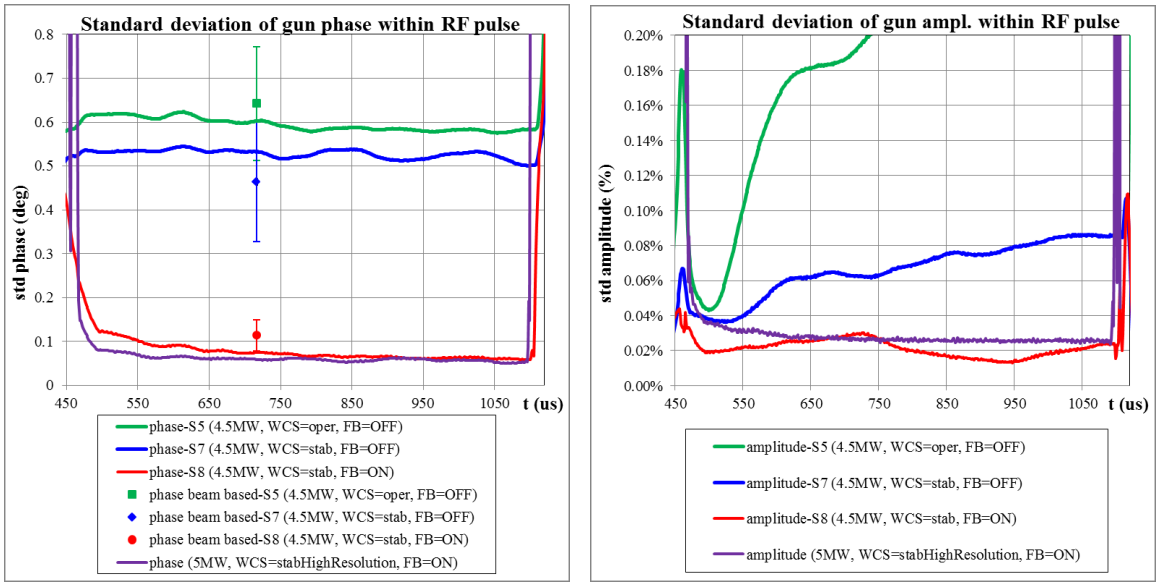

(a) (b)

Figure 3.12: RF gun stability measurements: RMS jitter of the phase (a) and amplitude (b), measured applying various WCS modes, including high resolution of the temperature readout, with and without μTCA LLRF feedback (FB). Corresponding beam based phase jitter measurements are shown with markers in the left plot.

3.5 Phase stability measurement results

Phase stability measurements before implementation of the upgraded WCS (particularly the stabilization mode) and the μTCA based LLRF gave phase jitter around 0.2° RF and 1.5 % laser pulse energy jitter. Examples of the measurements are presented in Fig. 3.13 and Fig. 3.14 for on-line and 2D scan techniques, respectively.

The gun phase stability measurements shown in Fig. 3.13 and Fig. 3.14 were obtained for the same operating parameters of the gun. The RMS phase jitter obtained from the on-line monitoring tool is 0.210° and 0.254° obtained from 2D scan tool. The RMS value of the laser pulse jitter, obtained from the 2D scan tool, is 1.22 %.

Increasing the number of pulses in a train did not improve the phase stability (see Fig. 3.15) because the phase along a pulse train was not exactly constant and slightly changed from measurement to measurement. However, there is a clearly visible improvement in the phase stability by applying the FB.

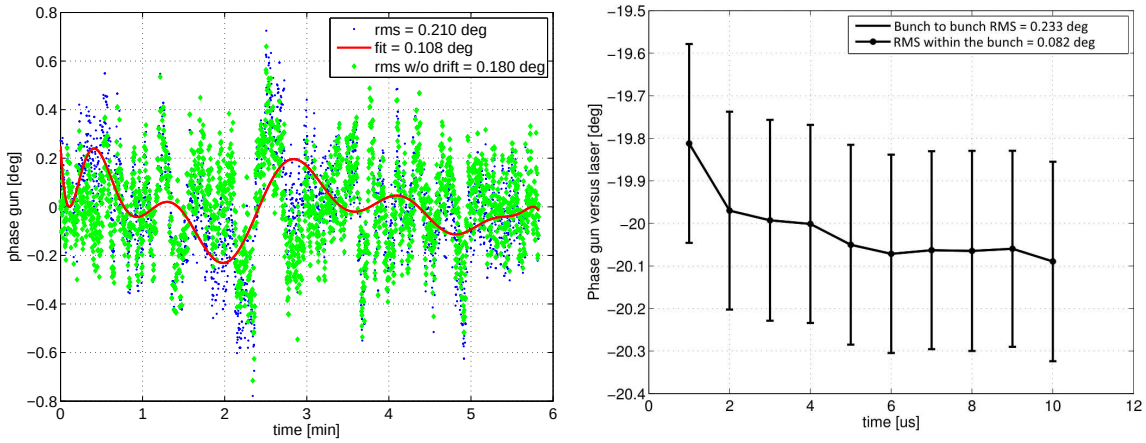

(a) (b)

Figure 3.13: Phase stability measurement by the on-line monitoring tool: (a) phase fluctuations in time and (b) phase stability across the macro pulse.

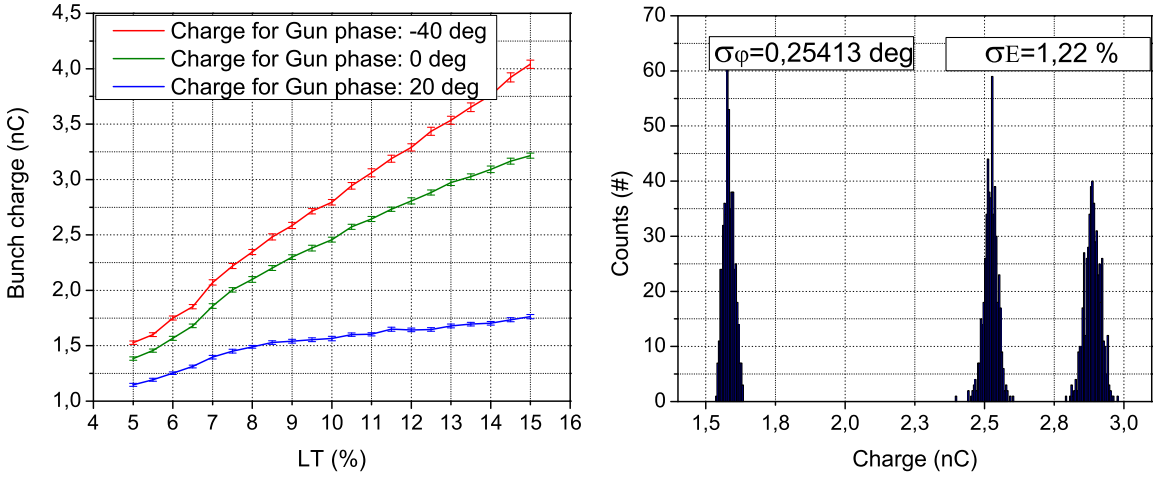

(a) (b)

Figure 3.14: Phase stability measurement by the 2D scan tool: (a) bunch charge measurements vs laser energy and (b) charge histograms used for calculations.

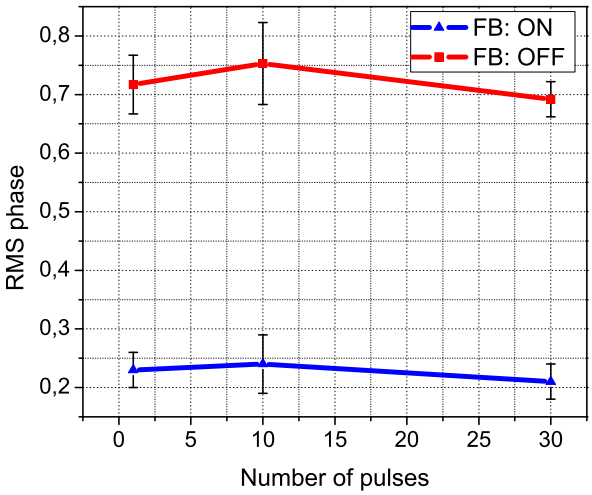

Figure 3.15: Phase stability measured by on-line tool for different number of pulses.

After implementation of the upgraded WCS and the μTCA LLRF system the RF phase and amplitude became significantly reduced, which made the monitoring complicated. It was not possible to distinguish between charge measurement noise and the phase jitter. Fig. 3.16 shows an example of the charge measurements by the on-line technique. The RMS number of the charge at the plateau of the phase scan (ϕ=-45 °) has to be smaller than the fluctuations measured at the phase where a significant charge slope (ϕ=30 °) occurs due to the reduction of the charge jitter dependence on the phases at the plateau. However, the measurements show an opposite situation. That implies that the measurement is completely dominated by the laser energy jitter or measurement noise, but not by the phase jitter.

In order to measure the phase jitter for the case of the laser energy jitter or measurement noise dominating the more precise measurement tool based on GaussPSF technique was applied. The phase stability measurements resulting from the GaussPSF technique are summarized in Table 3.1. The measurements were performed at 600 μs RF pulse length for two peak RF power levels in the gun and different combinations of the WCS modes and FB settings. The charge measurements were done by the Low.FC2 installed in the low energy section 1.4 m downstream the cathode because the background noise level, detected from it, was lower than for the Low.FC1 (usually used for charge measurements) in the beamline.

The RF gun phase and the amplitude stability using the μTCA readout (see section 3.4.5) was measured as a function of the feedback gain for a peak power of 6 MW and 200 μs RF pulse length as well as for 5 MW and 600 μs. Results of the measurements are shown in Fig. 3.17, where RMS phase and amplitude jitters are plotted as a function of the FB gain.

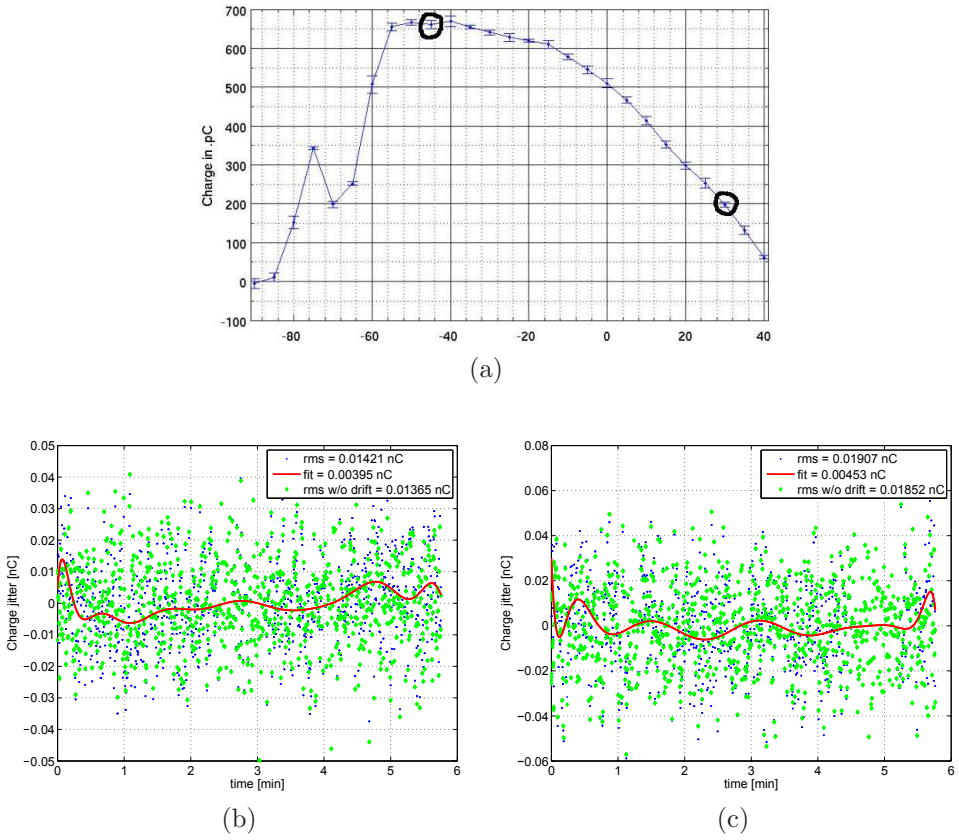

(a) (b) (c)

Figure 3.16: (a) charge phase scan used for stability measurements; (b) charge jitter measurements at the phase = 30 ° (point at the phase scan slope), the jitter is 0.014 nC; (c) charge jitter measurements at the phase = -45 ° (point at the phase scan plateau), the jitter is 0.019 nC.

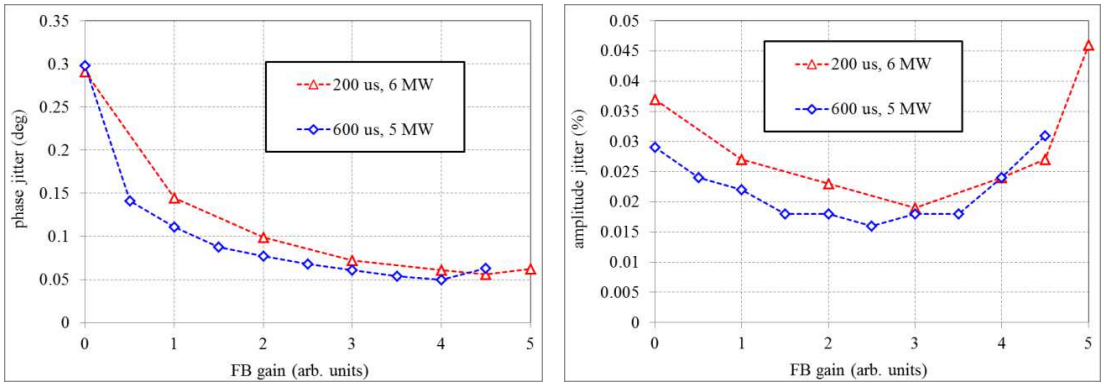

(a) (b)

Figure 3.17: (a) phase jitter and (b) amplitude jitter dependence on FB gain settings. The measurements are done by the μTCA readout.

Power, MW	**WCS mode**	**FB**	**Phase jitter, deg**	**Laser energy jitter, %**	**Charge noise, pC**
4.5	operation	Off	0.642 ± 0.223	0.951	1.39
4.5	operation	On	0.180 ± 0.247	0.951	1.98
4.5	stabilization	Off	0.464 ± 0.391	0.951	2.04
4.5	stabilization	On	0.114 ± 0.060	0.951	1.98
5	operation	Off	0.445 ± 0.286	0.934	2.10
5	operation	On	0.131 ± 0.048	0.934	2.10
5	stabilization	Off	0.410 ± 0.228	0.934	2.13
5	stabilization	On	0.138 ± 0.391	0.934	2.14

Table 3.1: Phase stability results for the beam based GaussPSF technique.

Recently, the Pulse Width Modulation (PWM) tool was implemented in the LLRF [54], which allows additional resonance tuning of the gun cavity. The tool generates small RF pulse length variations within the range of 10 μs. Corresponding stability measurements were performed for the peak RF power of 6.35 MW (60 MV/m - XFEL nominal gradient) and 200 μs RF pulse duration. The WCS stabilization mode with the high-resolution readout setup was used, the RF FB gain was 2.5 (the value at which the amplitude jitter was the smallest). The results of these measurements are shown in Fig. 3.18 and in Table 3.2, where also the RMS gun temperature fluctuations are presented.

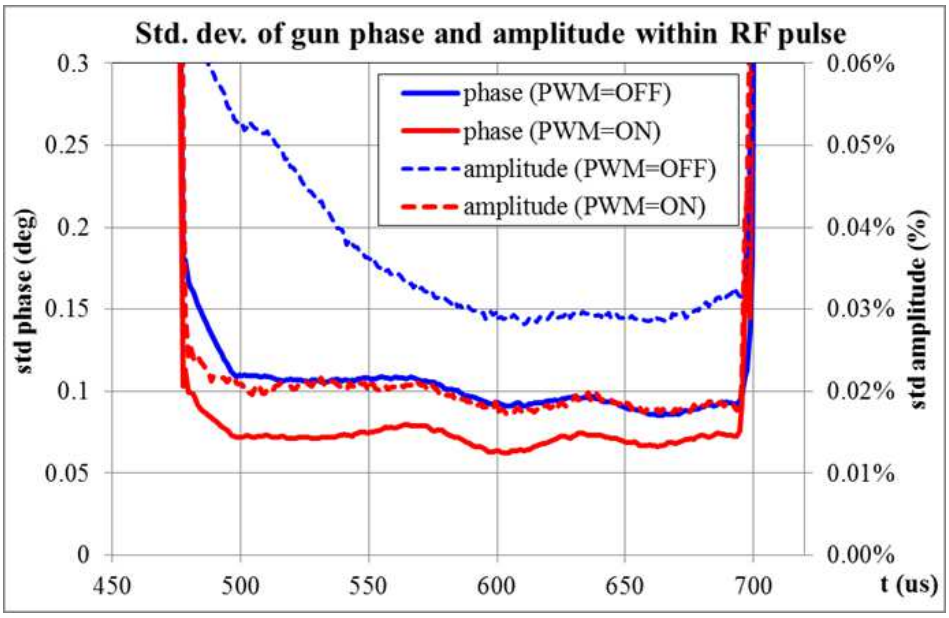

Figure 3.18: Phase and amplitude RMS jitter within an RF pulse during PWM tests.

PWM	σ_{temp}, °C	σ_{phase}, °	$\sigma_{amplitude}$, %
Off	0.023	0.0926	0.0295
On	0.006	0.0633	0.0187

Table 3.2: Phase stability measurement results with and without PWM system.

A further improvement of the RF gun stability seems to be systematically limited by 20 kHz modulations observed in the μTCA amplitude and phase signals (Fig. 3.19), which are very probably originating from the klystron Thomson modulator. Fig. 3.19 shows the voltage and current signals from the modulator and the klystron. The upper graph contains a time domain plot of a single pulse (cutout of the flattop). The data is scaled by a relative amplitude error. The lower plot shows the spectrum of the voltage and current signals averaged over 600 pulses. A 20 kHz oscillation was clearly visible in the spectrum.

3.6 Conclusions on stability and jitter studies

The introduced systems for the PITZ gun (pulse width modulation [54], μTCA low-level RF with feedback [56], stabilization mode of the water cooling system with improved readout) helped to decrease the RF phase jitter by ∼90%. However, it is still a factor of 6 higher than the XFEL specifications (0.01 ° RMS phase jitter). At the same time the measured RF amplitude stability of the gun is already coming close to the XFEL specifications (0.01 % RMS).

The next step of improvement is removing the 20 Hz noise, which is probably coming from the Thomson modulator. It is important to mention that the PPT modulator at FLASH does not have this problem. Also, there is still a remaining problem with the reliable gun operation at 650 μs RF pulse length at full power of ∼6.5 MV/m, which is described in the next chapter.

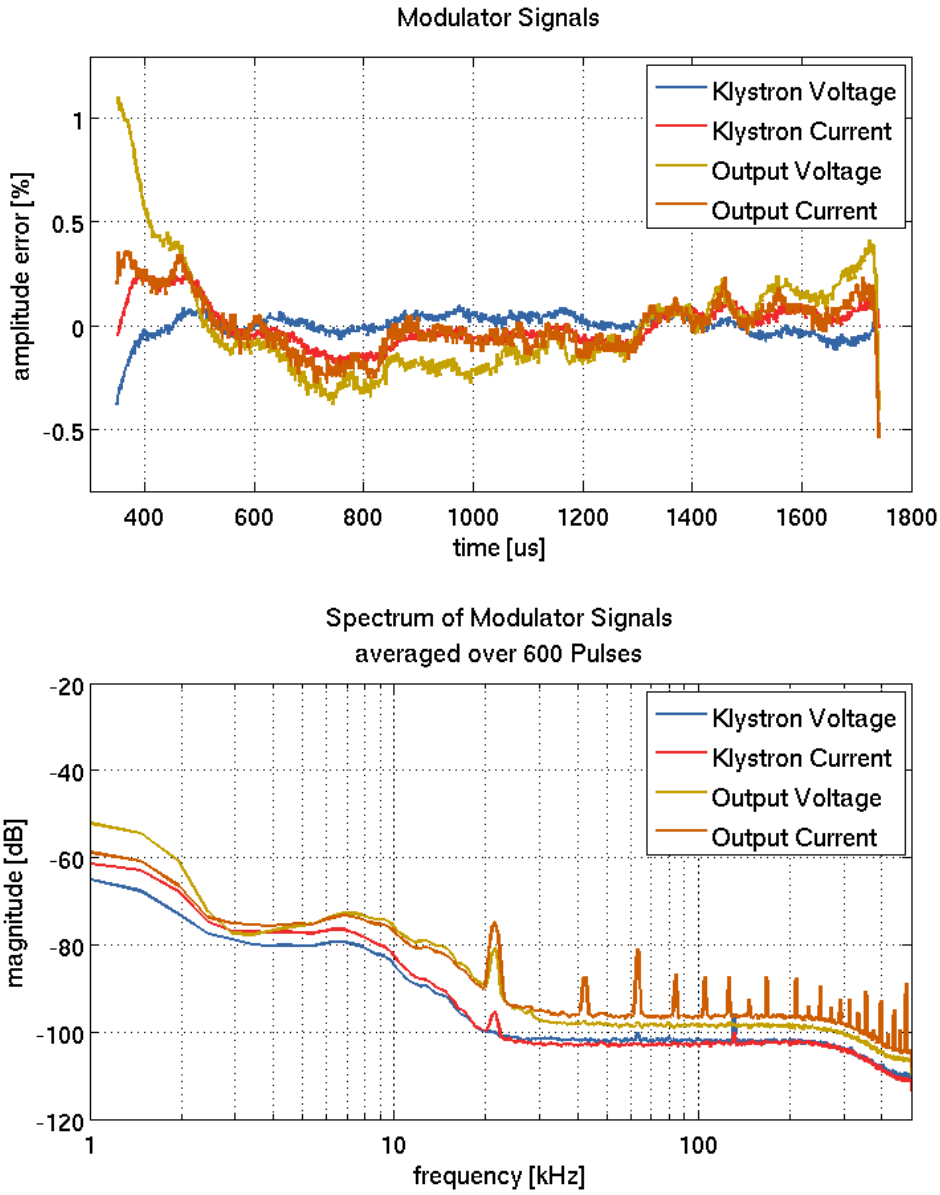

Figure 3.19: Modulator and klystron voltage signals, cutout of flattop in time domain (top) and spectrum (bottom).

Chapter 4

Reliability and conditioning

Besides output parameters of a device, reliability is one of the main characteristics. A device which has worse parameters but shows reliable and stable operation is preferable compared to a device with optimal parameters but with an unreliable operation.

Reliability belongs to the most important specifications of the high brightness RF photoelectron guns because the reliability of the full facility depends on this device. It becomes an especially challenging problem at the specifications required at modern FELs. For example, the European XFEL specifications for the gun are operation at 60 MW/m at the cathode (corresponds to ∼6.5 MW in the cavity), 650 μs RF pulse length, 10 Hz repetition rate. Despite the extreme parameters, gun failures should not exceed 1.7 events per week for operation in the "24/7" regime, if recovery time after such an event takes around 30 – 60 minutes [57].

The stable operation of an accelerating cavity directly depends on its conditioning process. Conditioning is the main instrument to reach the desirable performance of an RF gun. The conditioning quality affects the cavity total performance.

Stability parameters include the following aspects of the gun operation:

- Gun parameters jitter. A jitter of any gun parameter has an influence on the beam quality (pulse-to-pulse jitter as well as jitter within the train). It introduces beam property distortions, smearing or degradation.

- Gun parameters drift. A drift means a relatively slow change of a value. Gun parameters drift leads to a change of the beam parameters. If there is no system which would watch the important parameters and detect drifts, it is possible to loose the required beam parameters for lasing.

- Gun operation failures. Since the gun setup consists of non-perfect components, undesirable events can happen, for example, sparks in the vacuum system, subsystem failures, etc. In order to prevent any damages of the cavity, an interlock system is used. It stops the operation of a cavity in case of the appearance of this kind of events. Due to the interruption of operation the full facility also

stops operation (it is a weak point of single-pass machines). The minimization or complete elimination of all of these factors becomes the most important task of the gun development after the demonstration of a beam with the necessary parameters has been done.

The gun operation failures will be discussed in details in the present chapter. Operation failures or so-called trips are among the most critical points of operation.

4.1 Motivation. XFEL and FLASH specifications

The successful operation of a user facility, such as European XFEL or FLASH, requires a very high reliability of the injector operation.

The assumed total operational cost of the XFEL facility is 83.6 M Euro per year (accounted on the 2005 year basis) and 11.5 M Euro is dedicated only for electricity consumption cost [1]. Each gun operation failure would reduce the availability of the machine. In case of gun failures, the rate of produced laser power will be reduced and therefore the number of possible user experiments will be decreased.

An event when a device must be stopped to preserve the system from damage is called interlock (IL) event or just interlock. In the case of gun operation, these events usually happen due to sparks in the vacuum system. Interlocks also happen due to different auxiliary systems failures. After each interlock event the RF forward power stops. If a vacuum activity above a defined threshold is observed in the vacuum system of the gun, a special procedure to recover gun operational parameters must be applied, and the event is called a trip (see more details on recovery procedure in section 4.5).

If the usual time for recovering after a usual interlock at high peak power and long RF pulse length is of the order of 30 – 40 minutes, the recovery time after a trip increases up to some hours. The significant time loss decreases the availability and effectiveness of the full facility significantly.

The required gun interlock rate which is assumed for XFEL operation is one per week. This value is more or less acceptable for a FEL user operation facility.

4.2 Theory of the conditioning process

The RF conditioning is a process of intensive RF training of an accelerating structure aiming to achieve the required or the best possible operating parameters, such as high peak power, long pulse length, low failure rate, etc.

A typical live cycle of a normal conducting accelerating cavity consists of few basic steps: production (machining, assembling), tuning, mechanical or chemical cleaning, installation and connection to an RF source, baking, and conditioning. Sometimes at the production step, the inner surface undergoes polishing if the machined surface is not smooth enough. Since particle accelerating cavities must work under high or ultra-high

vacuum conditions, the residual molecules must be removed from the inner surface by heating at different steps of the cavity lifetime. The final heating must be done when it is at its final place after the cavity installation and connection to an RF system.

RF conditioning of a vacuum RF component, like an RF gun, a cavity or a coupler, is a surface cleaning process using a low-density plasma in RF fields. Electrical fields cause a field emission, support residual gas ionization and can be a reason for the secondary emission. The combined process changes the surface properties and as effect cleans the surface. Conditioning is only possible in a vacuum system, it is not expected that conditioning effects take place in an air system, where only surface burning and deterioration are possible.

Conditioning effect and progress are assessed by indirect and direct plasma density measurements. Indirect method is based on biased electron probes and photomultipliers, a direct method is a vacuum chamber pressure measurement.

During the conditioning process, one aims to keep running at high plasma density. However, it is important not to fall into an avalanche-like event which increases the pressure exponentially, nor completely extinguishing the activity. A good balance must be found. After some time, the activity drops down and all cavity characteristics get stabilized at a steady-state and conditioning is considered as completed. But in rare cases a cavity damage can also happen by the conditioning process.

Normally, the conditioning with RF power is done starting with short RF pulses in range 10-20 μs. The power is increased controlling the plasma density (thus limiting the RF power rise) until a maximum available (or specified) value (several MWs). The reached power is kept for some hours. Then the pulse length is doubled and the RF power is increased again from P_{min} to P_{max}. This is done until the needed operating pulse length ($\sim$0.8 ms) or CW mode (if this is a goal) is reached. At the end of the RF conditioning, an RF power sweep (going up/down between P_{min} and P_{max}) is done to check for multipacting resonances, in case there are some. The detailed description of the conditioning procedure applied at PITZ is presented in section 4.5.

There is also an alternative strategy of the conditioning when initially ramped up power is fixed at the maximum while the shortest pulse length is kept and then the pulse length started to be increased to a nominal value. This is a quick strategy but does not fully satisfy the conditioning for the whole parameters range. It is sufficient for devices that work with fixed operation parameters (fixed user operation at FLASH and XFEL), but not suitable for cases with changing operation parameters (at PITZ) or during parameters tuning in machine studies.

Conditioning is typically accompanied by multiple breakdowns, high dark current, increased radiation level, sparks, multipacting and increased vacuum activity.

4.2.1 Dark current

The dark current of an accelerating structure is unwanted electron current appearing in a cavity by undesired field emission. Some of the electrons can be captured by

accelerating fields and transported downstream in the beamline.

Dark current is one of the phenomena which appear under high-gradient operation before a structure begins to break down.

Field-emitted electrons are generated in the accelerator structure, preferentially in the high-field regions: cathode or disk-edges. The variety of the trajectories and the points where the electrons hit a cavity wall is vast, and it depends on the combination of multiple factors: the particle emission place, initial energy, emission direction, emission moment relative to the RF field phase. Together with secondary electrons produced by primary electrons, they end up producing the equivalent of an electron gas in each cavity. An example of these trajectories is presented in Fig. 4.1. This example is a part of the simulations presented in section 4.3.1. Captured electrons parasitically absorb

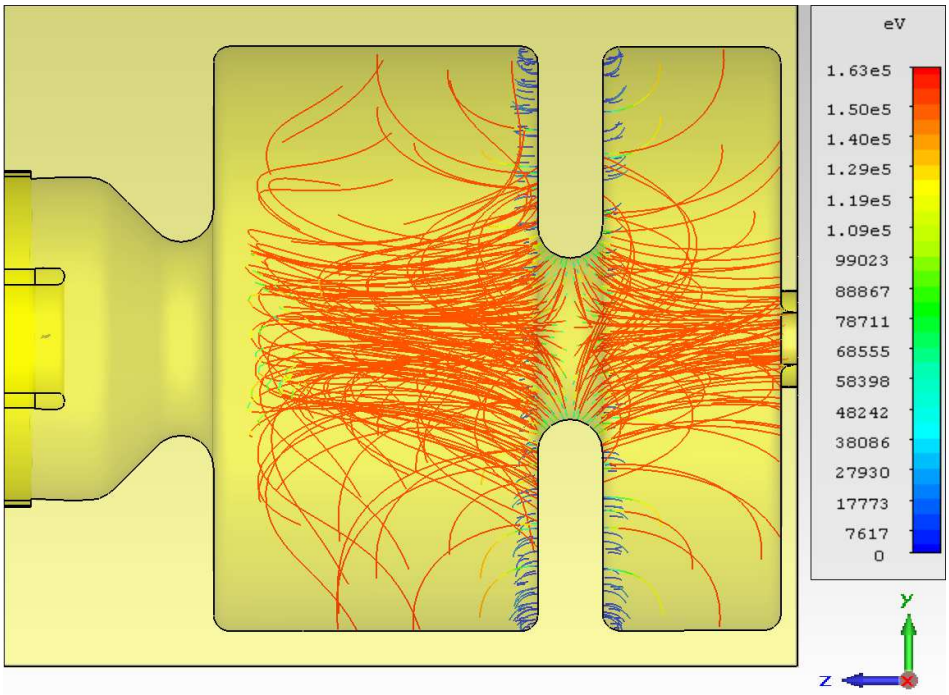

Figure 4.1: An example of dark current trajectories in the PITZ RF gun cavity. Each line represents a trajectory of a dark current electron. The color of the lines indicates the energy of the electrons.

RF energy, cause increased radiation, backgrounds, noise in instruments, and possibly wakefields.

4.2.2 Field emission

The electron field emission is the main reason for dark current in an RF cavity. It also causes breakdown and multipacting phenomena. The description of the field emission can be started from the consideration of the DC field case.

DC field emission

Field Emission (FE) in a constant electric field was carefully described by Fowler and Nordheim [58] They calculated the quantum mechanical tunneling effect of conduction electrons via a modified potential barrier at an ideal metal surface with a constant electric field. The effective potential energy $V(z)$ was defined as:

$$V(z) = \begin{cases} -W_a, & \text{for } z < 0 \\ -eEz - \frac{e^2}{16\pi\varepsilon_0 z}, & \text{for } z > 0 \end{cases}, \tag{4.1}$$

where the term $-e^2/16\pi\varepsilon_0 z$ describes the interaction of the emitted electron with the image charge induced by it. W_a represents the potential energy of the electron inside the metal. The illustration of the potential barrier according to Eq. 4.1 is presented in Fig. 4.2.

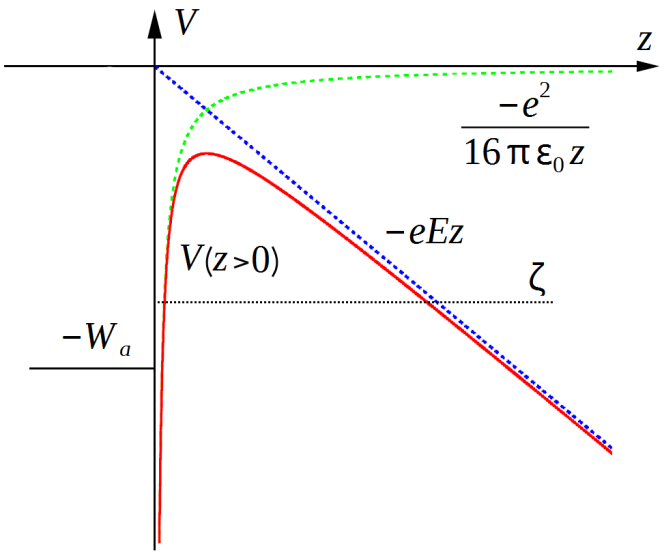

Figure 4.2: The potential energy dependence of the modified electric field potential barrier for an ideal metal surface case. W_a is the electron potential energy inside the metal, ζ is the Fermi energy.

The total number of electrons that overcome the barrier can be obtained via the integral tunneling effect, which gives the field emission current density for the low-temperature body case (T < 300 °K) in a form [59]:

$$j_{FN} = \frac{1.54 \times 10^{-6} \times 10^{4.52\phi^{-0.5}} E^2}{\phi} \exp\left[\frac{-6.53 \times 10^9 \, \phi^{1.5}}{E}\right], \tag{4.2}$$

where E is the surface electric field in V/m, and ϕ is the work function of the emitting material in eV. The field emission current density j_{FN} is given in A/m^2.

However, any surface irregularities will induce field perturbations around them. The electric field at these irregularities will be enhanced and the equation Eq. 4.2 must be modified.

Enhanced Field Emission

There are several effects that can produce surface irregularities, which become a high emitting spots (called emitters) and contribute to the Enhanced Field Emission (EFE): a) surface roughness due to imperfect surface treatment (imperfect machining, scratches, microprotrusions, "tip-on-tip" protrusions), b) dust or microparticles, c) grain boundaries, d) melted craters after breakdown, e) dielectric inclusions and layers, f) absorbed gas particles and g) metal-insulator-vacuum or metal-insulator-metal layers. The idea of EFE can be understood by a simplified model where surface irregularities are represented by ordinary metallic shapes: a sphere above a plane, a cylinder topped by a semi-sphere, and an ellipsoid. The field enhancement factor, β, by which the ideal surface field E is increased to a local microscopic value, E_m, was calculated in Ref. [60] and is given by:

$$\beta = \frac{E_m}{E}\,. \tag{4.3}$$

The field emitted current I_F in this case can be derived from Eq. 4.2, by introducing the effective emitter area A_e, as follows:

$$I_{FN} = \frac{1.54 \times 10^{-6} \times 10^{4.52\phi^{-0.5}} A_e \beta^2 E^2}{\phi} \exp\left[\frac{-6.53 \times 10^9\, \phi^{1.5}}{\beta E}\right], \tag{4.4}$$

where the current is given in A. The β value can be obtained from the so-called Fowler-Nordheim plot, where I_{FN}/E^2 versus $1/E$ on semilog axes is drawn. The resulting graph shows linear dependence. Knowing I_{FN}, E and ϕ, one can obtain β, because the slope of the line on the plot is given by:

$$\frac{d(\log_{10} I_{FN}/E^2)}{d(1/E)} = -\frac{2.84 \times 10^9\, \phi^{1.5}}{\beta}\,. \tag{4.5}$$

The crossing of the plotted line with the $\log_{10}(I_{FN}/E^2)$ axis gives the value of A_e.

Electron Field Emission in RF Fields

The EFE for the RF fields case can be described by assuming that the microscopic electric field on a metal surface has the form $E_0 \sin(\omega t)$. The average field emission

current can be calculated by integrating Eq. 4.4 over time:

$$\begin{aligned} \overline{I}_{FN} &= \frac{1}{T}\int_0^T I_{FN}(t)dt = \\ &= \frac{1.54\times10^{-6}\times10^{4.52\phi^{-0.5}}A_e\beta^2E_0^2}{\phi}\times \\ &\times\frac{2}{T}\int_0^{\frac{T}{4}}\sin^2(\omega t)\ \exp\left[\frac{-6.53\times10^9\,\phi^{1.5}}{\beta E_0\sin(\omega t)}\right]dt\,, \end{aligned} \tag{4.6}$$

where E_0 is the amplitude of the sinusoidal macroscopic surface field in V/m, T is the total time period of the RF field and ω is the field frequency. An approximate solution gives the field-emitted current, which can be expressed as:

$$\overline{I}_{FN}\approx\frac{5.7\times10^{-12}\times10^{4.52\phi^{-0.5}}A_e(\beta E_0)^{2.5}}{\phi^{1.75}}\exp\left[\frac{-6.53\times10^9\,\phi^{1.5}}{\beta E_0}\right], \tag{4.7}$$

where the average field-emitted current is given in A. Similarly to the DC field case, one can make a Fowler-Nordheim plot, where β can be obtained from the slope of the line given by:

$$\frac{d(\log_{10}I_{FN}/E^{2.5})}{d(1/E)}=-\frac{2.84\times10^9\,\phi^{1.5}}{\beta}\,. \tag{4.8}$$

4.2.3 Secondary electron emission

Additionally, to the field emission phenomena, there is the secondary electron emission process which significantly contributes to the dark current.

An electron that hits a surface, can produce further electrons traveling away from the surface. These electrons are called secondary electrons, and the incident electrons are primary. The secondary electrons are divided into three types [61]:

a) "back-scattered electrons" – when the secondary electrons are reflected off the surface primary electrons,

b) "re-diffused electrons" – when the primary electrons penetrate the surface and diffuse through the body, scatter off atoms back towards the surface, and leave the body,

c) "true secondary electrons" – when the electrons interact with the material and release more electrons.

The process of the secondary electrons generation is presented in Fig. 4.4.

Typically, the secondary electron emission is characterized by a dependence of the Secondary electron Emission Yield (SEY) on the primary electron energy. The secondary electron emission yield is defined as a relation of the emitted electrons number

over the incident electrons number. The secondary electron emission yield depends on the material, surface treatment, special coating of the metal (if any) and on the impact energy of a primary electron. An example of secondary electron emission yield for copper and molybdenum is presented in Fig. 4.3.

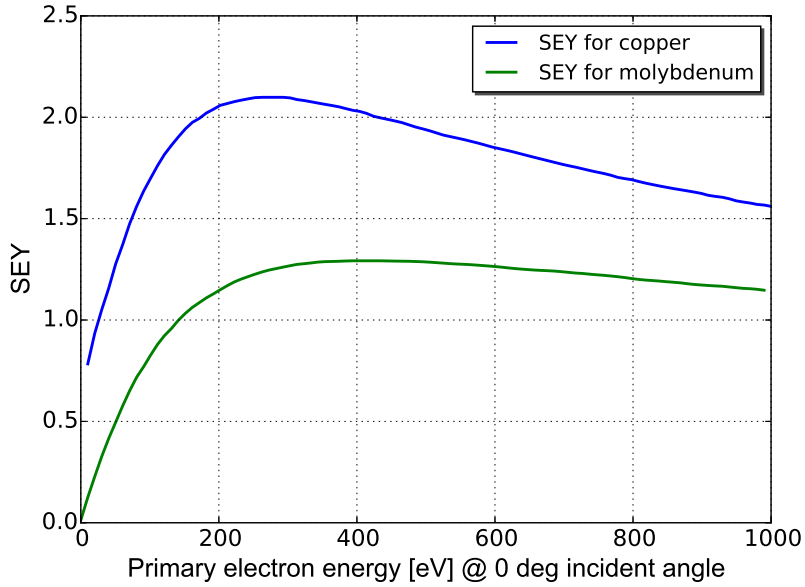

Figure 4.3: Secondary electron emission yield for copper and molybdenum at 0 ° incident angle of primary electron.

For detailed description of the process a quantum mechanical approach should be applied. Following the description from Ref. [61], one can denote the probability that an electron with incident energy E_0 yields n secondary electrons while striking the surface at an angle θ_0 as $P_n(E_0, \theta_0)$. Taking into account all possible final states $(n = 1, 2, \ldots, \infty)$ one can express the total SEY as

$$\delta = \sum_{n=1}^{\infty} n P_n \,. \tag{4.9}$$

Following the above presented description and experimental data from Ref. [62, 63] the SEY for the backscattered electrons at normal incidental angle $\delta(E_0, \theta = 0)$ can be described by the function:

$$\delta_{bs}(E_0, 0) = P_{1,bs}(\infty) + [P_{1,bs}(E_0) - P_{1,bs}(\infty)] e^{-(|E_0 - E_{bs}|/W)^p/p} \,, \tag{4.10}$$

and for the rediffused electrons by:

$$\delta_{rd}(E_0, 0) = P_{1,rd}(\infty)[1 - e^{-(E_0/E_{rd})^r}] \,, \tag{4.11}$$

where W, p and r are fit parameters. The SEY for the true secondary electrons can be calculated by the simplified expression:

$$\delta_{ts}(E_0, 0) = \delta_{max} \cdot \frac{E_0}{E_{0,max}} \cdot \frac{s}{s - 1 + (E_0/E_{0,max})^s}, \tag{4.12}$$

where δ_{max} is the maximum secondary yield that occurs at the primary electron energy $E_{0,max}$ and s is a fit parameter.

The SEY dependence for metals has its maximum value at several hundred eV energy of the primary electron, $E_{p,max}$. The SEY growth at E_p values lower than $E_{p,max}$ is characterized by the increase of primary electron penetration depth and consequently the growing number of produced secondaries while they are at the depth which is lower than the escape body depth. The SEY decay at E_p values larger than $E_{p,max}$ is due to the fact that the penetration depth by the primary electrons becomes larger than the escape depth so, that the generated secondary electrons cannot reach the surface.

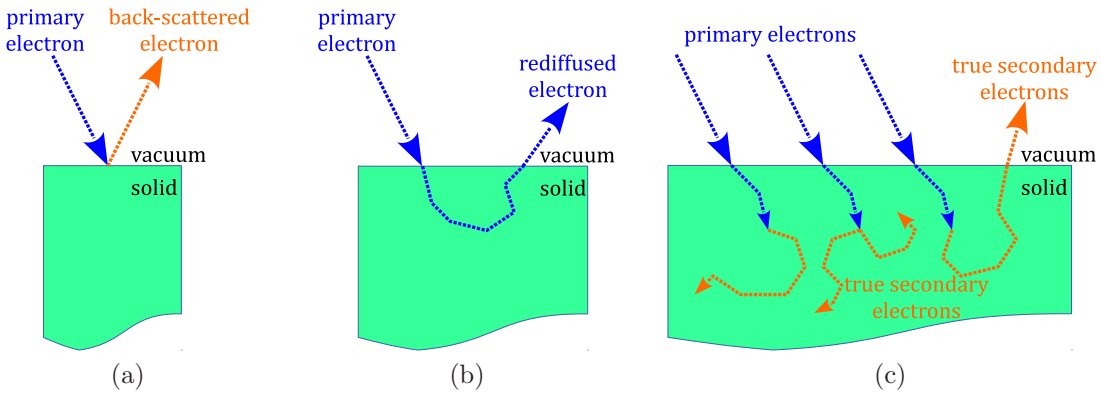

Figure 4.4: The secondary electrons generation processes of: (a) back-scattered electrons, (b) rediffused electrons and (c) true secondary electrons.

4.2.4 Multipacting

Multipacting (multipactor discharge) is the undesirable resonant discharge in RF fields which is supported by secondary electron emission (see section 4.2.3). Stable multipacting requires fixed resonance conditions which depend on the RF field configuration, the RF structure geometry and surface properties (usually characterized by the SEY).

Multipacting occurs when electrons, initially accelerated by RF fields, produce secondaries, which are also accelerated by the same alternating RF field, then impinge the surface, and produce more secondaries. If there are fixed places of the surface where secondaries impact and the trajectories are stable, the process becomes resonant, and an electron avalanche will appear.

This process is always characterized by an exponential growth of the number of free electrons in the vacuum chamber. An example of multipacting for an RF cavity is presented in Fig. 4.5.

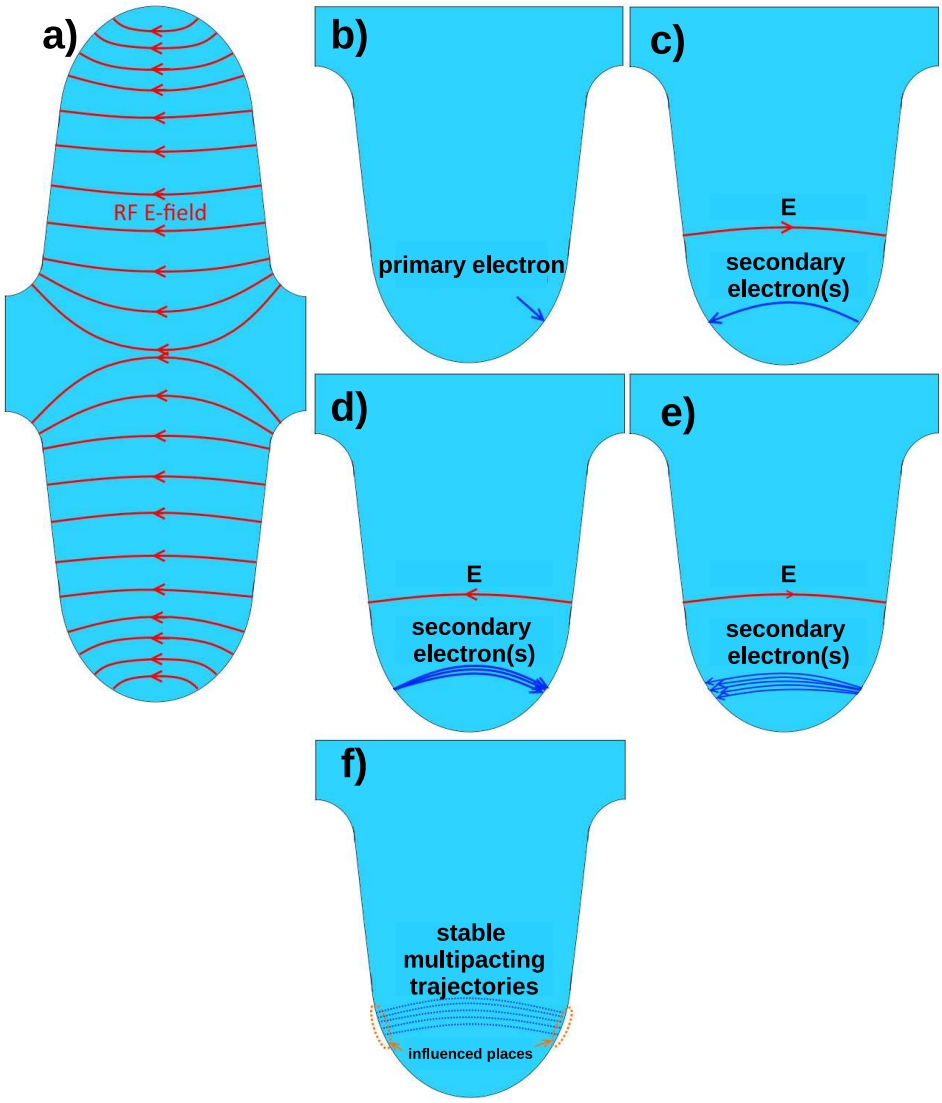

Figure 4.5: Multipacting formation in an RF cavity. Plot a) the RF cavity cross section with an electric RF field, b) - e) formation of the multipacting avalanche within 3 RF cycles, f) stable multipacting trajectories (blue dotted lines) and the cavity places influenced by the multipacting (indicated by orange areas).

The multipactor discharge is an undesirable phenomenon. It can lead to problems of RF system operation, for example vacuum breakdown, RF power loss, overheating and damage to RF components and, in the case of superconducting cavities, it may cause a quench when the material becomes normal conducting.

4.2.5 Radiation

The dark current electrons that hit the walls of a structure will produce X-rays, via bremsstrahlung process, in all directions due to the random distribution of trajectories. This radiation depends on the impinging electron energy spectrum and on the amount of copper, electron traverses before reaching the ambient devices.

The increased radiation level can be a problem for operation of a device. It can damage auxiliary system, especially semiconductor electronics, like digital cameras, and change the property of plastic parts of different kind of switches (e.g. pneumatic tubes and switches of actuators) or even of cables.

4.3 Simulations of the dark current and multipacting trajectories

Simulations of the dark current and multipacting particle trajectories provide a better understanding of these processes in a cavity. The simulations also help to reveal critical places of the cavity which are influenced by discharges, to develop tools and methods for particular conditions and in general are important for future designs.

The first single electron simulations for the PITZ gun electron trajectories were presented in Ref. [51], where beam dynamics simulations of the dark current were done by means of the ASTRA software [39]. An example of the trajectories is shown in Fig. 4.6. The simulations presented in Ref. [51] show that electrons starting at the cathode plug and the cathode vicinity area can be accelerated downstream and measured with the Faraday cup. The electrons emitted from other parts of the gun and RF coaxial coupler can not leave the gun cavity because their trajectories do not meet the correct fields conditions in order to be accelerated and transported downstream. These electrons do not make problems for accelerator parts downstream the gun, but nevertheless, they can locally heat up the cavity surface and thus may create secondary electrons. The multipactor simulations presented in Ref. [51] showed that the multipacting takes place at the front surface of the cathode.

Since the previous simulations from Ref. [51] were performed by ASTRA software, there were limitations on the modeling of the real gun structure and only the gun cavity was considered. The following dark current simulations performed by the CST studio software was intended to simulate the full geometry of the vacuum system of the gun and refine the previously obtained results.

4.3.1 Dark current simulations

The task for dark current simulations was to prove the reliability of the ASTRA simulations and to quantify the dark current process in the gun.

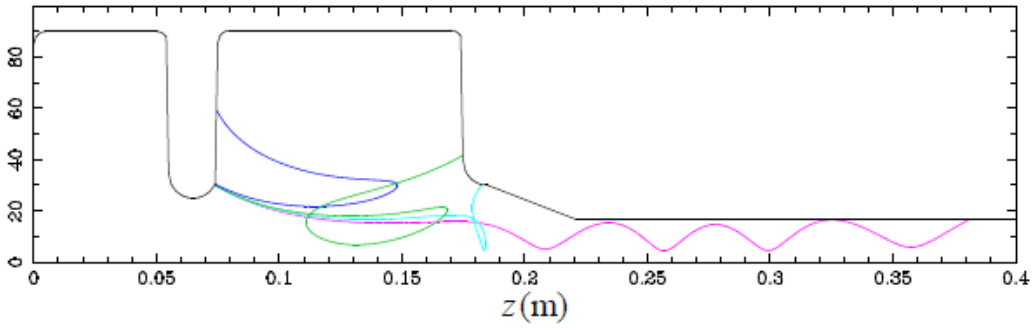

Figure 4.6: An example of dark current trajectory in the PITZ RF gun cavity from Ref. [51].

The simulations were performed in the CST Particle studio. The RF fields were taken the same as for the coupler kick tracking in section 2.1. The fields were simulated for the model that includes the gun cavity with simplified cathode area and the RF coupler at the end of which one RF port is located. The electric field is presented in Fig. 4.7.

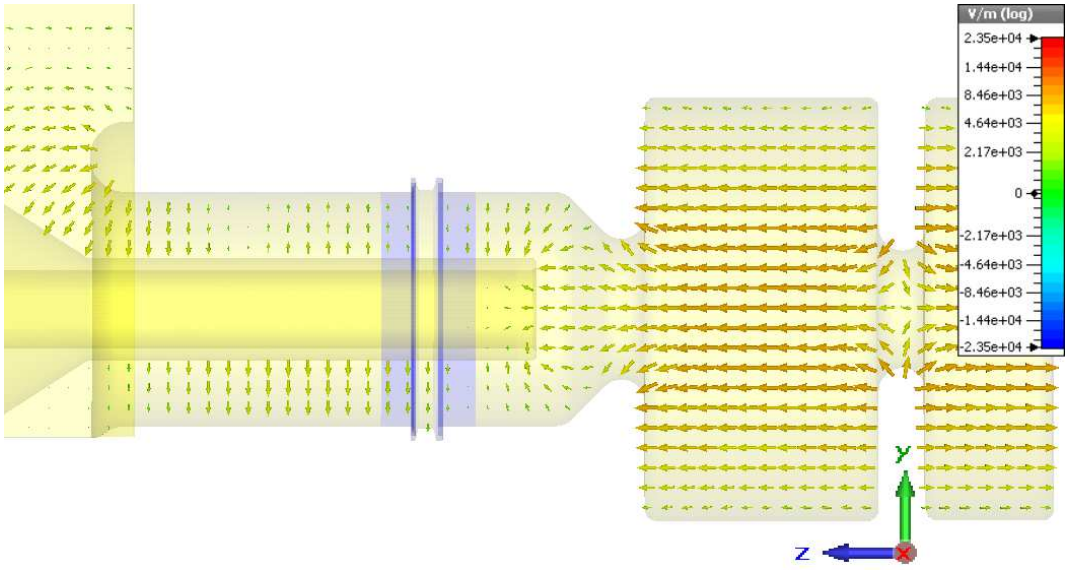

Figure 4.7: An example of the electric RF field in the PITZ RF gun cavity and coupler setup.

The tracking of the dark current was done by the Particle-In-Cell (PIC) solver of the CST studio. The PIC solver was selected due to the capability of continuous particle emission within a predefined time period. The continuous particle emission simplifies the tracking simulation process because particles are emitted not only for a fixed RF field phase but for a range of phases. The emission time for the simulations was set to

800 ps, which is longer than the RF period (769 ps for the case of 1300 MHz), in order to cover the full range of phases for the dark current emission. The space charge calculation option of the PIC solver was switched off in order to accelerate the simulation process.

The full inner model surface was divided into several parts, and each of these parts was selected as a particle source. The surface division was done in order to distinguish and characterize the dark current from the different parts of the gun and RF coupler surface.

For simplicity, the initial particle parameters were chosen identical for all sources: the initial kinetic particle energy is 0.04 eV [1], kinetic spread 50 %, angular spread 45° and total charge of 1 pC. In order to generate approximately constant current within the emission time, a Gaussian emission model with a huge sigma and short cut off length was applied. The window with source settings and schematic presentation of the temporal structure is presented in Fig. 4.8. The parts of the inner surface of the model selected as the sources are presented in Fig. 4.9.

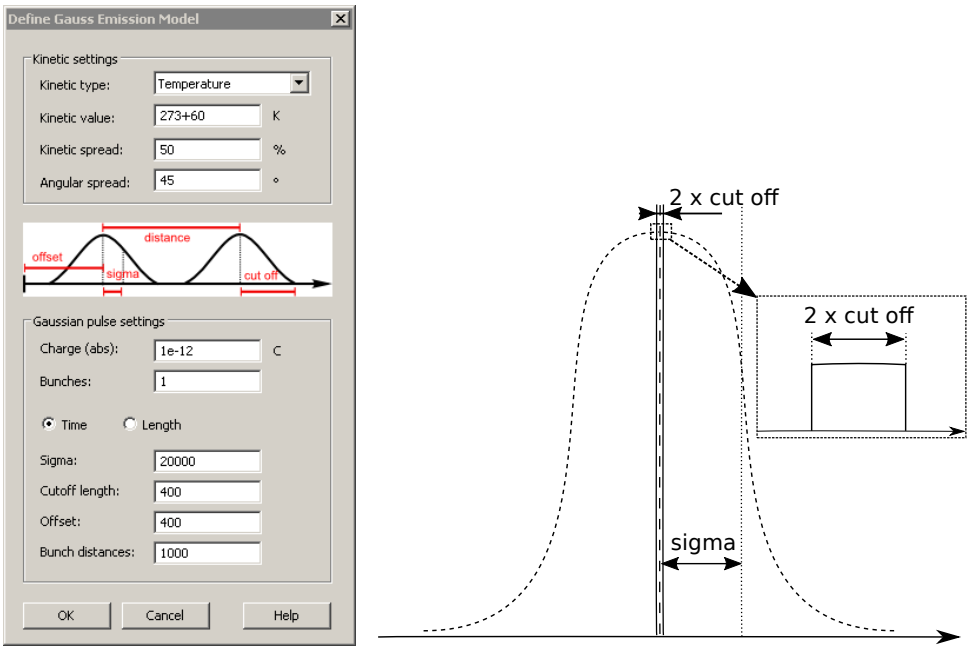

(a) (b)

Figure 4.8: The CST Particle studio window with the particle source settings (a) which were used for simulations and schematic presentation of the temporal structure (b). The time structure settings are shown at the bottom part of the plot (a).

[1] defined via temperature as $E_{kin} \approx (500 \cdot k)$eV, where k is the Boltzmann constant in $eV/°K$

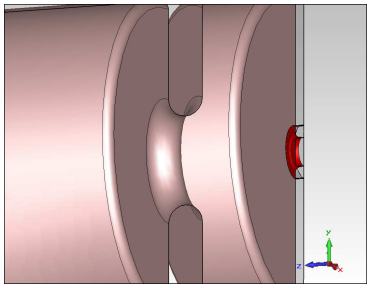

(a) Cathode plug and vicinity

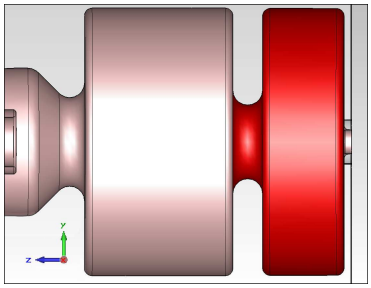

(b) Half cell and iris

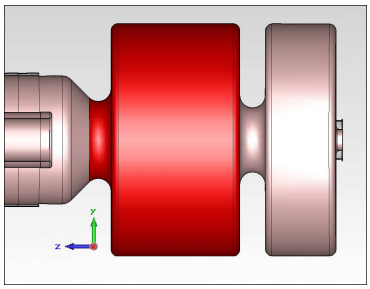

(c) Full cell and output iris

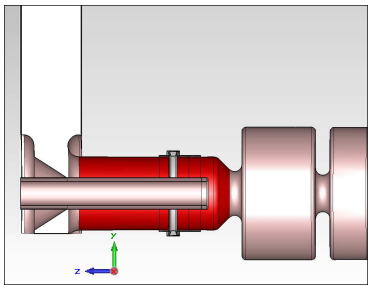

(d) Outer conductor of the coaxial waveguide

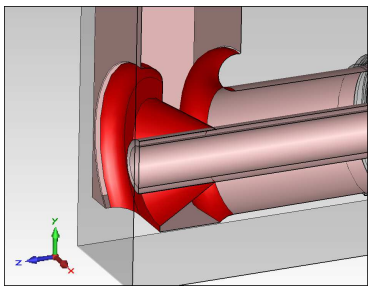

(e) RF coupler transition parts

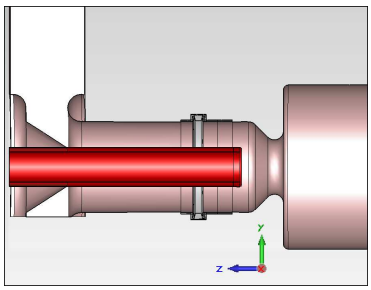

(f) Inner conductor of the coaxial waveguide

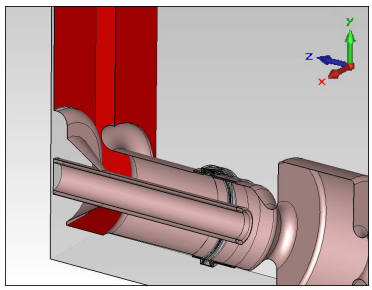

(g) Rectangular waveguide walls

Figure 4.9: The particle sources for the dark current simulations. The numbers seen in the image are irrelevant in context and can be ignored.

Amount of detected dark current

The results of the simulations proved that only particles emitted from the cathode and the cathode vicinity can be transported to the beamline. These particles can be detected by a charge measurement device like the Faraday Cup which is located at z=0.803 m downstream the cathode. The example of such trajectories is shown in Fig. 4.10.

The number of particles that escape the gun is only 0.6 % of the total emitted particles from the half cell and iris (particle source in Fig. 4.9(b)) and 30.9 % of the total emitted particles from the cathode and cathode vicinity (particle source in Fig. 4.9(a)). The particles emitted from all other regions of the gun can not escape the gun cavity or RF coupler volume at all.

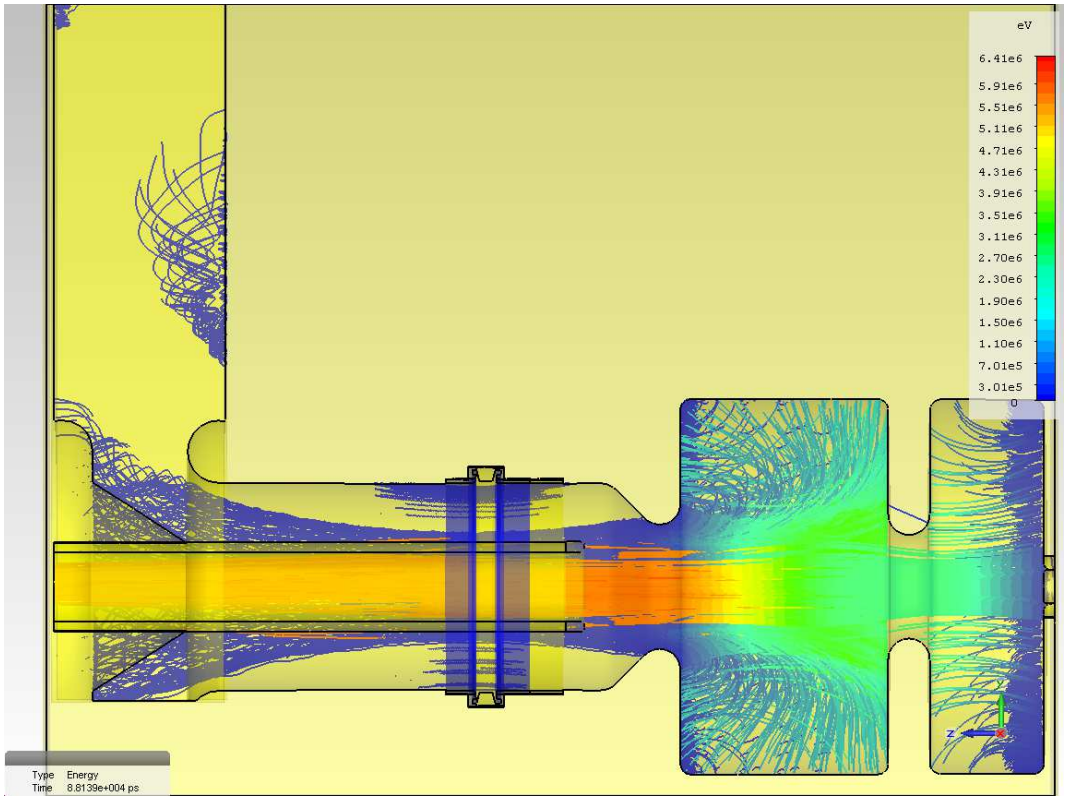

Figure 4.10: Example of the dark current particle trajectories simulated by the CST Particle studio. The color code indicates the particle energy.

In order to make an estimation of the total amount of dark current particles present in the gun cavity volume, the relation between the number of particles escaping the gun body to the total number of dark current particles in the gun cavity volume was calculated. Only 10.5 % of the totally emitted particles from the gun cavity can be transported downstream the cathode to the beamline for zero magnetostatic solenoid fields.

Energy spectra of dark current

The dark current from the gun can lead to heating of the cavity surface, X-rays generation, and production of secondary electrons (secondaries). Those additional electrons enhance the dark current so that at certain conditions stable (when the number of secondaries constantly increases) or non-stable (when stable trajectories of secondaries exist only for some limited number of RF periods) multipacting processes can occur. To calculate the probability of secondary electron production, which depends on the primaries energy, and to estimate the heat load by dark current, one should know the particle distribution in a cavity volume (including a portion of the particle that can be measured) and the particles energy spectrum at the moment when a particle hit the surface.

Energy spectra of the electrons impacting with the gun parts were obtained by simulations for different parts of the gun and RF coupler. The selected parts are the rectangular waveguide, the coaxial waveguide, the coaxial antenna nose, the gun cavity, and the molybdenum cathode plug. The sum spectrum of all particles hitting the surface is presented in Fig. 4.11. The example shows the combined spectrum for the coaxial waveguide and the gun cavity. The incident electrons energies have values up to 6.4 MeV. The spectrum consists of two energy regions 0 – 3.4 MeV and 5.7 – 6.4 MeV with the most amount of the electrons. The trajectories of the electrons with the highest energies lie in the region near the gun cavity center, where the RF fields provide high energy to the electrons due to the synchronized motion in the alternating fields.

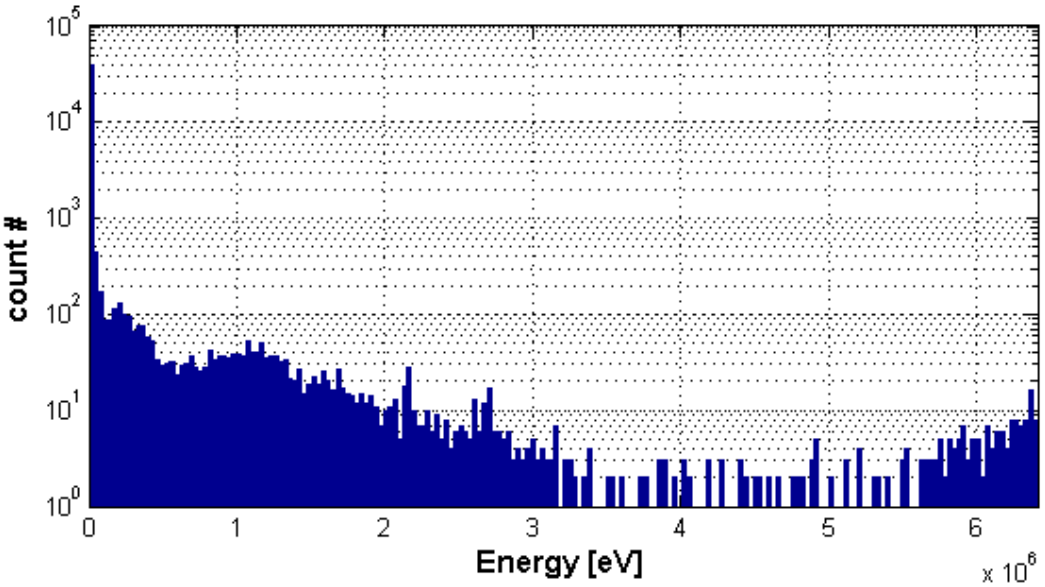

Figure 4.11: Combined energy spectrum of the free electrons hitting the coaxial waveguide and the gun cavity.

The energy spectra simulations can be described by the following results:

- Molybdenum cathode plug
  - total energy range is from 0 eV to 2.73 MeV
  - most of particles (72 %) have energies in the range from 0 eV to 56 keV
  - 9 % of the particles have energies in the range between 2.3 MeV and 2.7 MeV
- Rectangular waveguide
  - the spectrum consists of exponential decrease toward the lower energies and a flat distribution at a wide range in the high energy part
  - the decreasing part of the spectrum can be roughly described by the following dependency: count $\sim 92.68 \cdot \exp(0.0226\,[1/\mathrm{eV}] \cdot \mathrm{E}\,[\mathrm{eV}])$, where the maximum counts value occur at 0.8 eV
  - the total energy range is 0 eV to 40 keV
  - the main part of all particles (99 %) have energy from 0 eV to 10 keV
- Coaxial waveguide (all parts)
  - the total energy range is 0 eV to 6.36 MeV. The highest energies of the spectrum are possible due to the collision of particles with the surface of the inner coaxial conductor. These particles, started from the back wall of the half cell or the cathode surface, accelerate in the RF fields with synchronous phase and travel to the inner conductor of the RF coupler.
  - 88 % of particles are in the range 0.3 eV to 57 keV
  - and 88 % of particles are in the range 3.18 MeV to 4.678 MeV
- The coaxial antenna (inner conductor) nose (this part is exposed by the dark current particles with the highest energies in the gun)
  - the total energy range is 0.3182 eV to 6.36 MeV
  - the particle distribution with highest energies 0.137 MeV to 4.678 MeV consist of 19 % of particles
- The gun cavity. The cavity consists of two cells, two irises and back wall of the half cell, where the cathode plug is inserted.
  - 98.33 % of all particles are in the range 0.311 eV to 2.733 MeV
  - the range from 0.311 eV to 0.3265 keV has the highest concentrations of the particles of the low energy region which non-exponentially decrease toward the higher energy part. The rang consists of 36.54 % of all particles.

These results show that the gun back wall, the cathode plug, and the coaxial antenna nose undergo interaction with high energy electrons (up to 6.4 MeV). Therefore these places most prone to damage in case of high dark current. This demands high accuracy in design, fabrication, installation, and manipulation with these parts.

4.3.2 Multipactor discharge simulations

The multipactor discharge simulations were preformed with the CST Particle studio. The simulations were split into a few parts: simulations of the gun body with the RF coupler and simulations of two models of the cathode vicinity with different cathode spring designs. The simulations of the gun cavity and the watch band cathode spring design were performed in collaboration with a summer student [64] using the Trk solver whereas the contact stripe cathode spring design simulations were performed by means of the PIC solver. As it was mentioned before, the difference between the solvers, in this case, is the possibility to make continuously emitting sources. In case of the Trk solver, the emission particle time was adjusted to the whole RF phase range each time. The space charge calculation during simulations does not play a significant role in this case because the current and its density are relatively small.

The process of multipacting simulations, as well as all previously described particle tracking simulations, consists of two steps: the RF and static fields simulation and the particles tracking simulations. The multipacting simulations employed three parts of the CST studio: the CST Microwave studio for the RF field simulations by the frequency domain solver, the CST EM studio for the external magnetostatic fields (the solenoids fields) simulations by the magnetostatic solver, and the CST Particle studio for particle tracking in combined RF and constant fields.

The simulation for the cathode vicinity used the Furman model [61] of the secondary emission for copper and molybdenum with the default CST Particle studio parameters for particle tracking simulations. The used SEY curves are presented in Fig. 4.3. The maximum number of generations which the primary electron sources can produce was set to 25 and the maximum secondaries per hit is set to 10. These parameters are chosen to achieve accurate simulations within a realistic time period.

As the initial electron source position there were selected the cathode surface and the surface of the gun around the cathode in order to consider all possible options of initial electron emitters. There was used a model simplification which applies 1/4 of the cathode area as the electrons source in order to save memory and reduce computational time. This simplification was valid due to the axial symmetry of fields and geometry. A common strategy of the multipacting indication and verification is the evaluation of the particle number in the cavity volume over time. The growth of electrons number means presence of multipacting in the simulated geometry with the defined field configuration. This dependence evaluation was done for a few combinations of the electric field levels and two intensities of the solenoid fields.

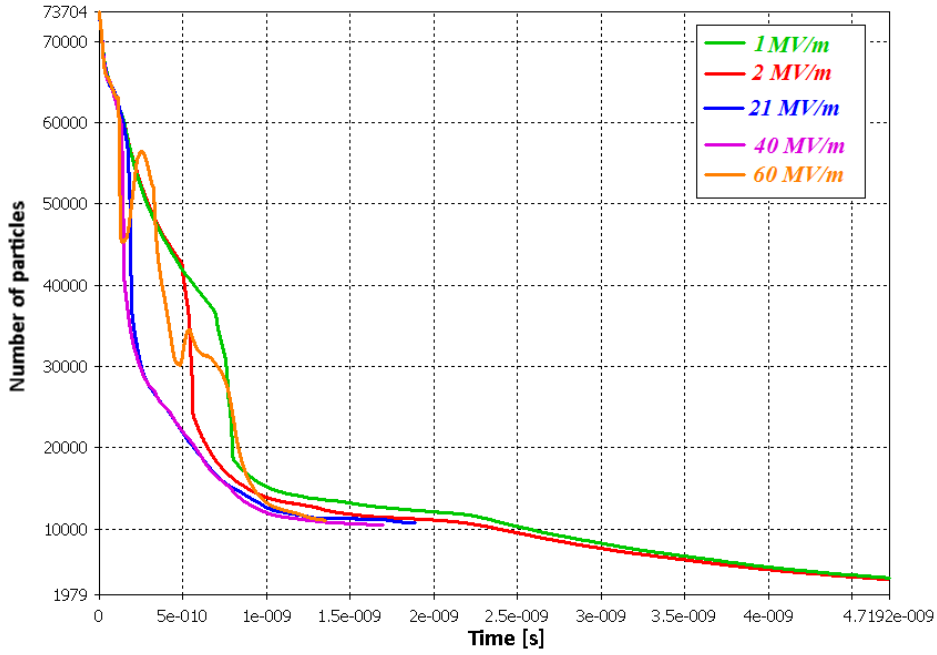

(a)

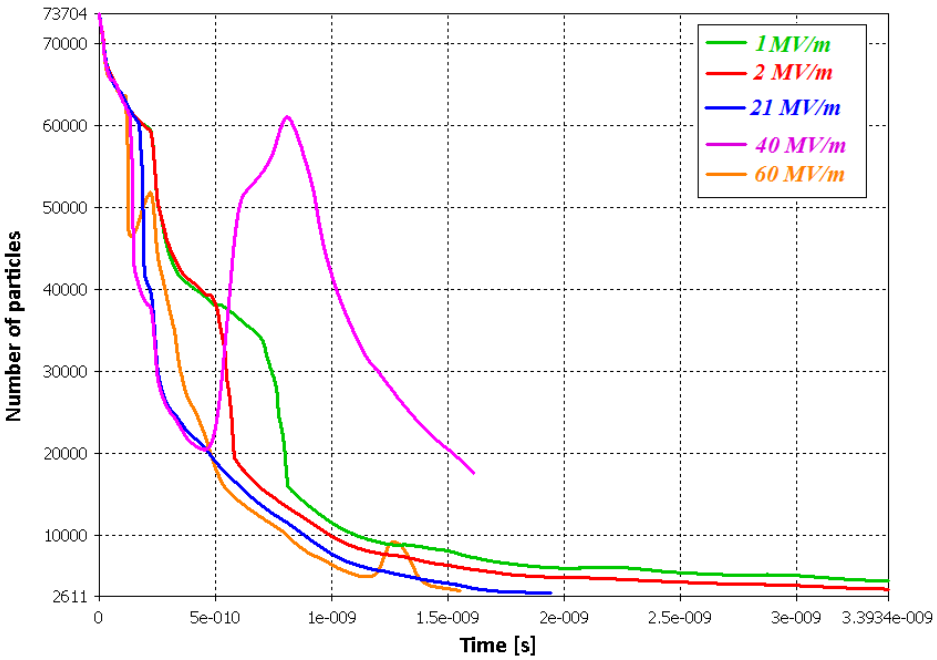

(b)

Figure 4.12: Multipacting simulations for the cathode vicinity with watchband RF contact spring design . The number of particles in the gun is presented as a function of time for the solenoid currents of 370 A (part a) and 200 A (part b), respectively.

The multipacting simulations of the cathode vicinity with the watchband contact design indicated the gradual decrease of the number of electrons over time at all investigated gradients and for both external magnetic field configurations (Fig. 4.12). The simulations also showed some growth in the number of particles at some RF field levels for a short time period, and this behavior implicate that resonant conditions for secondary emission can appear, but it does not lead to multipacting because there is no synchronization between the field and particle motion.

The investigation of particle trajectories showed that the major part of the secondary electrons is concentrated in the gap between the cathode and the cathode vicinity at the place close to the cavity area. Some of these secondaries can be captured by the accelerating fields and transported downstream the cathode, where they are considered as dark current electrons. An example of this behavior is presented in Fig. 4.13. The example shows the simulations for the 60 MV/m accelerating gradient at the cathode and the external magnetic field corresponding to the main solenoid current of 370 A. The dependence of the particle count vs. time (see Fig. 4.13a) shows that no conditions for multipacting are visible.

Multipacting simulations for the gun cavity and the gun coupler were performed in a way similar to the simulations of the cathode vicinity with watchband spring design but with the difference that the surfaces of the gun cavity and RF coupler were used as the source of the initial particles.

The simulations revealed that multipacting trajectories can appear at an accelerating gradient on the cathode surface of 60 MV/m (~ 6.5 MW power in the gun). The stable multipacting trajectories are located inside the coaxial waveguide (between walls of outer conductor) and at the outer cylinder of the gun full cell. Examples of the trajectories and number of particles versus time are shown in Figs. 4.14 and 4.15 for the coaxial waveguide and gun full cell, respectively.

The simulations also revealed places where stable (but not multipacting) trajectories are observed for an accelerating gradient at the cathode of 60 MV/m (~ 6.5 MW power in the gun). The locations of the stable trajectories are the cone and the its surrounding parts of the gun coupler (see Fig. 4.16), the inner conductor of the coaxial waveguide (see Fig. 4.17) and the gun cavity (outer cylinders of the cells) (see Fig. 4.18). A typical plot of the number of particles versus time for this kind of trajectories is presented in Fig. 4.19.

Multipacting trajectories were found at an accelerating gradient at the cathode of 1 MV/m (~ 2 kW power in the gun) that corresponds to the residual high voltage level of the RF modulator present in the gun when the RF pulse is not yet present or is already stopped. In other words, a power level of ~ 2 kW, which corresponds to an accelerating gradient at the cathode of 1 MV/m, can be associated with the baseline of the RF signal. The schematic presentation of this power level is shown in Fig. 4.20. The trajectory locations are the back wall of the first cell (see Fig. 4.21), the space between the inner conductor of the coaxial coupler and the back wall of the rectangular

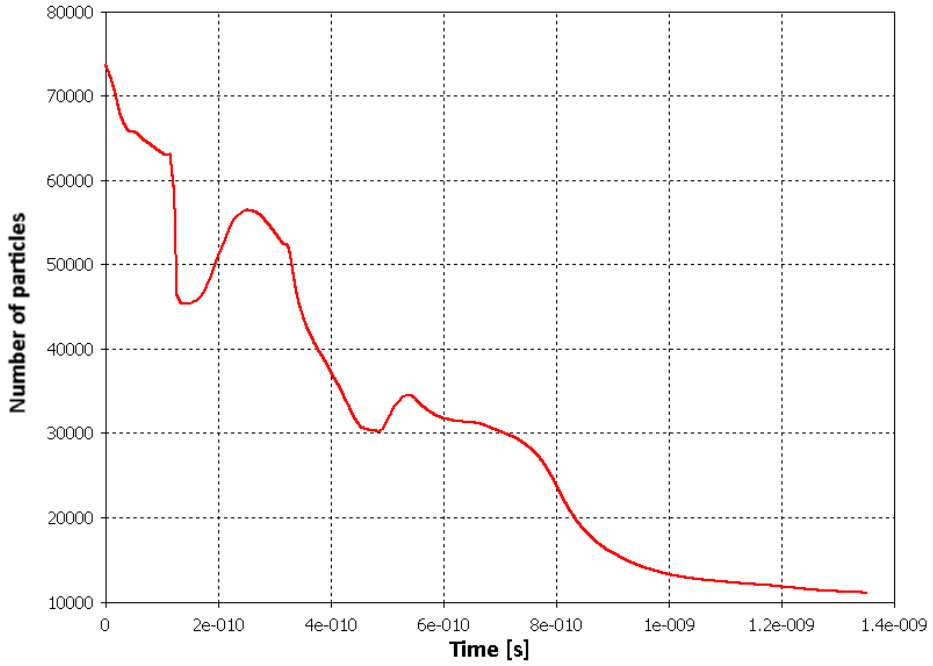

(a)

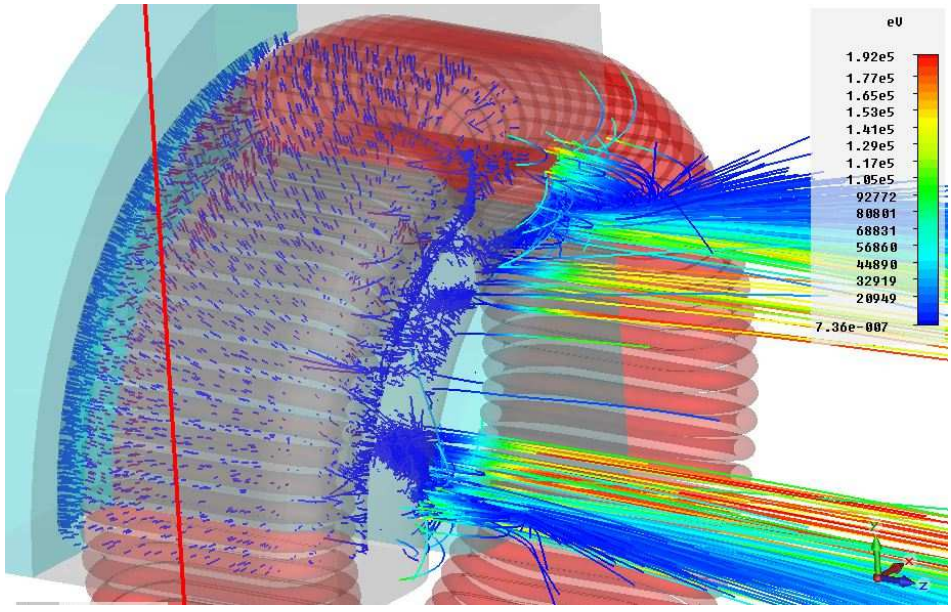

(b)

Figure 4.13: Multipacting simulations of the cathode vicinity with watchband RF contact spring design. The number of particles in the gun as a function of time for 60 MV/m at the cathode (part a) and secondary electron trajectories in the cathode area (part b).

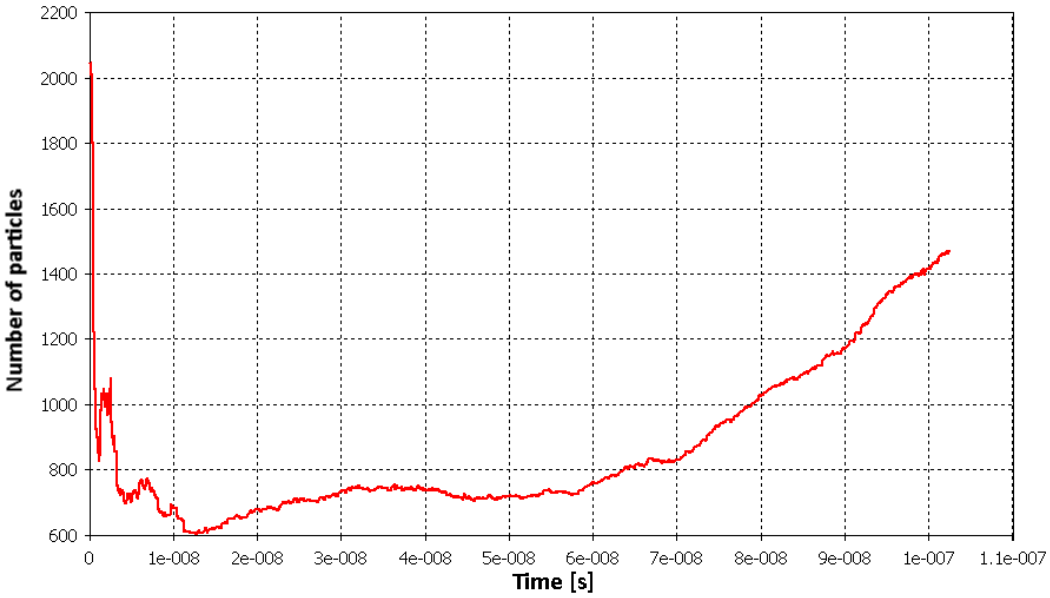

(a)

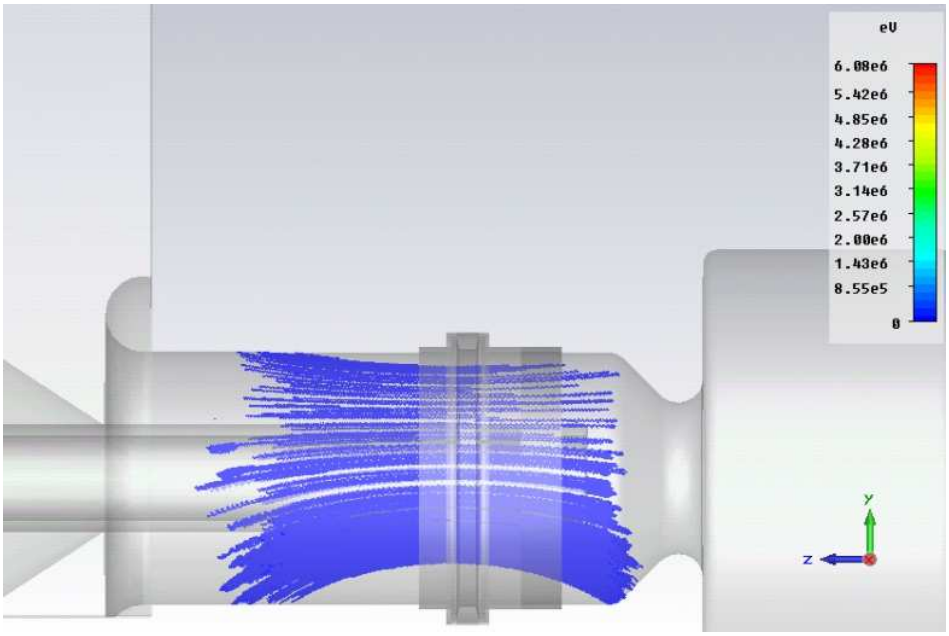

(b)

Figure 4.14: Number of particles in the gun as a function of time for 60 MV/m and 370 A current of the main solenoid (part a) and secondary electron trajectories in the coaxial coupler (part b).

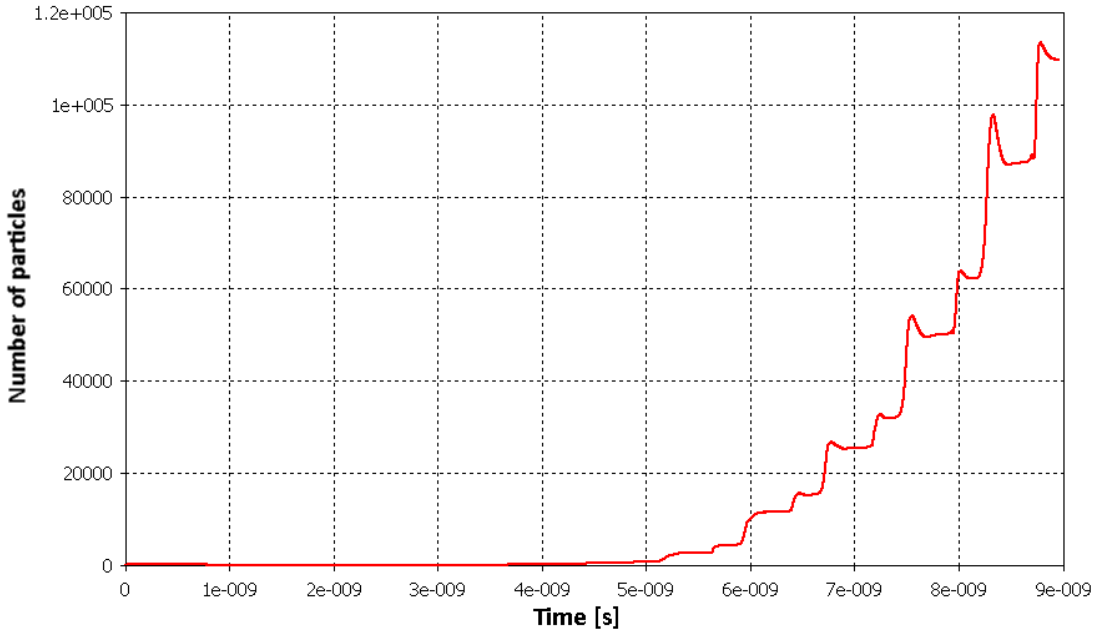

(a)

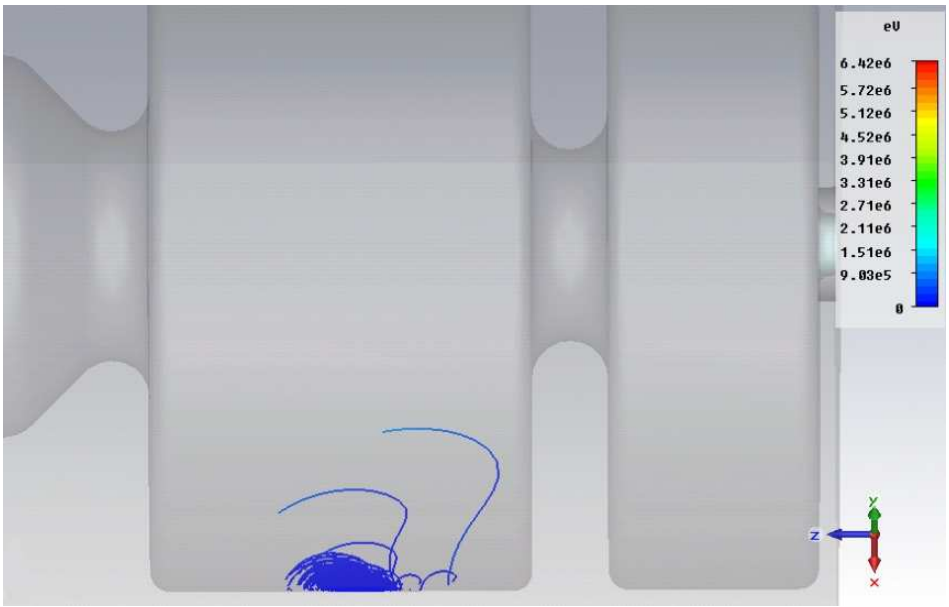

(b)

Figure 4.15: Number of particles in the gun as a function of time for 60 MV/m and 370 A current of the main solenoid (part a) and secondary electron trajectories in the gun cavity (part b).

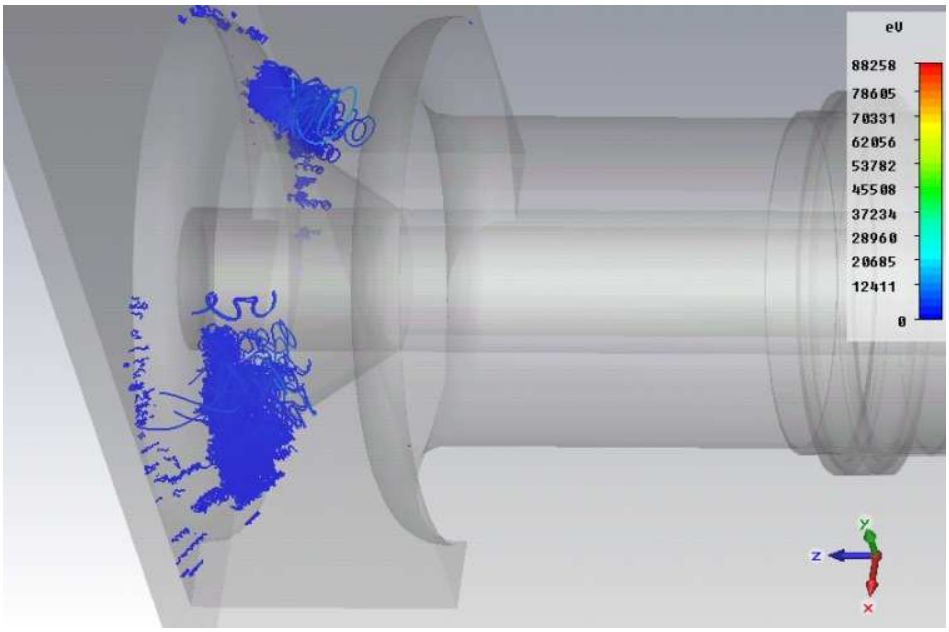

Figure 4.16: Stable multipacting trajectories at the cone part and cone surrounding part of the gun coupler.

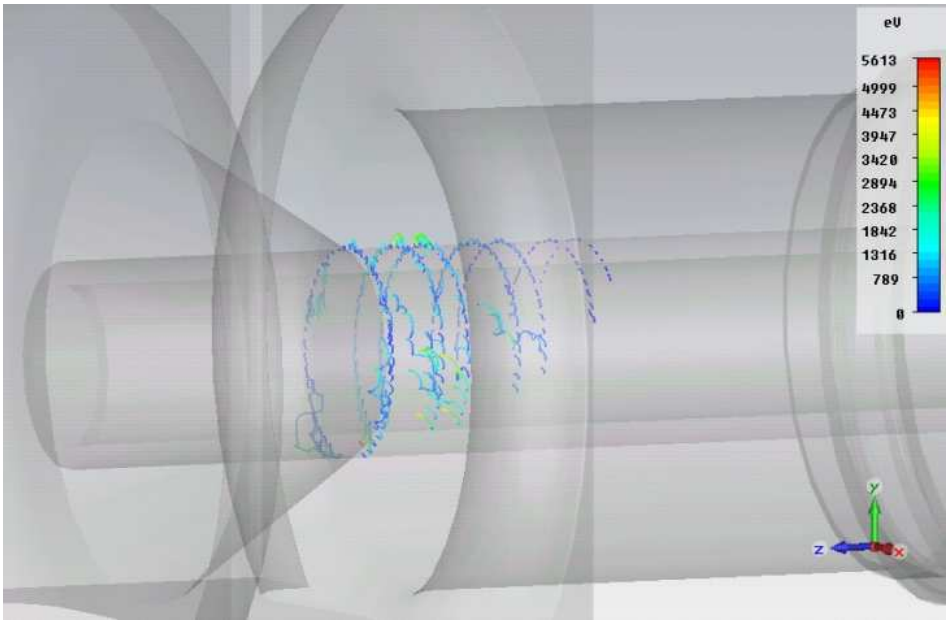

Figure 4.17: Stable multipacting trajectories at the outer side of the inner conductor of the coaxial waveguide.

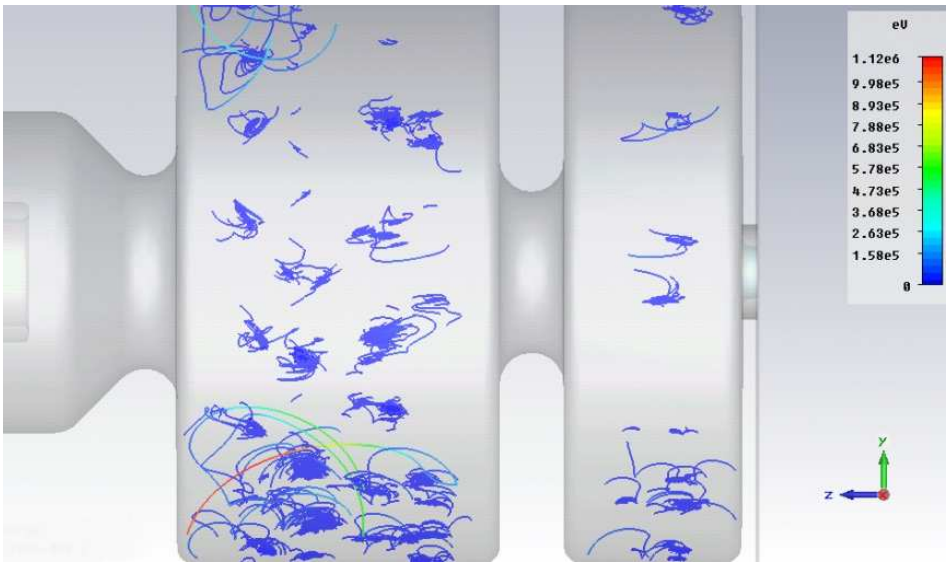

Figure 4.18: Stable multipacting trajectories in the gun cavity.

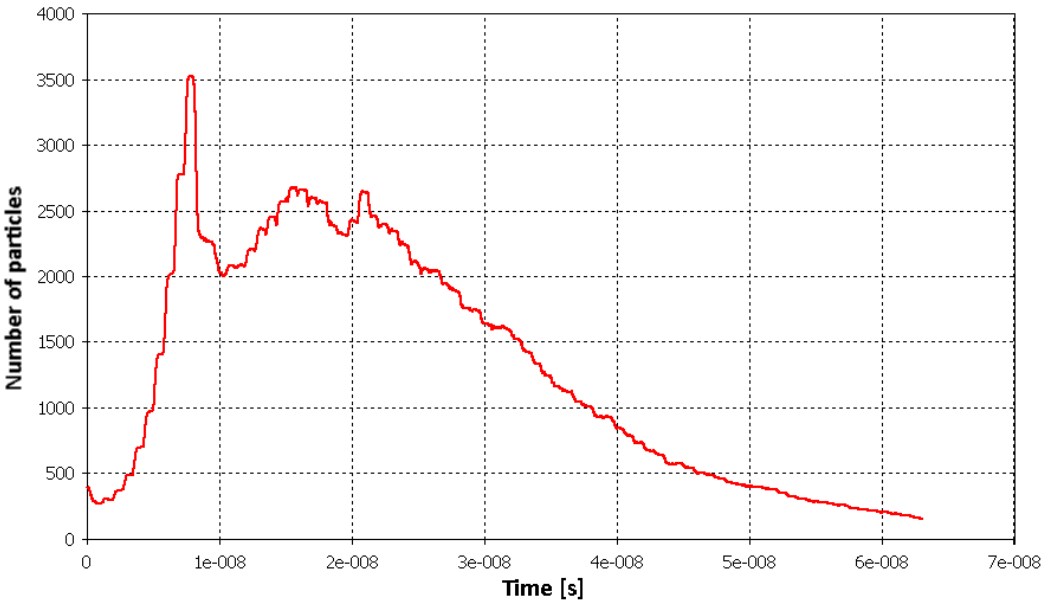

Figure 4.19: Number of particles in the gun as a function of time.

waveguide (vacuum pump port location)(see Fig. 4.22) and the surface of the second gun iris (to coaxial coupler) (see Fig. 4.23).

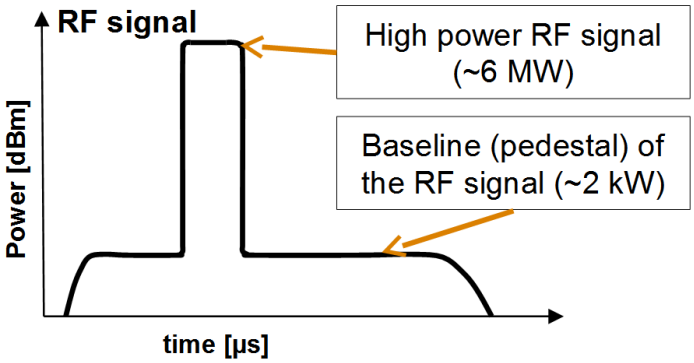

Figure 4.20: The schematic presentation of RF power level.

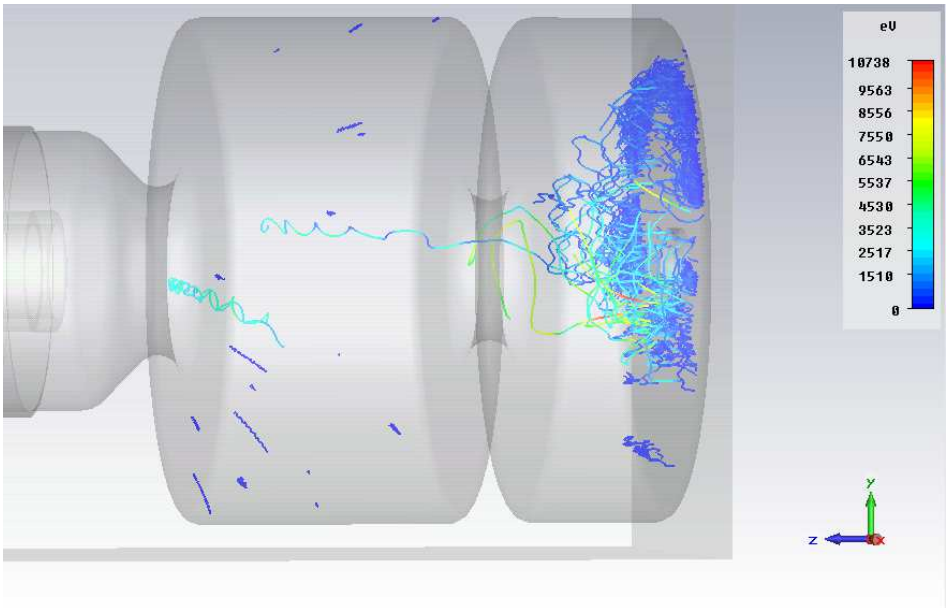

Figure 4.21: Multipacting trajectories at the back wall of the gun half cell.

Multipacting simulations for the cathode vicinity with the contact stripe design, which was applied at the gun prototypes 4.2, 4.3 and 4.4, were performed by means of the PIC solver, keeping settings (like particle source parameters) from the simulations of the cathode vicinity with the watch band spring design.

The simulations of the cathode vicinity with contact stripes design did not reveal any gun field conditions when multipacting appears inside the cathode vicinity. The results

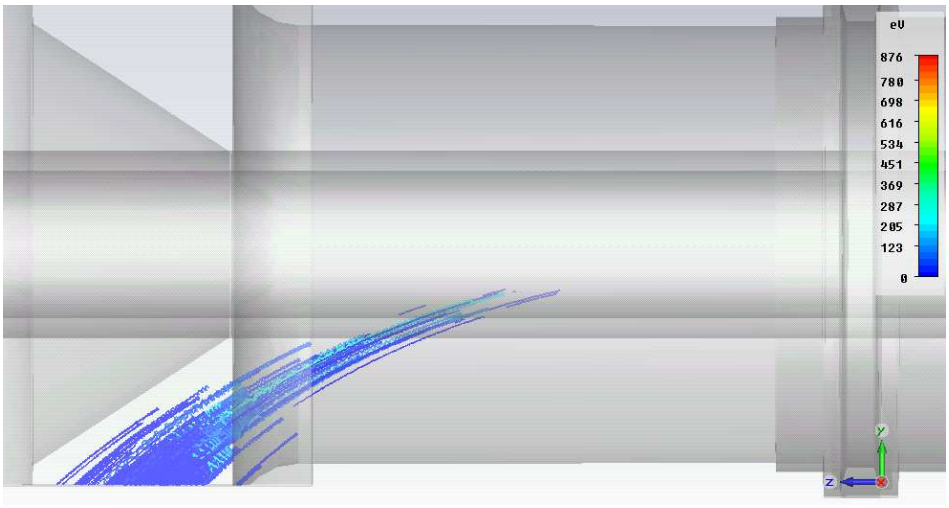

Figure 4.22: Multipacting trajectories in the RF coupler.

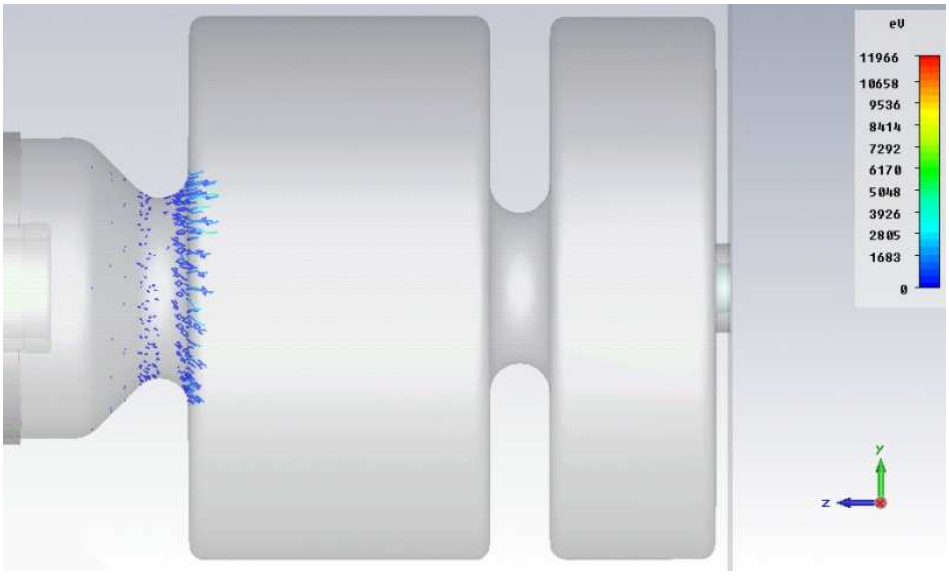

Figure 4.23: Multipacting trajectories at the iris between the coaxial coupler and the full cell.

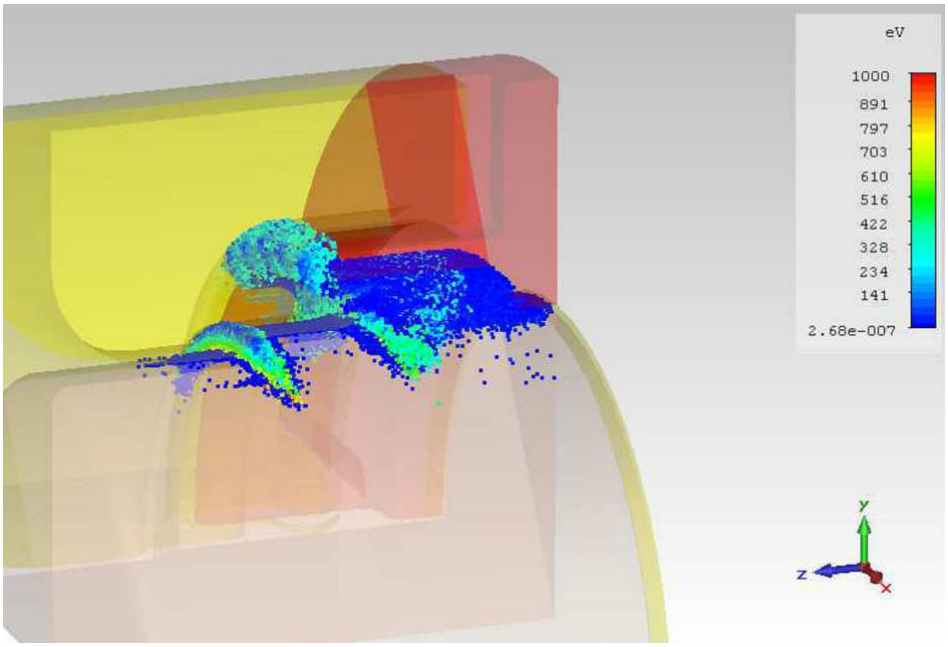

Figure 4.24: Particle distributions in the free space volume between cathode plug and cathode vicinity.

are similar to the simulations of the cathode vicinity with watch band spring design. An example of the particle distribution in free space volume between the cathode plug and the cathode vicinity is presented in Fig. 4.24.

The studies of the dark current and multipactor discharge by the simulations in the CST Particle studio showed that the high dark current can be especially dangerous for the coaxial antenna nose, the gun back wall, and the cathode plug. These areas undergo interactions with electrons of energies up to 6.4 MeV. Simultaneously, the multipactor discharge was not found in the cathode region, but it was observed at the gun cavity walls and the coaxial coupler. The found multipacting trajectories can also contribute to the dark current.

The results show that the dark current must be minimized in order to prevent the sensitive cathode surface and the cathode vicinity with the RF contact spring from damage.

4.4 Interlock system

The interlock (IL) system should prevent serious damage of the cavity and auxiliary systems from spark and related processes and at the same time allow a maximum of uninterrupted operational time at specified average and peak power. The implementation of the IL system has to include self-diagnostics and repair strategies on a module basis. Additional tasks for the IL system are the collection and temporary storage of status information of individual parameters and later transfer of this information to a higher level control system.

The PITZ facility has an IL system similar to the European XFEL. The RF system of PITZ consist of 3 RF stations supplying RF power at 1.3 GHz for the gun and the CDS booster cavities and at 3 GHz for the TDS cavity. Gun and booster RF stations generate RF pulses of up to 10 MW at a pulse duration up to 1.5 ms and a repetition rate up to 10 Hz. An RF station consists of a klystron, a pulse transformer, a pulsed high voltage power supply, a low-level RF system, auxiliary power supplies and an IL system.

The requirements for an IL system are specified in the following qualities:

- The IL system should be able to manage 3 types of errors: 1) hardware failures (errors like broken cables, damaged contacts, dead sensors) 2) soft errors (errors like sparks in the klystron, the wave guide system or cavity, temperature above a threshold, water flow, bad vacuum level) and 3) error conditions caused by transient noise from an RF station itself for example caused by the pulsed power operation.

- Errors should be treated with two types of thresholds: a) absolute maximum and minimum thresholds (any violation of these thresholds will force the interruption of one or more subsystems or of all components of the RF station) and b) software programmable thresholds (a violation of these conditions will generate an alarm message to the Control System. These thresholds are only for analog input channels).

- Input signals (except critical inputs) should have a masking function implemented that allows the exclusion of the channel from interlock functions.

- The system should be configurable.

- The system should be modular structured.

- Interlock functionality should be independent of low-level software.

- The system should support different signal types: digital (e.g. personal interlock system set, cooling water flow above a hardware threshold), optical fiber signals,

analog inputs and outputs (cooling water temperature, klystron filament voltage and current, vacuum pressure readings).

- The system self-test and reliability check on power-up.

The PITZ IL system consists of two types of IL detectors: fast IL detectors (Photo Multiplier Tubes (PMTs), electron detectors, photodiodes, spark detectors, maximum reflected power, etc.) and slow IL detectors (current of Ion Getter Pumps (IGPs), current of Pressure Gauges (PGs), Infrared (IR) sensors, temperature detectors, flow detectors, etc.). The signals communication for these types of detectors is organized by fast signal transfer protocols using optical cables for fast IL detectors and by normal speed signal transfer protocols for slow IL detectors. The IL system collects signals from all IL devices and produces a common IL signal which stops the RF power by quickly stopping the Low-Level RF (LLRF) driver.

The PITZ gun IL system works with the following types of detectors:

- PMTs: at the vacuum window and the coupler
- electron detectors: at the vacuum window and the coupler
- three different vacuum pressure readings in the gun section:
  - IGP with TSP, ion getter pump installed after Titanium Sublimation Pump (TSP). It provides high pumping speed after activation of the TSP, pressure reading usually is one order of magnitude better than without the TSP
  - IGP direct installation (depends on the gun setup), ion getter pump installed directly after a vacuum chamber. It provides quite sensitive pressure estimation in the gun section
  - PG, Pressure Gauge is a small sensor installed close to the Residual Gas Analyzer (RGA). The pressure reading is influenced by RGA on or off state
- Spark detectors: spread along the RF waveguide distribution system
- IR sensor, Infrared sensors: were installed on the gas side of the DESY-type RF windows
- Temperature sensors: spread along the RF waveguide distribution system, gun body, vacuum windows, cooling water pipes
- Water flow meters: are located in various parts of the cooling water system

The location of the gun IL detectors which was used in 2014 and 2015 years with the gun prototype 4.2 is presented in Fig. 4.25.

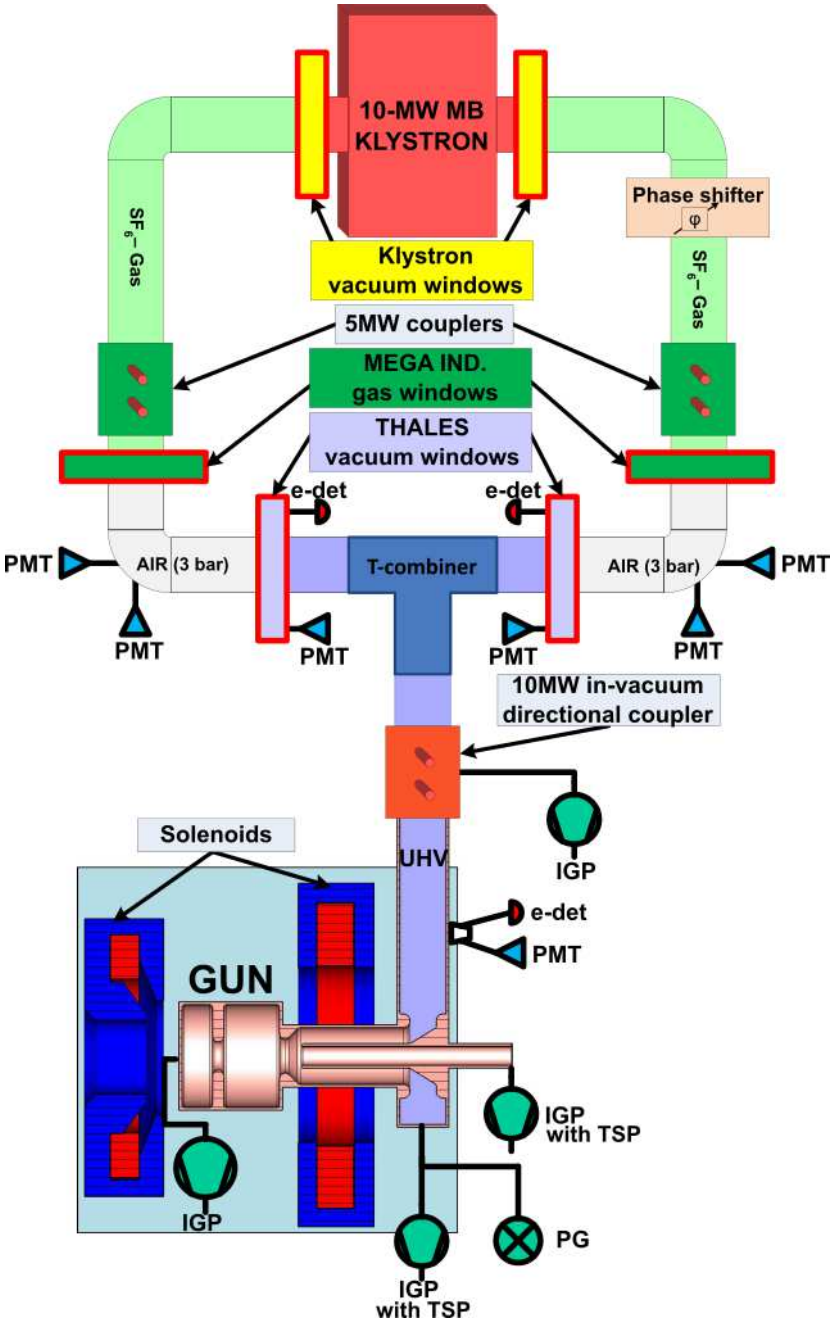

Figure 4.25: Schematic presentation of the PITZ gun interlock (IL) detectors for the gun setup with two THALES RF windows [65]. The setup consists of multiple IL detectors: photomultipliers (PMTs), electron detectors (e-dets), pressure gauges (PGs) and directional couplers. The detectors are installed in the two 5-MW and the 10-MW waveguides in order to have the complete control on the gun operation.

The schematic presentation of the signal propagation for the PITZ gun IL system (3rd generation) is presented in Fig. 4.26 and Fig. 4.27 for fast and medium/slow signals, respectively. As shown in Figs. 4.26 and 4.27, the total delay, which is defined as sum of all known delays, between a detector trigger and LLRF driver stop is at least $\sim 1.1\,\mu$s and $\sim 4.8\,\mu$s for fast and slow signals, respectively. These delays are much shorter than the RF pulse length, therefore the RF power can be stopped within the pulse duration.

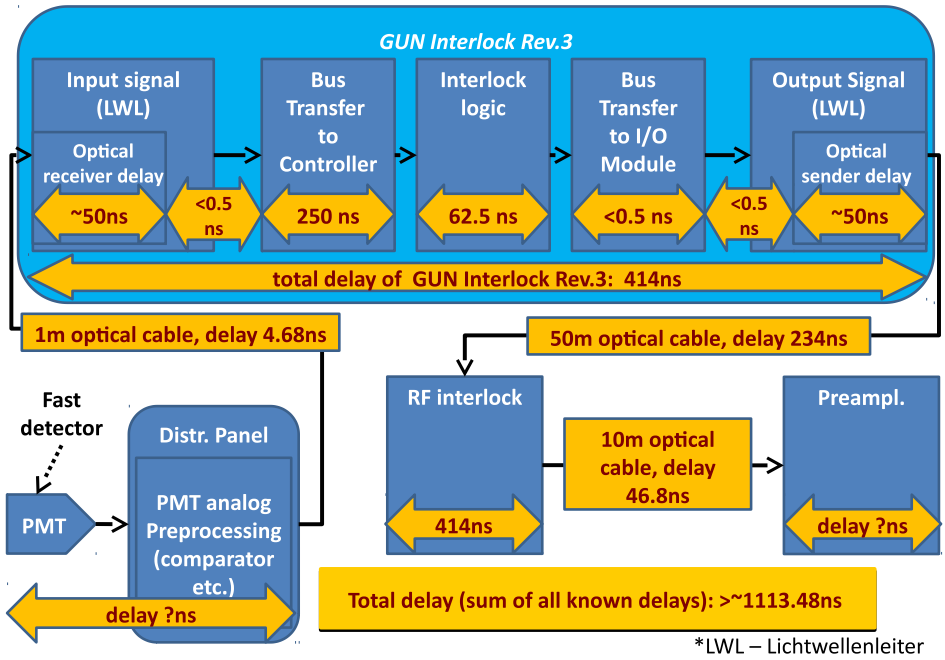

Figure 4.26: Schematic presentation of the fast signal propagation for the PITZ gun IL system (3rd generation).

Since the gun operation at early stages, especially during the conditioning, implies a lot of IL events, the author developed a tool which helps a facility operator to make quickly an IL analysis. The tool was named Last InterLock Investigator (LILI).

It interferes with the PITZ Data AcQuisition system (DAQ) and provides a user-friendly interface with synchronized spectra information about IL detectors and RF directional couplers, located in the gun section, for a requested time period. The time period is usually selected as the period when an IL event occurred, but any other time range, in which an operator is interested, can be defined. LILI provides plots with the combined spectra in such a way that is easy to read and to compare their behavior. The LILI interface is able to show each event (which comes every 0.1 sec during the normal gun operation) as well as a combination of several events. The combined events option helps to see a sequence of pulses (presented by different colors) and in case of an IL event, to understand its origin if there were a few IL detectors triggered.

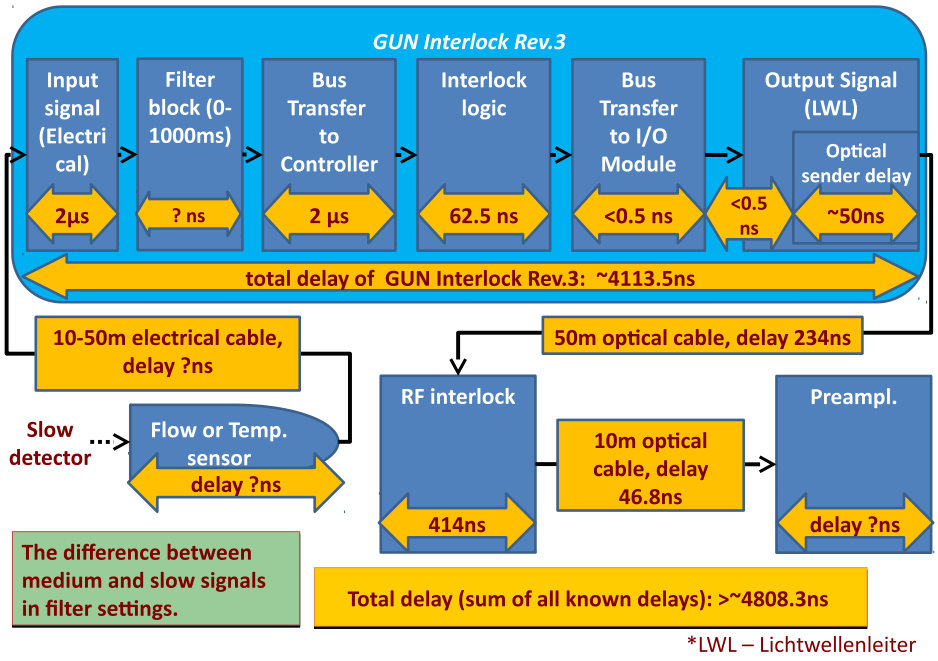

Figure 4.27: Schematic presentation of the slow signal propagation for the PITZ gun IL system (3rd generation).

A few examples of the LILI plots for the most demonstrative gun IL events are presented in Figs. 4.28 – 4.30.

The examples of the IL events are shown for the Gun 4.2 used at PITZ from July 2014 to November 2015. The used gun setup layout is presented in Fig. 4.25. The LILI plots for the IL events slightly differ from the original LILI plots provided to a PITZ operator. The plots modifications are done for the better view: two plots (usually the operator sees two plots) are combined into one, the interface control elements are removed, and the spectra of the electron detectors, located at the RF vacuum windows, are removed, because during the presented IL events the electron detectors signals show only noise without any valuable information.

The IL event shown in Fig. 4.28 is a vacuum IL. It was triggered by IGP located at the 10 MW directional coupler at 5.1 MW peak power in the gun and 600 μs RF pulse length on 22 May 2015. This IL event was considered as a trip, after which the gun restarted with a short RF pulse according to the applied conditioning procedure (see section 4.5). The LILI plots show that the IL event developed within three RF pulses (~0.3 sec). The first signature (the 2nd event in the legend, the light-green line) of the vacuum activity was detected by the directional couplers (increased signals of the reflected spectra), by the PMTs (small light-green spike), and electron detector at the RF coupler (increased signal). The next event (the 3rd event in the legend, the red line) had already higher intensity and was reflected by the spectra the same way as the

first event: spikes at PMTs spectra (still below threshold), activity at electron detector and increased reflection. After the last detected event (the 4th event in the legend, the yellow line), which showed small activity detected only by PMT and electron detector at the RF coupler, the forward RF power was switched off (the 5th event in the legend, the white line) by the IL system. Usually, it takes two or more RF pulses to get a vacuum trip. During the event the maximum reflection IL was not triggered because the signal growth was outside of the IL strobe, which was set to the range from 420 μs to 460 μs according to the RF signal time axis.

The IL event shown in Fig. 4.29 is a light IL. It was triggered by a PMT located at the RF coupler at 5.7 MW peak power in the gun and 600 μs RF pulse length on 19 May 2015. The light was detected by all PMTs and electron detector at the RF coupler (the 2nd event in the legend, the light-green line), but triggered only by PMT at the RF coupler because this signal intensity exceeds the threshold level. The development of the IL was not detected and the fast reaction of the IL system stopped the RF power within the pulse. The spikes at the reflected spectra show the only consequence of the quick power cut by the IL system.

The IL event shown in Fig. 4.30 is a maximum reflection IL. It was triggered by three directional couplers at 5.1 MW peak power in the gun and 600 μs RF pulse length on 22 May 2015. Additionally to the directional couplers, the event was detected by the IGPs pressure increases, by all PMTs located in the vacuum part and only by PMTs in the air part of the 2nd waveguide. It indicates that the event happened in the vacuum part, close to the RF vacuum window located in the 2nd waveguide.

The presented configuration of the IL system which is applied at PITZ satisfies all requirements of photoinjectors at the European XFEL (see the beginning of this section). The current IL system is able to prevent gun damages even at the conditioning phase (see section 4.5) which must be done very carefully.

The developed IL analysis tool LILI enables a detailed investigation of all possible interlocks. Based on this analysis, corrections to the RF conditioning process have been introduced resulting in more efficient preparation of the gun cavity for its consequent operation.

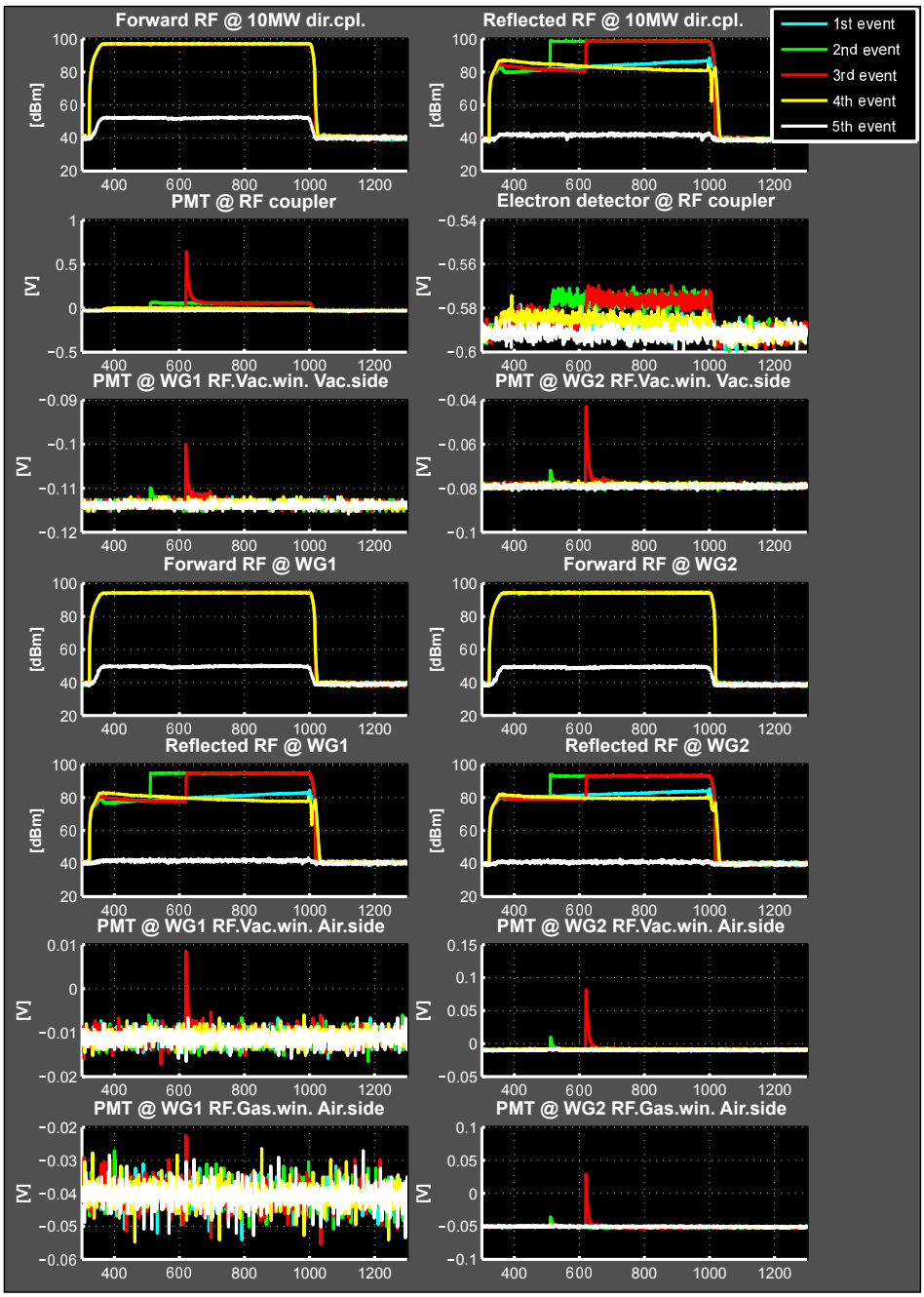

Figure 4.28: LILI plot of the vacuum IL event at the Gun 4.2 on 22 May 2015. The IL was triggered by the IGP located at the 10 MW directional coupler (see Fig. 4.25) at 5.1 MW peak power in the gun and 600 μs RF pulse length. The spectra of the electron detectors located at the RF vacuum windows are not shown here because during the IL event they showed only noise.

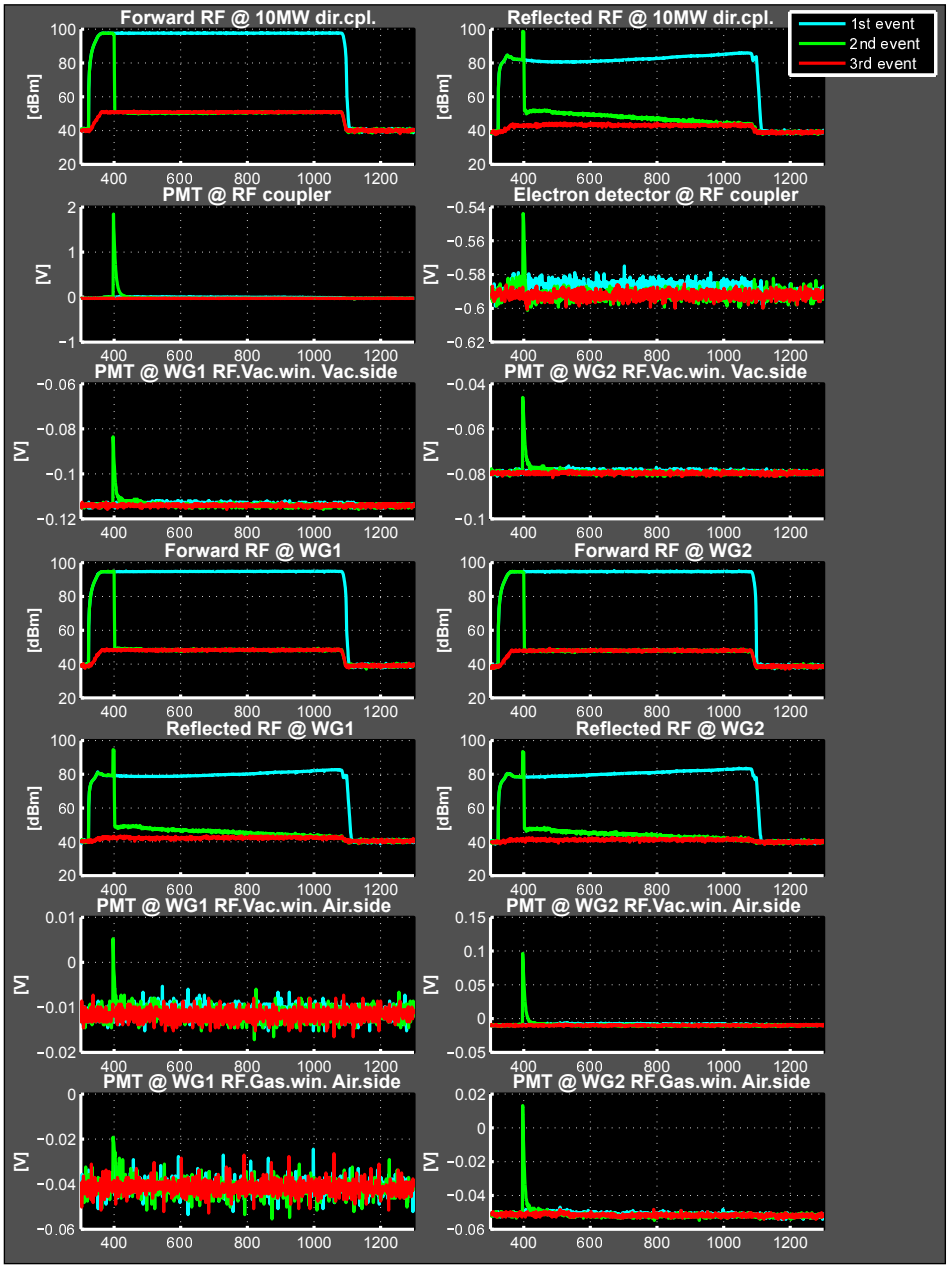

Figure 4.29: LILI plot of the light IL event at the Gun 4.2 on 19 May 2015. The IL was triggered by the PMT located at the RF coupler (see Fig. 4.25) at 5.7 MW peak power in the gun and 600 μs RF pulse length. The spectra of the electron detectors located at the RF vacuum windows are not shown here because during the IL event they showed only noise.

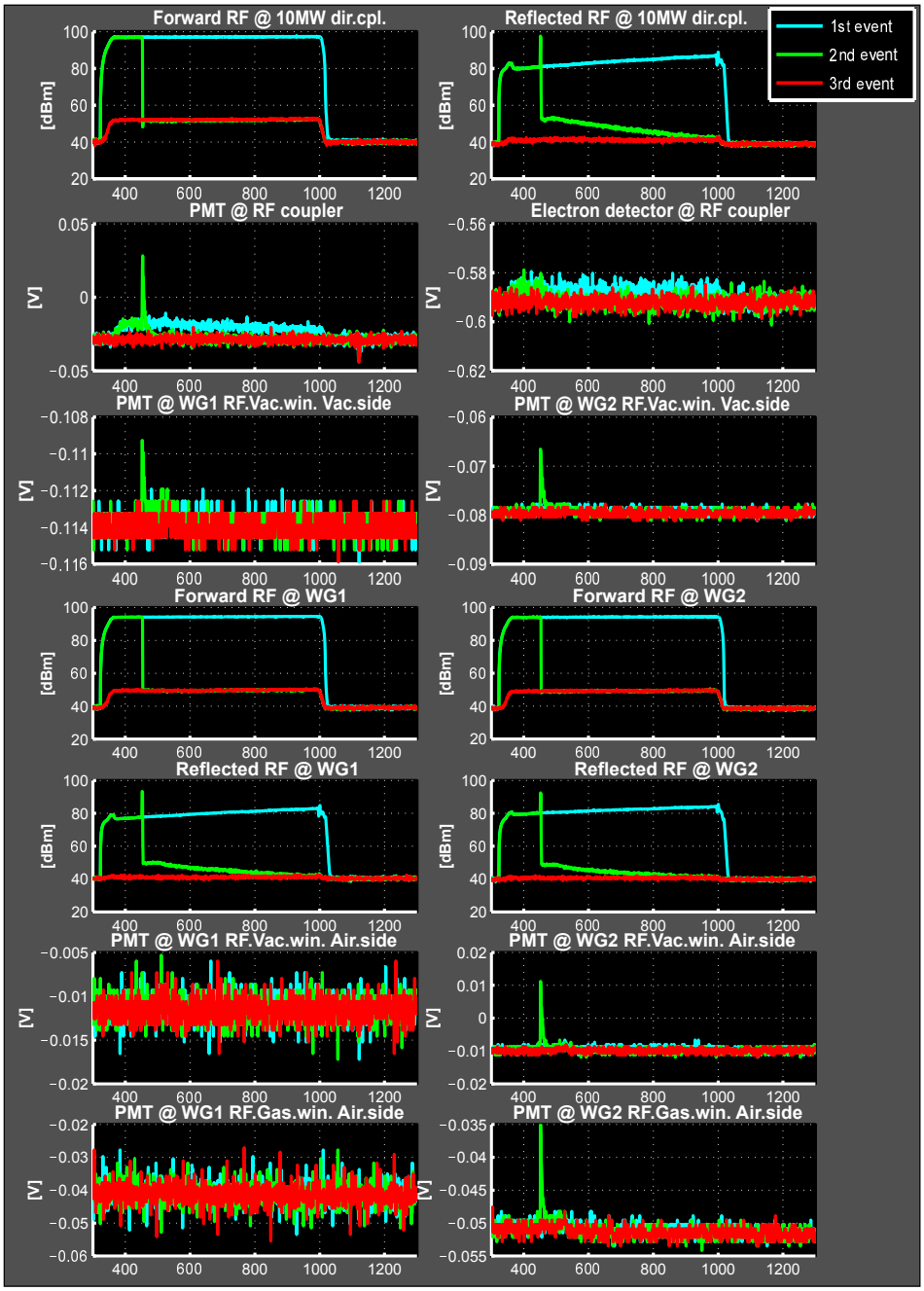

Figure 4.30: LILI plot of the maximum reflection IL event at the Gun 4.2 on 22 May 2015. The IL was triggered by the reflection signals from three directional couplers (see Fig. 4.25) (spikes at the reflection RF spectra) at 5.1 MW peak power in the gun and 600 μs RF pulse length. The spectra of the electron detectors located at the RF vacuum windows are not shown here because during the IL event they showed only noise.

4.5 Conditioning procedure

Starting from the gun prototype 3.1, which was installed at PITZ in August 2012, a new conditioning procedure was established and applied. The Gun 3.1 RF feed setup had only one RF vacuum window from the THALES company [65]. The window was installed between T-combiner and RF coupler. The RF system layout is presented in Fig. 4.31.

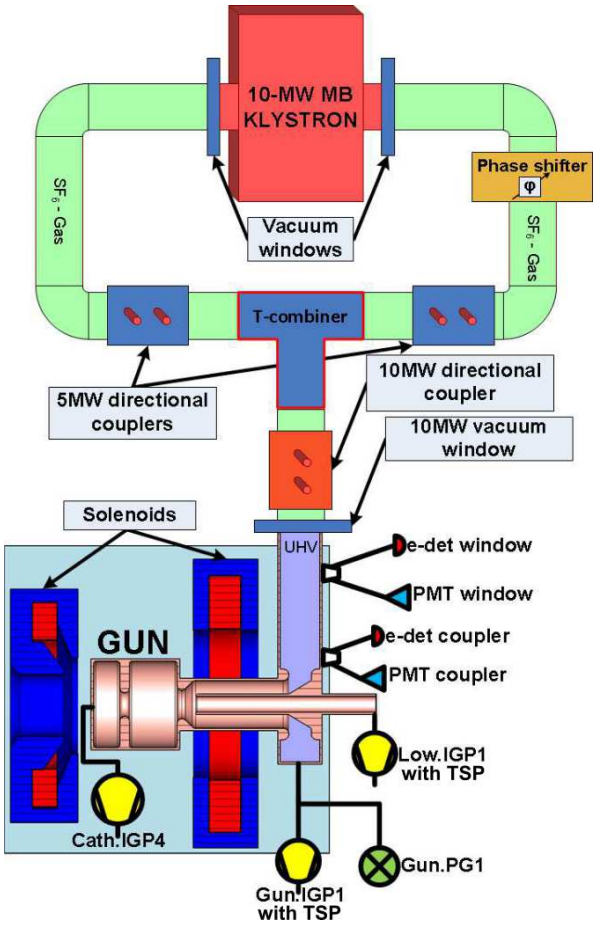

Figure 4.31: RF system overview for a setup with 1 RF window.

The conditioning procedure is determined by the rules that are coming from the THALES window conditioning requirements. The THALES requirements arise from the conception of careful degassing of the window ceramics. This material is used to separate the vacuum and gas parts in a vacuum window. The ceramics contain a lot of gas molecules inside. Before a vacuum window would be used at full specifications, the outgassing from the window ceramics should be minimized.

The outgassing process in a solid bulk material consists of two steps. At first, gas particles must diffuse from the solid body to the surface and then desorb from there.

By increasing the temperature, the speed of the gas escape increases exponentially.

Based on the outgassing idea the following recommendations on the RF power increase were obtained:

- an increase of the peak power at a fixed RF pulse length and repetition rate
- start at the shortest possible RF pulse length. When maximum peak power is reached, then switch off the power, set a longer RF pulse length and increase the peak power from zero to the maximum again for the new pulse length

The established conditioning procedure contains the following requirements for the ramp-up procedure:

- RF power increase by steps of max 0.2 MW every 15 minutes at a new RF pulse length
- vacuum pressure must be less than 10^{-7} mbar (fixed threshold coming according to THALES requirements)
- in a case of significant vacuum activity or other trips:

  re-ramp RF power from 0 with short pulses (10 μs)

  increase the pulse length in reasonable steps
- initially, the RF gun solenoids must be off (then solenoids sweep have to be applied)
- no Feed Back Loop should be used
- after a trip, the restart should be done at the same repetition rate at which the operation was interrupted (step 1 or step 5 in table 4.1)

The applied conditioning steps are shown in table 4.1.

The procedure allows mildly cleaning of the surface and bulky body from the residual gas and contamination. As it was mentioned before it is important to keep constantly relatively high plasma density close to the surface. However, too high plasma density increases the probability of discharge that leads to an interruption in the conditioning and can cause damage of the window. The plasma density is directly connected to the outgassing rate. In order to keep the outgassing rate below the level critical for the discharge, a slow RF peak and average power ramp is applied.

Considering the outgassing process, the RF peak power has more influence on the desorption of the molecules from the surface than on the gas molecules diffusion through the solid body, while the RF pulse length has more influence on the diffusion process.

The RF peak power impacts on the oscillation energy (rotational or vibrational) of molecules. The gas or other contaminating molecules located on a surface are desorbed, if their oscillation energy becomes higher than their binding energy. The ramping of the

Step	Rep. Rate, Hz	RF pulse length, μs	RF power range, MW
1	5	10	0..Max
2	5	20	0..Max
3	5	50	0..Max
4	5	100	0..Max
5	10	10	0..Max
6	10	50	0..Max
7	10	100	0..Max
8	10	200	0..Max
9	10	400	0..Max
10	10	650	0..Max

Table 4.1: Gun conditioning steps. Maximum power for the guns starting from the year 2012 is 6.5 MW.

peak power from zero to maximum at the shortest pulse length cleans slowly the top layer of the surface, starting from molecules with small binding energies towards high energies. Meanwhile, the molecules trapped in the dielectric body see a lower RF electric field, and after the RF pulse is switched off, are still kept in the body. Nevertheless, the diffusion process gets stronger and faster because of the dielectric body material, and the gas molecules obtain higher oscillation energies, and the temperature of the material increases.

Conditioning at a short RF pulse length is able to clean only the cavity surface and bulky body parts in smallest depth. The increase of the pulse length increases the body heating process and accelerates the molecules diffusion process. This allows to clean the deeper surface layers, while ramping of the peak power allows to control the outgassing rate. The schematic representation of the process is shown in Fig. 4.32 and Fig. 4.33.

The influence of the RF pulse length on the gas molecule diffusion distance inside a dielectric is shown in Fig. 4.32. The area where a molecule can diffuse is indicated by a circle and the diffusion distance is represented by the circle radius. If a molecule reaches the surface of the body, it is able to escape the body and be released to the vacuum. Fig. 4.32 shows the different cases: no RF power, short and long RF pulses. The circles for all three cases show the possible area of the molecule diffusion for a time period longer than the corresponding RF pulse length. The longer the RF pulse the larger the distance the molecule can pass. Thus the deeper layers of the body can release gas or contamination molecules. The same process for many molecules is illustrated in Fig. 4.33. The red line shows the level above which all molecules are able to leave the body and can escape into the vacuum.

In the case of a metal body, the RF fields can only penetrate in the skin-depth

where they create an RF current. A molecule trapped in the body deeper than the skin-depth does not get any additional oscillation energy by the RF fields but via body heating processes, which depends on the average RF power. The diffusion process of gas molecules in the case of a metal body should happen much slower than in the case of dielectrics, for example, ceramics, because in case of dielectrics the trapped molecules get energy from the RF electric field as well as from the heating of the dielectric body.

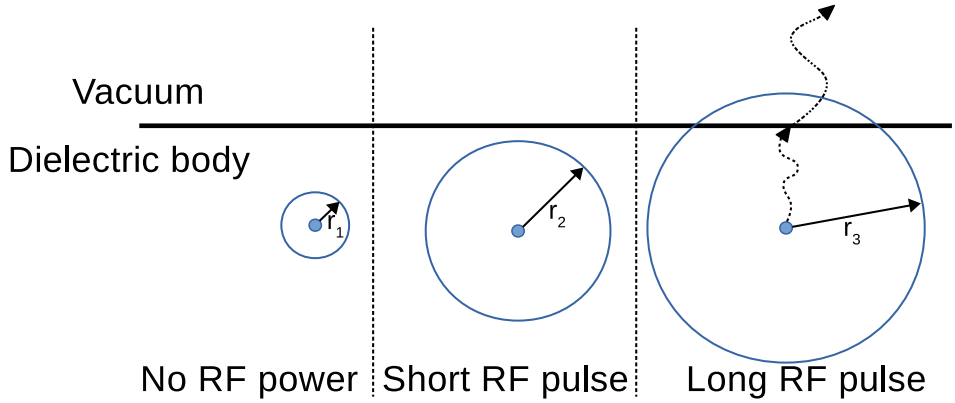

Figure 4.32: Schematic representation of the outgassing process in a dielectric body for a single molecule. The circle shows the area where a molecule is able to diffuse.

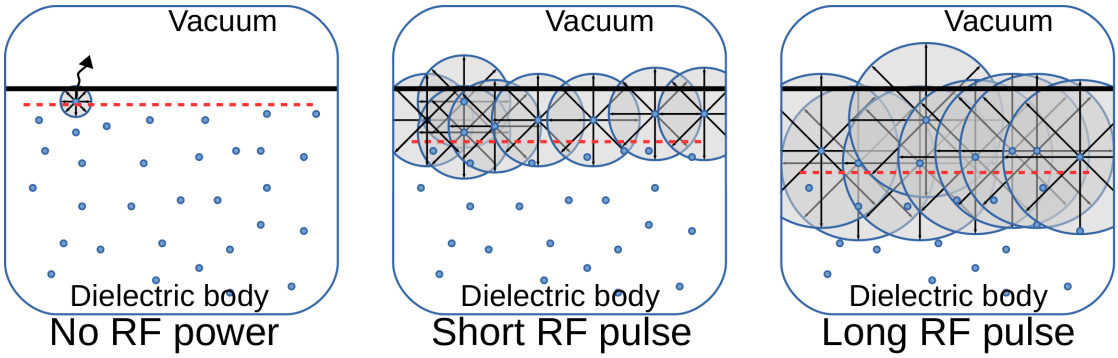

Figure 4.33: Schematic representation of the outgassing process in a dielectric body for many molecules. Circles show the area where a molecule can diffuse. The red line shows the level above which all molecules are able to leave the body and can escape into the vacuum.

There are two possible ways to increase the average RF power during a careful conditioning procedure. The first method was described before; the idea of the method is to increase the RF peak power while the RF pulse length is fixed, and to apply the peak power ramp-up from 0 to maximum for each change of pulse length. Currently,

this method is an established and applied procedure. The second method is to ramp up to the maximum peak power at short fixed RF pulse length and afterward to increase the RF pulse length while the RF peak power is kept at the maximum level. The schematic representation of both methods is shown in Fig. 4.34.

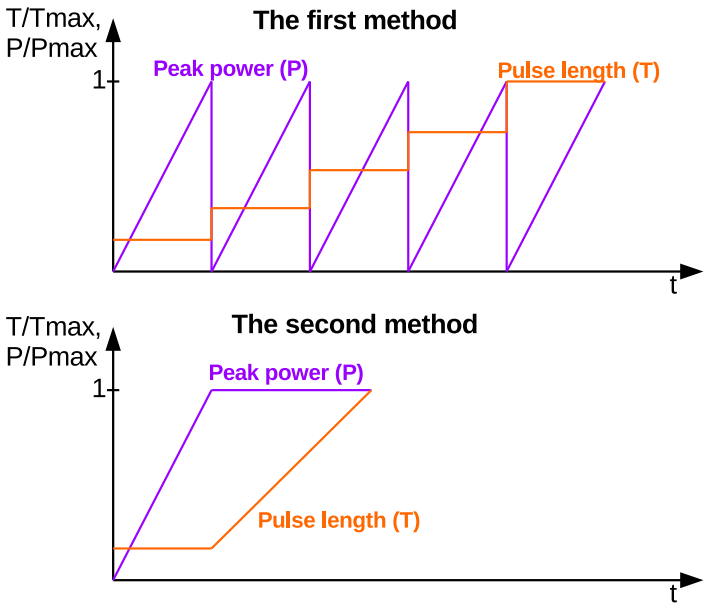

Figure 4.34: Two possible ways to increase the average RF power: blue line is the gun peak power normalized to its maximum value P_{max}, orange line is the RF pulse length normalized to its maximum value T_{max}.

The first method requires more time to achieve the maximum RF average power but it does a more careful and mild conditioning where the field emission process can be controlled more precisely. The second method achieves the maximum specifications faster but each increase of the RF pulse length at highest RF peak power leads to a significant increase of the average power, and it is dangerous to emit a huge portion of contaminating molecules that can initiate a discharge, leading to a breakdown.

From this point of view, the first method is more suitable for the time period when the conditioning process of a gun cavity is started and new combinations of peak power and pulse length must be discovered. Also, this method should be applied after each trip IL event when a high vacuum activity was observed and one of the reasons of the IL event was a signal in excess of the vacuum threshold. In this case, a huge portion of contaminating particles can be released into the vacuum space and settles afterwards on different surfaces of the vacuum chamber. From the safe conditioning point of view, the vacuum system must be considered as non-conditioned and the first method must be applied.

The second method can be used for the relatively fast ramping of the RF power and pulse length when a vacuum system is almost conditioned but only extreme

combinations of peak power and pulse length cause difficulties. The region of peak power ramps at small pulse lengths can be passed according to the second method in this case. Compared to the first method that makes almost complete conditioning for the whole parameter range, the second method can be used only for conditioning at fixed operation settings. Using this method, an operation becomes unsafe if one would change RF peak power at long pulse length, even to the lower values direction, because non-stable operation conditions (e.g. multipacting) can appear.

The effective conditioning should happen in a way consuming as little man power as possible. The continuous conditioning at PITZ is typically organized in one 8-hour shift (morning or late) with two operators followed by a 16-hours automatic run using the State Machine Automatic Conditioning (SMAC) program and with a responsible physicist who is able to control the machine parameters remotely. The SMAC is able to monitor all important machine parameters and reacts if necessary: power ramping or stopping the machine. The main machine parameters that are tracked are forward and reflected power, RF pulse length, the vacuum level in the gun, cavity resonance temperature, gun and klystron interlock signals. In the case of any vacuum interlock the program stops (no restart of the RF) and is waiting for the operator or responsible physicist who can decide about the a further procedure after that IL (this interlock is called "gun trip"). SMAC also stop to ramp-up the peak power if the vacuum level reaches the threshold value adjusted in the settings. In the case of other interlocks that are not accompanied with a vacuum interlock SMAC resets the interlock and starts ramping of the gun power according to the settings and the current status of the gun parameters. The main window of the SMAC GUI is shown in Fig. 4.35.

The presented conditioning procedure was developed and applied at PITZ. It allows to perform careful gun conditioning and to reach European XFEL specifications more efficiently. The PITZ experience shows that it is important to control all of the gun parameters during the conditioning and to analyze each of the IL events in order to prevent cavity damage and to enable running at the maximum specifications.

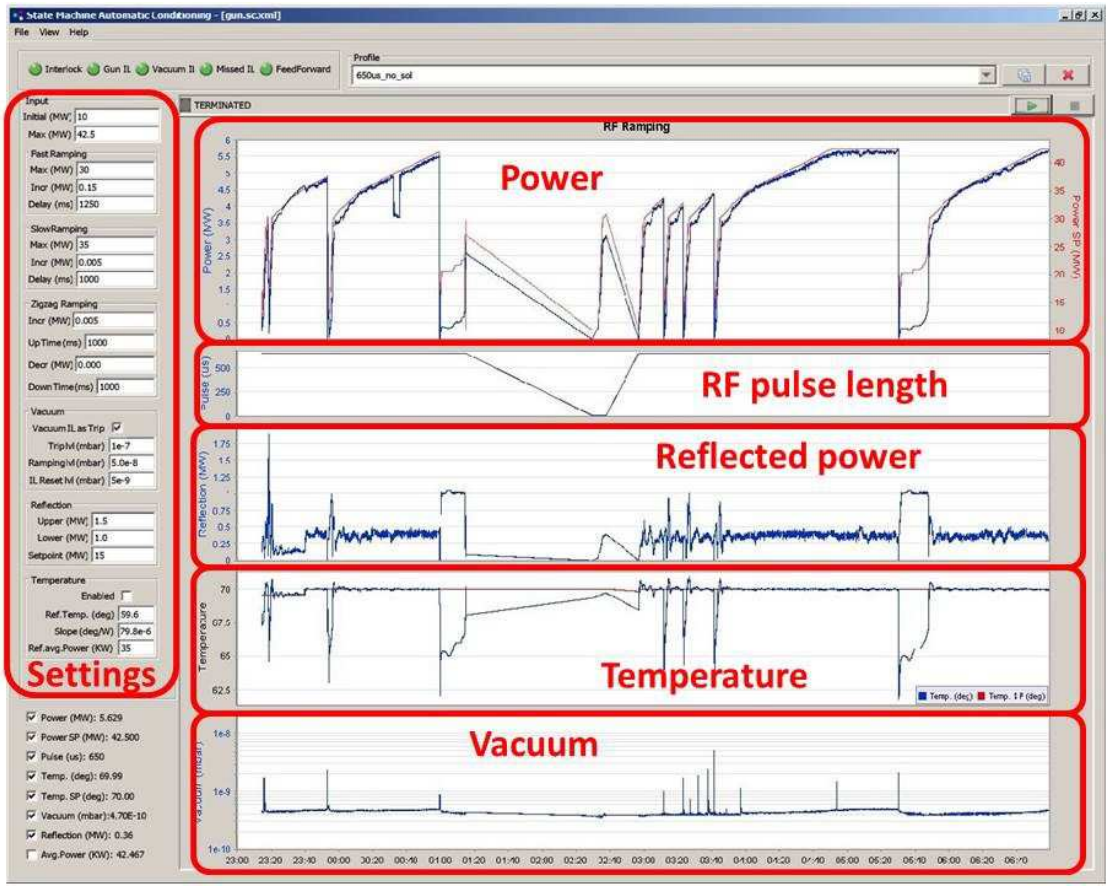

Figure 4.35: The main window of the State Machine Automatic Conditioning (SMAC) program. The main parts of the SMAC (needed to an operator) are indicated by the red rectangles: gun peak power, RF pulse length, reflected power, gun temperature, vacuum level, and settings. The settings consist of the technical data that is not relevant to the context.

4.6 Measurements of the dark current and multipacting

The dark current produced by a gun cavity can be measured by the electron beam diagnostics. But only the fraction of the dark current that leaves the cavity via the beamline tube can be measured.

The PITZ facility has several charge measurement devices installed in the low energy beamline section which are used for the dark current measurements: two insertable Faraday Cups (FCs) installed 0.8 m and 1.4 m downstream of the cathode, one Integrating Current Transformer (ICT) installed 0.9 m downstream of the cathode and one dedicated Dark Current Monitor[2] (DCM) [66] installed at 2.4 m . The main device for reliable and accurate dark current measurements at PITZ is a Faraday Cup (FC), namely Low.FC1. The FC charge measurement range well covers the region of dark current charge values produced by a gun. A FC is able to measure very low charges, while an ICT has a bad signal-to-noise ratio (see Fig. 4.36). The schematics of the measurement installation is presented in Fig. 4.37.

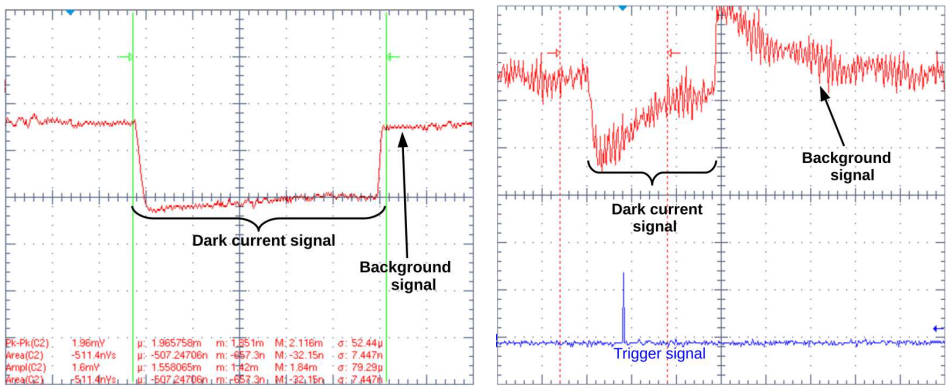

(a) (b)

Figure 4.36: (a) dark current signal from FC (dark current is 39.4 μA), (b) dark current signal from the ICT (dark current is 3.7 mA). The signal-to-noise ratio is less optimal for measurements from the ICT compared to the FC, although the measured dark current is a factor of 100 larger. The numbers seen in the images are irrelevant in the context and should be ignored.

The direct comparison of the DCM and FC measurements is complicated due to the fact that the DCM is located further downstream in the beamline and the dark current transport to the DCM is restricted (additionally it collects the dark current from the CDS booster which introduces more measurement uncertainties). The charge

[2]The DCM is a charge measurement device tuned to detect dark current. It is based on an RF resonator made from stainless steel.

measurements presented in this chapter are done by using the FCs. The difference between them is just their position in the beamline and the value of the main solenoid current for the best focusing at their measurement location. At different times of gun operation, different FCs were used for dark current charge measurements. For the measurements usually that FC is preferred that has smaller noise and jitter.

The energy of the dark current emitted by the gun cavity was measured by the Low Energy Dispersive Arm (LEDA), which consists of a dipole installed 1.1 m downstream of the cathode and an observation screen installed in the beamline of LEDA. The dipole deflects electrons from the gun cavity by 60 ° and the combination of the dipole magnetic field B_{dipole} and the deflection angle α (or beam position on the screen) is recalculated to a beam momentum p by:

$$p = \frac{eB_{dipole}L_{eff}}{\alpha}, \tag{4.13}$$

where e is the electron charge and L_{eff} is an effective length of the magnetic field of the dipole [67].

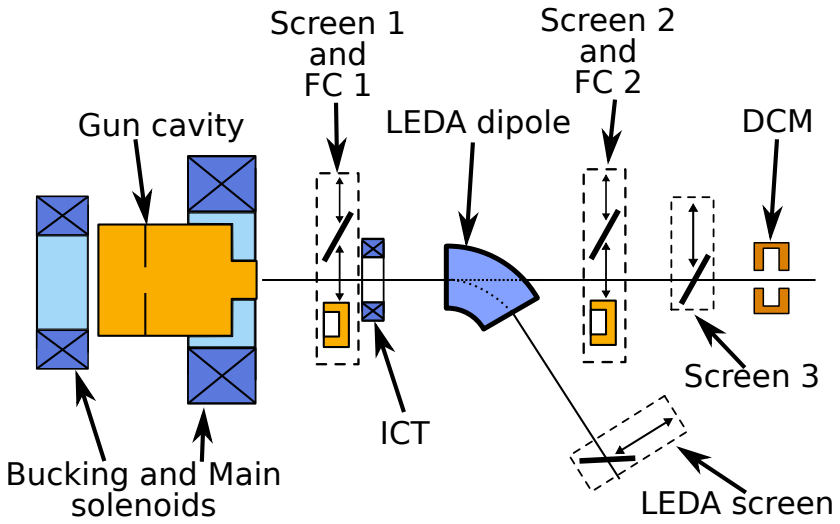

Figure 4.37: Schematic PITZ diagnostics used for dark current measurements. The diagnostics consist of three insertable observation screens located in the straight section, two insertable Faraday cups, one integrating current transformer, one dark current monitor, and the low energy dispersive arm.

The images of the dark current structure were taken from the different observation screens. The best screen for the observations of the dark current is the screen closest to the gun because it is able to collect larger amount of dark current particles. Therefore, it is possible to observe more dark current features. The dark current images at the three first screens are located at 0.8, 1.4 and 1.7 meters downstream of the cathode,

respectively (see Fig. 4.38). The dark current structure does not depend on the observation screen, only intensity and position of the features change.

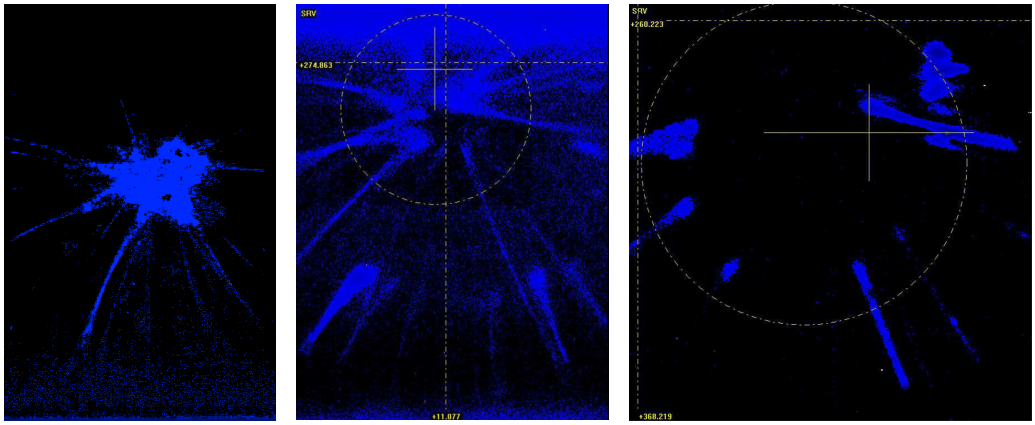

(a) Screen 1 (b) Screen 2 (c) Screen 3

Figure 4.38: Dark current at the first three observation screens. The dark current pictures were taken during operation of the gun prototype Gun 4.1 used at PITZ in the year 2010. The gun operational parameters are: 6 MW in the gun, 200 μs RF pulse length and main solenoid current fixed at 400 A.

The structure of the dark current was described in Ref. [51]. It has mainly a ring-like structure in the center and radial lines as hot spots that can be focused to the center of the dark current ring by changing the main solenoid magnetic field. The dark current images at the later stages of different guns operating at PITZ are presented in Fig. 4.39. The dark current for all of the guns, in general, has a similar structure but varies in the intensity of the line-like features and the solenoid field needed for the dark current focusing. According to the observed pictures of the dark current, it comes mainly from the region of the cathode vicinity, particularly from the back wall of the gun half cell and the cathode plug. There is always a clearly visible ring in the center of the dark current pictures that corresponds to the photocathode and its vicinity. The simulations in section 4.3.1 show similar result: there is a ring with increased intensity of the dark current, which is coming from the cathode vicinity edges.

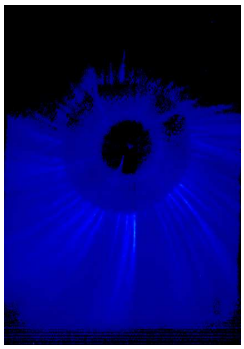

(a) Gun 3.1 in 2006

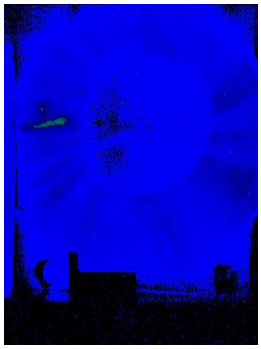

(b) Gun 3.2 in 2007

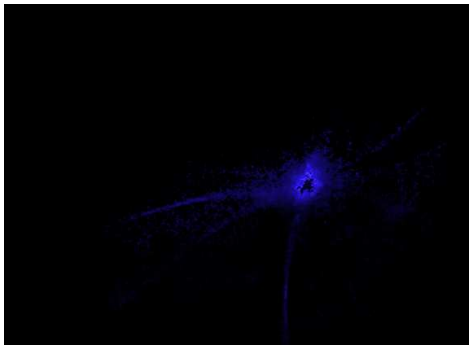

(c) Gun 4.2 in 2009

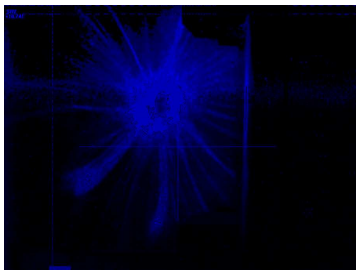

(d) Gun 4.1 in 2012

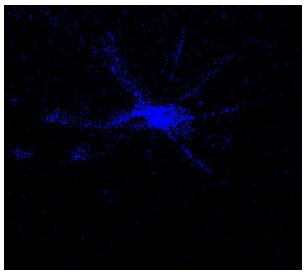

(e) Gun 3.1 in 2013

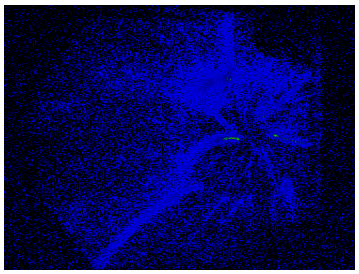

(f) Gun 4.3 in 2013

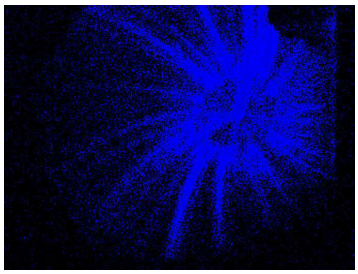

(g) Gun 4.4 in 2014

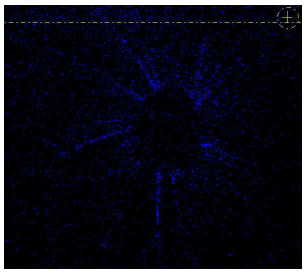

(h) Gun 4.2 in 2015

Figure 4.39: Dark current images at the first observation screen for different gun prototypes during the final stage of operation at PITZ.

The dark current is emitted from a gun cavity during the whole RF pulse length. It starts slowly with an RF pulse and quickly stops at the end of the RF pulse due to the fact that the RF pulse has a finite fill and decay time and the amount of the dark current is proportional to $(E/E_0)^2 \exp(-E_0/E)$, where $E\,[V/m]$ is the electrical field strength on the cavity surface and $E_0\,[V/m]$ is the constant which characterizes the gun geometry and surface state.

The dark current is not constant within an RF pulse that is why the characterization of the dark current is based on the maximum value that is calculated from the obtained oscilloscope signals as peak-to-peak or amplitude signal measurement. The signal analysis is done by an internal function of the digital oscilloscope [68] and the data collection is done by a MATLAB[3] script where a background subtraction and statistics are implemented. The mean value with an RMS error is given as result.

The measured dark current value depends not only on the electrical field strength at the gun cavity surface but also on the values of the main and bucking solenoid currents. The magnetic field configuration produced by the main and bucking solenoids affects the trajectories of the dark current particles. By varying the solenoid field configurations and strengths it is possible to change the gun cavity surface area from which a particle can be transported to the accelerator beamline. Moreover, the solenoid magnetic field focuses the dark current beam as well as the electron beam emitted from the cathode. By changing the dark current focus position, one can change the amount of the dark current, which can be detected. The characterization of the dark current is always done when it is focused on a FC for maximizing the collection of the dark current particles.

Since the dark current value depends on the magnetic field of the solenoid it is necessary to perform a solenoid scan. Dark current measurements are usually made versus the main solenoid current while the bucking solenoid is automatically adjusted for compensation of the main solenoid magnetic field at the cathode surface. The dark current dependence on the main solenoid current for different guns installed at PITZ is presented in Fig. 4.40. For the dark current characterization, the maximum value of this dependence is taken into account.

[3]MATLAB (MATrix LABoratory) programming language developed by MathWorks [69].

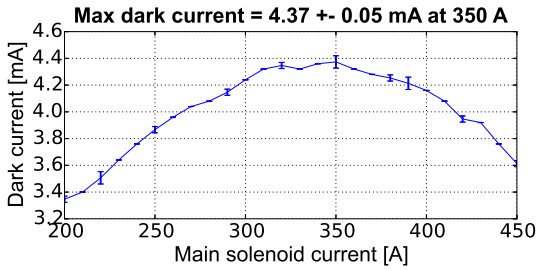

(a) Gun 3.2 in 2007

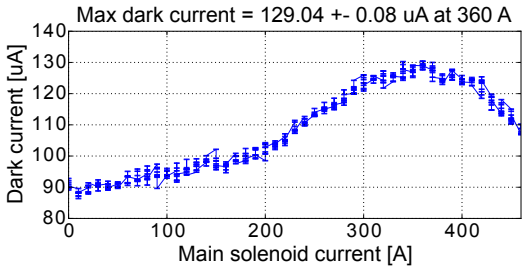

(b) Gun 4.2 in 2009

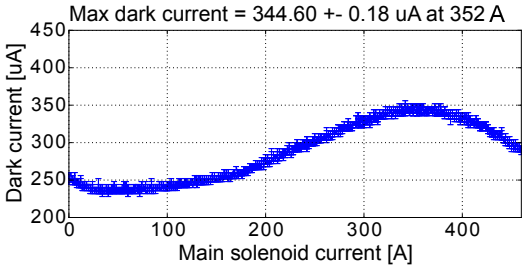

(c) Gun 4.1 in 2012

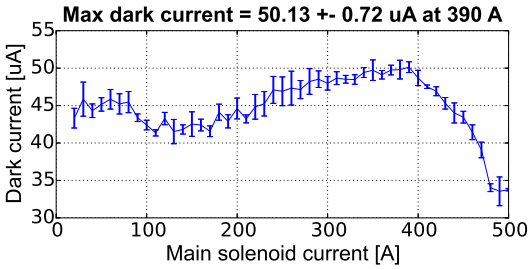

(d) Gun 3.1 in 2013

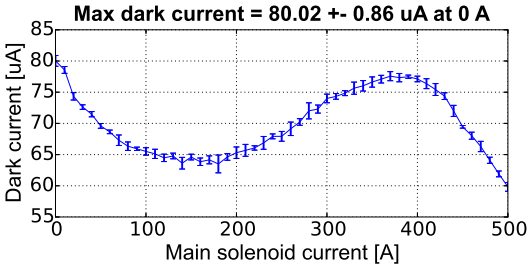

(e) Gun 4.3 in 2013

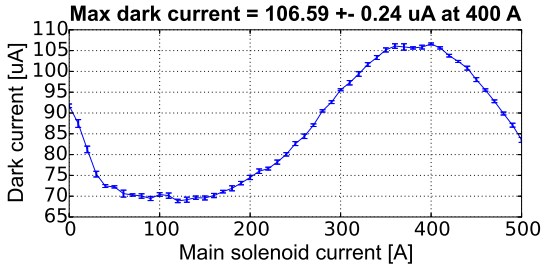

(f) Gun 4.4 in 2014

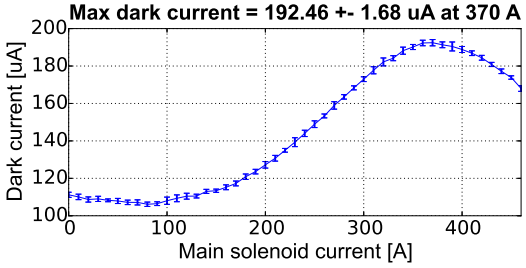

(g) Gun 4.2 in 2015

Figure 4.40: Dark current solenoid scans for different gun prototypes during the final stage of operation at PITZ.

The dependence of the maximum dark current on the gun power is presented in Fig. 4.41 and 4.42. The value of the solenoid current was always readjusted for each value of the power in the gun in order to obtain the maximum dark current. The dependence well correlates with the theory of enhanced field emission.

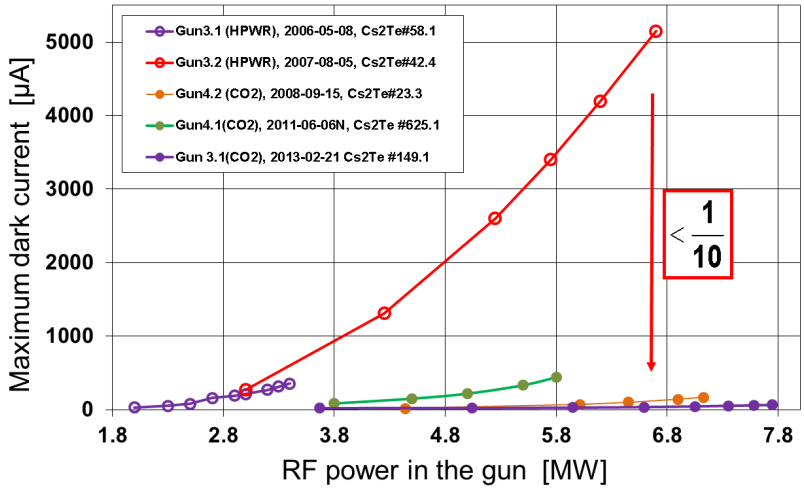

Figure 4.41: Dark current versus RF peak power for different guns installed at PITZ.

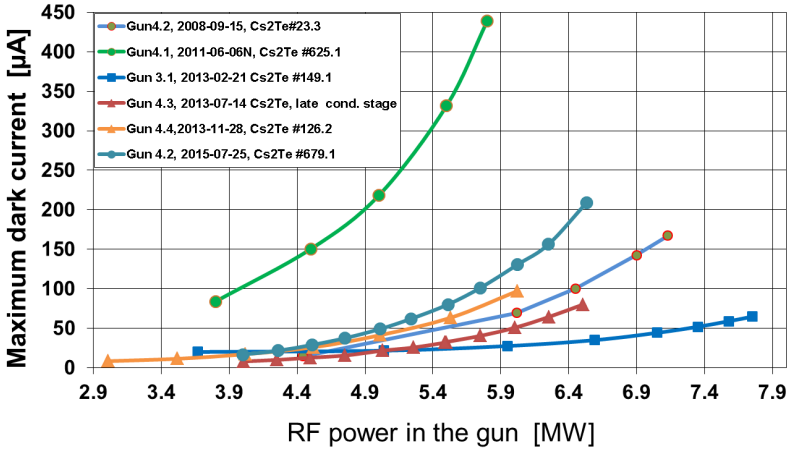

Figure 4.42: Dark current versus RF peak power for different guns installed at PITZ that all have been treated with CO_2 cleaning.

The significant drop of the dark current from the cavity prototype Gun 3.2 to the cavity prototype Gun 4.2 was due to a change of the cavity cleaning procedure. Starting from the gun cavity prototype Gun 4.2, a Dry-Ice Cleaning (DIC) [70] replaced the High

Water Pressure Rinse (HWPR) cleaning and became the standard procedure for gun cavity preparation.

High-pressure rinsing with ultra-pure water is the well-proven standard cleaning step after chemical or electrochemical surface treatment of Superconducting Radio-Frequency (SRF) cavities, but dry-ice cleaning is a powerful additional cleaning option which is based on the sublimation-impulse method. Dry-ice cleaning allows to avoid a wet cavity surface, removes carbohydrates and is applicable to ceramics.

In comparison with HWPR where a mechanical effect is the major cleaning contribution, DIC additionally offers thermal and chemical cleaning effects. Relaxation of liquid CO_2 in a nozzle results in a snow-gas mixture with approximately 45 % snow-rate with a temperature of 194 °K. To ensure an acceleration and to focus the CO_2-stream, a supersonic jet of N_2 is used as an environment. At the same time, the N_2 prevents condensation on the cavity surface.

The mechanical cleaning effect is based on shock-freezing of the contamination, strong impact of the snow crystals and increasing volume after sublimation by a factor of 500. The contamination becomes brittle and starts to flake off from the surface. When snow particles hit the surface and melt at the point of impact, the chemical cleaning effect occurs. Liquid CO_2 is a good solvent, especially for hydrocarbons and silicon contamination. To achieve an optimal cleaning process it is necessary to reach a high thermal gradient between jet and surface. It is absolutely essential to keep the cavity warm ($20 - 30\,°C$) during the cleaning process. Furthermore, a sufficient exhaust system is needed to keep down the CO_2 and N_2 rate in the clean room atmosphere.

In order to reduce the dark currents in the gun cavity, a dedicated vertical cleaning set-up (Fig. 4.43) was constructed [70]. Compared to the previously applied cleaning using HWPR, the risk of an unwanted oxidation of the sensitive RF surface is significantly reduced. A special nozzle system with a 110 ° rotatable nozzle (Fig. 4.44) was built [70]. This design is necessary in order to assure a complete and effective cleaning of the RF gun geometry, especially the surface close to the cathode and the first cell of reduced length. In order to avoid any recontamination, created by the motion of the nozzle, the nozzle system is exhausted.

During the operation of the gun prototype 4.1 a strong increase of the FC signal was noticed while the RF pulse rise. Also the spikes in the dark current signal described in Ref. [51] [4] were observed. The picture of the signals from the FC is presented in Fig. 4.45. The studies of that behavior revealed that the level of the signal depends on the solenoids field combinations. Solenoid field maps were produced to understand the behavior of the signal on the magnetic fields. The solenoid scan maps for two power levels in the gun and different RF pulse lengths are presented in Fig. 4.46. There is a visible growth of the signal at high magnetic field strength. That, however, does not

[4] The DC measurements at Low.FC1 described in Fig.5.1 of Ref. [51] showed sharp spikes in addition to the DC within the RF pulse: one at the RF pulse rising edge, but before the DC signal, and a second one approximately 7 μs after the RF pulse. These spikes were described by multipacting in Ref. [51].

Figure 4.43: Vertical cleaning set-up for gun cavities [70].

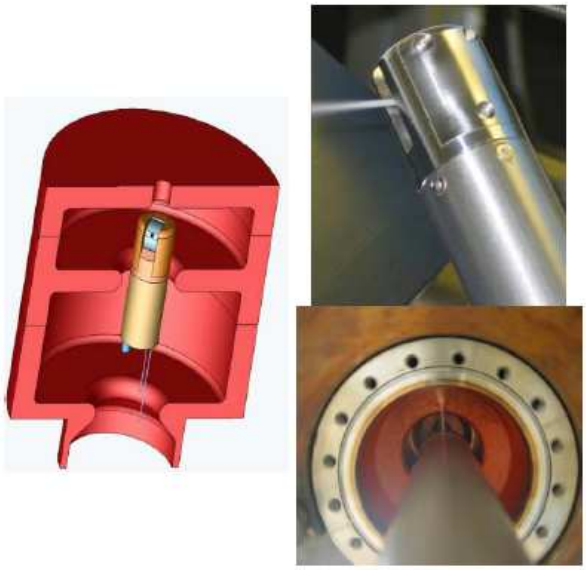

Figure 4.44: 3D-model of the gun cavity with a rotatable nozzle (left); rotatable nozzle (upper right); bottom-up view of the cleaning of the gun cavity (lower right) [70].

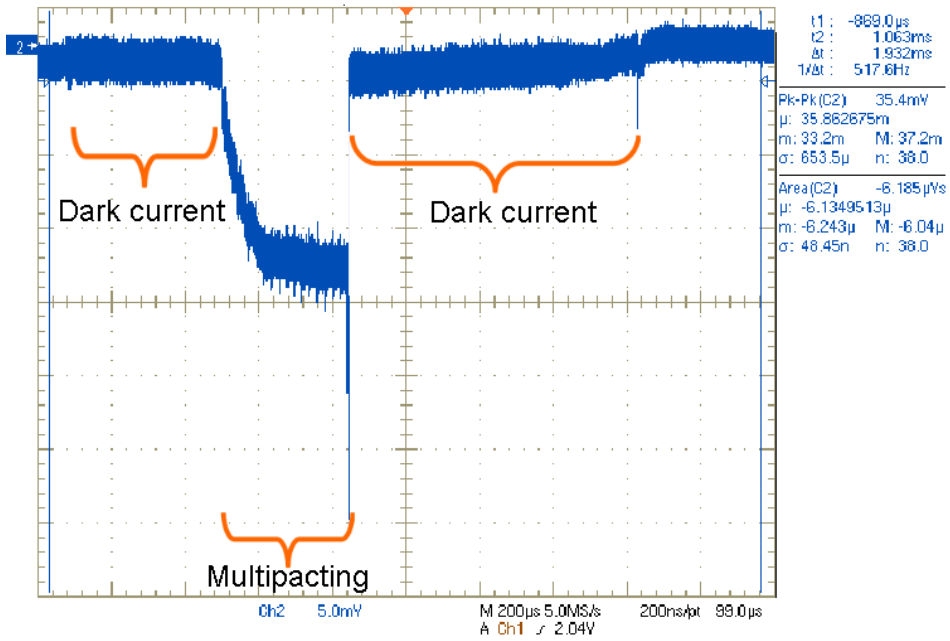

Figure 4.45: FC signal at the oscilloscope during multipacting. The measurements were performed for the Gun 4.1. The numbers seen in the image are irrelevant in this context and can be ignored.

disturb the usual operation of the gun because the normal operating solenoid range is located outside of the multipacting area.

According to the simulations in section 4.3 the detected signal growth is coming from the multipacting electrons produced by the low power RF generated at the high voltage base level and specific solenoid fields. The simulations show that the source of the electrons is the back wall of the gun half cell (Fig. 4.21).

For later operation, the tuning of the I and Q modulator parameters was improved to reduce the pedestal level of the RF before the real RF pulse starts. It helped to decrease the range of the gun operation parameters where the multipactor discharge appears.

The experimental observations of the multipactor discharge and dark current showed the behavior similar to one predicted by the simulations in section 4.3: the dark current has ring-like structure due to the cathode vicinity edges, and the high increase of the dark current at low peak power levels occurs due to multipacting at the gun back wall.

4.7 Conditioning history

Over fifteen years of photoelectron guns operation, the PITZ facility accumulated significant experience on gun conditioning, operation, and characterization. Many gun

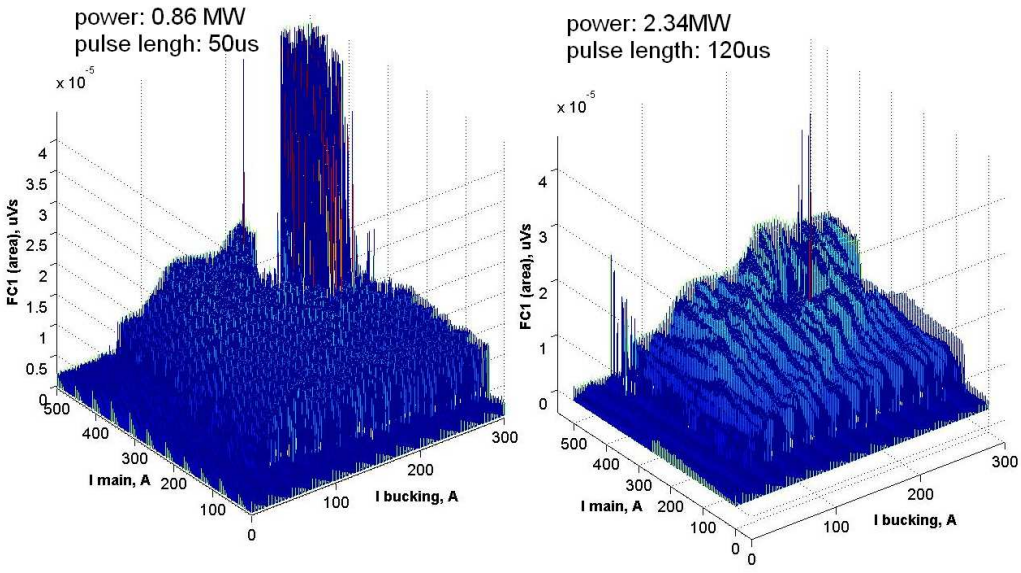

Figure 4.46: Multipacting measurements for different combinations of the main and the bucking solenoid currents. The scope measurements were adjusted to the calculation of the area of the oscilloscope signal (in units of μVs).

prototypes were installed at PITZ for conditioning and subsequent operation. The schematic presentation of operated guns at PITZ is shown in Fig. 4.47. The gun cavities are named according to the time when they were produced. There are 4 gun cavity generations:

- First generation: Gun 1 and Gun 2.
- Second generation (modified water cooling): Gun 3.1 and Gun 3.2.
- Third generation (further modification of the water cooling): Gun 4.1, 4.2, 4.3, 4.4 and 4.6 (4.5 is ready for tests).
- Fourth generation: Gun 5 (has a new design: the physics design finished, technical design ongoing).

Except of the 4th generation, the internal geometry of the guns is similar: 1.6 cylindrical cells with rounded edges. The Gun 5 of the 4th generation will have an elliptically shaped cell design. In addition, Gun 5 will have an RF pickup and a strongly modified water cooling concept to allow an operation with higher average power [71].

The guns operated at PITZ have all different history and different procedures were applied for their production, for example for the cleaning process. The details of the guns operated at PITZ are summarized in Figs. 4.48 and 4.49. The tables show the time periods of operation at PITZ, the type of cleaning procedures, differences in the

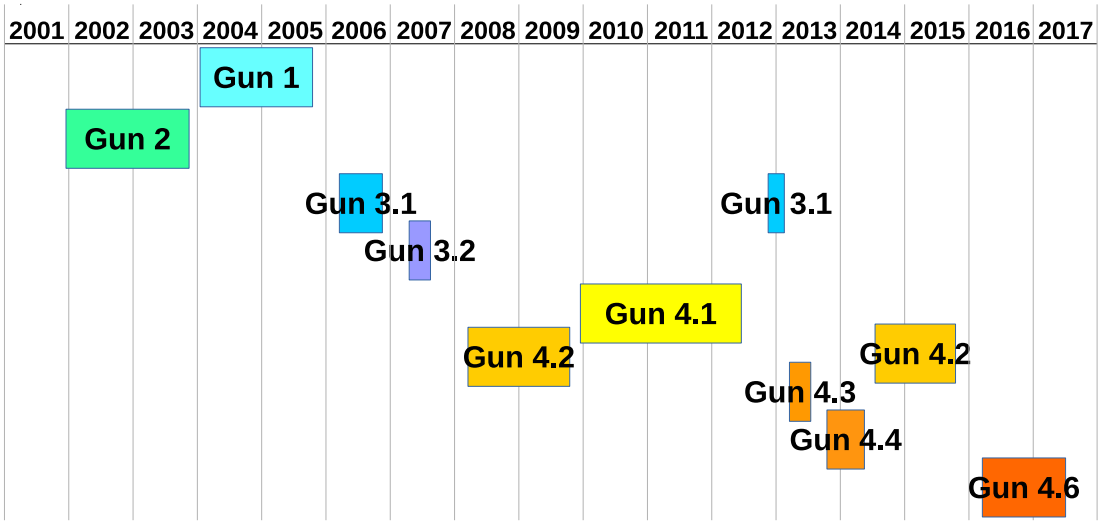

Figure 4.47: Schematic presentation of the installed gun prototypes at PITZ (situation for May 2017).

design (e.g. the number of cooling channels and cathode spring design) and specialties that appeared during their operation (shown in the column comment).

Together with the development of the gun cavities also the RF system dedicated for the gun operation underwent several changes.

The first two guns were using a klystron, pre-amplifier, and modulator dedicated for operation at 5 MW peak power only. There was only one waveguide from the klystron to the gun, and a DESY-type RF vacuum window, which is dedicated for 5 MW peak power operation, was used (see Fig. 4.50(a)).

The first significant RF system upgrade included the installation of a THALES [65] multibeam klystron dedicated for operation at 10 MW peak power. The RF output of the 10 MW klystron is via 2 waveguides (WR650). In order to combine the RF power from two waveguides, a power T-combiner has been developed [72] and installed. DESY-type RF vacuum windows were installed in both RF waveguides because they are specified only up to 5 MW forward peak power. The schematic is presented in Fig. 4.50(b). A phase shifter had to be implemented in one of the waveguides to match the phases of the RF waves at the T-combiner.

The next RF system upgrade happened with the installation of Gun 4.1 in 2010. A newly developed 10-MW in-vacuum directional coupler has been installed after the T-combiner (see Fig. 4.50(c)). Compared to the previous setup, where signals from two directional couplers (5-MW each) have been used to control the RF power in the gun cavity, an additional 10-MW in-vacuum directional coupler allowed to implement a feedback loop for a better RF stability control. The old setup with two 5-MW directional couplers had the problem of a possible cross-talk of the RF waves in both

directional couplers and a feedback loop was unreliable and could be used for the beam measurements. This resulted in large gun phase fluctuations since only the RF feed-forward has been applied. The main advantage of the 10-MW directional coupler is a direct control of the combined forward wave and of the wave reflected from the gun cavity. This improved RF regulation allowed to significantly improve the stability of the emittance measurements and allowed to demonstrate a new world record in projected emittance in the charge range from 0.02 nC to 2 nC [73].

Since the gun setup with in-vacuum directional coupler, T-combiner, and two RF windows has a quite large dimension it was decided to test a setup with only one RF window downstream the 10-MW directional coupler. Together with Gun 3.1, in 2012 two RF vacuum windows were replaced by one 10-MW RF vacuum window from the company THALES, and the 10-MW in-vacuum directional coupler was placed on the gas side (see Fig. 4.50(d)). The RF scheme was used for the conditioning procedure established, and the first gun for the European XFEL (Gun 4.3) was conditioned and characterized utilizing this setup.

The first DESY experience with RF THALES windows revealed numerous problems during the window operation. For example, it turned out that the THALES RF windows in the one-RF-window configuration after some operation time got leaks at FLASH, PITZ, and XFEL. Therefore a total windows production process revision was done [74]. In addition, it was decided to come back to an RF gun setup with two THALES windows installed in the 5-MW waveguides for reduction of the transmission power through the windows, including an in-vacuum T-combiner and a 10-MW directional coupler. This was constructed and used with Gun 4.2, starting from the year 2014. The waveguide sections before the THALES windows were filled with air in order to make the RF setup close as much as possible to the XFEL setup, which does not use SF_6 gas but waveguides filled with dry pressurized air. In addition, the air waveguide section allows an easier exchange of the gun vacuum section due to simplified working safety rules. The schematic presentation of the current setup is presented in Fig. 4.51.

All of these RF layouts except their main specialties also differ in the number and locations of interlock detectors, which were used for the gun and for the RF system protection during the operation and, particularly, during the conditioning (see Figs. 4.50 and 4.51). The latest RF layout consists of seven PMTs and three electron detectors. Photodiodes in the previous RF schemes were exchanged step by step with PMTs due to the possibility of threshold level and sensitivity adjustments.

Gun proto-type	Period of location at PITZ	Cleaned by:	Cathode spring design	Water cooling channels design	Comment
Gun 1	January 2004 – October 2005	HPWR	Watchband	13 channels, common I/O volumes	
Gun 2	December 2001 – November 2003	HPWR	Watchband	13 channels, common I/O volumes	• opening the gun showed damages in the cathode spring area
Gun 3.1	• March 2006 – November 2006 • November 2012 – February 2013	• HPWR • Dry-ice	Watchband	8 channels, common I/O volumes	• cathode problem was observed in 2006 • cathode area was remachiened • now installed at **FLASH**
Gun 3.2	April 2007 – August 2007	HPWR	Watchband	8 channels, common I/O volumes	• showed extreme traces from dark current emission as well as heavy damages in the cathode spring area

Figure 4.48: History of guns operated at PITZ (part 1) The situation for May 2017.

Gun proto-type	Period of location at PITZ	Cleaned by:	Cathode spring design	Water cooling channels design	Comment
Gun 4.1	December 2009 – June 2012	Dry-ice	Watchband	14 channels, separate I/O volumes	the gun with which the best emittances were achieved
Gun 4.2	• March 2008 – October 2009 • July 2014 – October 2015	Dry-ice	• Watchband • Contact stripe	14 channels, separate I/O volumes	• damages in the cathode spring area after dismounting from FLASH due to IL problems • contact stripe cathode spring implemented in autumn 2012
Gun 4.3	March 2013 – July 2013	Dry-ice	Contact stripe	14 channels, separate I/O volumes	• problem in the cathode spring area discovered during production • the cathode area was remachined and contact stripe design applied • currently installed at **XFEL**
Gun 4.4	October 2013 – May 2014	Dry-ice	Contact stripe	14 channels, separate I/O volumes	• first gun with contact stripe spring design from the beginning • cathode spring replaced by gold-plated spring with rhodium layer
Gun 4.5	-	Dry-ice	Contact stripe	14 channels, separate I/O volumes	• produced in 2014 with contact stripe RF spring design • ready for tests
Gun 4.6	• March 2016 - Now	Dry-ice	Watchband reloaded	14 channels, separate I/O volumes	• first gun with watchband reloaded cathode spring design • currently installed at **PITZ**

Figure 4.49: History of guns operated at PITZ (part 2) The situation for May 2017.

The initial main effort of the PITZ facility was focused on beam quality optimization. The resulting data showed that the photoelectron injector is able to satisfy the European XFEL requirements for beam quality: a projected beam emittance of less than 0.9 mm mrad was measured. The best emittance results were achieved during the operation with Gun 4.1 in the year 2011. The lowest emittance results [73] are summarized in Table 4.2.

After the required beam parameters were achieved, the main task of PITZ shifted to the obtainment of a high operation stability of the gun. Starting from the new installation of the re-used Gun 3.1 (the gun was additionally dry-ice cleaned before installation) in 2012, the main goal of PITZ became to achieve the European XFEL requirements on the gun peak power, RF pulse length, and duration of stable operation. Additionally, a conditioning procedure for the THALES RF window (see section 4.5) was established.

Bunch charge, nC	**Projected normalized RMS emittance, mm mrad**
0.02	0.121±0.001
0.1	0.212±0.006
0.25	0.328±0.010
1	0.696±0.020
2	1.251±0.064

Table 4.2: Measured optimized RMS emittance for various bunch charges.

The example of a gun life cycle showing the quickest conditioning progress is Gun 4.4, which is dedicated to the European XFEL as the second or spare gun. The gun was constructed in 2012 and dry-ice cleaned in June 2013. The gun was delivered to PITZ in September 2013 and the conditioning started in October of 2013. This gun is the first that has a new RF spring design (contact stripe) right from the beginning of the construction. The RF layout used together with Gun 4.4 is shown in Fig. 4.50(d) According to the described procedure, the conditioning of Gun 4.4 started with the shortest RF pulse of 10 μs and very slow RF peak power ramping. The beginning of the conditioning is presented in Fig. 4.52. The repetition rate of the facility was switched to 5 Hz. Even with a low average power, a high vacuum activity was detected right from the beginning by the IGP (the name of the device is IGP1), and a pressure gauge was installed at the RF coupler.

Almost three days were needed to reach 6 MW RF peak power in the cavity (the green line in Fig. 4.52 top plot). The speed of the power ramp was limited by the vacuum activity. Only after a high RF peak power was reached at 10 μs RF pulse length and the vacuum activity dropped, the RF pulse length was increased ($20 \rightarrow 50 \rightarrow 100\,\mu$s). The repetition rate was switched to 10 Hz only after 6 MW peak power was achieved at

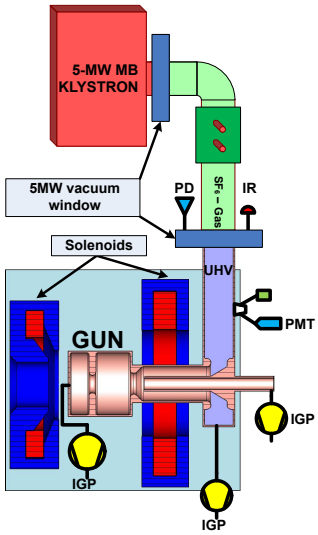

(a) used with Guns 1 and 2 in 2001 - 2005

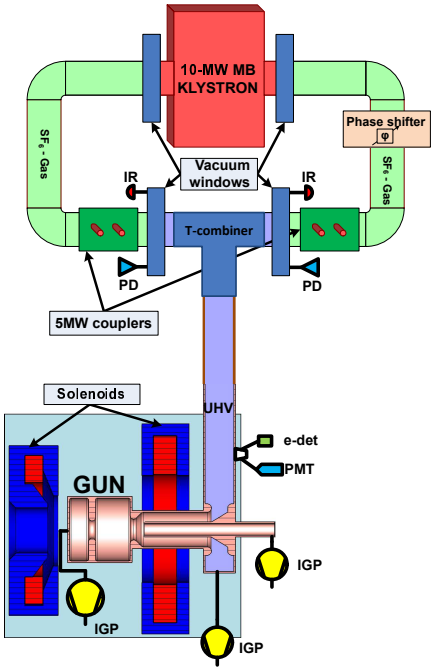

(b) used with Guns 3.1, 3.2 and 4.2 in 2006 - 2009

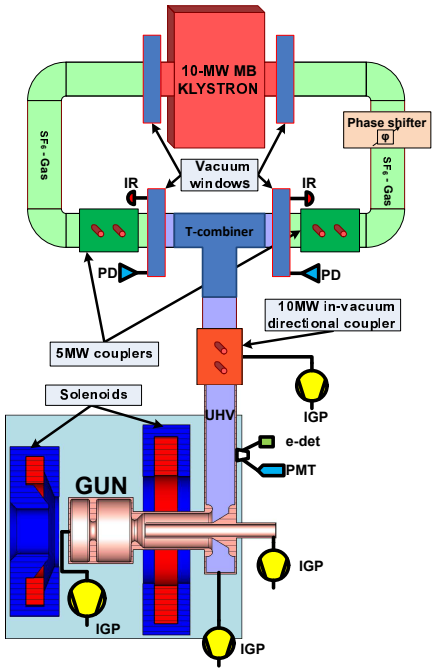

(c) used with Gun 4.1 in 2010 - 2012

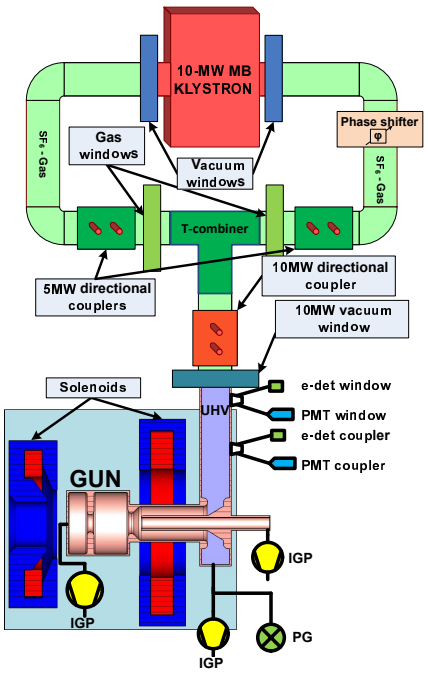

(d) used with Guns 3.1, 4.3, 4.4 in 2012 - 2014

Figure 4.50: RF system used with different gun prototypes.

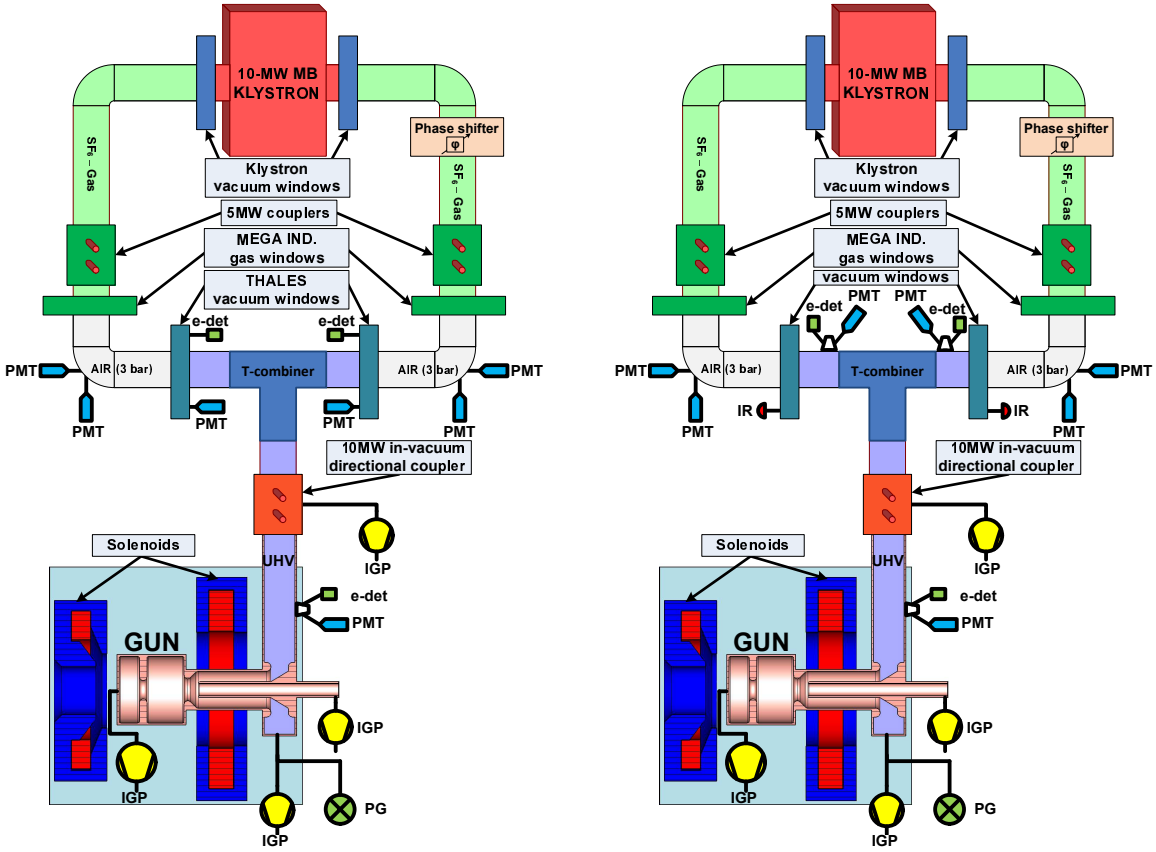

(a) used with Gun 4.2 in 2014 - 2015

(b) in use with Gun 4.6 since 2016

Figure 4.51: RF system used at PITZ with the gun prototypes 4.2 and 4.6 since 2014.

100 μs. The vacuum activity during this time period was kept at the highest possible level. After each vacuum interlock event, which is called a trip, (always accompanied with spikes in the vacuum plot) ramping was restarted from 10 μs RF pulse length. It is visible in the RF pulse length history plot of Fig. 4.52.

It was noticed that after some trips the vacuum level can stay relatively high for some time even if the pulse length was only 10 μs. This vacuum behavior might be an indicator of a surface cleaning process when a bunch of contamination particles emitted from a surface point settles at other surface places. Another reason can be an outgassing from ceramics.

History plots from the time period, when the conditioning happened at longer RF pulse length, are presented in Fig. 4.53. The conditioning occurred similar to the conditioning at the beginning and was following the PITZ conditioning procedure. The first time the maximum peak power at 650 μs pulse length was reached, was 24 days after the start of the conditioning. Afterwards, a solenoid magnetic field was applied. For better conditioning for all combinations of the RF power and solenoid field strength,

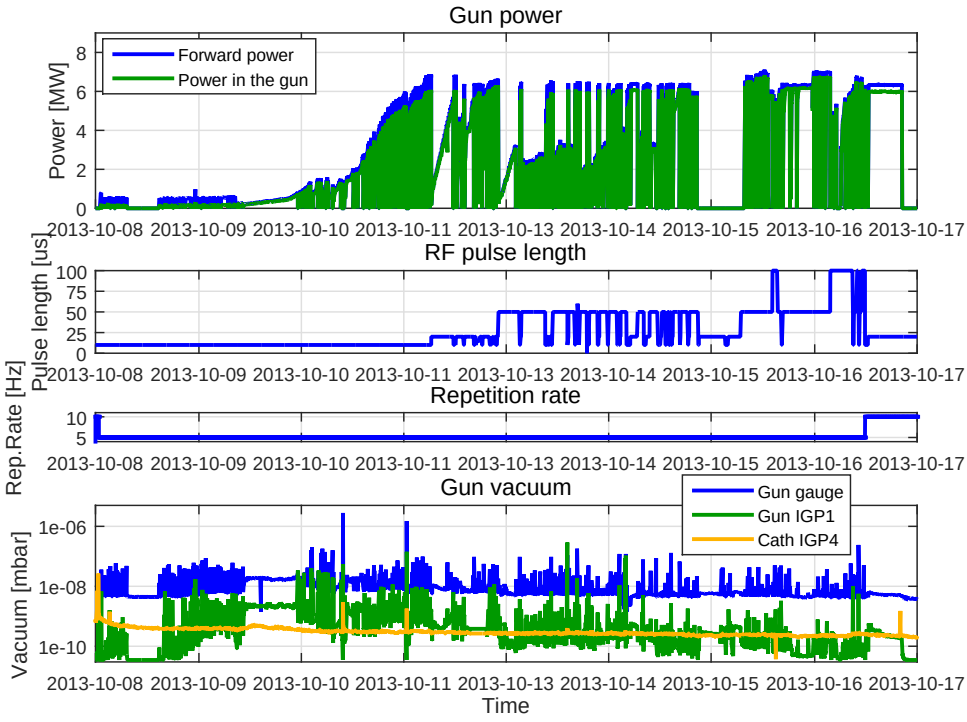

Figure 4.52: Beginning of the conditioning of the gun cavity 4.4.

the solenoid current was swept. This is visible in the main solenoid current (I_{main}) plot in Fig. 4.53. Conditioning with solenoid resulted in a reduction of the maximum reachable RF pulse length. There was a 10 days time period of operation with solenoid, when the maximum reachable RF pulse length became 400 μs. Later on, the vacuum level continuously improved and the full RF pulse length at 650 μs was reached again, but with a solenoid sweep.

The full gun life cycle period is presented in Fig. 4.54. This time can be divided into a few parts. The first part is the conditioning process start-up, the main goal of which is the achievement of the specified gun operating parameters, particularly 6.0 – 6.5 MW peak RF power in the gun at 650 μs pulse duration (the period from 08 October 2013 to 04 December 2013). The second period is dedicated for long term tests and achieving a specified minimum unperturbed run time (the period from 04 December 2013 to 01 February 2014). The third period is measurement time, when the gun characterization is completed (the period from 01 February 2014 to 30 March 2014).

During operation with the Gun 4.4 also a cathode spring upgrade was done, and an RF vacuum windows leak appeared. The cathode spring exchange took place in the time indicated in Fig. 4.54. The previous contact stripe design spring made of CuBe was replaced with a spring of the same design but coated by a gold and a rhodium layer. Also, the cathode plug was replaced by a polished one. The replacements were

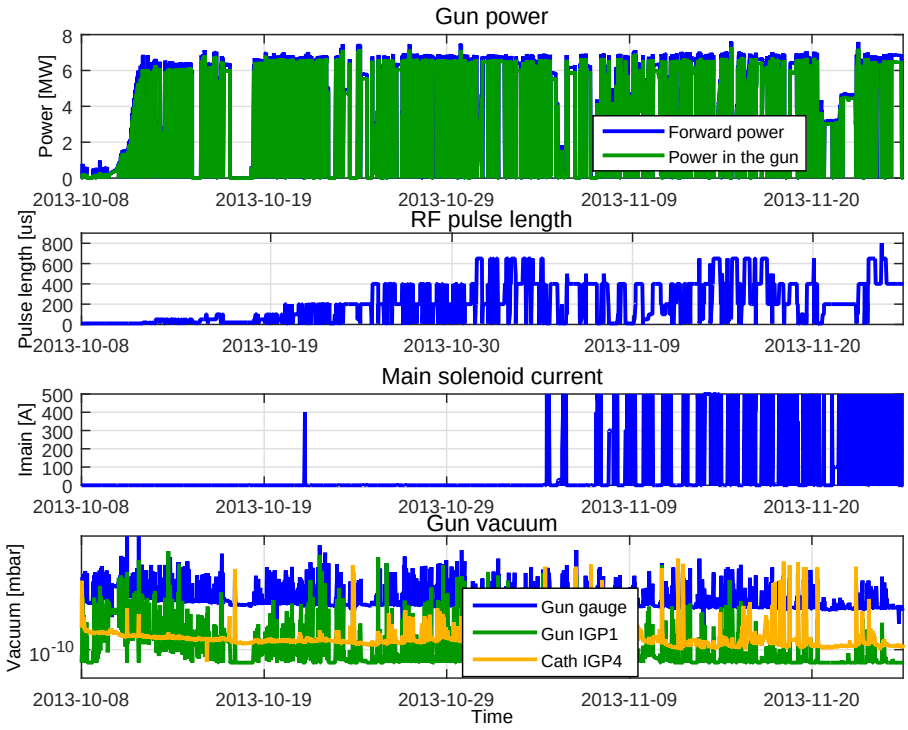

Figure 4.53: History of Gun 4.4 conditioning.

done for improving electrical contact between the cavity and the cathode plug within the development program for the cathode vicinity area. After the exchange a short re-conditioning took place. Shortly later, a leak in the 10-MW THALES RF vacuum window appeared (see section 4.9 for more details).

Another characterization parameter of the conditioning progress is the interlock statistics. On a par with the reached RF power (peak power and pulse length) and the vacuum activity, the interlock statistics describes the gun performance. The history plot of different interlocks during operation of Gun 4.4 at PITZ is shown in Fig. 4.55. Interlocks are presented as colored crosses, each color corresponding to a separate interlock type. By the density of the crosses on the plot, one can roughly estimate on the interlock rate for a certain time period. The Sum IL signal indicates the sum of all interlocks that appeared in the gun. Besides vacuum, PMT and electron detector interlocks, it also includes all technical interlock signals, for example the status during cathode insertion.

To be noted from Fig. 4.55, that the initial conditioning time period was accompanied with a high rate of all interlocks that decayed closer to the end of the period of long term tests and became rather small during the operation period, when RF pulse duration was reduced. The presence of the volume plasma inside the vacuum chamber at the beginning of the conditioning can be proven by the electron detector

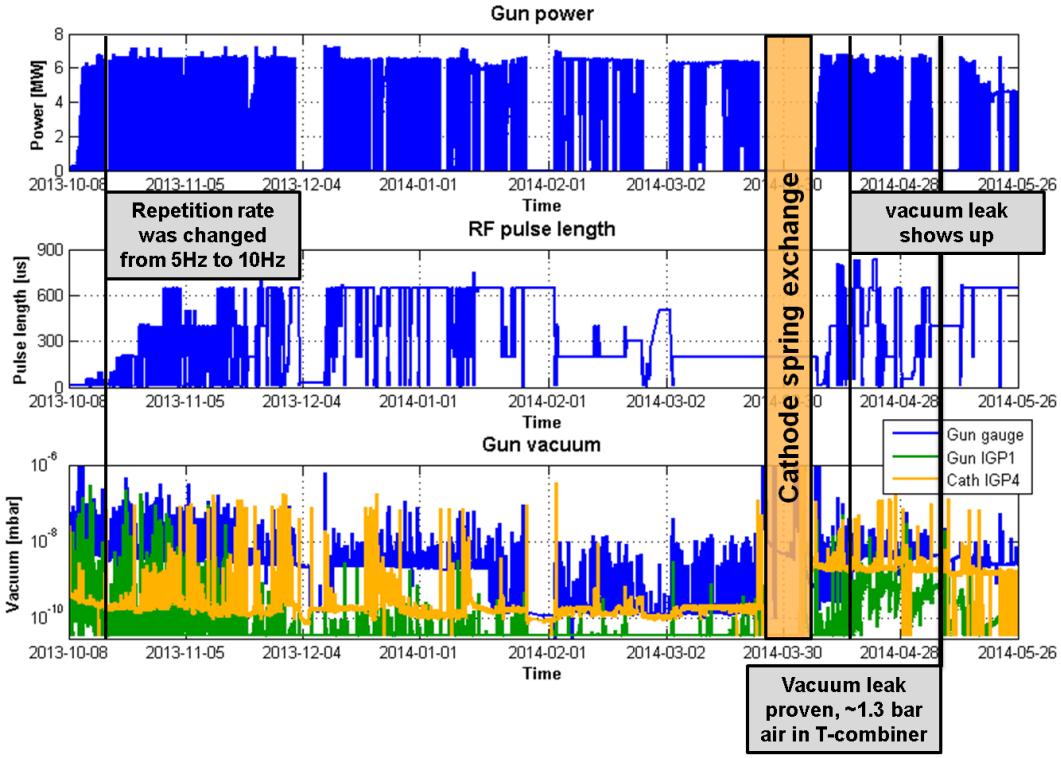

Figure 4.54: The full Gun 4.4 life cycle period at PITZ.

interlock rate. The electron detector interlocks were mainly observed at the time when the surface cleaning should take place, as it was described above in this chapter. The same experience is also supported by the observation of the electron detectors spectra signals that were much smaller during the later operation periods than at the beginning of the conditioning.

The significant increase of the interlock rate from all detectors, which is visible close to the end of the gun operation, is connected with the cathode spring exchange and the later RF vacuum window leak. The events during this time period will be described in section 4.9.

According to the PITZ experience on the RF gun conditioning and run at various RF system setups a two-window layout (two RF vacuum windows installed in 5-MW waveguides, an in-vacuum T-combiner, and in-vacuum 10-MW directional coupler) is the most reliable for the European XFEL specifications on peak and average power performance.

Summarizing conditioning history of several gun cavities yields a typical conditioning time of 3 to 4 months.

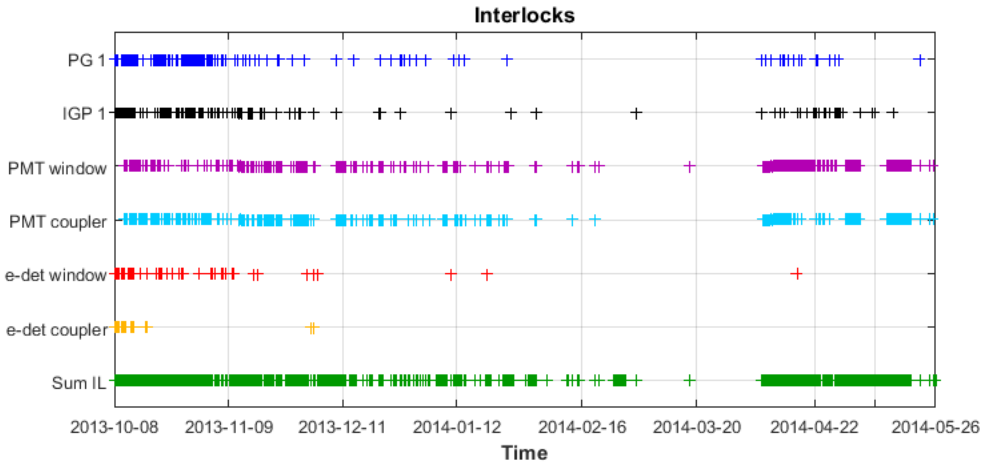

Figure 4.55: Interlocks history of Gun 4.4.

4.8 Power histograms. Comparison of the guns

4.8.1 Statistical analysis of Gun 4.4. Power histograms

One more quantitative description of the cavity operation can be done by a statistical analysis of the operation time of the gun at different peak or average power levels, so-called power histograms. The power histograms were produced by means of an algorithm which protects from data failures (data losses or unphysical values due to communication errors). The algorithm includes the following criteria for data processing: each data point must be weighted by a time period when it was acting (to avoid data irregularities), only power higher than 0.1 MW was taken into account (values below 0.1 MW are considered as noise due to power measurements specialties), spike values higher than 8 MW were not taken into account due to unrealistic measurements state (the spikes appear due to communication errors). The power histograms provide a good overview of the power values, at which a gun was operated.

The power histograms for Gun 4.4 are presented in Figs. 4.56 and 4.57. The upper parts of the plots are power histograms and the bottom parts represent the RF power exposure time, i.e. the time a cavity has been operated at the given power or higher. The power histograms of peak and average power of Gun 4.4 (see Fig. 4.56) show that the gun was operated mainly at average powers of ~ 13 kW and ~ 42 kW. Although the average power histograms show the main operation time in two ranges, the peak power lays in the range $6.0 - 6.6$ MW, i.e. the gun was mainly operated at high peak power. This means that the RF pulse length basically had two values, a high one and a lower one. Fig. 4.54 shows that the lower value was around 250 μs while the larger one was around 650 μs.

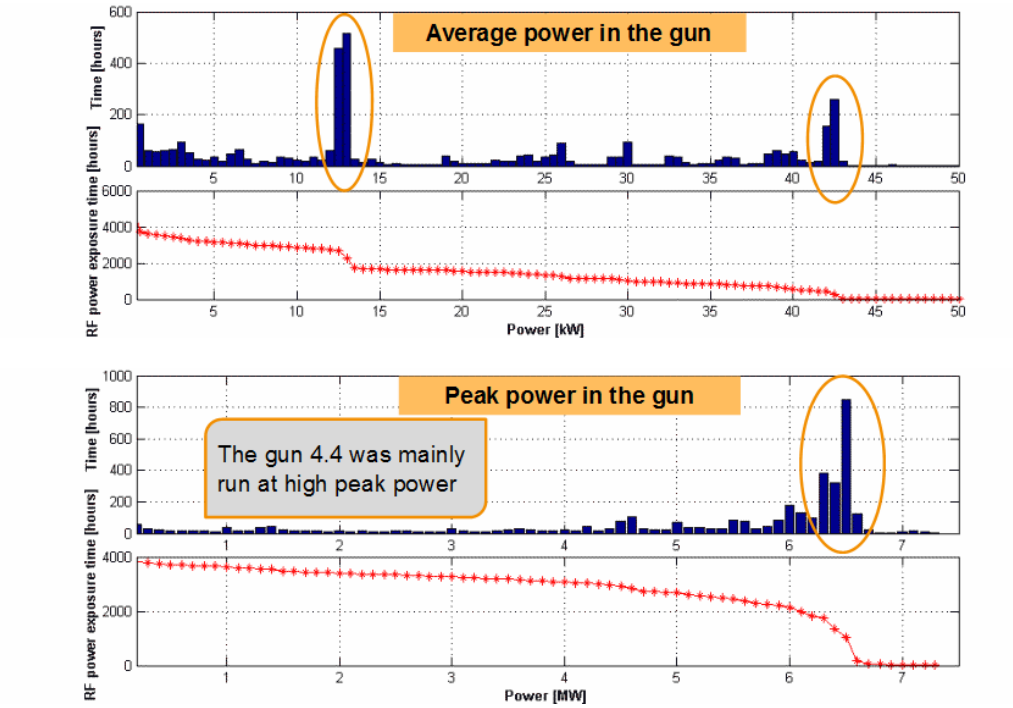

Figure 4.56: Gun 4.4 power statistics for average and peak power.

A comparison of Gun 4.4 performance with the old spring and the new (gold coated with rhodium layer) spring is shown in Fig. 4.57. Compared to the gun operation with the spring before the exchange, the gun operation time with the new spring was spent at a few different peak power levels: 4.5, 5, 5.5, 6 and 6.5 MW. These statistic results were obtained due to checking the operation conditions at these peak power levels.

Long-term test results can be described by a statistical analysis of the unperturbed operation periods, which are presented in Fig. 4.58. The plots show the time duration of unperturbed runs for two run periods: before and after cathode spring exchange.

The longest unperturbed periods have the following values:

- for the run period before spring replacement
  - 40 hours at peak power of 6.5 MW and 650 μs
  - 115 hours at peak power of 6.5 MW and 200 μs
- for the run period after spring replacement
  - 58 hours at 4.5 MW peak power and 650 μs

The statistics of the run hours shows a logarithmic dependence of the maximum unperturbed operation time on the peak power in the cavity. This dependence is shown in the insert of Fig. 4.58.

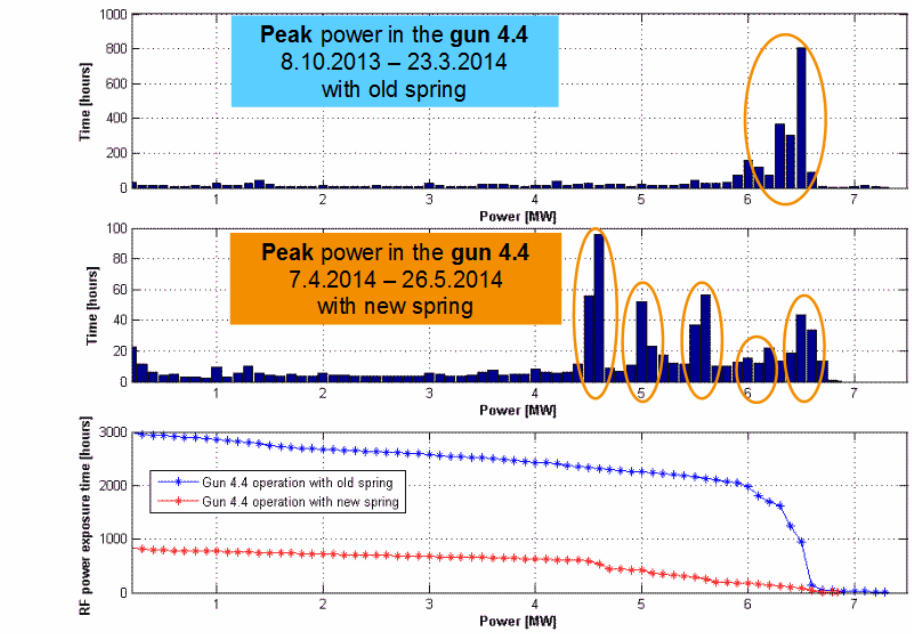

Figure 4.57: Gun 4.4 power statistics for time periods before and after cathode spring exchange.

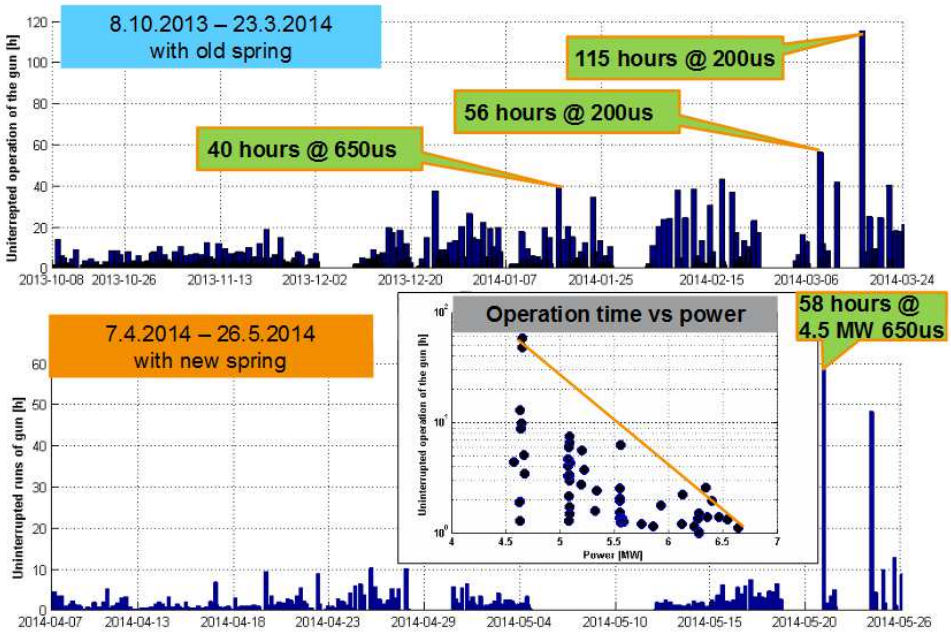

Figure 4.58: Unperturbed runs of Gun 4.4 before and after spring exchange, and unperturbed operation time vs. peak power in the gun (see insert).

4.8.2 Comparison of the guns

A comparison of the guns operated at PITZ can be done by analysis of the normalized statistics results. The results for the comparison of different gun cavities are presented for the gun prototypes 4.1, 3.1, 4.3, 4.4 and 4.2 in Figs. 4.59 - 4.64. All of these cavities were working for different time intervals at PITZ, therefore their comparison was performed for the statistics with normalized time. The total operation time of a gun was chosen as a normalization factor.

The statistics for all gun cavities except of Gun 3.1 and 4.3 show that there are specific power levels, at which those guns were working most of the time: 5.6 MW for Gun 4.1 (Fig. 4.59), 6.5 MW for Gun 4.4 (Fig. 4.62), 5 and 6 MW for Gun 4.2 (Fig. 4.63). There is no certain emphasized peak in the histogram plots for Guns 3.1 and 4.3 (see Fig. 4.60 and Fig. 4.61) because the operational time was mostly spent for the conditioning, almost without long term tests and only reduced time for measurements at specific power levels. Both cavities have been delivered to the user facilities FLASH (operated at 5 MW peak power with RF pulse length up to 800 μs, without interlocks) and European XFEL (currently operated with reduced RF pulse length and peak power of 5 MW, without interlocks) within short time scale. Gun 3.1 is now running at FLASH and Gun 4.3 is running at European XFEL.

A good comparison of the statistical data for all of the guns is represented by RF power exposure time plots (see Fig. 4.64). The absolute value of the line derivative shows the relative time spent at a certain power. The previously noticed power levels for the gun cavities 4.1, 4.4 and 4.2 and relatively smooth curves for Guns 3.1 and 4.3 are clearly visible.

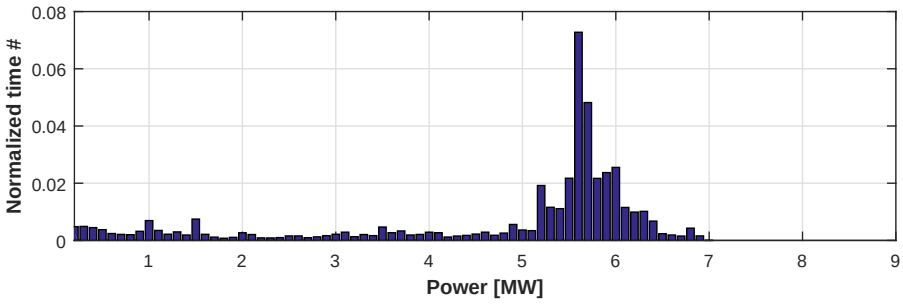

Figure 4.59: Power histogram for the gun cavity 4.1.

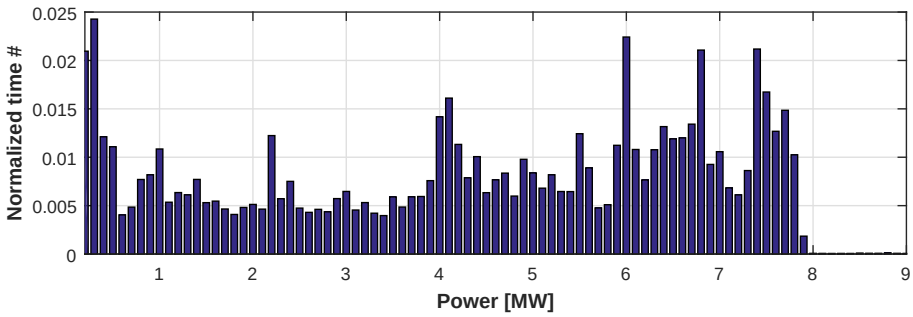

Figure 4.60: Power histogram for the gun cavity 3.1.

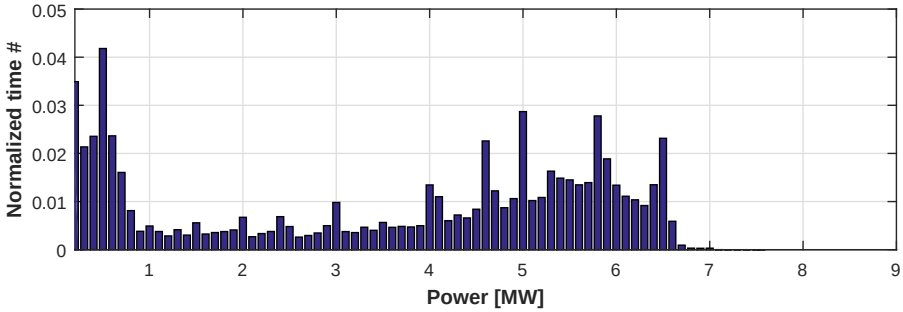

Figure 4.61: Power histogram for the gun cavity 4.3.

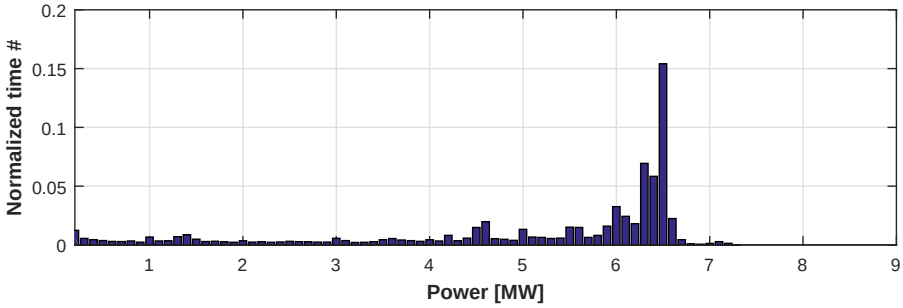

Figure 4.62: Power histogram for the gun cavity 4.4.

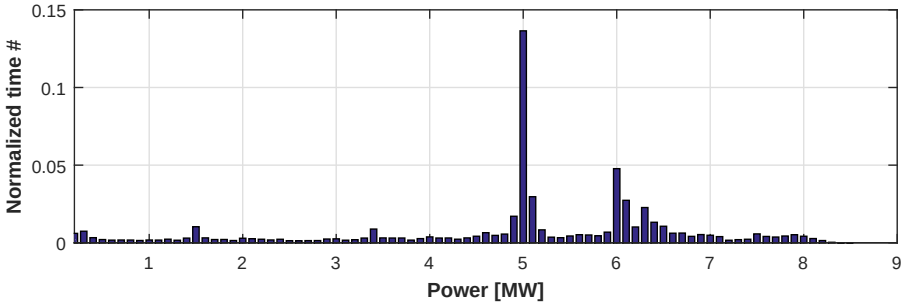

Figure 4.63: Power histogram for the gun cavity 4.2.

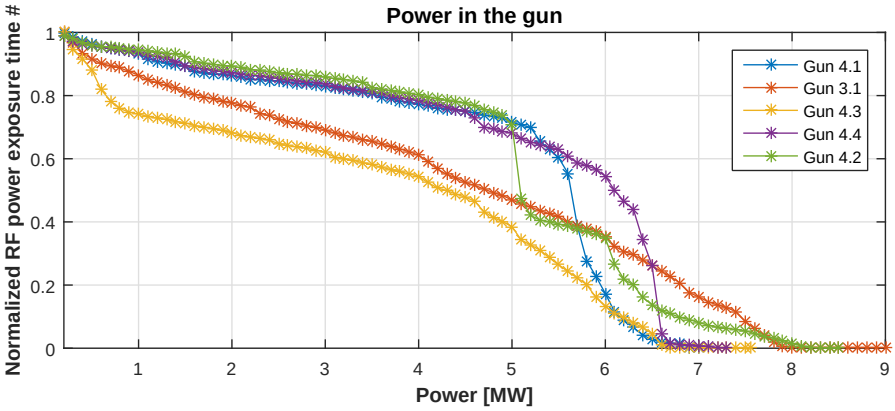

Figure 4.64: RF power exposure time for the gun cavities 4.1, 3.1, 4.3, 4.4 and 4.2.

4.9 RF vacuum window break at Gun 4.4

One of the events during Gun 4.4 operation at PITZ was the THALES RF vacuum window break. After an exchange of the gun cathode spring Gun 4.4 was restarted on 07 April 2014 in order to check the performance of the gun together with the updated cathode vicinity. However, after 9 days of operation, a significant vacuum growth was detected by the gun PG and IGP. The history of the restarted gun is presented in Fig. 4.65.

Despite the vacuum leak it was decided to continue the operation of the gun due to a small rate of the vacuum leak. Nevertheless, since the vacuum window separates the vacuum and the gas part is filled with SF_6, the T-combiner was filled with air in order to prevent a significant contamination of the gun vacuum part by compounds produced from the SF_6 gas. The part of the RF waveguide, where SF_6 was replaced by air, is shown in Fig. 4.66. This configuration of the RF system allowed to continue operation of the gun to proceed with the operation, although the run statistics was already negatively affected.

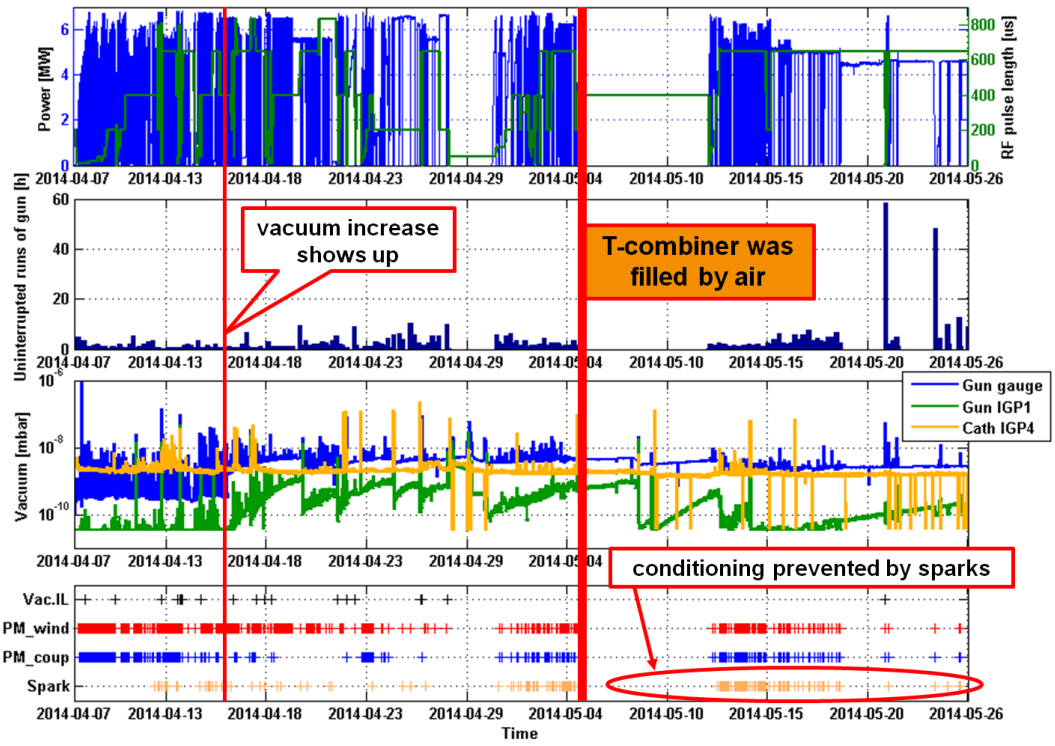

Figure 4.65: Gun 4.4 history of the restarted gun. After the vacuum increase shown-up, the T-combiner was filled with air in order to prevent the gun pollution by SF_6 gas. The restarted gun conditioning was mainly prevented by sparks in the waveguides.

Investigation of the interlock events before the window break did not reveal any specific behavior of interlock detectors. The history of gun operation at the moment of the window break is shown in Fig. 4.67. A few interlock events right before the break were considered in details.

The events right before the RF window break (indicated on the bottom plot of Fig. 4.67 by numbers) are presented by LILI plots in Fig. 4.68. All of plots do not show any specific behavior. The moment of the window break is accompanied by significant growth of the vacuum level and light detected by the PMT located closer to the window. There is no PMT window IL signals in plots 1, 3, 4, 5 of Fig.4.68, because the triggering signals (spikes) are outside of the RF pulse and ADC acquisition timing.

The PITZ experience (also the experience of FLASH and XFEL) on operation with RF photoelectron guns showed that the RF vacuum windows can be one of the most critical parts in the gun setup. A window can break without any specific prerequisite. Therefore an RF vacuum window must be carefully designed for a certain installation location and conditions, and exceptional attention must be paid to the production of the windows.

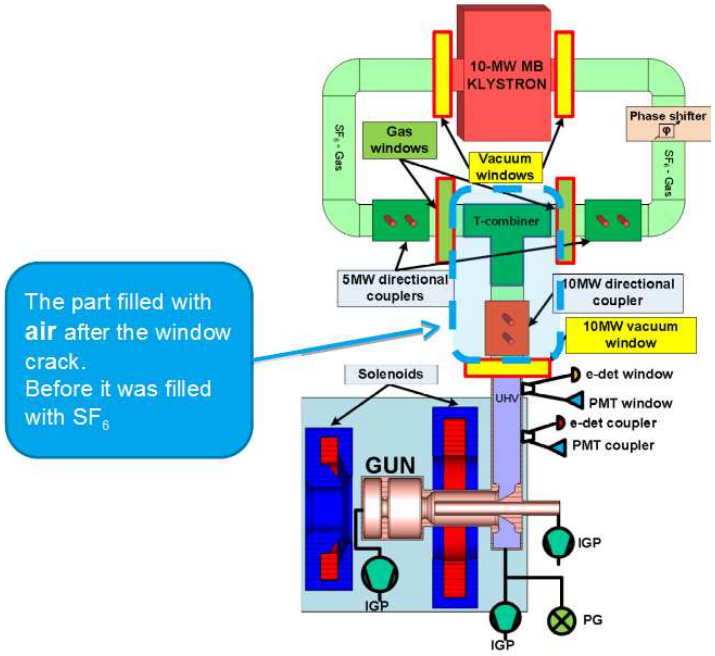

Figure 4.66: The part of the RF waveguide, where SF_6 was replaced by air.

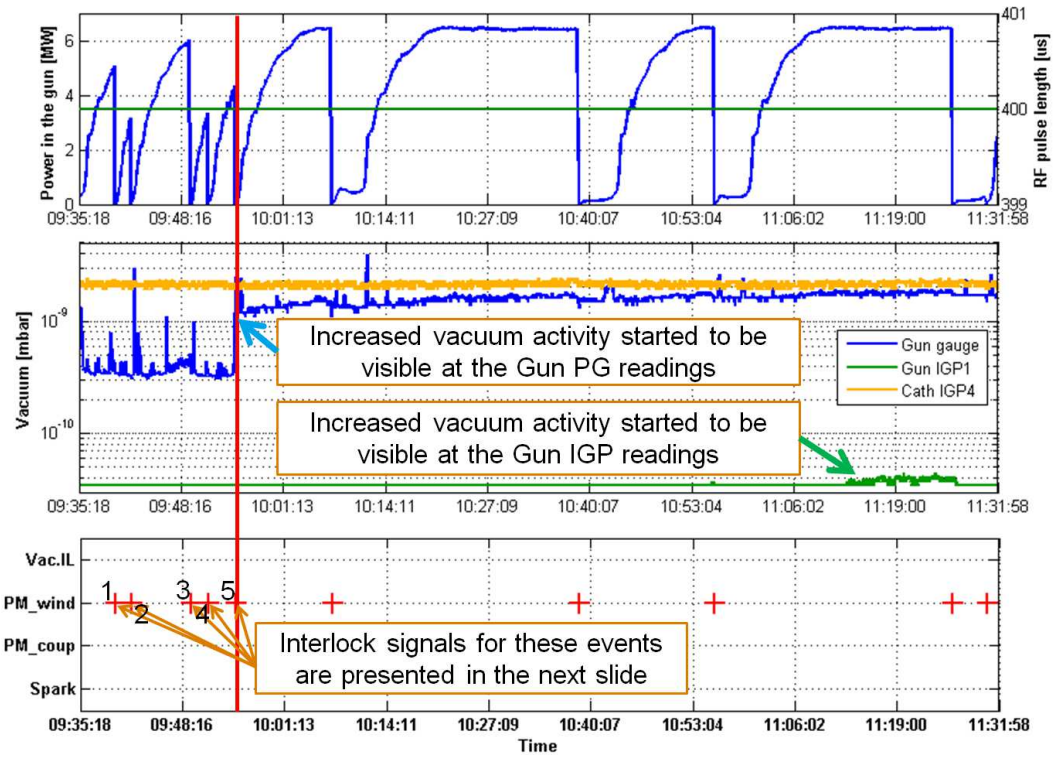

Figure 4.67: Gun 4.4 history around the window break. For more details see the main text.

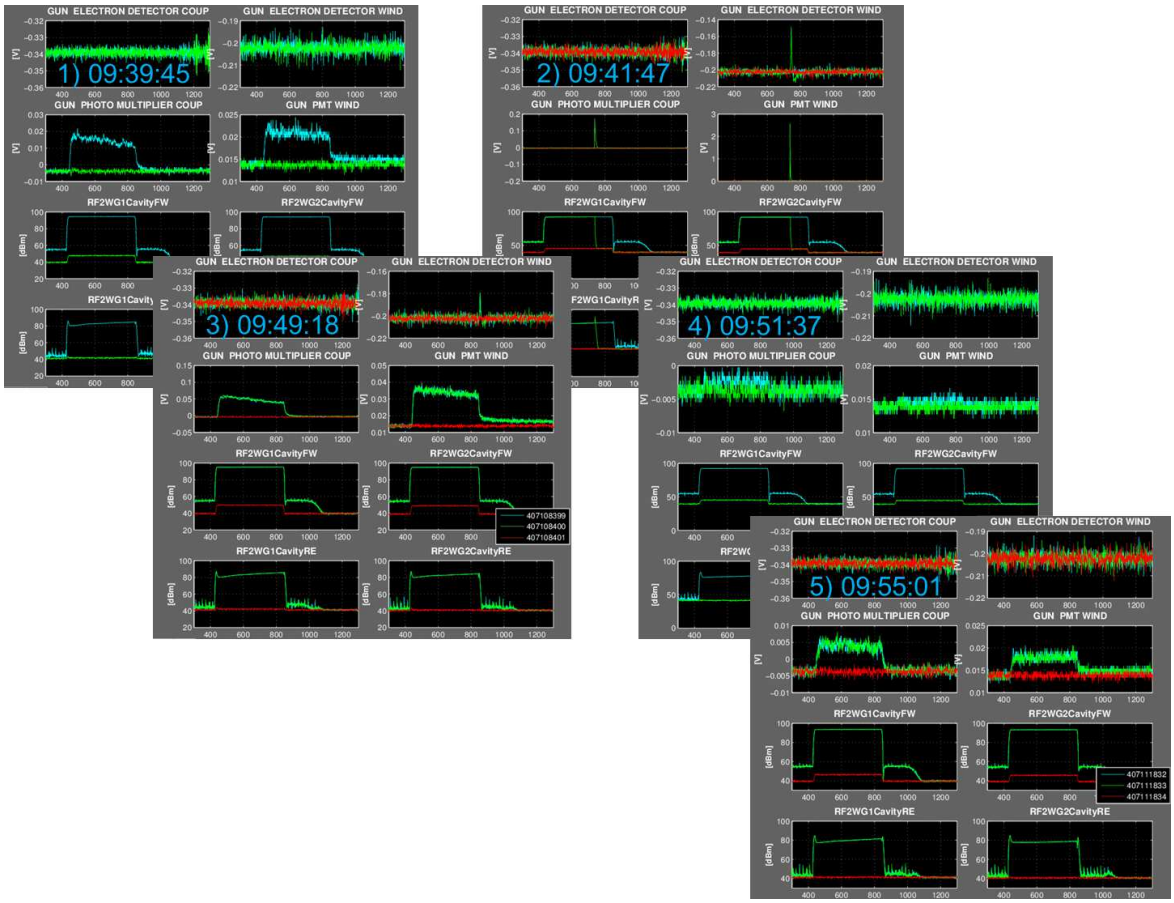

Figure 4.68: LILI plots for the IL events before the vacuum windows break. The events are presented on the bottom plot of Fig. 4.67 and marked by corresponding plot numbers. The plots do not show any specific signal behavior: no PMT activity was detected on the plots 1, 3, 4 and 5; and the spikes on the plot 2 for electron detector and PMTs have shown a rather common structure.

4.10 Dark current history

During the gun operation, a procedure for observing of dark current evolution was established. The dark current measurements were performed with a solenoid scan, from which the maximum value was taken at the fixed combination of peak power and RF pulse length of 6.5 MW and 200 μs, respectively. The dark current history of Gun 4.4 is presented in Fig. 4.69.

Initially, relatively low dark current ($\sim 50\,\mu$A) has been measured. After some time the dark current increased up to $\sim 100\,\mu$A. This can be related to the partial destruction of the contact stripe of the cathode plug, which was exchanged later [75]. After the cathode spring exchange, the dark current level was at about 150 μA. Since the first dark current measurement in this period was done after the RF vacuum window break, the relatively high level of dark current can occur due to worse vacuum conditions.

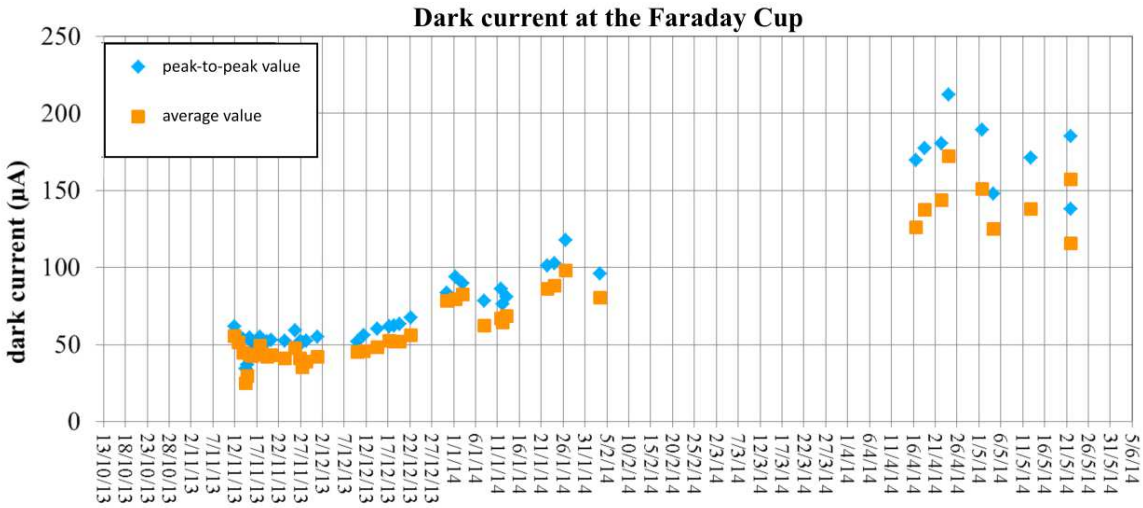

Figure 4.69: Dark current history of Gun 4.4. The dark current measurements were performed at the gun power 6.5 MW and the RF pulse length 200 μs. Each point is the maximum value of the solenoid scan curve.

4.11 Resonance gun temperature drift

The operation of the gun cavities (starting from Gun 4.3) revealed one more feature of the gun behavior. It was noticed that the resonance gun temperature changes with time.

The gun resonance frequency eigenvalue is defined by the internal geometry and particular dimensions. A gun frequency control organized by the cooling water temperature introduces changes in the gun dimensions, mainly cavity radii. But also variations in the inner dimensions of the cavity and in the cooling efficiency and capacity (water velocity or temperature differences) can lead to a resonance temperature change.

As a first step, a well-defined procedure for the resonance temperature observation was established. The water temperature set point was always adjusted for an RF power reflection of 4 % at the fixed forward power of 3.6 MW and pulse length of 400 μs. Recorded resonance temperature of the gun cavity 4.4 is presented in Fig. 4.70, upper plot. Over 7 month the temperature drifted by 6.5 °. The temperature drift is especially noticeable at the beginning of the gun operation.

In order to understand the origin of the resonance temperature drift, a cooling water data analysis was done [76]. For the analysis the data from the following temperature sensors were taken: incoming water temperature from the sensor TF380; cavity temperature from the sensor TF392; outcoming water temperature from the sensor TF382 (see Fig. 3.3). The idea of the studies was to calculate the heat transfer from the gun cavity to the cooling water. Since the heat transfer (HT) is proportional to the water flow, and the difference of incoming and outcoming water temperature (see Eq. 4.14), it can be an indicator of the heating process in the gun cavity.

$$HT \propto V_{flow}(T_{out} - T_{in})\,. \tag{4.14}$$

The heat transfer was calculated for different resonance temperature points, indicated in Fig. 4.70 (upper plot). Functions of the power in the cavity and the cavity temperature were calculated and plotted for the selected points (see the bottom plots of Fig. 4.70). The plots show that there is no dependence of the heat transfer neither on the gun cavity temperature nor on the power in the cavity. This indicates a physical process and excludes possible errors in the measurements.

Additionally, the same resonance temperature drift was observed at various gun temperature sensors, which all can be used for temperature regulation controls. Also, cathode re-insertion and exchange experiments showed that these manipulations cannot explain the observed temperature drift.

Up to now, no correlation of the resonance gun temperature to any parameter of the gun and its environment found. So, the reason of the resonance temperature drift is not fully understood. It remains a subject of monitoring and future studies.

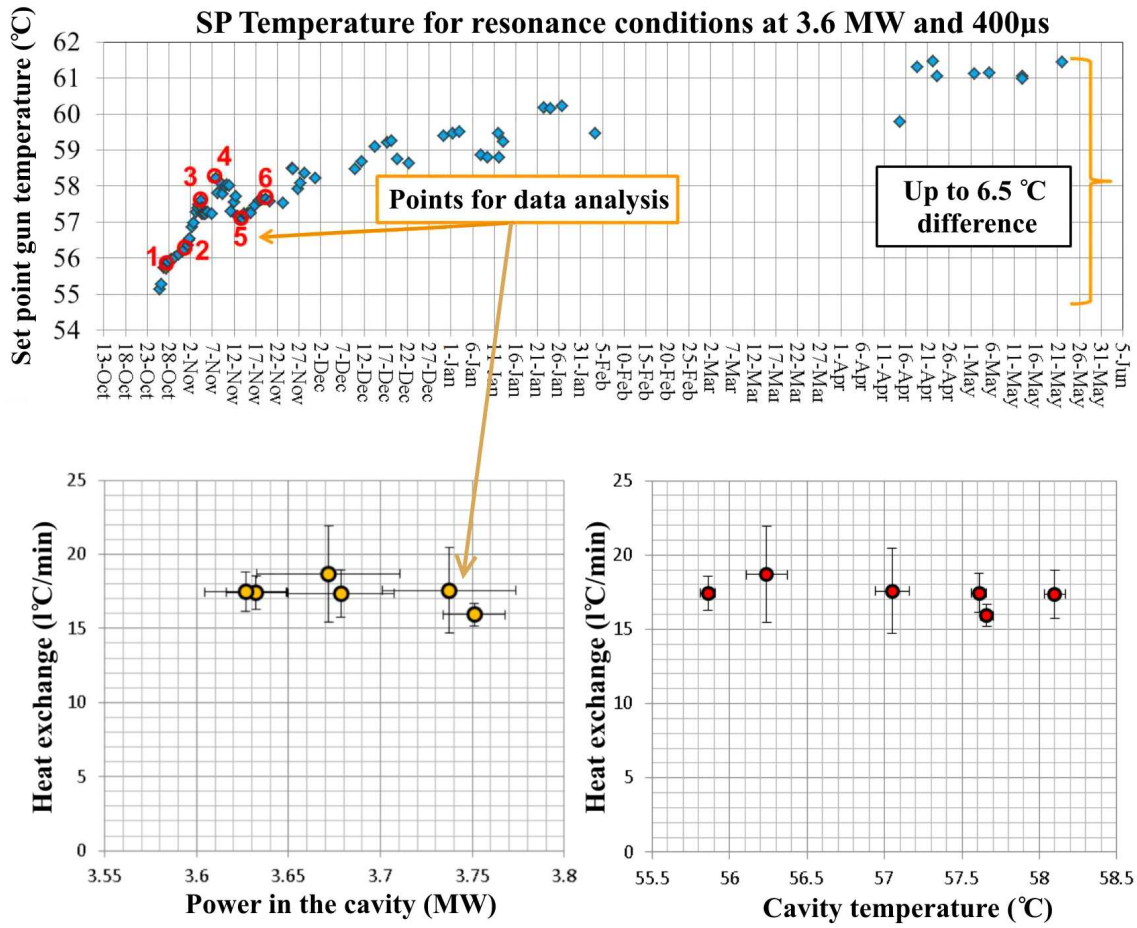

Figure 4.70: History of the resonance temperature drift of Gun 4.4 (upper plot) and heat transfer dependence on power in the cavity (bottom left) and on cavity temperature (bottom right).

Chapter 5

Conclusions

High brightness electron sources for modern superconducting linac-based FELs (like FLASH and European XFEL) must possess the following parameters at supreme level:

peak performance: the beam quality of each bunch

average performance: the beam quality along a pulse train (that kind of operation is required for superconducting linacs)

stability of beam parameters: pulse-to-pulse stability as well as stability within a pulse train

reliability: low interlock rate

The PITZ RF photoelectron gun is able to provide such parameters. Nevertheless, a few things became an issue during the gun characterization and during continuous operation.

Detailed performance studies revealed that the coupler kick is an issue for the operation of the PITZ gun. The simulations of the RF coupler fields show the presence of an asymmetry on the central axis of the coaxial RF coupler, the place where it can disturb the electron beam. In addition to a beam transverse kick, the field asymmetry introduces asymmetries to the beam phase space.

Several experiments were performed on the RF field asymmetry studies. The experiment on the Larmor angle showed that the origin of the beam distortion is located at the position around the main solenoid and the coaxial coupler transition to the full cell. But the experiment on the cathode surface scan, experiment on the beam acceleration outside of the forward power pulse, and experiment on the main solenoid tilt did not help to shine further light on the beam asymmetries problem.

As a possible solution of the RF field asymmetry, additionally to the studies on the actual coupler design a few different RF coupler designs were proposed. The studies on RF coupler modification showed that only the lengthening of the coaxial part of

the RF coupler can decrease the relation between asymmetrical and symmetrical waves and damp the asymmetry at the place where it can have influence on the beam. The studies on other RF coupler designs for the PITZ gun showed that only the design with symmetrical transition from the rectangular to the coaxial waveguides can provide a symmetrical wave at the exit of the coaxial coupler.

The conclusion of these studies is that the most probable reason of the beam distortions are the coupler field asymmetry or main solenoid imperfections. Future experiments on the coupler asymmetry will take place but are beyond the scope of this thesis.

Gun jitters and instabilities, which are essential for a stable electron beam production, were studied and described in chapter 3.

Additionally to the on-line beam based phase monitoring tool, two new beam based methods were introduced and tested. The RF feedback system which utilizes the directional coupler installed after the T-combiner helps to improve the phase stability by a factor of 4. An upgrade of the water cooling system increased the water temperature stability and, as a result, also the phase stability.

The pulse width modulation system [54], which has recently been put in operation, increases the water temperature stability by another 30 percents.

The finally achieved RF amplitude and phase stability are around 0.02 % and 0.07 °, respectively. The stability is still not optimal, but further improvement of the RF gun stability seems to be systematically limited by 20 kHz modulations observed in the μTCA amplitude and phase signals that are very probably originating from the klystron modulator.

Starting from the year 2002, significant experience with the operation of RF guns was accumulated at PITZ. Over this 15 years time period 9 gun cavities were operated with various setups and IL sensors. A conditioning procedure (procedure of power ramping and solenoid operation during the cavity RF training) as described in chapter 4 was established and tested on several guns. The outgassing process for different peak power levels and RF pulse lengths was described. The gun operation experience showed that the typical time of the gun conditioning process takes around 3 to 4 months. Optimal power ramping strategies are discussed for the conditioning process and for gun recovery after interlocks. The main phenomena during the conditioning are multipacting and field emission that produces dark current. Their investiganions, observations, and simulations led to a better understanding of the gun behavior (behavior of the detector signals) during the conditioning process.

The installation of Gun 4.2 with two THALES RF windows showed that this solution can work reliably up to European XFEL specifications after the required conditioning time. During the operation period, no problems from the THALES RF windows were found. But Gun 4.2, which is 10 years old, can not reliably support the XFEL specifications. For this reason the run at XFEL specifications took only 3 month with

many interlocks from the gun. Afterward, the run at 5 MW, 650 μs, 10 Hz was much more stable.

Based on observation of the behavior of various guns, a setup with two RF vacuum windows and a newly produced gun cavity finally satisfies XFEL specifications. This is currently under test with Gun 4.6 and two DESY-type RF windows, which are more cost-efficient than the THALES windows.

Bibliography

[1] M. Altarelli, R. Brinkmann, M. Chergui, W. Decking, B. Dobson, S. Düsterer, G. Grübel, W. Graeff, H. Graafsma, J. Hajdu, *et al.*, "XFEL: The European X-Ray Free-Electron Laser. Technical design report," Tech. Rep. DESY-06-097, DESY XFEL Project Group, 2006.

[2] P. Schmüser, M. Dohlus, and J. Rossbach, *Ultraviolet and soft x-ray free-electron lasers: Introduction to physical principes, experimental results, technological challenges*, vol. 229 of *Springer Tracts in Modern Physics*. Springer, 2009.

[3] T. Tajima and J. M. Dawson, "Laser electron accelerator," *Physical Review Letters*, vol. 43, p. 267, 1979.

[4] M. Litos *et al.*, "High-efficiency acceleration of an electron beam in a plasma wakefield accelerator," *Nature*, vol. 515, no. 7525, pp. 92–95, 2014.

[5] H. Wiedemann, *Particle Accelerator Physics*. Graduate Texts in Physics, Berlin: Springer, 2015.

[6] S. Schreiber, "FLASH-Beam commissioning and operation after upgrade." PITZ collaboration meeting, December 2010.

[7] Homepage of the FLASH Project: `http://flash.desy.de/`.

[8] Homepage of the SLAC LCLS Project: `https://portal.slac.stanford.edu`.

[9] P. Emma, Z. Huang, K.-J. Kim, and P. Piot, "Transverse-to-Longitudinal Emittance Exchange to Improve Performance of High-Gain Free-Electron Lasers," *Physical Review Special Topics - Accelerators and Beams*, vol. 9, p. 100702, 2006.

[10] C. H. Lee, P. E. Oettinger, E. R. Pugh, R. Klinkowstein, J. H. Jacob, J. S. Fraser, and R. L. Sheffield, "Electron Emission of over 200 A/cm2 from a Pulsed-Laser Irradiaied Photocaihode," *IEEE Transactions on Nuclear Science*, vol. 32, no. 5, pp. 3045–3047, 1985.

[11] J. S. Fraser, R. L. Sheffield, and E. R. Gray, "A new high-brightness electron injector for free electron lasers driven by RF linacs," *Nuclear Instruments and Methods in Physics Research Section A: Accelerators, Spectrometers, Detectors and Associated Equipment*, vol. 250, no. 1, pp. 71–76, 1986.

[12] The PITZ team, "The project PITZ 2 - development of optimized photo injectors for free electron lasers," tech. rep., DESY, November 2004.

[13] Homepage of the European XFEL project:
`http://xfel.desy.de/`.

[14] D. Malyutin, *Time resolved transverse and longitudinal phase space measurements at the high brightness photo injector PITZ.* PhD thesis, Universität Hamburg, 2014.

[15] V. Paramonov *et al.*, "The PITZ CDS Booster Cavity RF Tuning and Start of Conditioning," in *Proceedings of the* 25^{th} *International Linear Accelerator Conference, LINAC2010, Tsukuba, Japan*, September 2010. (MOP081).

[16] G. Asova, *Tomography of the Electron Beam Transverse Phase Space at PITZ.* PhD thesis, Institute of Nuclear Research and Nuclear Energy at Bulgarian Academy of Sciences, 2012.

[17] F. Stephan *et al.*, "Detailed characterization of electron sources yielding first demonstration of European X-ray Free-Electron Laser beam quality," *Physical Review Special Topics - Accelerators and Beams*, vol. 13, p. 020704, 2010.

[18] I. Will, G. Koss, and I. Templin, "The upgraded photocathode laser of the TESLA Test Facility," *Nuclear Instruments and Methods in Physics Research Section A: Accelerators, Spectrometers, Detectors and Associated Equipment*, vol. 541, no. 3, pp. 467–477, 2005.

[19] Homepage of Max-Born-Institut for Nonlinear Optics and Short Pulse Spectroscopy:
`https://www.mbi-berlin.de/`.

[20] G. Vashchenko, *Transverse phase space studies with the new CDS booster cavity at PITZ.* PhD thesis, Universität Hamburg, 2013.

[21] M. Krasilnikov, "Motivation of emission studies at PITZ." DESY-TEMF Meeting, June 2015.

[22] M. Krasilnikov, "Update on Beam Imperfections Studies at PITZ." PITZ Collaboration Meeting, June 2016.

[23] R. A. Powell, W. E. Spicer, G. B. Fisher, and P. Gregory, "Photoemission Studies of Cesium Telluride," *Physical Review B*, vol. 8, pp. 3987–3995, 1973.

[24] K. Flöttmann, "Note on thermal emittance of electrons emitted by Cesium Telluride photo cathodes," Tech. Rep. TESLA-FEL 97-01, DESY, February 1997.

[25] K. Flöttmann, "RF-induced beam dynamics in RF guns and accelerating cavities," *Physical Review Special Topics - Accelerators and Beams*, vol. 18, no. 6, p. 064801, 2015.

[26] Hompage of CST-Computer Simulation Technology: `https://www.cst.com/`.

[27] C. D. Child, "Discharge From Hot CaO," *Physical Review (Series I)*, vol. 32, pp. 492–511, 1911.

[28] J. Orloff, *Handbook of Charged Particle Optics*. CRC Press, 2^{nd} ed., 2008.

[29] B. E. Carlsten, "New photoelectric injector design for the Los Alamos National Laboratory XUV FEL accelerator," *Nuclear Instruments and Methods in Physics Research Section A: Accelerators, Spectrometers, Detectors and Associated Equipment*, vol. 285, no. 1–2, pp. 313–319, 1989.

[30] M. Reiser, *Theory and design of charged particle beams*. Wiley series in beam physics and accelerator technology, Wiley-VCH, 2008.

[31] H. Goldstein, *Classical mechanics*. Addison-Wesley, 3^{rd} ed., 2001.

[32] K. Flöttmann, "Some basic features of the beam emittance," *Physical Review Special Topics - Accelerators and Beams*, vol. 6, p. 034202, 2003.

[33] D. H. Dowell, "Analysis and Cancellation of RF Coupler-Induced Emittance Due to Astigmatism," tech. rep., SLAC/LCLS-II, March 2015.

[34] L. Staykov, *Characterization of the transverse phase space at the photo-injector test facility in DESY, Zeuthen site*. PhD thesis, Universität Hamburg, 2008.

[35] M. Dohlus, I. Zagorodnov, E. Gjonaj, and T. Weiland, "Coupler Kick for Very Short Bunches and its Compensation," in *Particle accelerator. Proceedings of the* 11^{th} *European Conference, EPAC08, Genoa, Italy*, June 2008. (MOPP013).

[36] N. Sobenin and O. Milovanov, *RF technics*. Moscow: Atomizdat, 1980.

[37] M. Marcuvitz, *Waveguide handbook*. Peter Peregrinus Limited, 1986.

[38] A. B. El-Kareh and J. C. El-Kareh, *Electron Beams, Lenses and Optics*. Orlando: Academic, 1970.

[39] Homepage of ASTRA (A Space charge TRacking Algorithm):
`http://www.desy.de/~mpyflo`.

[40] D. H. Whittum, "Introduction to electrodynamics for microwave linear accelerators," in *Frontiers of accelerator technology. Proceedings of the Joint US-CERN-Japan International School, Hayama and Tsukuba, Japan*, September 1996. (SLAC-PUB-7802).

[41] B. Dwersteg, D. Kostin, M. Lalayan, C. Martens, and W. D. Möller, "TESLA RF power couplers development at DESY," in *Proceedings of the* 10^{th} *Workshop on RF Superconductivity, Tsukuba, Japan*, September 2001.

[42] Y. Kang, "Coupler Electromagnetic Design." HPC Workshop, TJNAF, October–November 2002.

[43] J. W. McKenzie, P. A. Goudket, T. J. Jones, and B. L. Militsyn, "High repetition rate S-band photoinjector design for the CLARA FEL," in *Proceedings of the* 36^{th} *International Free Electron Laser Conference, FEL2014, Basel, Switzerland*, August 2014. (THP064).

[44] M. Otevrel *et al.*, "Conditioning of a New Gun PITZ equipped with an upgraded RF Measurement System," in *Proceedings of the* 32^{th} *International Free Electron Laser Conference, FEL2010, Malmö, Schweden*, August 2010. (WEPB05).

[45] C. T. Dervos and P. Vassiliou, "Sulfur hexafluoride (SF6): global environmental effects and toxic byproduct formation," *Journal of the Air & Waste Management Association*, vol. 50, no. 1, pp. 137–141, 2000.

[46] Hompage of the Mega Industries, LLC:
`www.megaind.com`.

[47] R. Romaniuk, "LLRF System Components Development," Tech. Rep. TESLA 2008-03, DESY, March 2008.

[48] E. Vogel, W. Koprek, and P. Pucyk, "The gun RF control at FLASH (and PITZ)." FLASH Seminar, December 2006.

[49] Hompage of the Siemens AG:
`www.siemens.com`.

[50] Hompage of the National Instruments:
`www.ni.com`.

[51] J.-H. Han, *Dynamics of Electron Beam and Dark Current in Photocathode RF Guns*. PhD thesis, Universität Hamburg, 2005.

[52] H. Schlarb, N. Heidbrook, H. Kapitza, F. Ludwig, and N. Nagad, "Precision RF gun phase monitor system for FLASH," in *Proceedings of the* 10^{th} *European Particle Accelerator Conference, EPAC06, Edinburgh, Scotland*, June 2006. (TUPCH025).

[53] M. Krasilnikov, "Beam based monitoring of the RF Photo Gun stability at PITZ," in *Proceedings of the* 14^{th} *Beam Instrumentation Workshop, BIW10, Santa Fe, New Mexico, USA*, May 2010. (TUPSM104).

[54] M. Hoffmann and S. Pfeiffer, "Activities and Laboratory Reports - Gun Water Stability." PITZ collaboration meeting, November 2015.

[55] M. Krasilnikov, "Improved beam-based method for RF photo gun stability measurements." DESY-TEMF meeting, June 2015.

[56] M. Hoffmann, "LLRF System at the PITZ RF Gun." PITZ collaboration meeting, October 2011.

[57] S. Schreiber. Personal communication.

[58] R. H. Fowler and L. Nordheim, "Electron emission in intense electric fields," *Proceedings of the Royal Society*, vol. A119, pp. 173–181, 1928.

[59] J. W. Wang and G. A. Loew, "Field emission and RF breakdown in high gradient room temperature linac structures," in *Frontiers of accelerator technology. Proceedings of the Joint US-CERN-Japan International School, Hayama and Tsukuba, Japan*, September 1996. (SLAC-PUB-7684).

[60] F. Rohrbach, *On Mechanisms That Lead to Very High Voltage Electric Spark Formation in a Vacuum for Measuring Breakdown Delay Time*. PhD thesis, Ecole Polytechnique, 1971.

[61] M. A. Furman and M. T. F. Pivi, "Probabilistic model for the simulation of secondary electron emission," *Physical Review Special Topics - Accelerators and Beams*, vol. 5, p. 124404, 2002.

[62] P. A. Redhead, J. P. Hobson, and E. V. Kornelsen, *Physical Basis of Ultrahigh Vacuum*. London: Chapman and Hall, 1968.

[63] H. Bruining, *Physics and Applications of Secondary Electron Emission*. New York: Pergamon Press, McGraw-Hill Book Co., 1954.

[64] I. Petrushina, "Multipacting Simulation for the PITZ RF Photo Gun." DESY Summer Student Programme, August 2012.

[65] Hompage of Thales S.A.:
`thalesgroup.com`.

[66] D. Lipka, W. Kleen, J. Lund-Nielsen, D. Nölle, S. Vilcins, and V. Vogel, "Dark current monitor for the European XFEL," in *Proceedings of the* 10^{th} *European Workshop on Beam Diagnostics and Instrumentation for Particle Accelerators, DIPAC2011, Hamburg, Germany*, May 2011. (WEOC03).

[67] M. Otevrel, "Open Momentum Analysis code: OMA," tech. rep., DESY, September 2013.

[68] Homepage of Tektronix:
`www.tek.com`.

[69] Homepage of MathWorks:
`www.mathworks.com`.

[70] A. Brinkmann, J. Iversen, D. Reschke, and J. Ziegler, "Dry-ice cleaning on SRF cavities," in *Particle accelerator. Proceedings of the* 10^{th} *European Conference, EPAC06, Edinburgh, Scotland*, June 2006. (MOPCH154).

[71] N. Brusova, V. Paramonov, I. Rybakov, and A. Skasyrskaya, "Physical specifications of the Gun 5 RF cavity for X-FEL requirements," tech. rep., INR Moscow, DESY Zeuthen, DESY Hamburg, July 2016.

[72] A. Oppelt *et al.*, "Status and first results from the upgraded PITZ facility," in *Proceedings of the* 27^{th} *International Conference on Free Electron Lasers, FEL2005, Palo Alto, California*, August 2005. (THPP043).

[73] M. Krasilnikov *et al.*, "Experimentally minimized beam emittance from an L-band photoinjector," *Physical Review Special Topics - Accelerators and Beams*, vol. 15, p. 100701, 2012.

[74] F. Eints, "Status Thales Windows and Quality Management Measures." Gun Review meeting, DESY Hamburg, September 2014.

[75] S. Lederer, "RF-contact spring designs." PITZ collaboration meeting, May 2014.

[76] M. Krasilnikov and I. Isaev, "PITZ: Gun 4.4 resonance temperature drift investigation." PITZ Physics Seminar, November 2013.

Acknowledgments

There are many people who have contributed to the success of this work and whom I would like to express my sincerest gratitude. First of all this is my supervisor Prof. Dr. Jörg. Roßbach. I am very thankful for his time, effort and precious comments on my thesis. Furthermore, I would like to thank Dr. Frank Stephan who gave me the great opportunity to work for the PITZ group and who exercised lots of patience over the years of my PhD. I really appreciate the time I spend with Dr. Mikhail Krasilnikov on amazing motivating discussions, it was always an important help for me.

Furthermore, I am extremely thankful to Dr. G. Vashchenko, Dr. A. Oppelt, Dr. M. Groß, Dr. H. Qian, Dr. Y. Chen, Dr. Q. Zhao, Dr. M. Otevrel, Dr. G. Asova, Dr. Y. Renier, Dr. B. Marchetti, Dr. S. Rimjaem, Dr. D. Richter, Dr. H. Huck, Dr. X. Li, Prof. N. Sobenin and MEPhI RF-lab team, J. D. Good, G. Loisch, P. Boonporn-prasert, Dr. D. Malyutin, Dr. Y. Ivanisenko, Dr. G. Kourkafas, Dr. G. Trowitzsch, B. Petrosyan, Dr. D. Kalantaryan, D. Melkumyan, S. Weisse, M. Pohl, Dr. F. Brinker, Dr. S. Schreiber, Dr. D. Kostin, technical staff of DESY Zeuthen and all members of the PITZ group. All of you gave me the great time during my work (and sometimes even "adventure time").

Finally, I want to thank my family: my lovely wife, parents, and sister. The support you gave me made my progress possible and means a lot to me!

Eidesstattliche Versicherung

Hiermit versichere ich an Eides statt, die vorliegende Dissertationsschrift selbst verfasst und keine anderen als die angegebenen Hilfsmittel und Quellen benutzt zu haben.

Die eingereichte schriftliche Fassung entspricht der auf dem elektronischen Speichermedium.

Die Dissertation wurde in der vorgelegten oder einer ähnlichen Form nicht schon einmal in einem früheren Promotionsverfahren angenommen oder als ungenügend beurteilt.

Ort, Datum Unterschrift der Doktorandin / des Doktoranden